UC San Diego

UC San Diego Electronic Theses and Dissertations

Title

Modulation of intermolecular interactions in single- molecule magnets

Permalink

https://escholarship.org/uc/item/8hc2p08c

Author

Heroux, Katie Jeanne

Publication Date

2010

Peer reviewed|Thesis/dissertation

eScholarship.org Powered by the California Digital Library
University of California

UNIVERSITY OF CALIFORNIA, SAN DIEGO

Modulation of Intermolecular Interactions in Single-Molecule Magnets

A dissertation submitted in partial satisfaction of the requirements of the degree

Doctor of Philosophy

in

Chemistry

by

Katie Jeanne Heroux

Committee in charge:

Professor David N. Hendrickson, Chair
Professor Seth M. Cohen
Professor Andrew C. Kummel
Professor Melvin Y. Okamura
Professor Arnold L. Rheingold

2010

The Dissertation of Katie Jeanne Heroux is approved, and it is acceptable in quality and form for publication on microfilm and electronically:

_____

_____

_____

_____

_____
Chair

University of California, San Diego

2010

DEDICATION

for Mom

EPIGRAPH

I got a feeling I'm gonna be much smarter than you pretty soon.

-George Costanza

TABLE OF CONTENTS

Signature Page……iii
Dedication……iv
Epigraph……v
Table of Contents……vi
List of Figures……x
List of Tables……xxi
Acknowledgements……xxiii
Vita……xxv
Abstract of the Dissertation……xxvii

Chapter 1: *Single-Molecule Magnets*……1
1.1. Introduction……2
1.2. Magnetic Susceptibility……4
1.2.1. Direct current measurements……4
1.2.2. Alternating current measurements……10
1.3. Mixed-Valent [Mn_4] Dicubanes……12
1.4. Magnetization Hysteresis and Berry Phase……15
1.5. High-Frequency Electron Paramagnetic Resonance (HFEPR)……22
1.6. Structural Considerations and Environmental Coupling……25
1.7. Outline of Dissertation……34
1.8. References……36

Chapter 2: *Ferrocene-Substituted Single-Molecule Magnets*……43
2.1. Introduction……44
2.2. Experimental Section……46
2.2.1. Preparation……46
2.2.2. X-Ray Crystallography……49
2.2.3. Physical Measurements……54
2.3. Results and Discussion……55

2.3.1. Synthesis……55
2.3.2. Description of Crystal Structures……..57
2.3.3. DC Magnetic Susceptibility Studies……..65
2.3.4. AC Magnetic Susceptibility Studies……..76
2.3.5. Electrochemistry……82
2.4. Conclusions……..87
2.5. References……...89

Chapter 3: *Sterically-Isolated [Mn_4] Single-Molecule Magnets Exhibiting Novel Quantum Properties*..... 92
3.1. Introduction ……93
3.2. Experimental Section……99
3.2.1. Preparation……99
3.2.2. X-Ray Crystallography……..……..102
3.2.3. Physical Measurements……..……105
3.3. Results and Discussion…….…….108
3.3.1. Synthesis……...…108
3.3.2. Description of Crystal Structures……..……..109
3.3.3. Crystal Packing and Intermolecular Interactions……..…..116
3.3.4. DC Magnetic Susceptibility……127
3.3.5. AC Magnetic Susceptibility……..……..146
3.3.6. Single Crystal HFEPR Studies……..……..159
3.3.7. Single Crystal Magnetization Hysteresis…….....167
3.4. Conclusions……..…..179
3.5. References……..181

Chapter 4: *Single-Stranded Manganese Wheels*.....184
4.1. Introduction……..……..185
4.1.1. Wheel-Shaped SMMs……..…185
4.1.2. [Mn_{12}] Single-Stranded Wheels……..……187

4.1.3. [Mn_{16}] Single-Stranded Wheels……..……197
4.2. Experimental Section……..……207
4.2.1. Preparation……..…….207
4.2.2. X-Ray Crystallography……..…..208
4.2.3. Physical Measurements……..….208
4.3. Results and Discussion……..…….210
4.3.1. Synthesis and Structure……..……210
4.3.2. Magnetic Susceptibility Studies…….……216
4.4. Conclusions……..……..225
4.5. References……..……226

Chapter 5: *Hexanuclear Manganese Rod-Shaped Single-Molecule Magnets*…....229
5.1. Introduction……..…..230
5.2. Experimental Section……..…231
5.2.1. Preparation……..…….231
5.2.2. X-Ray Crystallography……..……..234
5.2.3. Physical Measurements……..….237
5.3. Results and Discussion……...237
5.3.1. Description of Crystal Structures……..…..237
5.3.2. DC Magnetic Susceptibility……..……..251
5.3.3. AC Magnetic Susceptibility……..…..264
5.3.4. Structural Considerations……..…..269
5.4. Conclusions……..……..270
5.5. References……..…272

Chapter 6: *Superexchange through Dicyanamide Bridges in Dinuclear Complexes and Single-Molecule Magnets*……..….273
6.1. Introduction……..……..274
6.2. Experimental Section……..……281
6.2.1. Preparation……..…....281

6.2.2. X-Ray Crystallography……..…..282
6.2.3. Physical Measurements…….……..……285
6.3. Results and Discussion……..…….285
6.3.1. Infrared Spectroscopy……..……285
6.3.2. Description of Crystal Structures……..……..286
6.3.3. Magnetic Susceptibility Studies……..……291
6.3.4. Structural Considerations……..……..294
6.3.5. Implications for Dicyanamide-Linked SMMs……..…...300
6.4. Conclusions……..……..302
6.5. References……..……303

LIST OF FIGURES

Figure 1.1. Molecular structure of $[Mn_{12}O_{12}(O_2CMe)_{16}(H_2O)_4] \cdot CH_3CO_2H \cdot 4H_2O$ ($Mn_{12}AC$).....3

Figure 1.2. Two J-value Kambe vector coupling scheme for $[Mn_4]$ butterfly and dicubane complexes.……....6

Figure 1.3. (top) PovRay plot of $[Mn^{II}_2Mn^{III}_2(O_2CPh)_4(mdea)_2(mdeaH)_2]$ with hydrogen atoms omitted for clarity and (bottom) ORTEP of $[Mn^{II}_2Mn^{III}_2(O_2CPh)_4(bdea)_2(bdeaH)_2]$ with thermal ellipsoids drawn at 50% probability level……14

Figure 1.4. Temperature-dependent magnetization vs. field plot for $Mn_{12}Ac$.....16

Figure 1.5. Potential energy, E_m, *vs.* spin projection, m_s, for a S = 10 SMM……16

Figure 1.6. Double-well potential plot in an applied field, H……....18

Figure 1.7. Parallel transport of a vector in a loop along a flat surface (left) and a curved surface (right)…….……19

Figure 1.8. Unit sphere with the minima **A** and **B** connected by two paths; clockwise and counterclockwise. The x, y and z axes are the hard, medium and easy axes, respectively……...19

Figure 1.9. Molecular structure and spin orientations in the S = 10 complex $[Fe_8O_2(OH)_{12}(C_6H_{15}N_3)_6]Br_8 \cdot 9H_2O$ (Fe_8)……..21

Figure 1.10. Tunnel splitting measured as a function of transverse field ($\varphi = 0°$) for the Fe_8 SMM, where n = 0, 1, 2 for the tunneling transitions m_s = -10 to m_s = 10-n……...21

Figure 1.11. Temperature-dependent HFEPR spectra in the hard plane of $[Mn^{III}_3Ni^{II}(hmp)_3O(N_3)_3(O_2CPh)_3]$ from 2-20 K at 59.9 GHz……24

Figure 1.12. Energy level diagram for the hard plane of $[Mn^{III}_3Ni^{II}(hmp)_3O(N_3)_3(O_2CPh)_3]$ where blue and red arrows indicate the EPR transitions **a-g** and **X** in Figure 1.10, respectively.…..24

Figure 1.13. Frequency-dependent HFEPR peak positions for $[Mn^{III}_3Ni^{II}(hmp)_3O(N_3)_3(O_2CPh)_3]$ at 50-135 GHz with the field oriented (a) close to the easy axis and (b) exactly in the hard plane. Solid curves represent best simulations of the experimental data……...26

Figure 1.14. ORTEP of $[Mn_4O_3Cl_4(O_2CEt)_3(py)_3]_2$, $[Mn_4]_2$, showing intermolecular H-bonding contacts……28

Figure 1.15. Temperature-dependent magnetization hysteresis plot for $[Mn_4]_2$……..29

Figure 1.16. Energy vs. magnetic field plot for $[Mn_4]_2$ showing levels likely to be populated at very low temperatures……..29

Figure 1.17. Magnetization vs. field plot for $[NEt_4]_3[Mn_3Zn_2(salox)_3O(N_3)_6Cl_2]$ with an ORTEP shown in top inset and the growth of $k = 1$ QTM resonance with application of a transverse field, H_T, shown in bottom inset……...…..32

Figure 2.1. ORTEP of $[Mn_3O(O_2CCH_3)_6(py)_3]$ with hydrogen atoms omitted for clarity……56

Figure 2.2. ORTEP of **1a** with thermal ellipsoids drawn at 50% probability level. Solvent and hydrogen atoms omitted for clarity……58

Figure 2.3. Intermolecular H-bonding in **1a**……..59

Figure 2.4. ORTEP of **2** with hydrogen atoms omitted for clarity and thermal ellipsoids at 30% probability level……61

Figure 2.5. ORTEP of **3** (top) and **4** (bottom) with hydrogen and solvate atoms omitted for clarity and thermal ellipsoids drawn at 30% probability level……63

Figure 2.6. (left) $\chi_M T$ *vs.* T in applied dc field of 1 T and (right) reduced magnetization, $M/N\mu_B$ *vs.* H/T for **1**……...66

Figure 2.7. Field-dependence of $\chi_M T$ *vs.* T for **2**……...68

Figure 2.8. $\chi_M T$ *vs.* T for **2** in applied dc field of 0.1 T with theoretical fit shown as red curve……..69

Figure 2.9. Reduced magnetization *vs.* H/T for **2** with theoretical fit shown as black curves……70

Figure 2.10. Field-dependence of $\chi_M T$ *vs.* T for **3** (top) and **4** (bottom)……..72

Figure 2.11. $\chi_M T$ *vs.* T in applied dc field of 0.1 T for **3** (top) and **4** (bottom) with theoretical fits shown as red curves……73

Figure 2.12. Reduced magnetization *vs. H/T* for **3** (top) and **4** (bottom) with theoretical fits shown as solid black curves……75

Figure 2.13. In-phase (χ_M') and out-of-phase (χ_M'') ac susceptibility for **2**…….77

Figure 2.14. In-phase (χ_M') and out-of-phase (χ_M'') ac susceptibility for **3**……..…78

Figure 2.15. In-phase (χ_M') and out-of-phase (χ_M'') ac susceptibility for **4**…….....80

Figure 2.16. Arrhenius plot of out-of-phase ac susceptibility for **4**…….81

Figure 2.17. Extrapolation of 10 Hz $\chi_M'T$ *vs. T* data for **2-4**. Ground state spin estimates from spin-only formula……82

Figure 2.18. Electrochemistry of 5 mM solution of "Mn_3O-Ac" Triangle (top) and **1** (bottom) in DMF with 0.1 M TBAH and glassy carbon working, platinum wire counter, and Fc/Fc^+ reference electrodes…….83

Figure 2.19. Electrochemistry of **3** (top, 1 mM solution in CH_2Cl_2; bottom, 0.1 mM solution in THF) with 0.1 M TBAH and glassy carbon working, platinum wire counter, and Fc/Fc^+ reference electrodes……...85

Figure 2.20. Electrochemistry of 1 mM solution of **4** in CH_2Cl_2 (top) and THF (bottom) with 0.1 M TBAH and glassy carbon working, platinum wire counter, and Fc/Fc^+ reference electrodes……..86

Figure 3.1. Molecular structures of (top) glycine betaine, Bet, and (bottom) pyridyl betaine, pyBet……..95

Figure 3.2. Schematic of a polyCBMA-grafted surface (left) with immobilized proteins (right). CBMA is carboxybetaine methacrylate, EDC is 1-ethyl-3-(3 dimethylaminopropyl)-carbodiimide, and NHS is N-hydroxysuccinimide……95

Figure 3.3. Core structure of $[Mn_{12}O_{12}(Bet)_{16}(EtOH)_4](PF_6)_{14} \cdot 4MeCN \cdot H_2O$…...97

Figure 3.4. ORTEP of **5** with BPh_4^- anions and H-atoms omitted for clarity. Thermal ellipsoids drawn at 30% probability level……..…….110

Figure 3.5. ORTEP of **6** with BPh_4^- anions and H-atoms omitted for clarity. Thermal ellipsoids drawn at 30% probability level……..…….110

Figure 3.6. ORTEP of **7** with BPh_4^- anions and H-atoms omitted for clarity. Thermal ellipsoids drawn at 30% probability level……..….111

Figure 3.7. ORTEP of **8** with BPh_4^- anions and H-atoms omitted for clarity. Thermal ellipsoids drawn at 30% probability level……..…….111

Figure 3.8. ORTEP of **9** with BPh_4^- anions, H-atoms, and solvate molecules omitted for clarity. Thermal ellipsoids drawn at 30% probability level……..…...112

Figure 3.9. Alignment of Jahn-Teller axes in the unit cell of **5**. Only The dicubane cores are shown with Jahn-Teller axes highlighted in black……..…….117

Figure 3.10. Crystal packing of **5** as viewed down a-axis (left) and b-axis (right). BPh_4^- anions highlighted in black…… ……..…...117

Figure 3.11. Stereo-view of the unit cell of **5**……..……..118

Figure 3.12. Crystal packing of $[Mn_4(O_2CPh)_4(mdeaH)_2(mdea)_2]$ (top) And $[Mn_4(O_2CPh)_4(bdeaH)_2(bdea)_2]$ (bottom) as viewed down the b-axis……..119

Figure 3.13. (Left) Alignment of Jahn-Teller axes in the unit cell of **6**, with only the dicubane cores are shown and Jahn-Teller axes highlighted as black sticks. (Right) Face-indexed single crystal of **6** with (0 0 -1), (0 1 0), and (-1 0 1) faces labeled……..…...121

Figure 3.14. Crystal packing of **6** as viewed down a*-axis (top) and c-axis (bottom) with BPh_4^- anions highlighted in black……..…..123

Figure 3.15. Stereo-view of the unit cell of **6**……..……..124

Figure 3.16. Space-filling model of BPh_4^- anions encapsulating a single $[Mn_4]$ unit of **6**……..…….124

Figure 3.17. Stereo-view of the unit cell of **7**……..…..126

Figure 3.18. $\chi_M T$ *vs. T* at (top) various applied fields and at (bottom) 0.1 T with theoretical fit shown as solid red curve for **5**…….....128

Figure 3.19. Reduced magnetization *vs. H/T* for **5** with theoretical fits shown as solid black curves……..……130

Figure 3.20. $\chi_M T$ *vs. T* at (top) various applied fields and at (bottom) 0.1 T with theoretical fit shown as solid red curve for **6**……....132

Figure 3.21. Reduced magnetization *vs. H/T* for **6**, with theoretical fits shown as solid black curves……..……133

Figure 3.22. $\chi_M T$ *vs. T* at (top) various applied fields and at (bottom) 0.1 T with theoretical fit shown as solid red curve for **7**……..……..135

Figure 3.23. Reduced magnetization *vs. H/T* for **7** with theoretical fits shown as solid black curves……..……136

Figure 3.24. Field-dependence of $\chi_M T$ *vs. T* for **8 (**left) and **9** (right)……..….138

Figure 3.25. $\chi_M T$ *vs. T* in applied field of 0.1 T **8** (left) and **9 (**right) with theoretical fits shown as solid red curves……..……138

Figure 3.26. Reduced magnetization *vs. H/T* for **8** (left) and **9** (right) with theoretical fits shown as solid black curves……..…140

Figure 3.27. (Top) Two *J*-value and (bottom) three *J*-value coupling Schemes for complex **6**……..……142

Figure 3.28. Dc magnetic susceptibility for **6**, in applied fields of 1-5 T and a temperature range of 300-1.8 K. Least-squares fit to the spin Hamiltonian (by full-matrix diagonalization) represented by solid black curves for two J-value model (top) and three J-value model (bottom)……..…143

Figure 3.29. Zero-field eigenvalue spectrum of **6**, for parameters from two J-value fit as discussed in the text……..145

Figure 3.30. In-phase (χ_M') and out-of-phase (χ_M'') ac susceptibility for **5** in an oscillating field up to 1 kHz……..……...148

Figure 3.31. In-phase (χ_M') and out-of-phase (χ_M'') ac susceptibility for **5** in an oscillating ac field up to 10 kHz……...…149

Figure 3.32. Arrhenius plot of high-frequency ac susceptibility for **5**……...…...149

Figure 3.33. In-phase (χ_M') and out-of-phase (χ_M'') ac susceptibility for **6** in an oscillating field up to 1 kHz……..…...150

Figure 3.34. Arrhenius plot of low-frequency ac susceptibility for **6**……..…...150

Figure 3.35. In-phase (χ_M') and out-of-phase (χ_M'') ac susceptibility for **6** in an oscillating field up to 10 kHz……..……..…152

Figure 3.36. Arrhenius plot of high-frequency ac susceptibility for **6**……...152

Figure 3.37. In-phase (χ_M') and out-of-phase (χ_M'') ac susceptibility for **7**……..….153

Figure 3.38. Arrhenius plot of out-of-phase ac susceptibility for **7**……...153

Figure 3.39. In-phase (χ_M') and out-of-phase (χ_M'') ac susceptibility for **8** (left) and **9** (right) in an oscillating field up to 1 kHz…….…..….155

Figure 3.40. In-phase (χ_M') and out-of-phase (χ_M'') ac susceptibility for **8** (left) and **9** (right) in an oscillating field up to 10 kHz……...……...156

Figure 3.41. Extrapolation of 10 Hz $\chi_M'T$ vs. T data. Ground state spin estimates from spin-only formula……..……158

Figure 3.42. (Left) Temperature-dependent HFEPR spectra measured along the easy axis of **6** in the temperature range of 1.7-20 K and a frequency of 139.5 GHz. (Right) Enlargement of 20 K spectrum…....161

Figure 3.43. Temperature-dependent HFEPR spectra measured in the hard plane of **6** in the temperature range of 1.7-20 K and a frequency of 67.3 GHz……..…….161

Figure 3.44. Frequency-dependent HFEPR spectra of **6** measured (top) along the easy axis at 3 K and 128-290 GHz and (bottom) in the hard plane at 10 K and 50-211 GHz……..…163

Figure 3.45. Trimer model used to simulate frequency-dependent EPR data for **6** where **A** and **B** represent S = 4 and S = 5/2 spins, respectively, *J* is the coupling interaction between **A** and **B**, and *JT* is the Jahn-Teller axis of each ion tilted from the easy axis (z-axis) by angles ϕ and θ …….....164

Figure 3.46. Simulation of easy axis (top) and hard plane (bottom) EPR spectra from Figure 3.44. All zfs tensors are parallel……...….166

Figure 3.47. (Left) Alignment of a single-crystal of **6** with respect to Jahn-Teller orientation from crystallographic data and (right) the actual position of the easy axis……..……...168

Figure 3.48. (Top) Temperature-dependence of the magnetization (M/M_s) *vs.* longitudinal field (H_z) at a sweep rate of 0.02 T/min. (Bottom) First-derivative of M/M_s *vs.* H_z plot showing QTM resonances regularly spaced 0.2 T apart……..……..169

Figure 3.49. Two different views of the tunneling probability, P, at resonance $k = 0$ as a function of the angle, ϕ, of the applied transverse field. The hard axis is assigned along the 123°-303° direction……..……172

Figure 3.50. Tunneling probability, P, at resonance $k = 0$ (top) and $k = 1$ (bottom) as a function of transverse field, H_T, applied at angle, ϕ, in the hard plane……..……173

Figure 3.51. Contour plots of the data in Figure 3.49 for $k = 0$ (top) and $k = 1$ (bottom). The hard axis is represented by the dotted line at $\phi = 122°$ in both plots……..……...175

Figure 3.52. Symmetry of the Berry phase upon reversal of the transverse field, H_T, for $k = 0$ and $k = 1$ (top) and upon reversal of both H_T and the longitudinal field, H_z, for $k = 1$ (bottom)……..…...178

Figure 4.1. ORTEP of [Mn_{12}-allyl] with hydrogen atoms omitted for clarity and thermal ellipsoids at 50% probability level……..…….188

Figure 4.2. $\chi_M T$ *vs.* T for [Mn_{12}-allyl] collected at applied fields of 1, 0.1, and 0.01 T in the temperature range of 300-1.8 K……..…...188

Figure 4.3. Reduced magnetization (M/N_β) vs. H/T for [Mn_{12}-allyl] collected in applied fields of 5, 4, 3, and 2 T (top) and 1, 0.5, and 0.1 T (bottom) in the temperature range of 1.8 to 10 K. Theoretical fits are shown as solid curves with parameters (top) $S = 9$, $g = 1.9$ and $D/k_B = -0.47$ K (-0.33 cm^{-1}) and (bottom) $S = 9$, $g = 2$, $D/k_B = -0.33$ K (-0.23 cm^{-1})…….....189

Figure 4.4. In-phase (χ_M') and out-of-phase (χ_M'') ac magnetic susceptibility for [Mn_{12}-allyl] collected in an ac field of 3 Oe oscillating at frequencies of 50-1000 Hz……..191

Figure 4.5. (Top) Single-crystal magnetization vs. applied magnetic field hysteresis loops for [Mn_{12}-allyl] collected at 0.27 K and sweep rates of 0.1, 0.2 and 0.4 T/min. (Bottom) First derivative (dM/dH) plotted vs. applied field (H)……..……..192

Figure 4.6. Magnetic field behavior of lowest-lying energy states for a rigid S = 7 spin system……..…..194

Figure 4.7. Schematic representation of two ferromagnetically coupled S = 7/2 halves of the [Mn_{12}-allyl] wheel……..….194

Figure 4.8. (a) Lowest-lying energy levels of exchange-coupled dimer model for [Mn_{12}-allyl] (b) Magnetic field behavior of the lowest energy levels assuming rigid S = 7. (c) Magnetic field behavior of the energy levels assuming the exchange-coupled model…….196

Figure 4.9. ORTEP of [Mn_{16}]-MeCN (top) and [Mn_{16}]-$CHCl_3$ (bottom) with thermal ellipsoids drawn at 30% probability level and hydrogen atoms omitted for clarity……..…….198

Figure 4.10. Intramolecular H-bonding in [Mn_{16}]-MeCN (top) and [Mn_{16}]-$CHCl_3$ (bottom) with Jahn-teller axes highlighted in black……..……199

Figure 4.11. $\chi_M T$ *vs.* T for [Mn_{16}]-MeCN (top) and [Mn_{16}]-$CHCl_3$ (bottom) collected in applied fields of 1, 0.1 and 0.01 T…….....201

Figure 4.12. Reduced magnetization (M/N_β) vs. H/T for [Mn_{16}]-MeCN collected in applied fields of (top) 5, 4, 3, and 2 T and (bottom) 2, 1, 0.5, and 0.1 T in the temperature range of 1.8 to 10 K. Theoretical fits are shown as solid curves with parameters (top) S = 13, g = 2.1 and D/k_B = -0.19 K (-0.13 cm^{-1}) and (bottom) S = 13, g = 1.8, D/k_B = -0.04 K (-0.03 cm^{-1})…….....….202

Figure 4.13. Reduced magnetization (M/N_β) vs. H/T for [Mn_{16}]-$CHCl_3$ collected in applied fields of (top) 5, 4, 3, and 2 T and (bottom) 2, 1, 0.5, and 0.1 T in the temperature range of 1.8 to10 K. Theoretical fits are shown as solid curves with parameters (top) S = 14, g = 2.0 and D/k_B = -0.12 K (-0.08 cm^{-1}) and (bottom) S = 13, g = 1.9, D/k_B = -1.21 K (-0.84 cm^{-1})……..203

Figure 4.14. Ac magnetic susceptibility for [Mn_{16}]-MeCN (left) and [Mn_{16}]-$CHCl_3$ (right) collected in an applied ac field of 0.99 Oe oscillating at frequencies of 50-10,000 Hz……..……205

Figure 4.15. Temperature-dependent single-crystal magnetization hysteresis plot for [Mn_{16}]-$CHCl_3$ in the temperature range of 0.04-1 K and a sweep rate of 0.2 T/ min……..……...206

Figure 4.16. ORTEP of (top) asymmetric unit with labeling scheme and (bottom) full structure of **10** with thermal ellipsoids drawn at 50% probability level and hydrogen atoms omitted for clarity…....211

Figure 4.17. Crystal packing of **10** as viewed down the a-axis (left) and c-axis (right) of the unit cell……..……215

Figure 4.18. Space-filling model of **10**……..……215

Figure 4.19. Top (left) and side (right) views of a [Mn_{12}] single-stranded wheel emphasizing the C_i symmetry. Highlighted carbon atoms represent four of the η^1,η^2,μ_3-acetate bridges……..…...216

Figure 4.20. Top (left) and side (right) views of a [Mn_{16}] single-stranded wheel emphasizing the S_4 symmetry. Highlighted carbon atoms represent four of the η^1,η^1,μ_2-acetate bridges between Mn1 and Mn4 ions……..……...216

Figure 4.21. Top (left) and side (right) views of a [Mn_{24}] single-stranded wheel (**10**) emphasizing the S_6 symmetry. Highlighted carbon atoms represent four of the η^1,η^1,μ_2-acetate bridges between Mn3 and Mn4 ions……..…...217

Figure 4.22. χ_MT vs. T for **10** at applied dc fields of 0.01, 0.1, and 1 T in the temperature range 300-1.8 K……..……219

Figure 4.23. Reduced magnetization (M/N_B) vs. H/T for **10** at applied dc fields of 5, 4, 3, 2, and 1 T in the temperature range of 4-1.8 K. Theoretical fit shown as solid black curve……..….220

Figure 4.24. In-phase (χ_M') and out-of-phase (χ_M'') ac magnetic susceptibility for **10** collected in an ac field of 3 Oe oscillating at frequencies of 50-1000 Hz……..…..222

Figure 4.25. Extrapolation of 10 Hz $\chi_M'T$ *vs.* T data for **10** to zero K suggesting a ground state spin of $S = 11$ from the spin-only formula……..……224

Figure 5.1. Comparison of metal-oxygen cores of some [Mn_6] rods……...232

Figure 5.2. Mn-oxo core connectivity for complexes **11-14**……..…….238

Figure 5.3. Mn-oxo core connectivity for $[Mn_6(O_2CMe)_6(teaH_2)_2(tmp)_2]$ · 2MeCN (top) and $[Mn_6(O_2CMe)_8(thme)_2(py)_4]$ · 2py (bottom)…….....241

Figure 5.4. ORTEP of **11** (top) and **12** (bottom) with thermal ellipsoids drawn at 50% probability level. Hydrogen atoms omitted for clarity…….....242

Figure 5.5. Unit cell of **11** as viewed down the a-axis (left) and the c-axis (right)……..……245

Figure 5.6. Unit cell of **12** as viewed down the a-axis (left) and the c-axis (right)……..……245

Figure 5.7. ORTEP of **13** (top) and **14** (bottom) with thermal ellipsoids drawn at 50% probability level. Hydrogen atoms and solvate molecules omitted for clarity……..……...247

Figure 5.8. Unit cell of **13** as viewed down the a-axis (left) and the c-axis (right)……..……250

Figure 5.9. Intermolecular interactions in the crystal packing of **13**……..…….250

Figure 5.10. Unit cell of **14** as viewed down the a-axis (left) and the c-axis (right). Only the *ipso* carbon atoms of the benzoate ligands are shown……..……252

Figure 5.11. Plot of $\chi_M T$ *vs. T* for **11** (top) and **12** (bottom) in an applied dc field of 1 T……..……..253

Figure 5.12. Plot of $\chi_M T$ *vs. T* for **13** (top) and **14** (bottom) in an applied dc field of 1 T……..…..254

Figure 5.13. Coupling scheme for $[Mn^{III}_2Mn^{II}_4]$ complexes, where Mn1, Mn2, Mn3, and Mn6 are in the +2 oxidation state and Mn4 and Mn5 are in the +2 oxidation state……..…….258

Figure 5.14. Plot of μ_{eff} *vs. T* for **11-14** in an applied dc field of 0.1 T with theoretical fits shown as solid black curves……..…258

Figure 5.15. Reduced magnetization for **12** with fitting parameters of $S = 5$, $g = 1.9$ (fixed), and $D/k_B = -0.91$ cm^{-1} at high fields (top) and $S = 4$, $g = 1.8$, and $D/k_B = -0.52$ cm^{-1} at low fields (bottom)……..…...261

Figure 5.16. Reduced magnetization for **11** at high fields (left) and low fields (right)……..……..262

Figure 5.17. Reduced magnetization for **13** at high fields (left) and low fields (right)……..…..262

Figure 5.18. Reduced magnetization for **14** at high fields (left) and low fields (right)……..……..263

Figure 5.19. (Top) In-phase, $\chi_M'T$, and (bottom) out-of-phase, χ_M'', ac magnetic susceptibility for **11**……...…265

Figure 5.20. (Top) In-phase, $\chi_M'T$, and (bottom) out-of-phase, χ_M'', ac magnetic susceptibility for **12**……...…266

Figure 5.21. (Top) In-phase, $\chi_M'T$, and (bottom) out-of-phase, χ_M'', ac magnetic susceptibility for **13**……..…….267

Figure 5.22. Top) In-phase, $\chi_M'T$, and (bottom) out-of-phase, χ_M'', ac magnetic susceptibility for **14**……..…….268

Figure 6.1. Coordination modes of the dicyanamide anion……..…...275

Figure 6.2. (Left) core structure and (right) crystal packing diagrams of $[Mn_4(hmp)_4(Hpdm)_2(dca)_2](ClO_4)_2 \cdot 2H_2O \cdot 2MeCN$……..….275

Figure 6.3. ORTEP of $[Cu(L^1)(dca)(L^1)Cu](ClO_4)$ with ClO_4^- anion omitted for clarity……..……280

Figure 6.4. ORTEP of **15** with thermal ellipsoids drawn at 50% probability level and hydrogen atoms omitted for clarity…….....287

Figure 6.5. Crystal packing of **15** with the $[Cu_2(tren)_2(dca)]^{3+}$ units in blue and the BPh_4^- anions in grey……..287

Figure 6.6. ORTEP of **16** with thermal ellipsoids drawn at 50% probability level and hydrogen atoms omitted for clarity……..……..289

Figure 6.7 Intermolecular H-bonding pathway in **16**……..……289

Figure 6.8. (Top) The structure of $[Cu_2(bpy)_4(dca)](ClO_4)_3 \cdot 0.5$ EtOH and (bottom) $[Cu(bpy)_2(dca)]ClO_4$ with displacement ellipsoids drawn at 40% and 50% probability levels, respectively, and hydrogen atoms shown as small spheres of arbitrary radii……..…..291

Figure 6.9. μ_{eff}/Cu vs. T for **15** with theoretical fit shown as solid red curve...…...293

Figure 6.10. Through-space Cu(II)···Cu(II) distances in **15** (top) and **16** (bottom)……..……...295

Figure 6.11. μ_{eff} *vs. T* for **16** in applied dc field of 0.1 T……..….296

Figure 6.12. ORTEP of $[Cu_2(tren)_2(BZD)](NO_3)_4$ with nitrate anions and hydrogen atoms omitted for clarity…….……298

LIST OF TABLES

Table 2.1. Crystallographic data and refinement parameters for **1**……..50

Table 2.2. Crystallographic data and refinement parameters for **2-4**……...51

Table 2.3. Bond valence sum analysis for **1**…….52

Table 2.4. Bond valence sum analysis for **2**…….52

Table 2.5. Bond valence sum analysis for **3** and **4**……...53

Table 2.6. Selected interatomic bond distances [Å] and angles [°] for **1a**……...58

Table 2.7. Selected interatomic bond distances [Å] and angles [°] for **2** and **4**……64

Table 2.8. Selected interatomic bond distances [Å] and angles [°] for **3**.……64

Table 3.1. Crystallographic data and refinement parameters for **5-7**……..…...103

Table 3.2. Crystallographic data and refinement parameters for **8** and **9**……..….104

Table 3.3. Bond valence sum analysis for **5**……..…….106

Table 3.4. Bond valence sum analysis for **9**……..…….106

Table 3.5. Bond valence sum analysis for **6, 7** and **8**…….....107

Table 3.6. Selected interatomic bond distances [Å] and angles [°] for **5**……....112

Table 3.7. Selected interatomic bond distances [Å] and angles [°] for **6**, **7**, and **8**……..……...113

Table 3.8. Selected interatomic bond distances [Å] and angles [°] for **9**……..….114

Table 3.9. Dipole-dipole contributions to the zero-field splitting parameter, D_{dd}, for given Mn···Mn distances and a *g*-value of 1.9……..…...126

Table 3.10. Summary of low-lying spin states from fitting of $\chi_M T$ *vs. T* data for **5-9**……..……..140

Table 3.11. Summary of ground state spin determination for **5-9**……..…..158

Table 4.1. Crystallographic data and refinement parameters for **10**……..…209

Table 4.2. Selected bond distances and bond valence sum analyses for **10**…..….212

Table 5.1. Crystallographic data and refinement parameters for **11** and **12**…..….235

Table 5.2. Crystallographic data and refinement parameters for **13** and **14**…..….236

Table 5.3. Bond valence sum analysis for **11** and **12**……..…...238

Table 5.4. Bond valence sum analysis for **13** and **14**……..…...239

Table 5.5. Selected interatomic bond distances [Å] and angles [°] for **11**…..…...243

Table 5.6. Selected interatomic bond distances [Å] and angles [°] for **12**…..…...243

Table 5.7. Selected interatomic bond distances [Å] and angles [°] for **13**…….....248

Table 5.8. Selected interatomic bond distances [Å] and angles [°] for **14**…….248

Table 5.9. Comparison of J-values for **11- 14** (block diagonalization) with selected mixed-valent [Mn_6] complexes reported in the literature (DFT calculations)……..……...259

Table 6.1. Crystallographic data and refinement parameters for **15** and **16**……..……283

Table 6.2. Selected interatomic distances [Å] and angles [°] for complexes **15** and **16**……..…...284

Table 6.3. Coupling constants (J) for **15** and selected dinuclear Cu(II) complexes……..…….298

Table 6.4. Coupling constants (*J*) for selected single dca-bridged Cu(II) networks……..……..299

ACKNOWLEDGEMENTS

First and foremost I would like to extend my sincerest gratitude to my research advisor, Professor David Hendrickson, for teaching me how to be a scientist without telling me how to. I am honored to have had the opportunity to work and teach for such a brilliant chemist and will continue to use the knowledge I have gained from him in my professional future. I would also like to thank my co-advisor, Professor Arnold Rheingold for allowing me to learn X-ray crystallography from a true expert.

I would like to acknowledge Professor Stephen Hill at the National High Magnetic Field Laboratory (NHMFL) and Professor Enrique del Barco at the University of Central Florida whose elegant work and insightful commentary have played an integral role in understanding the physics of some of the complexes presented herein. Many thanks also to Dr. James O'Brien at Quantum Design in San Diego, CA and Professor Motohiro Nakano at Osaka University in Japan for their valuable contributions and enthusiasm. Drs. Antonio DiPasquale and Curtis Moore have also been instrumental in helping me work through some of the many pitfalls encountered in X-ray crystallography over the years.

I would also like to thank my fellow graduate students (past and present) especially, Kristina Muñoz, H. Paul Martinez, Kristina Mitchell, Chris Beedle, Patrick Feng, John Goeltz, and Jonathan Smieja for all the support, ridicule, and good times. And last, but certainly not least, I couldn't have done this without the unconditional love and support of my family. I want to thank them for trusting me to choose my own path and, though they may not always understand it, for being proud of me no matter the outcome.

Chapter 2, in part, is a reprint of the material as it appears in: Heroux, K. J.; Rheingold, A. L.; Hendrickson, D. N. "Ferrocene-substituted [Mn_4] dicubane single-molecule magnets", *European Journal of Inorganic Chemistry,* **2009***,* 3541. The dissertation author was the primary investigator and author of this paper.

Chapter 4 includes material currently being prepared for submission for publication: Heroux, K. J.; Hendrickson, D. N. "A single-stranded [Mn_{24}] wheel: synthesis, crystal structure, and magnetic properties". The dissertation author was the primary investigator and author of this paper.

Chapter 5, in part, is a reprint of the material as it appears in: Heroux, K. J.; Shah, S. J.; O'Brien, J. R.; DiPasquale, A. G.; Nakano, M.; Hendrickson, D. N. "Rod-shaped [Mn_6] complexes as single-molecule magnets", *Inorganica Chimica Acta,* **2010**, doi:10.1016/j.ica.2010.04.013, *in press.* The dissertation author was the primary author of this paper.

Chapter 6 includes material currently being prepared for submission for publication: Heroux, K. J.; DiPasquale, A. G.; Rheingold, A. L.; Hendrickson, D. N. "The viability of dicyanamide as a superexchange pathway between paramagnetic metal centers". The dissertation author was the primary investigator and author of this paper.

VITA

2005	Bachelor of Science, University of New Hampshire
2007	Master of Science, University of California San Diego
2005-2010	Research Assistant, University of California San Diego
2010	Doctor of Philosophy, University of California San Diego

PUBLICATIONS

Heroux, K. J.; DiPasquale, A. G.; Rheingold, A. L.; Hendrickson, D. N. The viability of dicyanamide as a superexchange pathway between paramagnetic metal centers. *Written draft under professorial review.*

Heroux, K. J.; Hendrickson, D. N. Single-stranded [Mn_{24}] wheel. *Inorganic Chemistry,* **2010***, submitted manuscript.*

Liu, J.-L.; Guo, F.-S.; Meng, Z.-S.; Zheng, Y.-Z.; Leng, J.-D.; Lin, Z.-J.; Tong, M.-L.; Heroux, K. J.; Hendrickson, D. N. Isomeric [$Dy^{III}_6Mn^{III}_{12}$] cores with different magnetic anisotropies. *Angewandte Chemie Int. Ed.*, **2010**, *submitted manuscript.*

Heroux, K. J.; Shah, S. J.; O'Brien, J. R.; DiPasquale, A. G.; Nakano, M.; Hendrickson, D. N. Rod-shaped [Mn_6] complexes as single-molecule magnets. *Inorganica Chimica Acta,* **2010**, DOI: 10.1016/j.ica.2010.04.013, *in press.*

Beedle, C. C.; Ho, P-C.; Sayles, T.; Hamilton, J. J.; Del Barco, E.; Nakano, M.; O'Brien, J.; Heroux, K. J.; Maple, M. B.; Hendrickson, D. N. Ferromagnetic-ordering and simultaneous fast magnetization tunneling in the single-molecule magnet [Ni(hmp)(dmb)Cl]$_4$. *Inorganic Chemistry,* **2010**, *49*, 5780-5782.

Heroux, K. J.; Rheingold, A. L.; Hendrickson, D. N. Ferrocene-substituted [Mn_4] dicubane single-molecule magnets. *European Journal of Inorganic Chemistry,* **2009***,* 3541.

Beedle, C. C.; Stephenson, C. J.; Heroux, K. J.; Wernsdorfer, W.; Hendrickson, D. N. Mn_4 photoluminescent single-molecule magnet: a potential probe for studying quantum dynamics. *Inorganic Chemistry*. **2008**, *47(23),* 10798. (Cover Article)

Shah, S. J.; Ramsey, C. M.; Heroux, K. J.; DiPasquale, A. G.; Dalal, N. S.; Rheingold, A. L.; del Barco, E.; Hendrickson, D. N. Molecular wheels: new Mn_{12} complexes as single-molecule magnets. *Inorganic Chemistry*. **2008**, *47(20)*, 9569.

Shah, S. J.; Ramsey, C. M.; Heroux, K. J.; O'Brien, J. R.; DiPasquale, A. G.; Rheingold, A. L.; del Barco, E.; Hendrickson, D. N. Wheel-shaped Mn_{16} single-molecule magnets. *Inorganic Chemistry*. **2008**, *47,* 6245.

Beedle, C.C.; Heroux, K. J.; Nakano, M.; DiPasquale, A. G.; Rheingold, A. L.; Hendrickson, D. N. Antiferromagnetic tetranuclear manganese complex: wheel or dicubane? *Polyhedron.* **2007**, *26(9-11),* 2200.

Jacobsen, F. E.; Lewis, J. A.; Heroux, K. J.; Cohen, S. M. Characterization and evaluation of pyrone and tropolone chelators for use in metalloprotein inhibitors. *Inorganica Chimica Acta.* **2007**, *360(1)*, 264.

Evans, W. J.; Miller, K. A.; Ziller, J. W.; DiPasquale, A. G.; Heroux, K. J.; Rheingold, A. L. Formation of $(C_5Me_5)_2U(EPh)Me$, $(C_5Me_5)_2U(EPh)_2$, and $(C_5Me_5)_2U(\eta^2\text{-}TeC_6H_4)$ from $(C_5Me_5)_2UMe_2$ and PhEEPh (E = S, Se, Te). *Organometallics*. **2007**, *26(17),* 4287-4293.

Heroux, K. J.; Woodin, K. S.; Tranchemontagne, D. J.; Widger, P. C. B.; Southwick, E.; Wong, E. H.; Weisman, G. R.; Tomellini, S. A.; Wadas, T. J.; Anderson, C. J.; Kassel, S.; Golen, J. A.; Rheingold, A. L. The long and short of it: the influence of *N*-carboxyethyl *versus N*-carboxymethyl pendant arms on *in vitro* and *in vivo* behavior of copper complexes of cross-bridged tetraamine macrocycles. *Dalton Transactions.* **2007**, 2150.

Woodin, K. S.; Heroux, K. J.; Boswell, C. A.; Wong, E. H.; Weisman, G. R.; Niu, W.; Tomellini, S. A.; Anderson, C. J.; Zakharov, L.; Rheingold, A. L. Kinetic inertness and electrochemical behavior of copper(II)tetraazamacrocyclic complexes: possible implications for in vivo stability. *European Journal of Inorganic Chemistry*. **2005**, 4829.

ABSTRACT OF THE DISSERTATION

Modulation of Intermolecular Interactions in Single-Molecule Magnets

by

Katie Jeanne Heroux

Doctor of Philosophy in Chemistry

University of California San Diego, 2010

Professor David N. Hendrickson, Chair

Polynuclear manganese clusters exhibiting interesting magnetic and quantum properties have been an area of intense research since the discovery of the first single-molecule magnet (SMM) in 1993. These molecules, below their blocking temperature, function as single-domain magnetic particles which exhibit classical macroscale magnetic properties as well as quantum mechanical phenomena such as quantum tunnelling of magnetization (QTM) and quantum phase interference. The union of classical and quantum behavior in these nanomaterials makes SMMs ideal candidates for high-density information storage and quantum computing.

However, environmental coupling factors (nuclear spins, phonons, neighboring molecules) must be minimized if such applications are ever to be fully realized. The focus of this work is making small structural changes in well-known manganese SMMs in order to drastically enhance the overall magnetic and quantum properties of the system. Well-isolated molecules of high crystalline quality should lead to well-defined energetic and spectral properties as well. An advantage of SMMs over bulk magnetic materials is that they can be chemically altered from a "bottom-up" approach providing a synthetic tool for tuning magnetic properties.

This systematic approach is utilized in the work presented herein by incorporating bulky ligands and/or counterions to "isolate" the magnetic core of [Mn_4] dicubane SMMs. Reducing intermolecular interactions in the crystal lattice (neighboring molecules, solvate molecules, dipolar interactions) is an important step toward developing viable quantum computing devices. Detailed bulk magnetic studies as well as single crystal magnetization hysteresis and high-frequency EPR studies on these sterically-isolated complexes show enhanced, and sometimes even unexpected, quantum dynamics. The importance of intra- and intermolecular interactions remains a common theme throughout this work, extending to other SMMs of various topology including large wheel-shaped complexes, hexanuclear rods, and even small dinuclear species.

Chapter 1:

Single-Molecule Magnets

1.1. Introduction

Single-molecule magnets (SMMs) are polynuclear transition metal complexes that possess a large spin ground state (S) and an appreciable negative axial zero-field splitting parameter (D) which give rise to an energy barrier to the reversal of the direction of magnetization ($D\hat{S}_z^2$).[1-3] The single-ion axial zero-field interactions result from a combination of spin-orbit and crystal field interactions (often Jahn-Teller distortion) at the individual metal ions in the SMM.[4] These single-domain magnetic complexes were first discovered in 1993 when the mixed-valent manganese complex $[Mn_{12}O_{12}(O_2CMe)_{16}(H_2O)_4] \cdot 2HO_2CMe \cdot 4H_2O$ (or $Mn_{12}Ac$), shown in Figure 1.1, was found to possess both classical and quantum magnetic properties.[1,5,6] Due to their small size, SMMs bridge the gap between classical and quantum understanding of magnetism resulting in fascinating effects that had not been previously observed or explained.[7]

Before the discovery of SMMs, evidence of quantum mechanical behavior in magnetic systems had eluded scientists due to the inhomogeneity of previously studied systems such as small grains, spin glasses, and thin films, etc.[6,8-12] The well-defined crystalline structures and magnetic properties of SMMs (monodisperse in size, shape, spin, anisotropy, and orientation) make them ideal materials for studying the fundamental origins of quantum phenomena.[13-15] Such quantum effects observed for the first time in SMMs include quantum tunneling of the magnetization (QTM),[16] spin-spin cross relaxation,[17] exchange-biased quantum tunneling,[18-20] spin-parity effects,[21 22,23]and quantum phase interference.[24 25]

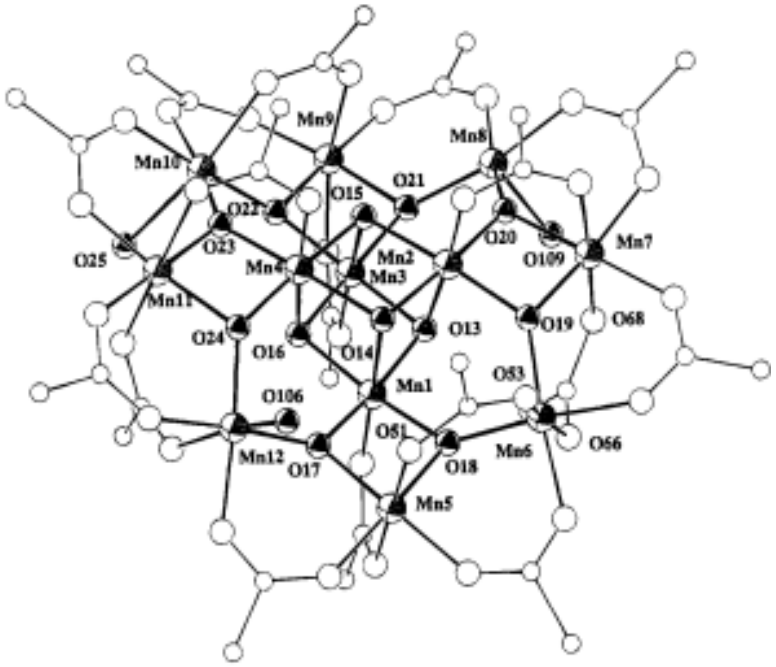

Figure 1.1. Molecular structure of $[Mn_{12}O_{12}(O_2CMe)_{16}(H_2O)_4] \cdot CH_3CO_2H \cdot 4H_2O$ ($Mn_{12}AC$).

In addition to the valuable insight into the fundamental principles governing these quantum phenomena, the study of SMMs is also important for possible applications in high-density information storage and quantum computing devices. Such "Quantum Information Processing Systems" (QIPS) involve the manipulation of coupled wavefunctions that are comprised of multiple sub-systems in the QIPS and are extremely complex in nature.[7,15,26-30] The wavefunctions of the individual components lose all meaning and only the coupled or "entangled" wavefunction of the entire system has physical relevance. It is the entanglement of multiple states that allows for the superposition of many computations at once making QIPS a powerful tool.[7] Though the details of such applications are beyond the scope of this work, it is worth noting how easily these systems can be disturbed by even the most subtle interactions with the environment.[26] Therefore, the development of well-isolated, clearly defined SMMs with minimal environmental coupling factors should provide a platform for the manipulation of individual spin states and a thorough understanding of the underlying physics necessary to construct a viable QIPS device.[31]

1.2. Magnetic Susceptibility

1.2.1. Direct Current (dc) Measurements

In the following chapters, the dc magnetic susceptibilities of transition metal complexes are measured in low and high fields (from 0.01 T up to 5 T) and in a temperature range of 300-1.8 K. The first type of dc susceptibility plot we will see throughout this thesis is plotted as the product of molar susceptibility and temperature ($\chi_M T$) vs. absolute temperature (T) in relatively low dc fields (0.01-1 T). Aside from an

estimate of the ground state spin based on the magnitude of magnetic susceptibility, the presence and even the nature of magnetic exchange (ferromagnetic, antiferromagnetic, diamagnetic, etc.) can often be deduced just from the shape of the $\chi_M T$ *vs. T* curve.

Depending on the complexity and symmetry of the structure, the $\chi_M T$ *vs. T* data can be fit to a theoretical model to determine the ground state spin (*S*) and exchange coupling constants (*J*). One such approach, which is used extensively in Chapters 2 and 3, is the simple Kambe method[32] which only accounts for isotropic Heisenberg exchange between pairs of metal ions (equation *1.1*) and does not account for zero-field splitting or Zeeman interactions. Figure 1.2 shows the Kambe vector coupling scheme used in previously reported [Mn_4] dicubanes and other tetranuclear manganese complexes comprised of this "butterfly-like" core with inversion symmetry.

Employing this two J-value model, the spin Hamiltonian for any [Mn_4] dicubane (like the complexes introduced in Chapters 2 and 3) is comprised of the pairwise exchange interactions as shown in equation *1.2*. (Note that the $J_{13}(\hat{S}_1 \cdot \hat{S}_3)$ term has been neglected because it is assumed that there is no direct exchange pathway between Mn(1) and Mn(3) as viewed in Figure 1.2.) Using the appropriate Kambe vector coupling for this system (defined in equation *1.3*) followed by substitution into equation *1.2*, the resulting eigenenergy, $E(S_T)$, equation (*1.4*) is derived.. The two coupling constants, J_{bb} and J_{wb}, represent the exchange interaction between the two Mn(III) ions in the "body" positions and between a Mn(III) body ion and a Mn(II) ion in the "wing" position of the dicubane core, respectively.[33,34]

$$\hat{H} = -2\sum_{ij} J_{ij}\hat{S}_i \cdot \hat{S}_j \qquad (1.1)$$

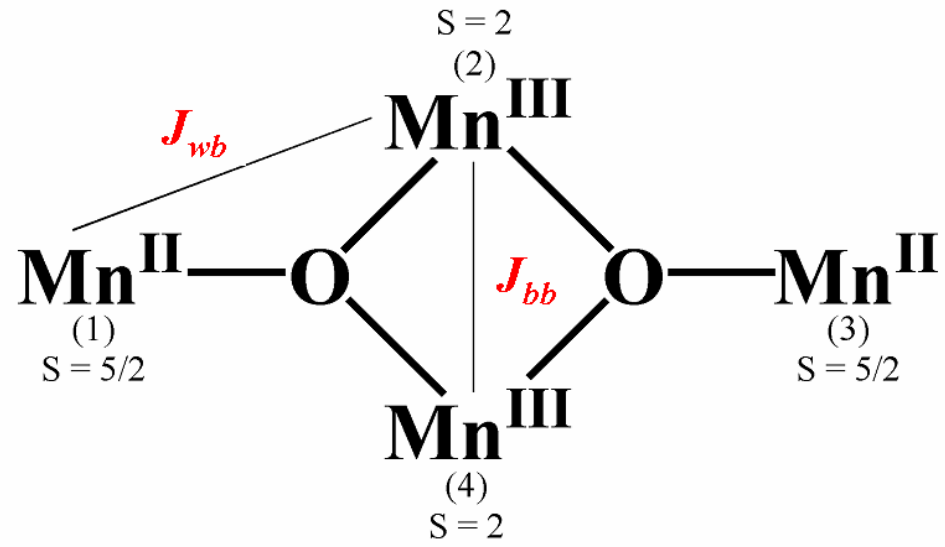

Figure 1.2. Two J-value Kambe vector coupling scheme for [Mn_4] butterfly and dicubane complexes.

$$\hat{H} = -2[J_{12}(\hat{S}_1 \cdot \hat{S}_2) + J_{23}(\hat{S}_2 \cdot \hat{S}_3) + J_{24}(\hat{S}_2 \cdot \hat{S}_4) + J_{34}(\hat{S}_3 \cdot \hat{S}_4) + J_{41}(\hat{S}_4 \cdot \hat{S}_1)] \quad (1.2)$$

$$\hat{S}_A = \hat{S}_1 + \hat{S}_3; \quad \hat{S}_B = \hat{S}_2 + \hat{S}_4; \quad \hat{S}_T = \hat{S}_A + \hat{S}_B \quad (1.3)$$

$$E(S_T) = -J_{wb}[S_T(S_T+1) - S_A(S_A+1) - S_B(S_B+1)] - J_{bb}[S_A(S_A+1)] \quad (1.4)$$

The observed data are least squares fit to the molar susceptibility calculated from the Heisenberg-Dirac-Van Vleck equation,[35] or HDVV, (equation *1.5*) where *g* is the Landé g-tensor, *N* is Avogadro's number, μ_B is the Bohr magneton, and k_B is the Boltzmann constant. This theoretical fit of the $\chi_M T$ *vs. T* data gives optimized values for the ground state spin, *S*, and the coupling constants, J_{bb} and J_{wb}.

$$\chi_M = \left(\frac{Ng^2\mu_B^2}{3kT}\right)\frac{\sum[S_T(S_T+1)(2S_T+1)e^{\frac{-E(S_T)}{k_BT}}}{\sum(2S_T+1)e^{\frac{-E(S_T)}{k_BT}}} \quad (1.5)$$

The second type of dc magnetic susceptibility plot frequently used throughout this thesis is the field-dependence of the magnetic susceptibility at low temperatures which is plotted as reduced magnetization, $M/N_{\mu B}$, vs. H/T. The theoretical fitting of these data does not account for magnetic exchange interactions as in the fitting of the $\chi_M T$ *vs. T* data (*vide supra*). Equation *1.6* shows the spin Hamiltonian used to fit the reduced magnetization data which includes both axial and rhombic (or transverse) zero-

field splitting (ZFS) terms, $D\hat{S}_z^2$ and $E\ (\hat{S}_x^2-\hat{S}_y^2)$, respectively, as well as a Zeeman splitting term, $g\mu_B\hat{S}B$, where B is the applied magnetic field and $\hat{S}_i$ is the spin projection operator along i (= x, y, z).

$$\hat{H} = D\hat{S}_z^2 + E\ (\hat{S}_x^2-\hat{S}_y^2) + g\mu_B\hat{S}B \qquad (1.6)$$

This full matrix diagonalization approach is still over-simplified in that it is assumes that only a single ground state is thermally populated (in other words, S is a good quantum number) and that the axes of anisotropy in the cluster (Jahn-Teller axes in [Mn_4] complexes for instance) are all aligned in the same direction. Assuming a fixed ground-state, a full powder average is calculated.[36] The resulting eigenvalues, E_i, and their dependency on the magnetic field, $\delta E_i/\delta B$, are used to calculate the magnetization according to equation *1.7,*

$$M = N\sum_i \left(\delta E_i/\delta B\right)\exp\left(-E_i/kT\right)\Big/\sum_i \exp\left(-E_i/kT\right) \quad , \qquad (1.7)$$

from which optimized values of g, D, and E can be determined.

Since the Kambe and limited full matrix diagonalization approaches discussed above do not always fully describe systems with low-lying excited states (as many manganese SMMs possess)**,** often times a full Hamiltonian matrix diagonalization approach is necessary. In addition to the isotropic HDVV type of super-exchange accounted for in the Kambe approach ($\hat{H}_{ex}$), the full matrix diagonalization method also

accounts for Zeeman interactions, zero-field splitting, and even antisymmetric Dzyaloshinsky-Moriya (DM)[37] exchange interactions which are rarely applicable. The fully modeled spin Hamiltonian of the system can then be described by equation *1.8* with the individual $\hat{H}_{ex}$, $\hat{H}_{DM}$, $\hat{H}_{zfs}$, and $\hat{H}_{Zeeman}$ Hamiltonians defined in equations *1.9-1.12*,

$$\hat{H} = \hat{H}_{\mathrm{ex}} + \hat{H}_{\mathrm{DM}} + \hat{H}_{\mathrm{zfs}} + \hat{H}_{\mathrm{Zeeman}} \qquad (1.8)$$

$$\hat{H}_{\mathrm{ex}} = -2J_{\mathrm{wb}}(\hat{S}_1 + \hat{S}_3) \bullet (\hat{S}_2 + \hat{S}_4) - 2J_{\mathrm{bb}}\hat{S}_1\hat{S}_3 = J_{\mathrm{wb}}(\hat{S}_{13}^2 + \hat{S}_{24}^2 - \hat{S}_{\mathrm{T}}^2) + J_{\mathrm{bb}}(\hat{S}_1^2 + \hat{S}_3^2 - \hat{S}_{13}^2) \qquad (1.9)$$

$$\hat{H}_{\mathrm{DM}} = \boldsymbol{d}_{12} \bullet \hat{S}_1 \times \hat{S}_2 + \boldsymbol{d}_{23} \bullet \hat{S}_2 \times \hat{S}_3 + \boldsymbol{d}_{34} \bullet \hat{S}_3 \times \hat{S}_4 + \boldsymbol{d}_{41} \bullet \hat{S}_4 \times \hat{S}_1 \qquad (1.10)$$

$$\begin{aligned} \hat{H}_{\mathrm{zfs}} &= \sum_{j=2,4} D(\hat{S}_{j\zeta}^2 - \frac{1}{3}\hat{S}_j^2) = \sum_{j=2,4} D\left[(\hat{S}_j^x \cos\phi_j \sin\theta_j + \hat{S}_j^y \sin\phi_j \sin\theta_j + \hat{S}_j^z \cos\theta_j)^2 - \frac{1}{3}\hat{S}_j^2 \right] \\ &= \sum_{j=2,4} D\left[(\frac{\sin\theta_j}{2} e^{-i\phi_j}\hat{S}_j^+ + \frac{\sin\theta_j}{2} e^{+i\phi_j}\hat{S}_j^- + \hat{S}_j^z \cos\theta_j)^2 - \frac{1}{3}S_j(S_j+1) \right] \end{aligned} \qquad (1.11)$$

$$\hat{H}_{\mathrm{Zeeman}} = -g\mu_{\mathrm{B}} \sum\nolimits_{j=1}^{4} (B_x\hat{S}_j^x + B_y\hat{S}_j^y + B_z\hat{S}_j^z), \qquad (1.12)$$

where $\hat{S}_j$ stands for the spin operator of *j*-th spin (*S* = 5/2 for Mn(II) and *S* = 2 for Mn(III)), $\hat{S}_{13} \equiv \hat{S}_1 + \hat{S}_3$, $\hat{S}_{24} \equiv \hat{S}_2 + \hat{S}_4$ and $\hat{S}_{\mathrm{T}} \equiv \hat{S}_{13} + \hat{S}_{24}$ are the partial-sum and the resultant spin operators, J_{wb} and J_{bb} are the exchange interaction parameters between

neighboring ions in a mixed-valent [Mn_4] dicubane (see Figure 1.2), d_{ij} is the Dzyaloshinsky-Moriya vector for the interaction between i-th and j-th ions, D is the uniaxial zero-field splitting parameter for each ion, ϕ_j and θ_j are the azimuthal and polar angles of single-ion anisotropy axes for j-th ion, and B_α is the α-component of external magnetic field, B.

Due to the inversion symmetry of the [Mn_4] clusters discussed herein, this full Hamiltonian can be further simplified by the fact that quantization axes in the anisotropy term $\hat{H}_{zfs}$ were taken as parallel, *i.e.* (ϕ_2, θ_2) = (ϕ_4, θ_4) = (0°, 0°). Also, the Dzyaloshinsky-Moriya vectors for the Mn-O-Mn interaction pathways were taken to be identical and perpendicular to the molecular plane, *i.e.* $d_{12} = d_{23} = d_{34} = d_{41} = (0, 0, d)$. The advantages to this approach are that the $\chi_M T$ *vs.* T and reduced magnetization data are fit simultaneously and the single-ion anisotropies can be determined, providing a more complete description of the energy Hamiltonian.

1.2.2. Alternating Current (ac) Measurements

We have already seen how the effective energy barrier to the reversal of the direction of magnetization in a SMM can be estimated from the ground state spin (S) and zero-field splitting parameter (D) determined from dc magnetic susceptibility studies. However, we can also experimentally determine this energy barrier by measuring the magnetic susceptibility of the complex in a small ac field, oscillating at various frequencies, and zero applied dc field.[38] Ac magnetic susceptibility, χ, is composed of two separate components: the in-phase signal, χ', and the corresponding

imaginary out-of-phase component, χ''. If no out-of-phase signal is observed, this tells us that the net magnetization of the complex relaxes fast enough to keep up with the oscillating ac field and therefore the in-phase signal should account for 100% of the dc susceptibility.

However, if there exists a significant energy barrier to magnetization relaxation (in comparison to the thermal energy, kT) then a nonzero out-of-phase component to the susceptibility, χ'', will emerge which is accompanied by a corresponding decrease in the in-phase susceptibility, χ'. Furthermore, if such a magnetization reversal barrier exists, then both χ' and χ'' will be frequency-dependent. The presence of a frequency-dependent out-of-phase signal in the ac susceptibility is a characteristic property of SMMs. However, this evidence alone does not confirm that a given complex is a SMM since other materials, such as spin-glasses, can also exhibit this behavior below their transition temperatures.[15,39]

If a frequency-dependent out-of-phase signal is observed at high enough temperatures, the effective energy barrier to the magnetization reversal, E_a, can be determined from an Arrhenius-type plot of the out-of-phase signal peak positions. Also, because these measurements are performed in the absence of an applied dc field, a good estimate of the ground state spin can often be determined by extrapolation of the low frequency in-phase data to zero K and comparison of the value to that predicted by the spin-only formula. These calculations will be further discussed in later chapters.

1.3. Mixed-Valent [Mn_4] Dicubanes

Chapters 2 and 3 will focus on the modification of tetranuclear manganese SMMs with the common dicubane topology. Interest in mixed-valent [Mn_4] complexes originated from attempts at modeling the photosynthetic water oxidation complex (WOC) of the photosystem II reaction center which requires four oxo-bridged Mn atoms for activity.[40,41] With the discovery of single-molecule magnets in 1993, however, the [$Mn^{III}_2Mn^{II}_2$] dicubane complexes were shown to possess interesting magnetic and quantum properties.

This class of SMMs contains the mixed-valent core with connectivity shown in Figure 1.2 where the "body" positions are occupied by Mn(III) ions and the "wing" positions occupied by Mn(II) ions. In 1999, a S = 8 [Mn_4] dicubane, [$Mn_4(O_2CMe)_2(pdmH)_6][ClO_4]_2$, was reported by Brechin *et. al.*[42,43] which was synthesized from an oxo-centered Mn triangle and the chelating ligand pyridine-2,6-dimethanol (or $pdmH_2$). Since then, similar synthetic techniques using different chelating ligands and carboxylate sources have lead to an entire family of these mixed-valent [Mn_4] dicubanes. Other ligands proven very effective in the synthesis of dicubanes are hydroxymethylpyridine (hmpH),[19,36,44] triethanolamine ($teaH_3$),[45,46] and N-alkylated diethanolamines ($RdeaH_2$).[46-48]

Aside from the first [Mn_4] dicubane SMM mentioned above, all of these complexes possess S = 9 ground states with ferromagnetic coupling between the body Mn(III) ions and in the wing-body Mn(III)-Mn(II) interaction (in other words, both J_{bb} and J_{wb} are positive values). The complexes [$Mn_4(O_2CPh)_4(mdeaH)_2(mdea)_2$][47] and [$Mn_4(O_2CPh)_4(bdeaH)_2(bdea)_2$][46] where $mdeaH_2$ and $bdeaH_2$ are N-methyl and N-

butyldiethanolamine, respectively, are the most structurally similar to the complexes discussed in Chapters 2 and 3 and are pictured in Figure 1.3. Despite the slight structural differences in this family of SMMs, the magnetic properties are fairly consistent. By the same Kambe vector coupling approach shown in the previous section, the dc magnetic susceptibility data for these complexes are fit to a S = 9 ground state with values of J_{wb} ranging from 0.22 to 4.2 cm^{-1} and J_{bb} ranging from 5.3 to 9.9 cm^{-1}. Also, from fitting of the reduced magnetization data, the zfs parameter, D, for [Mn_4] dicubanes is typically between -0.20 to -0.30 cm^{-1}.[19,36,44-46]

While all of the above [Mn_4] dicubanes show a frequency-dependent out-of-phase signal in their ac susceptibility, they do not all appear at high enough temperatures in order to determine the effective barrier to the reversal of magnetization. For those that do, however, the values for E_a extracted from the Arrhenius plot (as described in the previous section) were found to be 17 K for the S = 8 complex,[42,43] 20-22 K for the triethanolamine complexes reported by Wittick *et. al*.,[49] and 23-28 K for the benzoate complexes reported by Ako *et. al.*[46] All of these values are in good agreement with the uniaxial anisotropy, D, calculated from dc susceptibility fits. Lastly, it is also worth noting that all of the previously reported [Mn_4] complexes possess very low-lying excited states, as with many polynuclear manganese clusters.

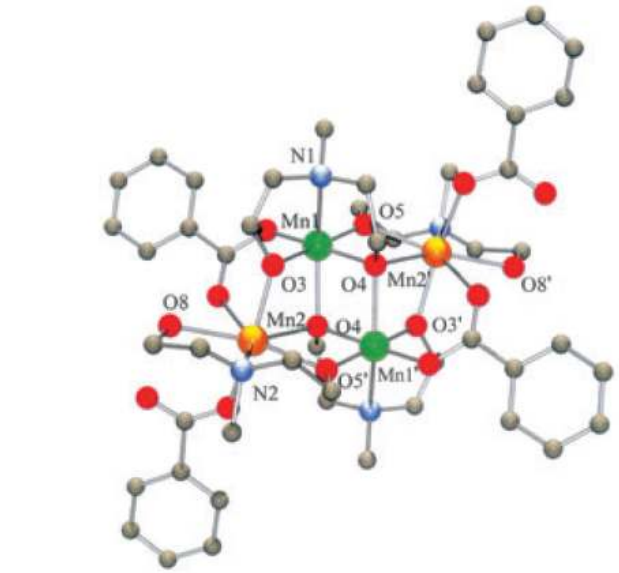

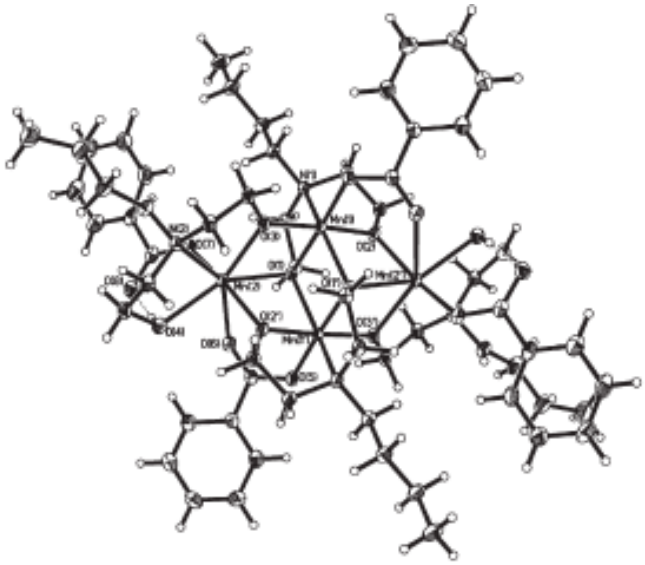

Figure 1.3. (top) PovRay plot of $[Mn^{II}_2Mn^{III}_2(O_2CPh)_4(mdea)_2(mdeaH)_2]$ with hydrogen atoms omitted for clarity and (bottom) ORTEP of $[Mn^{II}_2Mn^{III}_2(O_2CPh)_4(bdea)_2(bdeaH)_2]$ with thermal ellipsoids drawn at 50% probability level.

1.4. Magnetization Hysteresis and Berry Phase

Single-molecule magnets, like classical magnetic materials, exhibit hysteresis in their magnetization vs. applied field measurements. However, magnetization hysteresis loops for SMMs often exhibit unique features not observed in classical magnets. Figure 1.4 shows a plot of the magnetization vs. applied field for an oriented single crystal of $Mn_{12}Ac$, the first SMM described earlier, in which the magnetic field was applied exactly along the easy-axis of the crystal.[5,50] A prominent feature of Figure 1.4 is the presence of regularly spaced vertical steps in the hysteresis loops. These steps are attributed to quantum tunneling of the magnetization, or QTM.[16]

The large spin ground state and axial zero-field splitting intrinsic to SMMs leads to a potential energy barrier ($D\hat{S}_z^2$) between the "spin-up" and "spin-down" energy wells as depicted in Figure 1.5. Thermal activation over this barrier can occur as in classical magnets or in the case of SMMs, quantum tunneling of the magnetization (QTM) can occur through the barrier either in the ground state (ground-state tunneling) or between degenerate excited states (thermally-assisted tunneling).[16]

In order to obtain well-defined QTM steps as in Figure 1.4, it is important that the molecule crystallize with a single orientation in the unit cell. While this is not a necessity for hysteresis measurements, a single orientation provides the most discrete monodisperse magnetic unit which is often easier to align in a magnetic field. This criterion, however, precludes many SMMs which crystallize in space groups whose symmetry allows for more than one orientation of the molecule in the unit cell. Such structural considerations in the magnetic characterization of SMMs will be further discussed later in this Introduction.

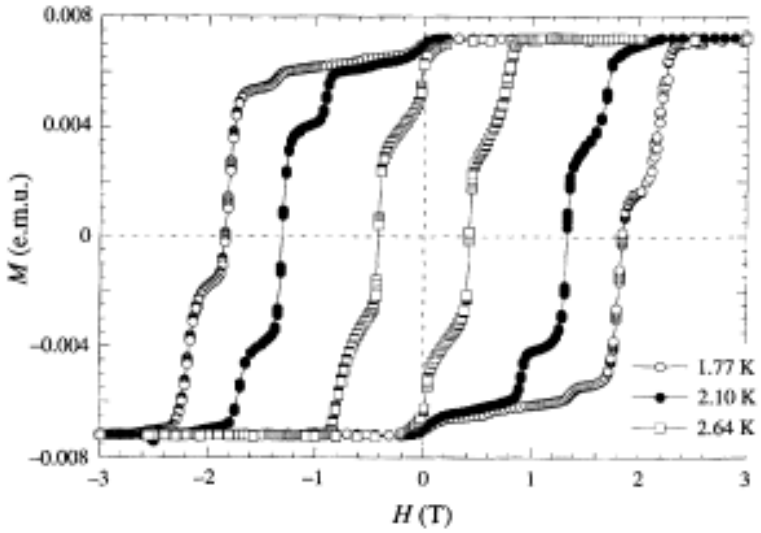

Figure 1.4. Temperature-dependent magnetization vs. field plot for $Mn_{12}Ac$.

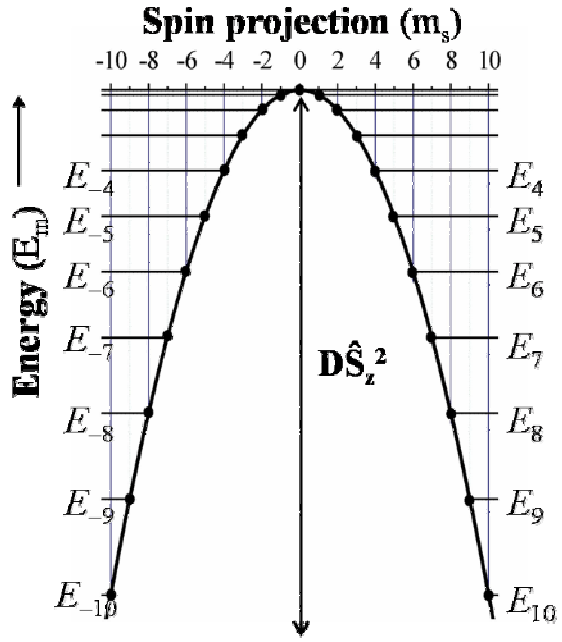

Figure 1.5. Potential energy, E_m, *vs.* spin projection, m_s, for a S = 10 SMM.

The vertical steps correspond to quantum tunneling transitions between the m_s levels (m_s is the projection of the spin, S, onto the magnetic quantization axis) of opposite spin projection, i.e. $m_s = -10$ to $m_s = +10$ at $H = 0$ T, and occur at regularly spaced field intervals of the axial zfs parameter, D.[2] As the longitudinal field is swept, the energy levels on opposing sides of the anisotropy barrier shift according to the Zeeman interaction, making QTM possible between spin states with $|\Delta m_s| \neq 0$ (see Figure 1.6).[50] Since both ground state and thermally activated tunneling can occur, this phenomenon is highly temperature and sweep-rate dependent.[1,50]

In 1983, Sir Michael Berry discovered that a quantum system, when adiabatically transported in a closed circuit, will acquire a phase that depends on the geometry of the circuit.[51] For example, consider a situation in which a vector is transported along a flat surface and a curved surface as depicted in Figure 1.7. The vector that is transported along the flat surface will remain unchanged while the vector transported along the curved surface will have been rotated a certain degree (dependent on the curvature of the surface) and thus has acquired a phase.[51]

Since electrons accumulate Berry phase, they may give rise to interference effects for the multiple pathways.[51] Figure 1.8 shows a unit sphere with the minima A and B, where A and B are the two spin states, connected by two different tunneling paths.[24] The positions of A and B depend on the transverse magnetic field where the x-axis and z-axis represent the hard and easy axes, respectively. The topological interference between the two tunneling paths of opposite direction is the Berry phase or quantum spin phase. Whenever the shaded region in Figure 1.8 is equal to $k\pi/S$ (k being an odd integer), destructive interference is observed leading to a quenching of the

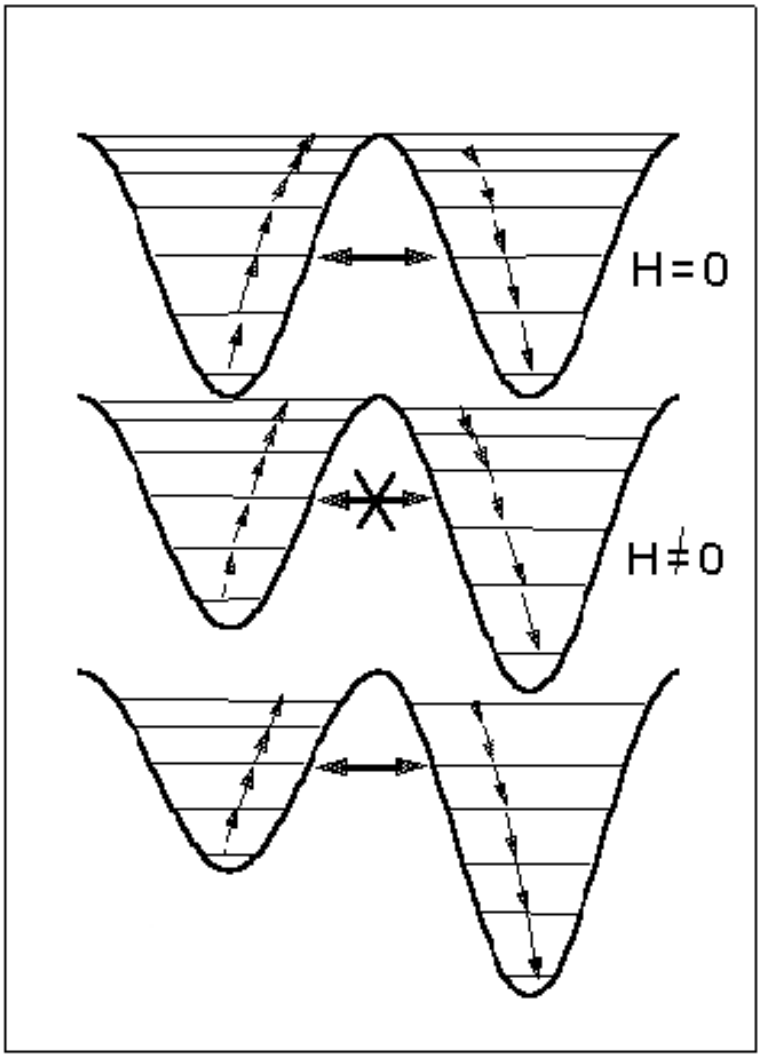

Figure 1.6. Double-well potential plot in an applied field, *H*.

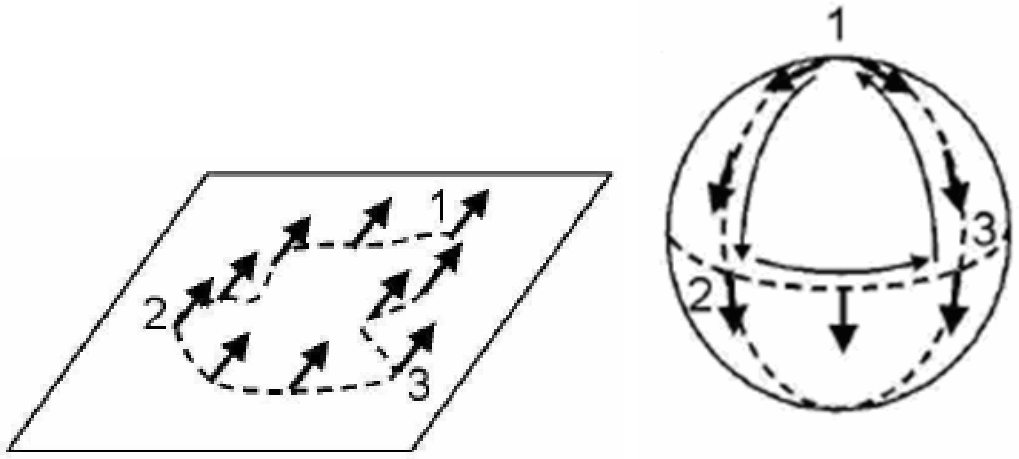

Figure 1.7. Parallel transport of a vector in a loop along a flat surface (left) and a curved surface (right).

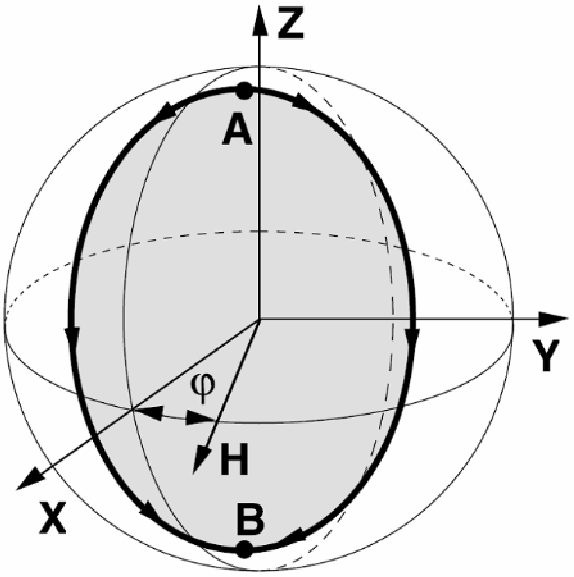

Figure 1.8. Unit sphere with the minima **A** and **B** connected by two paths; clockwise and counterclockwise. The x, y and z axes are the hard, medium and easy axes, respectively.

tunneling rate.[24,52-55]

Though Berry phase has been previously observed in quantum mechanics in the Aharonov-Bohm effect, a S =1/2 spin in a magnetic field, and in NMR experiments,[51,56] it was exhibited in SMMs for the first time in the extensively studied Fe_8 complex, $[Fe_8O_2(OH)_{12}(tacn)_6]Br_8 \cdot 9H_2O$, where tacn is triazocyclononane, shown in Figure 1.9.[24,57] Oscillations in the tunnel splitting (Δ) as a function of the transverse field (applied at an angle of $\varphi = 0°$) were observed in this S = 10 complex.[24] The tunnel splitting, Δ, is determined by placing the crystal in a high negative field, sweeping the magnetic field at a constant sweep rate over one of the quantum tunneling resonances, and measuring the resulting change in magnetization. The relaxed magnetization value, *M(N),* is then determined by the Landau-Zener model (equation *1.13*),[58,59]

$$M(N) \sim exp[-2PN] = exp(-\Gamma t), \qquad (1.13)$$

where N in the number of times the magnetic field was swept across a given quantum tunneling transition, Γ is the overall Landau-Zener transition rate, and P is the tunneling probability which is determined from the number of molecules that reversed their spin. Finally, the tunnel-splitting Δ can be calculated from equation *1.14*,[24]

$$P = 1- exp\,[- \pi\Delta^2 / (4hg\mu_B SdH/dt)]. \qquad (1.14)$$

Figure 1.10 shows the tunnel splitting measured for tunneling transitions between the M_s = -10 and M_s = 10-n states (where n = 0, 1, and 2 represent the transitions from M_S = -10 to +10, -10 to +9, and -10 to +8, respectively) for the Fe_8

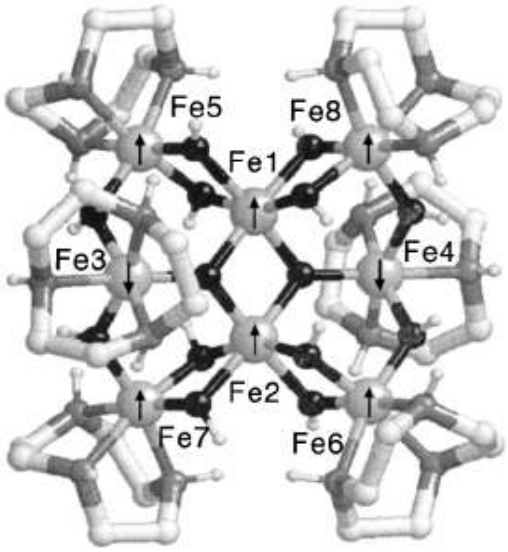

Figure 1.9. Molecular structure and spin orientations in the S = 10 complex $[Fe_8O_2(OH)_{12}(C_6H_{15}N_3)_6]Br_8 \cdot 9H_2O$ (Fe_8).

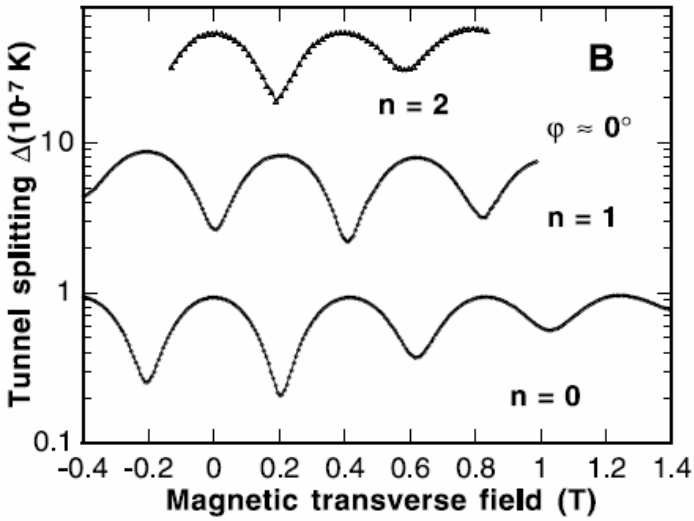

Figure 1.10. Tunnel splitting measured as a function of transverse field (φ = 0°) for the Fe_8 SMM, where n = 0, 1, 2 for the tunneling transitions m_s = -10 to m_s = 10-n.

SMM.[24] The observed Berry phase is the result of constructive and destructive interference between the two tunnel paths of opposite direction (*vide supra*). Note the different phasing of the oscillations that occurs depending on whether $|\Delta m_s|$ is odd or even, i.e. when $n = 1$ compared to when $n = 0$ or 2.[24] In Chapter 3, a new [Mn_4] SMM is described in which fascinating quantum behavior is observed, including a Berry phase.

1.5. High-Frequency Electron Paramagnetic Resonance (HFEPR)

Since ferromagnetic materials often exhibit magnetization hysteresis and some of the other magnetic properties also observed in SMMs, it is important to clearly distinguish between these two types of materials. The slow magnetization relaxation in ferromagnetic materials is due to long-range ordering of multiple domains as opposed to being attributed to a single-molecule in SMMs. One characterization technique proven useful for confirming the absence of long-range ordering in SMMs is high-frequency electron paramagnetic resonance (HFEPR).[60]

Although magnetization measurements on bulk polycrystalline samples yield reasonable estimates of Hamiltonian parameters, single-crystal HFEPR studies can unambiguously determine the ground state spin,[61-64] the sign and magnitude of the axial zfs parameter D,[65] and the characterization of transverse zfs terms [*e.g.* rhombic $E(\hat{S}_x^2 - \hat{S}_y^2)$ and fourth-order ($B_4^4\hat{O}_4^4$)].[16] The presence of transverse terms gives rise to the mixing of m_s states of opposite projection that leads to QTM.[66,67] The general Hamiltonian in equation *1.6* is expanded to include higher order ZFS terms and is given in equation *1.15*,

$$\hat{H} = \mu_B \hat{S} \cdot \vec{g} \cdot \vec{B} + D\hat{S}_z^2 + E(\hat{S}_x^2 - \hat{S}_y^2) + B_4^0 \hat{O}_4^0 + \hat{O}_{4,6..}^T + \hat{H}' \qquad (1.15)$$

where the additional terms represent fourth-order axial anisotropy (containing $\hat{S}_z^4$), possible higher-order (4^{th} and 6^{th} order) contributions to the transverse anisotropy, and finally, $\hat{H}'$, which parameterizes all other perturbations such as intermolecular dipolar and exchange interactions.

Magnetic-dipole transitions between the $2S+1$ ground spin states differing in m_s by ± 1 (*i.e.* -5 to -4, -4 to -3…etc.) are manifested in the peaks observed in the EPR spectra. When no zero-field splitting is present (isotropic), all $2S$ possible transitions are degenerate, therefore only a single EPR peak should be observed. However, anisotropic terms in the Hamiltonian split the spectrum into $2S$ discrete peaks which often require strong magnetic fields (B) and high frequencies (f) in order to be fully resolved.[63,68]

Analysis of the EPR spectra as a function of temperature allows for the determination of the absolute sign of D based on the thermal populations of m_s levels inferred from the spectra.[69,70] This was recently shown in a series of distorted $[Mn^{III}_3Ni^{II}]$ cubane SMMs with $S = 5$ ground states reported by Feng *et al.*[63,64] in 2008. Figure 1.11 shows the hard plane HFEPR spectra for $[Mn^{III}_3Ni^{II}(hmp)_3O(N_3)_3(O_2CPh)_3]$ measured at temperatures from 2 to 20 K. As the temperature decreases, the Boltzmann distribution of the spectra shifts toward the transitions taking place at higher magnetic fields, indicative of a negative D-value. (Similarly, if measured along the easy axis of the molecule, a negative D-value would be manifested in the thermal population of the

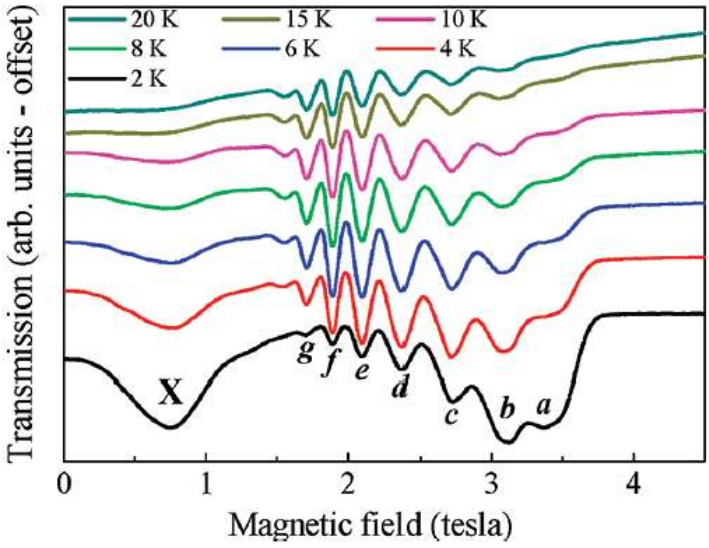

Figure 1.11. Temperature-dependent HFEPR spectra in the hard plane of $[Mn^{III}_3Ni^{II}(hmp)_3O(N_3)_3(O_2CPh)_3]$ from 2-20 K at 59.9 GHz.

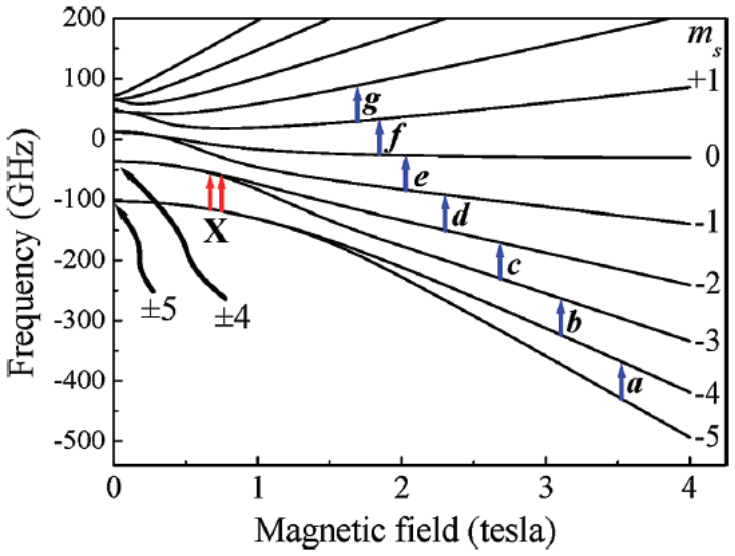

Figure 1.12. Energy level diagram for the hard plane of $[Mn^{III}_3Ni^{II}(hmp)_3O(N_3)_3(O_2CPh)_3]$ where blue and red arrows indicate the EPR transitions **a-g** and **X** in Figure 1.10, respectively.

transitions occurring at lower magnetic fields.) The peak assignments (**a-g**, and **X**) in Figure 1.11 correspond to the $|\Delta m_s| = 1$ transitions in the energy level diagram shown in Figure 1.12.[63,64] Asymmetry and line-broadening are often observed in EPR spectra as a result of ligand and/or solvent disorder in the crystal which leads to a distribution of local *g* and *D* tensors.[63,71-74]

Frequency-dependent EPR data can be fit by exact diagonalization of equation *1.15* to give the Hamiltonian parameters *S*, *D*, *g* and any higher-order terms present. Both easy axis and hard plane EPR measurements were obtained for $[Mn^{III}_3Ni^{II}(hmp)_3O(N_3)_3(O_2CPh)_3]$ at frequencies between 50 and 135 GHz. The observed peak positions are plotted in Figure 1.13 with the best simulations of the data represented by the solid black curves. A single set of parameters ($S = 5$, $D = -0.23$ cm^{-1}, $B_4^0 = -5.68 \times 10^{-5}$ cm^{-1}, $g_z = 2.02$, and $g_x = g_y = 1.95$) gave good agreement with the data obtained for both easy axis and hard plane orientations.[63,64] The spacing of these simulation curves provides valuable information regarding the isolation of the ground state as will be further discussed in single-crystal HFEPR experiments of a promising S = 9 [Mn_4] dicubane complex in Chapter 3.

1.6. Structural Considerations and Environmental Coupling

As was briefly mentioned in the discussion of QTM steps in the magnetization hysteresis loops of Mn_{12}Ac, there are many structural factors that must be considered when studying SMMs. For single-crystal studies (magnetization hysteresis, HFEPR, etc.), it is advantageous if the SMM crystallizes with only one orientation of the molecule in the unit cell. This ensures that the easy axis of each molecule in the crystal

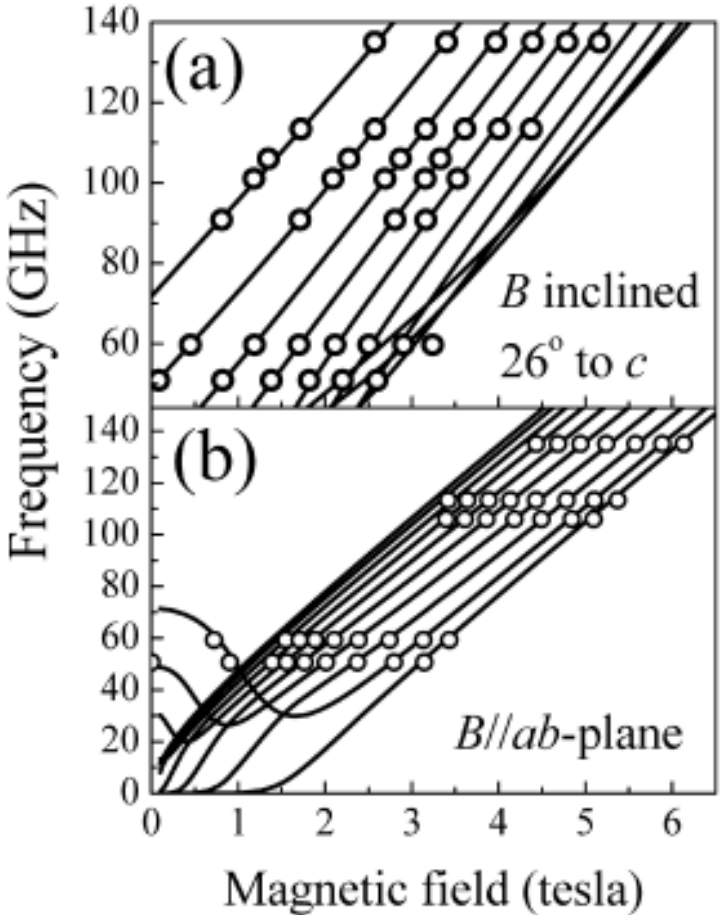

Figure 1.13. Frequency-dependent HFEPR peak positions for $[Mn^{III}_3Ni^{II}(hmp)_3O(N_3)_3(O_2CPh)_3]$ at 50-135 GHz with the field oriented (a) close to the easy axis and (b) exactly in the hard plane. Solid curves represent best simulations of the experimental data.

lattice is aligned in the same direction and can easily be oriented in a magnetic field.

Intermolecular interactions have also been shown to greatly affect the magnetic and quantum properties of SMMs. Both through-bond (magnetic exchange) and through-space (dipole-dipole) interactions can act as biasing magnetic fields resulting in so-called exchange-biased quantum tunneling.[75] This phenomenon was first observed in the $[Mn_4]_2$ SMM, $[Mn_4O_3Cl_4(O_2CEt)_3(py)_3]_2$ shown in Figure 1.14.[18,75] This complex packs in discrete head-to-head dimers in the crystal lattice in which two neighboring $[Mn_4]$ molecules are antiferromagnetically coupled through six C–H···Cl hydrogen bonds and a close Cl···Cl contact. The intermolecular exchange is very weak ($J \approx 0.07$ cm^{-1}) as compared to the intramolecular exchange in the individual $[Mn_4]$ SMMs which was found to be ~8 cm^{-1} for the ferromagnetic Mn(III)-Mn(III) interactions and ~23 cm^{-1} for the dominant antiferromagnetic Mn(IV)-Mn(III) interactions.[76] The weak intermolecular exchange interaction is still enough to cause mixing of wavefunctions of the individual molecules (S = 9/2 ground state) leading to QTM resonances different from those observed in the individual molecules.[18,75]

Most noticeably, in the temperature-dependent magnetization vs. field plots for this $[Mn_4]_2$ dimer (Figure 1.15), there is no QTM step at H = 0 (k = 0 resonance). This anomaly was explained by taking into account the linear combinations of spin states for the coupled $[Mn_4]_2$. The resulting energy level diagram of the thermally-populated spin states for this dimer (Figure 1.16) show that when H = 0, a transition from the (-9/2, -9/2) to the (9/2, 9/2) spin state would occur. This would require both molecules to reverse their spins simultaneously, the probability for which is very small, thus no QTM

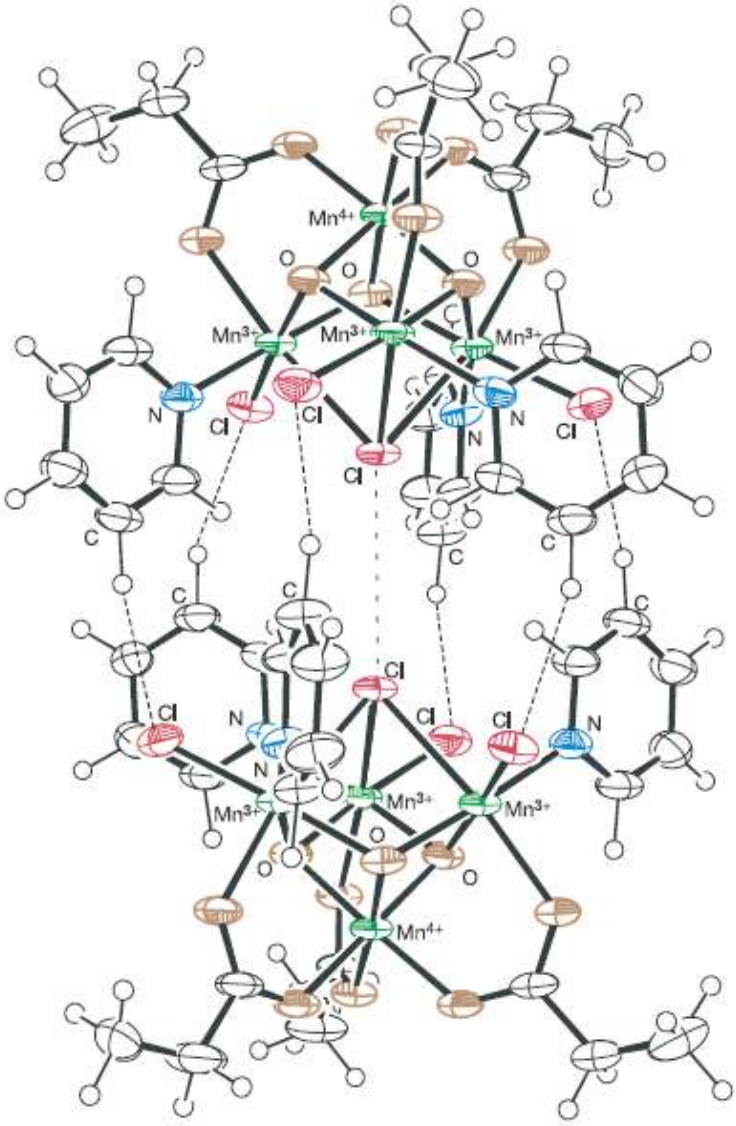

Figure 1.14. ORTEP of $[Mn_4O_3Cl_4(O_2CEt)_3(py)_3]_2$, $[Mn_4]_2$, showing intermolecular H-bonding contacts.

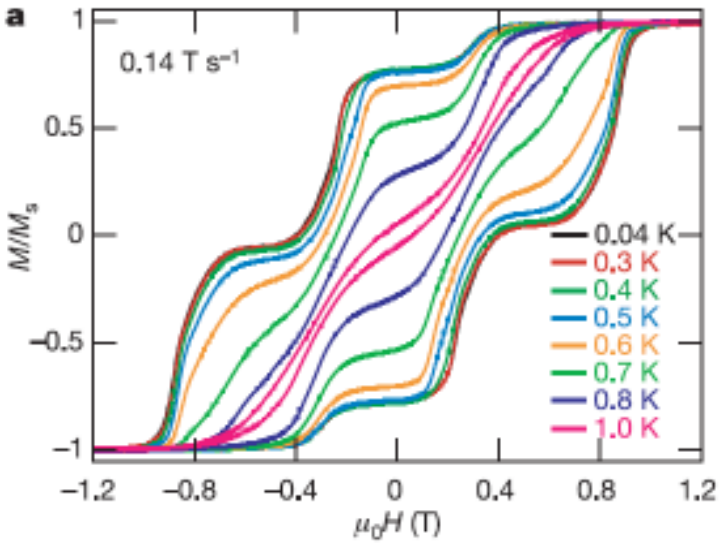

Figure 1.15. Temperature-dependent magnetization hysteresis plot for $[Mn_4]_2$.

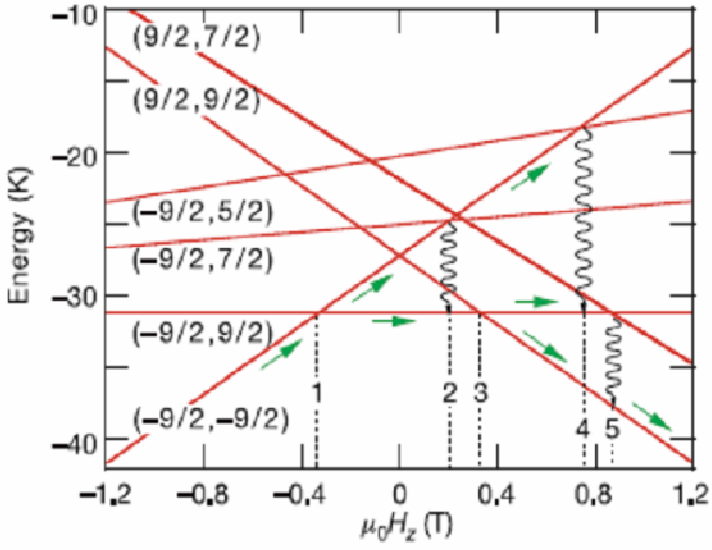

Figure 1.16. Energy vs. magnetic field plot for $[Mn_4]_2$ showing levels likely to be populated at very low temperatures.

is observed.[75] In Chapter 4, a [Mn_{12}] wheel-shaped SMM is introduced which shows similar quantum phase interference (extra QTM resonances) which can be explained by an intramolecular ferromagnetic coupling interaction.[77,78]

Other examples of exchange-biased QTM are less severe in that the intermolecular interactions are not strong enough to induce mixing of wavefunctions but merely act as a small bias, shifting the k = 0 QTM resonance slightly from H = 0. This is the case for a family of tetranuclear Ni(II) cubane complexes with the general formula of $[Ni(hmp)(ROH)Cl]_4$, where hmp^- is the anion of 2-hydroxymethylpyridine, and R = alkyl.[20] It was found that increasing the steric bulk surrounding the magnetic core of the molecule, through systematic substitution of the peripheral alcohol ligands, lead to near elimination of this field-bias. This basic principle of "isolating" the magnetic core of a SMM in order to decrease intermolecular interactions is the primary focus of Chapters 2 and 3 and will be further discussed therein.

Despite the significant intermolecular interactions in the family of $[Ni(hmp)(ROH)Cl]_4$ cubane SMMs discussed above, the magnetization hysteresis and HFEPR data were highly resolved and revealed well-defined QTM steps and spinstate transitions, respectively.[79] In fact, there are many documented cases of SMMs with appreciable intermolecular interactions which have shown some of the clearest demonstrations of quantum phenomena and have been the subject of many benchmark studies in the field molecular magnetism. [1,18,20,80]

High resolution magnetization hysteresis and HFEPR data has been proven to be largely due to the high crystalline quality of the complexes that give these results. Such high-quality SMMs normally meet the following criteria: (i) Crystallize with a single

orientation of the molecule in the crystal lattice; (ii) absence of co-crystallized solvate molecules; (iii) minimal disorder in the crystal structure; and (iv) significant isolation between neighboring molecules in order to limit intermolecular interactions. These criteria are not satisfied in many high-spin and high-nuclearity SMMs, such as the manganese wheel-shaped complexes described in Chapter 4,[81-83] which often have large amounts of ligand disorder and co-crystallized solvate molecules. These crystallographic artifacts result in a distribution of microenvironments which consequently leads to a broadening of magnetic transitions and less well-defined spectral properties. For example, as will later be discussed in more detail, the larger wheel-shaped SMMs such as the $[Mn_{84}]$ wheel, exhibits smooth hysteresis loops with no observable QTM steps even at low temperatures.[84]

When all of the above criteria are met, however, some astonishing quantum phenomena can be observed. For instance, recent work from our laboratory produced the $[NEt_4]_3[Mn_3Zn_2(salox)_3O(N_3)_6Cl_2]$ complex which consists of an oxo-centered $[Mn_3]$ triangle capped above and below the plane by two diamagnetic Zn(II) ions (see ORTEP in inset of Figure 1.17).[85] This complex (which has a S = 6 ground state) has no co-crystallized solvate molecules, no disorder, a single orientation of the molecule in the unit cell, and significant separation between adjacent $[Mn_3]$ units due to the Zn(II) ions and quaternary ammonium counter cations. In fact, the closest Mn···Mn separation in this complex is ~10 Å.[85] For the first time, QTM selection rules (governed by the symmetry of the molecule) were actually manifested in the magnetization hysteresis measurements for this SMM. Since this molecule possesses C_3 symmetry, only transitions where $\Delta|m_s| = 3n$ are allowed by QTM selection rules. Figure 1.17 shows a

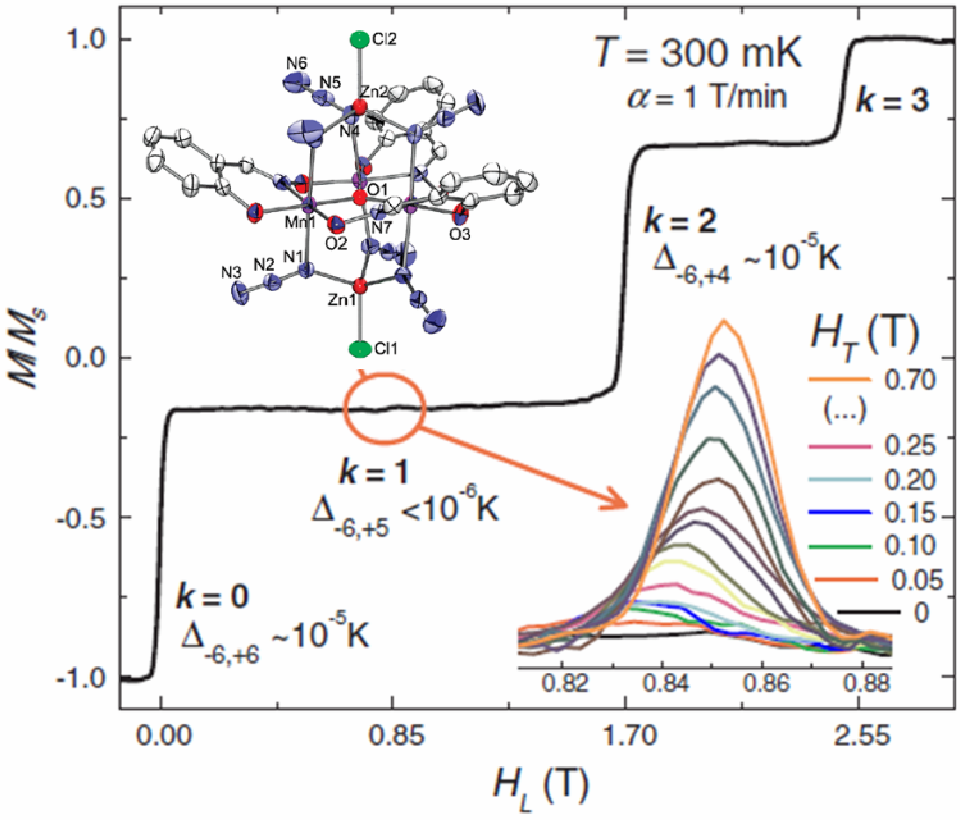

Figure 1.17. Magnetization vs. field plot for $[NEt_4]_3[Mn_3Zn_2(salox)_3O(N_3)_6Cl_2]$ with an ORTEP shown in top inset and the growth of $k = 1$ QTM resonance with application of a transverse field, H_T, shown in bottom inset.

portion of the hysteresis loop measured at 300 mK in which the $k = 1$ QTM resonance is absent and can only be observed by applying a transverse field, H_T.[85,86] This was yet another benchmark observation due to the high crystal quality and limited intermolecular interactions in this SMM.

Another quantum phenomenon that has been heavily sought after in the study of SMMs, is quantum coherence.[75] As discussed earlier, quantum tunneling of the magnetization (QTM) in a SMM is characterized by a periodic oscillation between the "spin-up" and "spin-down" energy states. When this oscillation occurs at a precise phase (Rabi oscillation), coherent tunneling is observed. This phenomenon is one of the basic principles behind construction of a viable QIPS device.[31] However, because of the tendency for SMMs to couple to their environment, the wavefunction cannot retain the memory of its phase resulting in decoherence, or non-specific QTM, and the subsequent loss of information.[26] Such environmental factors that cause decoherence in SMMs include phonon interactions, nuclear spins, and intermolecular interactions (as mentioned above).

In order for SMMs to one day be useful for applications in quantum computing and molecular spintronics devices, an appreciable spin decoherence time, T_2, must be achieved. If the decoherence time is too short, the spin energy levels cannot be manipulated on a measurable timescale.[79,87] In 2009, the aforementioned Fe_8 SMM was studied by pulsed HFEPR spectroscopy in order to determine its spin decoherence time, T_2.[88] A value of 712 ns for T_2 was estimated from the decay rate of the pulsed microwave spin-echo followed by spin polarization of the sample.[88] These single crystal

HFEPR results for Fe_8 were unprecedented and clearly demonstrated the ability to coherently manipulate the quantum spin states in a SMM.[29,88]

Though manganese clusters make up the majority of SMMs in the literature, no manganese complexes have shown a signal in pulsed HFEPR experiments. The high rate of spin decoherence in manganese SMMs is thought to be due to the large nuclear spin (I = 5/2) for Mn(III) metal centers whereas I = 0 for Fe(III) ions. Though studies have shown that nuclear spins can greatly affect QTM, it remains uncertain as to whether or not this is the primary source of decoherence in manganese SMMs.[28] The work of this thesis is aimed at systematically developing manganese complexes which meet the structural requirements necessary for an "ideal" SMM. We often have tremendous chemical control over many of the environmental interactions that cause decoherence. By taking these factors out of the equation, we can gain a better understanding of the underlying causes of decoherence in these systems and possibly uncover new and interesting quantum behavior.

1.7. Outline of Dissertation

In Chapters 2 and 3, two new families of mixed-valent tetranuclear manganese dicubane SMMs are introduced. Ferrocene- and betaine-based carboxylate ligands are used in Chapters 2 and 3, respectively, to add steric bulk to the magnetic core of well-known [Mn_4] SMMs. Furthermore, the redox properties of ferrocene carboxylate were exploited in an attempt to create cationic SMMs which could be further isolated by bulky couterions. In Chapter 3, the zwitterionic betaine carboxylates (Bet) resulted in +2 and +4 cations (depending on degree of substitution) in a one-step synthesis. One of

these complexes, $[Mn_4(Bet)_4(mdea)_2(mdeaH)_2](BPh_4)_4$, is significantly separated from neighboring molecules in the crystal lattice, contains no co-crystallized solvate molecules, and only has one orientation in the unit cell making it an ideal complex for single-crystal magnetization hysteresis and HFEPR measurements. This complex shows unprecedented features in its magnetization hysteresis and relaxation measurements including asymmetric Berry phase interference patterns.

Chapter 4 is focused on molecular wheels which function as SMMs and, in particular, the ever growing sub-group of single-stranded molecular wheels. The family of $[Mn_{12}]$[77,82,83] and $[Mn_{16}]$[81] single-stranded wheels are discussed in detail in the introduction as they have been extensively studied in our laboratory. The synthesis, structure, and magnetic properties of a new, and also the largest, single-stranded manganese wheel are also reported for the first time in Chapter 4. This $[Mn_{24}]$ molecular wheel has very high-symmetry (S_6 and crystallizes in a rhombohedral space group) which may be responsible for the seemingly small barrier to the reversal of magnetization despite its large spin ground state upwards of $S = 20$.

Yet another common topology for SMMs is discussed in Chapter 5; rod-shaped SMMs, in particular, hexanuclear manganese rods. Four new $[Mn_6]$ complexes employing the tripodal ligand, tris-hydroxymethylpropane ($tmpH_3$), are analyzed. Structurally, these complexes are similar to other rod-shaped complexes found in the literature but possess a slightly different core structure than any other $[Mn_6]$ rods studied thus far. Also, all four of the $[Mn_6]$ rods reported here possess non-zero ground states and SMM-like characteristics.

Lastly, Chapter 6 takes a look at superexchange interactions in the bridging ligand, dicyanamide ($N(CN)_2^-$), through a simple dinuclear Cu(II) system. Dinuclear copper complexes have been extensively studied in past years utilizing a variety of bridging ligands. In Chapter 6, magnetic susceptibility studies of a tren-capped dinuclear Cu(II) complex and its mononuclear counterpart show that dicyanamide provides a viable exchange pathway between paramagnetic metal centers which has further implications in recently reported dicyanamide-linked [Mn_4] SMMs. Furthermore, the antiferromagnetic coupling constant calculated for this dinuclear Cu(II) species is the largest value reported for a single-dicyanamide bridge to date.

1.8. References

(1) Sessoli, R.; Tsai, H. L.; Schake, A. R.; Wang, S. Y.; Vincent, J. B.; Folting, K.; Gatteschi, D.; Christou, G.; Hendrickson, D. N. *Journal of the American Chemical Society* **1993**, *115*, 1804-1816.

(2) Eppley, H. J.; Tsai, H. L.; Devries, N.; Folting, K.; Christou, G.; Hendrickson, D. N. *Journal of the American Chemical Society* **1995**, *117*, 301-317.

(3) Tsai, H. L.; Eppley, H. J.; DeVries, N.; Folting, K.; Christou, G.; Hendrickson, D. N. *Molecular Crystals and Liquid Crystals Science and Technology Section a-Molecular Crystals and Liquid Crystals* **1995**, *273*, A167-A173.

(4) Aubin, S. M. J.; Wemple, M. W.; Adams, D. M.; Tsai, H. L.; Christou, G.; Hendrickson, D. N. *Journal of the American Chemical Society* **1996**, *118*, 7746-7754.

(5) Lis, T. *Acta Crystallographica Section B-Structural Science* **1980**, *36*, 2042-2046.

(6) Sessoli, R.; Gatteschi, D.; Caneschi, A.; Novak, M. A. *Nature* **1993**, *365*, 141-143.

(7) Stamp, P. C. E.; Gaita-Arino, A. *Journal of Materials Chemistry* **2009**, *19*, 1718-1730.

(8) Loss, D.; Divincenzo, D. P.; Grinstein, G.; Awschalom, D. D.; Smyth, J. F. *Physica B* **1993**, *189*, 189-203.

(9) Harris, J. G. E.; Grimaldi, J. E.; Awschalom, D. D.; Chiolero, A.; Loss, D. *Physical Review B* **1999**, *60*, 3453-3456.

(10) Gider, S.; Awschalom, D. D.; DiVincenzo, D. P.; Loss, D. *Science* **1996**, *272*, 425-426.

(11) Mahata, P.; Natarajan, S.; Panissod, P.; Drillon, M. *Journal of the American Chemical Society* **2009**, *131*, 10140-10150.

(12) Sato, T. *Acta Crystallographica Section A* **2005**, *61*, 39-50.

(13) Gatteschi, D.; Caneschi, A.; Pardi, L.; Sessoli, R. *Science* **1994**, *265*, 1054-1058.

(14) Prokof'ev, N. V.; Stamp, P. C. E. *Journal of Low Temperature Physics* **1996**, *104*, 143-209.

(15) Prokof'ev, N. V.; Stamp, P. C. E. *Journal of Low Temperature Physics* **1998**, *113*, 1147-1152.

(16) Gatteschi, D.; Sessoli, R. *Angewandte Chemie-International Edition* **2003**, *42*, 268-297.

(17) Wernsdorfer, W.; Bhaduri, S.; Tiron, R.; Hendrickson, D. N.; Christou, G. *Physical Review Letters* **2002**, *89*, 197201.

(18) Wernsdorfer, W.; Allaga-Alcalde, N.; Hendrickson, D. N.; Christou, G. *Nature* **2002**, *416*, 406-409.

(19) Yang, E. C.; Harden, N.; Wernsdorfer, W.; Zakharov, L.; Brechin, E. K.; Rheingold, A. L.; Christou, G.; Hendrickson, D. N. *Polyhedron* **2003**, *22*, 1857-1863.

(20) Yang, E. C.; Wernsdorfer, W.; Zakharov, L. N.; Karaki, Y.; Yamaguchi, A.; Isidro, R. M.; Lu, G. D.; Wilson, S. A.; Rheingold, A. L.; Ishimoto, H.; Hendrickson, D. N. *Inorganic Chemistry* **2006**, *45*, 529-546.

(21) Wernsdorfer, W.; Sessoli, R.; Caneschi, A.; Gatteschi, D.; Cornia, A. *Journal of the Physical Society of Japan* **2000**, *69*, 375-382.

(22) Wernsdorfer, W.; Bhaduri, S.; Boskovic, C.; Christou, G.; Hendrickson, D. N. *Physical Review B* **2002**, *65*, 180403.

(23) Miyashita, S.; Saito, K.; Kobayashi, H. *Progress of Theoretical Physics* **2003**, *109*, 741-749.

(24) Wernsdorfer, W.; Sessoli, R. *Science* **1999**, *284*, 133-135.

(25) Kim, G. H. *Journal of Applied Physics* **2002**, *91*, 3289-3293.

(26) Dube, M.; Stamp, P. C. E. *Chemical Physics* **2001**, *268*, 257-272.

(27) Cuccoli, A.; Fort, A.; Rettori, A.; Adam, E.; Villain, J. *European Physical Journal B* **1999**, *12*, 39-46.

(28) Wernsdorfer, W.; Sessoli, R.; Gatteschi, D. *Europhysics Letters* **1999**, *47*, 254-259.

(29) Prokof'ev, N. V.; Stamp, P. C. E. *Journal of Physics-Condensed Matter* **1993**, *5*, L 663-L 670.

(30) Prokof'ev, N. V.; Stamp, P. C. E. *Reports on Progress in Physics* **2000**, *63*, 669-726.

(31) Leuenberger, M. N.; Loss, D. *Physical Review B* **2000**, *61*, 12200-12203.

(32) Kambe, K. *Journal of the Physical Society of Japan* **1950**, *5*, 48.

(33) Vincent, J. B.; Christmas, C.; Chang, H. R.; Li, Q. Y.; Boyd, P. D. W.; Huffman, J. C.; Hendrickson, D. N.; Christou, G. *Journal of the American Chemical Society* **1989**, *111*, 2086-2097.

(34) Libby, E.; Mccusker, J. K.; Schmitt, E. A.; Folting, K.; Hendrickson, D. N.; Christou, G. *Inorganic Chemistry* **1991**, *30*, 3486-3495.

(35) Van Vleck, J. H. *The Theory of Electric and Magnetic Susceptibilities*; Oxford Univ. Press., 1965.

(36) Yoo, J.; Yamaguchi, A.; Nakano, M.; Krzystek, J.; Streib, W. E.; Brunel, L. C.; Ishimoto, H.; Christou, G.; Hendrickson, D. N. *Inorganic Chemistry* **2001**, *40*, 4604-4616.

(37) Honda, M. *J. Phys. Soc. Jpn.* **1993**, *62*, 704-16.

(38) Gatteschi, D.; Kahn, O.; Miller, J. S.; Palacio, F. *Advanced Materials* **1991**, *3*, 161-163.

(39) Gao, S.; Su, G.; Yi, T.; Ma, B. Q. *Physical Review B* **2001**, *6305*, -.

(40) Wang, S. Y.; Folting, K.; Streib, W. E.; Schmitt, E. A.; Mccusker, J. K.; Hendrickson, D. N.; Christou, G. *Angewandte Chemie-International Edition in English* **1991**, *30*, 305-306.

(41) Wang, S. Y.; Wemple, M. S.; Yoo, J.; Folting, K.; Huffman, J. C.; Hagen, K. S.; Hendrickson, D. N.; Christou, G. *Inorganic Chemistry* **2000**, *39*, 1501-1513.

(42) Brechin, E. K.; Yoo, J.; Nakano, M.; Huffman, J. C.; Hendrickson, D. N.; Christou, G. *Chemical Communications* **1999**, 783-784.

(43) Yoo, J.; Brechin, E. K.; Yamaguchi, A.; Nakano, M.; Huffman, J. C.; Maniero, A. L.; Brunel, L. C.; Awaga, K.; Ishimoto, H.; Christou, G.; Hendrickson, D. N. *Inorganic Chemistry* **2000**, *39*, 3615-3623.

(44) Yamaguchi, A.; Kusumi, N.; Ishimoto, H.; Mitamura, H.; Goto, T.; Mori, N.; Nakano, M.; Awaga, K.; Yoo, J.; Hendrickson, D. N.; Christou, G. *Journal of the Physical Society of Japan* **2002**, *71*, 414-417.

(45) Wittick, L. M.; Murray, K. S.; Moubaraki, B.; Batten, S. R.; Spiccia, L.; Berry, K. J. *Dalton Transactions* **2004**, 1003-1011.

(46) Ako, A. M.; Mereacre, V.; Hewitt, I. J.; Clerac, R.; Lecren, L.; Anson, C. E.; Powell, A. K. *Journal of Materials Chemistry* **2006**, *16*, 2579-2586.

(47) Foguet-Albiol, D.; O'Brien, T. A.; Wernsdorfer, W.; Moulton, B.; Zaworotko, M. J.; Abboud, K. A.; Christou, G. *Angewandte Chemie-International Edition* **2005**, *44*, 897-901.

(48) Beedle, C. C.; Stephenson, C. J.; Heroux, K. J.; Wernsdorfer, W.; Hendrickson, D. N. *Inorganic Chemistry* **2008**, *47*, 10798-10800.

(49) Wittick, L. M.; Murray, K. S.; Moubaraki, B.; Batten, S. R.; Spiccia, L.; Berry, K. J. *Dalton Transactions* **2004**, 1003-1011.

(50) Thomas, L.; Lionti, F.; Ballou, R.; Gatteschi, D.; Sessoli, R.; Barbara, B. *Nature* **1996**, *383*, 145-147.

(51) Berry, M. V. *Proceedings of the Royal Society of London. A. Mathematical and Physical Sciences* **1984**, *392*, 45-57.

(52) del Barco, E.; Kent, A. D.; Rumberger, E. M.; Hendrickson, D. N.; Christou, G. *Physical Review Letters* **2003**, *91*, 047203.

(53) del Barco, E.; Kent, A. D.; Hill, S.; North, J. M.; Dalal, N. S.; Rumberger, E. M.; Hendrickson, D. N.; Chakov, N.; Christou, G. *Journal of Low Temperature Physics* **2005**, *140*, 119-174.

(54) Loss, D.; Divincenzo, D. P.; Grinstein, G. *Physical Review Letters* **1992**, *69*, 3232-3235.

(55) Leuenberger, M. N.; Loss, D. *Physical Review B* **2001**, *6305*, art. no.-054414.

(56) Sjöqvist, E. *Physical Review A* **2000**, *62*, 022109.

(57) Weighardt, K.; Pohl, K.; Jibril, I.; Huttner, G. *Angewandte Chemie International Edition in English* **1984**, *23*, 77-78.

(58) Wernsdorfer, W.; Sessoli, R.; Caneschi, A.; Gatteschi, D.; Cornia, A.; Mailly, D. *Journal of Applied Physics* **2000**, *87*, 5481-5486.

(59) Zener, C. *Proceedings of the Royal Society of London. Series A* **1932**, *137*, 696-702.

(60) Christou, G.; Gatteschi, D.; Hendrickson, D. N.; Sessoli, R. *Mrs Bulletin* **2000**, *25*, 66-71.

(61) Hill, S.; Datta, S.; Liu, J.; Inglis, R.; Milios, C. J.; Feng, P. L.; Henderson, J. J.; Barco, E. d.; Brechin, E. K.; Hendrickson, D. N. *Dalton Transactions* **2010**, *39*, 4693- 4707.

(62) Edwards, R. S.; Hill, S.; Bhaduri, S.; Aliaga-Alcalde, N.; Bolin, E.; Maccagnano, S.; Christou, G.; Hendrickson, D. N. *Polyhedron* **2003**, *22*, 1911-1916.

(63) Feng, P. L.; Beedle, C. C.; Koo, C.; Wernsdorfer, W.; Nakano, M.; Hill, S.; Hendrickson, D. N. *Inorganic Chemistry* **2008**, *47*, 3188-3204.

(64) Feng, P. L.; Beedle, C. C.; Koo, C.; Lawrence, J.; Hill, S.; Hendrickson, D. N. *Inorganica Chimica Acta* **2008**, *361*, 3465-3480.

(65) Rumberger, E. M.; Hill, S.; Edwards, R. S.; Wernsdorfer, W.; Zakharov, L. N.; Rheingold, A. L.; Christou, G.; Hendrickson, D. N. *Polyhedron* **2003**, *22*, 1865-1870.

(66) Hill, S.; Edwards, R. S.; Jones, S. I.; Dalal, N. S.; North, J. M. *Physical Review Letters* **2003**, *90*, -.

(67) Hill, S.; Maccagnano, S.; Park, K.; Achey, R. M.; North, J. M.; Dalal, N. S. *Physical Review B* **2002**, *65*, 224410.

(68) Hill, S.; Perenboom, J. A. A. J.; Dalal, N. S.; Hathaway, T.; Stalcup, T.; Brooks, J. S. *Physical Review Letters* **1998**, *80*, 2453-2456.

(69) Collison, D.; Murrie, M.; Oganesyan, V. S.; Piligkos, S.; Poolton, N. R. J.; Rajaraman, G.; Smith, G. M.; Thomson, A. J.; Timko, G. A.; Wernsdorfer, W.; Winpenny, R. E. P.; McInnes, E. J. L. *Inorganic Chemistry* **2003**, *42*, 5293-5303.

(70) McInnes, E. J. L.; Piligkos, S.; Timco, G. A.; Winpenny, R. E. P. *Coordination Chemistry Reviews* **2005**, *249*, 2577-2590.

(71) Parks, B.; Loomis, J.; Rumberger, E.; Hendrickson, D. N.; Christou, G. *Physical Review B* **2001**, *64*, 184426.

(72) Park, K.; Novotny, M. A.; Dalal, N. S.; Hill, S.; Rikvold, P. A. *Physical Review B* **2002**, *65*, 014426.

(73) Maccagnano, S.; Achey, R.; Negusse, E.; Lussier, A.; Mola, M. M.; Hill, S.; Dalal, N. S. *Polyhedron* **2001**, *20*, 1441-1445.

(74) Park, K.; Novotny, M. A.; Dalal, N. S.; Hill, S.; Rikvold, P. A. *Journal of Applied Physics* **2002**, *91*, 7167-7169.

(75) Hill, S.; Edwards, R. S.; Aliaga-Alcalde, N.; Christou, G. *Science* **2003**, *302*, 1015-1018.

(76) Aubin, S. M. J.; Dilley, N. R.; Pardi, L.; Krzystek, J.; Wemple, M. W.; Brunel, L. C.; Maple, M. B.; Christou, G.; Hendrickson, D. N. *Journal of the American Chemical Society* **1998**, *120*, 4991-5004.

(77) Shah, S. J.; Ramsey, C. M.; Heroux, K. J.; DiPasquale, A. G.; Dalal, N. S.; Rheingold, A. L.; del Barco, E.; Hendrickson, D. N. *Inorganic Chemistry* **2008**, *47*, 9569-9582.

(78) Ramsey, C. M.; del Barco, E.; Hill, S.; Shah, S. J.; Beedle, C. C.; Hendrickson, D. N. *Nat Phys* **2008**, *4*, 277-281.

(79) Leuenberger, M. N.; Loss, D. *Nature* **2001**, *410*, 789-793.

(80) del Barco, E.; Kent, A. D.; Yang, E. C.; Hendrickson, D. N. *Physical Review Letters* **2004**, *93*, 157202.

(81) Shah, S. J.; Ramsey, C. M.; Heroux, K. J.; O'Brien, J. R.; DiPasquale, A. G.; Rheingold, A. L.; del Barco, E.; Hendrickson, D. N. *Inorganic Chemistry* **2008**, *47*, 6245-6253.

(82) Rumberger, E. M.; Zakharov, L. N.; Rheingold, A. L.; Hendrickson, D. N. *Inorganic Chemistry* **2004**, *43*, 6531-6533.

(83) Rumberger, E. M.; Shah, S. J.; Beedle, C. C.; Zakharov, L. N.; Rheingold, A. L.; Hendrickson, D. N. *Inorganic Chemistry* **2005**, *44*, 2742-2752.

(84) Tasiopoulos, A. J.; Vinslava, A.; Wernsdorfer, W.; Abboud, K. A.; Christou, G. *Angewandte Chemie-International Edition* **2004**, *43*, 2117-2121.

(85) Feng, P. L.; Koo, C.; Henderson, J. J.; Nakano, M.; Hill, S.; del Barco, E.; Hendrickson, D. N. *Inorganic Chemistry* **2008**, *47*, 8610-8612.

(86) Henderson, J. J.; Koo, C.; Feng, P. L.; del Barco, E.; Hill, S.; Tupitsyn, I. S.; Stamp, P. C. E.; Hendrickson, D. N. *Physical Review Letters* **2009**, *103*, 017202.

(87) Bogani, L.; Wernsdorfer, W. *Nature Materials* **2008**, *7*, 179-186.

(88) Takahashi, S.; van Tol, J.; Beedle, C. C.; Hendrickson, D. N.; Brunel, L.-C.; Sherwin, M. S. *Physical Review Letters* **2009**, *102*, 087603.

Chapter 2:

Ferrocene-Substituted Single-Molecule Magnets

2.1. Introduction

As discussed in the Introduction Chapter, single-molecule magnets (SMMs) show promise for high-density information storage and quantum computing devices. However, many environmental factors such as phonon effects, nuclear spins, and intermolecular interactions must first be eliminated or controlled in order for these applications to come to fruition.[1,2] Thus there has been much effort directed at designing systems with minimal environmental coupling in order to reduce spin decoherence[1,3-5] in SMMs as introduced in the previous chapter.

One approach to this problem is to limit the intermolecular interactions between neighboring molecules in the crystal lattice by using bulky peripheral ligands to provide "insulation" around the magnetic core. This method has proven to be effective in reducing intermolecular magnetic exchange interactions in tetranuclear Ni(II) SMMs as evidenced by the near elimination of an exchange bias in the hysteresis loops when a bulky insulating ligand is complexes.[6] Another strategy is to synthesize highly-charged SMMs which can then be isolated by bulky counter anions. The ability to then vary the counter anion will provide another avenue to further tune the structural and magnetic properties of SMMs.

The well-known family of $[Mn_4]$ dicubane SMMs was chosen for this project for several reasons. Small metal clusters, though limited in spin, can have a high degree of anisotropy and tend to have less structural disorder, co-crystallized solvate molecules, and environmental degrees of freedom. Therefore, intermolecular interactions and other coupling factors intrinsic to the molecule are already at a minimum. These complexes are easily synthesized from simple metal sources and N-alkylated diethanolamine

chelating ligands which, due to their tunable nature, leads to high structural flexibility.[7,8] Also, there is a large number of these dicubanes which provides a vast amount of information readily available for a systematic study of these complexes.

Most [Mn_4] dicubanes in the literature[7,9-14] have S = 9 (one example of S = 8) ground states and exhibit weak intramolecular ferromagnetic coupling. The butterfly-like core (Mn(III) in the body positions and Mn(II) in the wing positions) is found in all [Mn_4] dicubanes which lends itself to the two J-value coupling scheme discussed in the introductory chapter; this model is used in fitting the magnetic data presented here. The two model [Mn_4] dicubanes (shown in Figure 1.3 of the Introduction Chapter) used for structural and magnetic comparison in this chapter are the S = 9 complexes $[Mn^{II}_2Mn^{III}_2(O_2CPh)_4(mdea)_2(mdeaH)_2] \cdot CH_2Cl_2 \cdot Et_2O$ and $[Mn^{II}_2Mn^{III}_2(O_2CPh)_4(bdea)_2(bdeaH)_2]$, where $MdeaH_2$ and $BdeaH_2$ are N-methyl- and N-butyldiethanolamine, respectively.[9,10]

These previously reported [Mn_4] complexes represent the starting point of this systematic study of limiting intermolecular interactions. Adding bulky alkyl substituents to the chelating amine ligands, though effective in the past with [Ni_4] cubane complexes, has not provided enough steric isolation in [Mn_4] dicubanes to date. On the contrary, in some cases this approach has actually caused the molecules to pack closer together as will be discussed in a later chapter. The focus of this project has since shifted toward substitution of the carboxylate ligands which can be readily exchanged or replaced in the synthesis of [Mn_4] dicubanes.

With these goals in mind, the ferrocene monocarboxylate $(FcCO_2)^-$ ligand was an attractive candidate for several reasons. First, the ferrocene substituent alone will provide some steric hindrance to the cluster which may lead to interesting structural and magnetic properties. Second, a cationic SMM could potentially be synthesized by taking advantage of the redox properties of ferrocene. The resulting ferrocenium (Fc^+) analog will have added electrostatic bulk and also allow for the incorporation of large anions such as BPh_4^- to further isolate the SMMs.

Previously reported metal clusters synthesized with ferrocene monocarboxylate ligands include transition metal coordination polymers (Pb, Zn, Cd),[15] oxo-centered triangle complexes of Cr or Fe,[16,17] a Cd_4O_4 cubane-type structure,[18] and various Mn clusters[19] ranging in nuclearity from two to four metal centers reported by Chen *et al.* in 2008. However, none of these complexes appear to have single-molecule magnetic properties. The ferrocene-1,1′-dicarboxylate ligand has also been used to synthesize a mixed-valent tin-oxygen cluster[20] as well as a family of high-nuclearity Mn clusters.[21] These ferrocene-rich Mn clusters reported by Masello *et al.*[21] were synthesized with the intention of eventually studying the Fc^+ analogs but, despite their non-zero ground state spins, none appear to be SMMs. Therefore, the following series of $[Mn_4]$ dicubanes represent the first ferrocene-substituted SMMs synthesized to date.

2.2. Experimental Section

2.2.1. Preparation

All reactions were performed under aerobic conditions. All reagents and ligands were purchased from Sigma Aldrich and used without further purification. The oxo-

centered trinuclear species, $[Mn_3(O_2CMe)_6(py)_3]$ was prepared according to a previously published synthesis.[22]

$[Mn_3O(O_2CFc)_6(py)_2(H_2O)]$ (1).

1a (1 · toluene · *i*Pr_2O**).** To a solution of $FcCO_2H$ (230 mg, 1.0 mmol) in 20 mL toluene was added excess Et_3N and $[Mn_3(O_2CMe)_6(py)_3]$ (77 mg, 0.1 mmol). The resulting dark brown solution was stirred and warmed for 30 minutes and filtered by gravity. X-ray quality crystals were obtained by slow evaporation or $_iPr_2O$ vapor diffusion of the toluene solution after 5-7 days in 40% yield. Elemental analysis for $C_{89}H_{88}Fe_6Mn_3N_2O_{15}$ (1925.53): calcd. C 55.5, H 4.61, N 1.71; found. C 53.89, H 4.56, N 1.71. Selected FT-IR Data (KBr, cm^{-1}): 3417 (s, br), 1583 (m, br), 1468 (m), 1385 (m,), 1358 (w), 1191 (w), 1105 (w), 1023(w), 818 (w), 619 (w), 511 (w).

1b (1 · 2 MeCN**).** $[Mn_3(O_2CMe)_6(py)_3]$ (50 mg, 0.065 mmol) was dissolved in 20 mL MeCN giving a dark brown solution. A solution of $FcCO_2H$ (150 mg, 0.65 mmol) in 10 mL MeCN and excess Et_3N (orange) was added dropwise to the Mn solution and stirred at room temperature for 2 hours. The resulting dark brown solution was filtered by gravity. X-ray quality crystals were obtained by $_iPr_2O$ vapor diffusion or layering of the MeCN solution after 5-7 days in 30% yield. Selected FT-IR Data (KBr, cm^{-1}): 3417 (s, br), 1583 (m, br), 1468 (m), 1385 (m,), 1358 (w), 1191 (w), 1105 (w), 1023(w), 818 (w), 619 (w), 511 (w).

$[Mn_4(O_2CFc)_4(teaH_2)_2(teaH)_2]$ (2). To a solution of $FcCO_2H$ (186 mg, 0.8 mmol) in 25 mL MeOH was added excess Et_3N and $Mn(O_2CMe)_2 \cdot 4H_2O$ (200 mg, 0.8 mmol). Triethanolamine, $teaH_3$, (0.22 mL, 1.6 mmol) was added dropwise to the suspension which was stirred at room temperature for 1-2 hours. The resulting

transparent dark orange-brown solution was filtered by gravity. X-ray quality crystals were obtained from *i*Pr_2O vapor diffusion of the MeOH solution after 2 days in 5-10 % yield. Elemental analysis for $C_{68}H_{90}Fe_4Mn_4N_4O_{20}$ (1726.60): calcd. C 47.30, H 5.25, N 3.24; found. C 47.26, H 4.95, N 3.30. Selected FT-IR Data (KBr, cm^{-1}): 3440 (s, br), 3348 (s, br), 2860 (m), 1601 (w), 1585 (s), 1475 (s), 1392 (m), 1360 (m), 1319 (s), 1178 (w), 1093 (m), 1022 (m), 633 (w), 590 (w), 513 (m).

$[Mn_4(O_2CFc)_4(mdeaH)_2(mdea)_2]$ · 4MeCN **(3).** To a solution of $FcCO_2H$ (300 mg, 1.3 mmol) in 75 mL MeCN was added excess Et_3N and $Mn(O_2CMe)_2 \bullet 4H_2O$ (128 mg, 0.52 mmol). $MdeaH_2$ (0.2 mL, 1.6 mmol) was added dropwise to the suspension which was allowed to reflux for 1 hour. The resulting dark orange-brown solution was cooled to room temperature and filtered by gravity. X-ray quality crystals were obtained by Et_2O vapor diffusion after 3-5 days in 33% yield (77 mg). Elemental analysis for $C_{66}H_{82}Fe_4Mn_4N_4O_{16}$ (1630.51): calcd. C 48.62, H 5.07, N 3.44; found. C 46.48, H 5.06, N 3.68. Selected FT-IR Data (KBr, cm^{-1}): 3433 (s, br), 2955 (w), 1605 (w), 1587 (w), 1545 (s), 1470 (s), 1389 (s), 1358 (s), 1321 (m), 1093 (m), 1070 (m, br), 912 (w), 515 (m).

$[Mn_4(O_2CFc)_4(bdeaH)_2(bdea)_2]$ · 2MeCN **(4).** Prepared by the same procedure as described for complex **1** except adding $BdeaH_2$ (0.2 mL, 1.6 mmol) in place of $MdeaH_2$. X-ray quality crystals obtained from Et_2O diffusion of the MeCN solution after 3-5 days in 48% yield (115 mg). Elemental analysis for $C_{76}H_{106}Fe_4Mn_4N_4O_{16}$ (1774.80): calcd. C 51.43, H 6.02, N 3.16; found. C 51.07, H 6.06, N 3.13**.** Selected FT-IR Data (KBr, cm^{-1}): 3442 (m, br), 3095 (w), 2956 (m), 2860 (m), 1606 (m), 1549 (m),

1470 (s), 1389 (s), 1358 (s), 1321 (s), 1178 (w), 1105 (m), 1076 (m), 910 (w), 766 (w), 513 (m).

2.2.2. X-Ray Crystallography

Crystals were mounted on a CryoLoop© with Paratone-N© oil. Diffraction intensity data were collected at 208(2) K for **1** and 100(2) K for **2-4** on a Bruker Smart Apex CCD diffractometer with Mo Kα radiation, integrated using the Bruker SAINT software program, and corrected for absorption using the Bruker SADABS program. Crystallographic data and refinement parameters for complex **1** are given in Table 2.1 and those for **2-4** are given in Table 2.2.

All complexes were solved by direct methods (SHELXS-97 for **1** and **2**, SIR-2004 for **3**, and DIRDIF-99 for **4**), developed by successive difference Fourier syntheses, and refined by full matrix least squares on all F^2 data. All non-hydrogen atoms were refined anisotropically by full-matrix least-squares (SHELXL-97). All hydrogen atoms were placed using a riding model and their positions were constrained relative to their parent atom using the appropriate HFIX command in SHELXL-97. Disordered toluene and isopropyl ether solvate molecules in **1a** were accounted for by the Squeeze method while acetonitrile solvate molecules in **3** and **4** were ordered and refined anisotropically. A positionally disordered N-methyldiethanolamine ligand in **3** was modeled in two parts (Part 1 = C2, C4, C5; Part 2 = C2A, C4A, C5A) and refined to a final occupancy of 68%. The oxidation states of the Mn ions were determined by charge considerations, the presence of Jahn-Teller distortion around the high-spin

Table 2.1. Crystallographic data and refinement parameters for **1.**

	1a	**1b**
Formula	$C_{89}H_{88}Fe_6Mn_3N_2O_{15}$	$C_{84}H_{72}Fe_6Mn_3N_4O_{14}$
FW	1925.53	1861.38
T [K]	208(2)	208(2)
λ [Å]	0.71073	0.71073
Crystal system	monoclinic	monoclinic
Space group	C(2)/c	C(2)/c
a [Å]	46.70(3)	45.55(2)
b [Å]	12.845(7)	12.631(5)
c [Å]	31.912(19)	31.389(14)
α [deg]	90	90
β [deg]	124.977(9)	123.247(5)
γ [deg]	90	90
V [Å^3]	15686(16)	15103(11)
Z	8	8
D_{calc} [mg m^{-3}]	1.631	1.637
Abs. coefficient [mm^{-1}]	1.612	1.671
F(000)	7896	7576
Theta range [deg]	2.06 to 25.03	2.09 to 25.03
Comp. to theta [25.00°]	99.9 %	98.7 %
Max. and min. transmission	0.9841 and 0.7387	0.9516 and 0.6341
Data / restraints / param.	13834 / 15 / 882	13150 / 0 / 918
Goodness-of-fit on F^2	0.884	0.917
R(F)[a] [I > 2σ(I)]	0.0787	0.0708
R(wF^2)[b] [I > 2σ(I)]	0.1577	0.1416
Largest diff. peak and hole [e.Å^{-3}]	1.010 and -0.604	0.621 and -0.718

[a] $R = \Sigma||F_o| - |F_c||/\Sigma|F_o|$. [b] $R(\omega F^2) = \{\Sigma[\omega(F_o^2 - F_c^2)^2]/\Sigma[\omega(F_o^2)^2]\}^{1/2}$;
$\omega = 1/[\sigma^2(F_o^2) + (aP)^2 + bP]$, $P = [2F_c^2 + \max(F_o, 0)]/3$

Table 2.2. Crystallographic data and refinement parameters for **2-4.**

	2	**3**	**4**
Formula	$C_{68}H_{80}Fe_4Mn_4N_4O_{20}$	$C_{72}H_{94}Fe_4Mn_4N_8O_{16}$	$C_{80}H_{112}Fe_4Mn_4N_6O_{16}$
FW	1726.60	1770.71	1856.92
T [K]	100(2)	100(2)	100(2)
λ [Å]	0.71073	0.71073	0.71073
Crystal system	monoclinic	triclinic	triclinic
Space group	P2(1)/c	P-1	P-1
a [Å]	12.9768(14)	11.1790(11)	12.5855(7)
b [Å]	11.4132(13)	12.8590(13)	13.1556(7)
c [Å]	23.702(3)	14.1230(14)	13.3954(7)
α [deg]	90	76.496(2)	73.3560(10)
β [deg]	105.277(2)	68.834(2)	70.5680(10)
γ [deg]	90	81.620(2)	86.7120(10)
V [Å^3]	3386.3(6)	1836.7(3)	2002.14(19)
Z	2	1	1
D_{calc} [mg m^{-3}]	1.693	1.601	1.540
Abs. coefficient [mm^{-1}]	1.630	1.503	1.382
F(000)	1780	914	966
Theta range [deg]	1.63 to 28.24	2.05 to 25.03	2.27 to 25.03
Comp. to theta [25.00°]	100.0 %	98.4 %	99.9 %
Max. and min. transmission	0.8539 and 0.5992	0.9563 and 0.7531	0.9729 and 0.7696
Data / restraints / param.	7887 / 0 / 454	6392 / 0 / 503	7058 / 0 / 500
Goodness-of-fit on F^2	1.019	1.046	1.031
R(F)[a] [I > 2σ(I)]	0.0294	0.0422	0.0342
R(wF^2)[b] [I > 2σ(I)]	0.0694	0.0984	0.0756
Largest diff. peak and hole [e.Å^{-3}]	0.760 and -0.630	1.036 and -0.521	0.658 and -0.486

[a] $R = \Sigma||F_o| - |F_c||/\Sigma|F_o|$. [b] $R(\omega F^2) = \{\Sigma[\omega(F_o^2 - F_c^2)^2]/\Sigma[\omega(F_o^2)^2]\}^{1/2}$;
$\omega = 1/[\sigma^2(F_o^2) + (aP)^2 + bP]$, $P = [2F_c^2 + \max(F_o, 0)]/3$

Table 2.3. Bond valence sum analysis for **1**.

Bond	**Distance (Å)**	**Valence**
Mn1-O1	2.034	0.465
Mn1-O2	2.170	0.358
Mn1-O3	2.157	0.333
Mn1-O5	2.233	0.271
Mn1-O7	2.142	0.347
Mn1-O9	2.213	0.286
Mn1 (2+)	**Bond valence sum**	**2.06**
Mn2-O1	1.847	0.770
Mn2-O4	2.008	0.498
Mn2-O6	2.005	0.502
Mn2-O11	2.043	0.453
Mn2-O13	2.031	0.468
Mn2-N1	2.243	0.357
Mn2 (3+)	**Bond valence sum**	**3.048**
Mn3-O1	1.836	0.793
Mn3-O8	2.050	0.445
Mn3-O10	2.040	0.457
Mn3-O12	2.060	0.433
Mn3-O14	2.061	0.432
Mn3-N2	2.208	0.393
Mn3 (3+)	**Bond valence sum**	**2.953**

Table 2.4. Bond valence sum analysis for **2**.

Bond	**Distance (Å)**	**Valence**
Mn1-O1	2.419	0.164
Mn1-O2	2.136	0.353
Mn1-O3	2.397	0.174
Mn1-O4	2.322	0.213
Mn1-O5	2.117	0.371
Mn1-O6	2.298	0.228
Mn1-N1	2.397	0.236
Mn1 (2+)	**Bond valence sum**	**1.739**
Mn2-O4	1.985	0.530
Mn2-O4′	2.207	0.291
Mn2-O5′	1.922	0.629
Mn2-O6	1.88	0.704
Mn2-O7	1.95	0.583
Mn2-N2	2.326	0.286
Mn2 (3+)	**Bond valence sum**	**3.023**

Table 2.5. Bond valence sum analysis for **3** and **4**.

Complex 3			**Complex 4**		
Bond	**Distance (Å)**	**Valence**	**Bond**	**Distance (Å)**	**Valence**
Mn1-O1	2.324	0.212	Mn1-O1	2.354	0.196
Mn1-O2	2.562	0.111	Mn1-O2	2.426	0.161
Mn1-O3	2.361	0.192	Mn1-O3	2.13	0.358
Mn1-O4	2.125	0.363	Mn1-O4	2.133	0.355
Mn1-O6	2.261	0.252	Mn1-O6	2.282	0.238
Mn1-O7	2.1	0.389	Mn1-O7	2.314	0.218
Mn1-N1	2.394	0.238	Mn1-N1	2.427	0.217
Mn1 (2+)	**Bond valence sum**	**1.757**	**Mn1 (2+)**	**Bond valence sum**	**1.743**
Mn2-O3	2.243	0.264	Mn2-O3	1.913	0.644
Mn2-O3′	1.879	0.706	Mn2-O6′	1.874	0.546
Mn2-O6′	1.947	0.588	Mn2-O7	1.972	0.549
Mn2-O7	1.914	0.642	Mn2-O7′	2.207	0.291
Mn2-O8	1.922	0.629	Mn2-O8	1.941	0.597
Mn2-N2	2.328	0.284	Mn2-N2	2.275	0.328
Mn2 (3+)	**Bond valence sum**	**3.113**	**Mn2 (3+)**	**Bond valence sum**	**2.955**

Mn(III) ions, and bond valence sum analyses (Tables 2.3-2.5). Also, this pseudo-dicubane mixed-valent core is a well-known topology for Mn SMMs.

2.2.3. Physical Measurements

FT-IR spectra were collected using a Thermo-Nicolet Avatar series spectrometer. Elemental analysis was performed by NuMega Resonance Labs (San Diego, CA). Dc magnetic susceptibility measurements were performed on finely ground polycrystalline samples of complexes **1-4**, restrained in eicosane to prevent torquing of the micro-crystallites in an externally applied magnetic field. Measurements were carried out on a Quantum Design MPMS-5 magnetometer equipped with a 5.5 T magnet. Magnetic susceptibility measurements were performed in the 1.8-300 K temperature range with applied fields of 0.1-50 kG. Ac magnetic susceptibilities measurements were obtained between 1-5 K with a 3 G ac field, at frequencies in the range of 10-997 Hz, with zero applied dc magnetic field on a Quantum Design MPMS-2 magnetometer. Data were corrected for diamagnetic contributions resulting from the sample rod, capsule and eicosane. Corrections for diamagnetism were estimated from Pascal's constants yielding the overall paramagnetic contribution to the molar magnetic susceptibility.

Electrochemistry was performed on a BAS CV-50W in DMF (for **1**) and CH_2Cl_2 or THF (for **3** and **4**) with 0.1 M tetrabutylammonium hexafluorophosphate (TBAH, recryst. from MeOH and dried under a vacuum at 80 °C), sample concentration of ~5 mM for **1** and ~0.1-1 mM for **3** and **4**, and at a scan rate of 25-100 mV/s. Measurements for **1** were performed under a N_2 atmosphere in a glove box. The working electrode was

a glassy carbon disk, counter electrode was a platinum wire, and the reference was ferrocene/ferrocenium. All $E_{1/2}$ values are reported vs. Fc/Fc^+ which were determined from the $[FeCp_2^*]/[FeCp_2^*]^+$ internal reference ($E_{1/2}$ = -480 mV in CH_2Cl_2, $E_{1/2}$ = -659 mV in THF).

2.3. Results and Discussion

2.3.1. Synthesis

Over the years, polynuclear manganese complexes have been synthesized by a variety of methods. One common approach is to use $[Mn_3(\mu_3\text{-}O)(O_2CR)_6(L)_3]$ triangles as starting materials which often leads to higher nuclearity complexes of various topologies. These include many $[Mn_4]$ dicubanes,[11,12,23] high-spin $[Mn_x]$ wheels,[24] the $[Mn_9]$ cluster,[25] and a family of rod-shaped structures with nuclearities ranging from six to twelve metal centers.[26,27] Since these triangles readily undergo carboxylate ligand exchange, the $[Mn_3O(O_2CCH_3)_6(py)_3]$ triangle[22] ("Mn_3O-Ac", shown in Figure 2.1), where py is pyridine, was reacted with $FcCO_2H$ to afford the fully-substituted $[Mn_3O(O_2CFc)_6(py)_2(H_2O)]$ (**1**), or "Mn_3O-Fc". Poor solubility of the Mn_3O-Fc trinuclear starting material resulted in very low-yielding reactions which led to the one-pot synthesis using Mn_3O-Ac, $FcCO_2H$, and the corresponding N-alkylated diethanolamine ligand.

The resulting ferrocene-substituted $[Mn_4]$ dicubanes crystallized as various solvated forms of **3** and **4**. Though these complexes initially showed promise as SMMs; low yields, mixed-products, and low-spin impurities proved to be detrimental to the complete/consistent characterization of their magnetic properties. At this point, the tri-

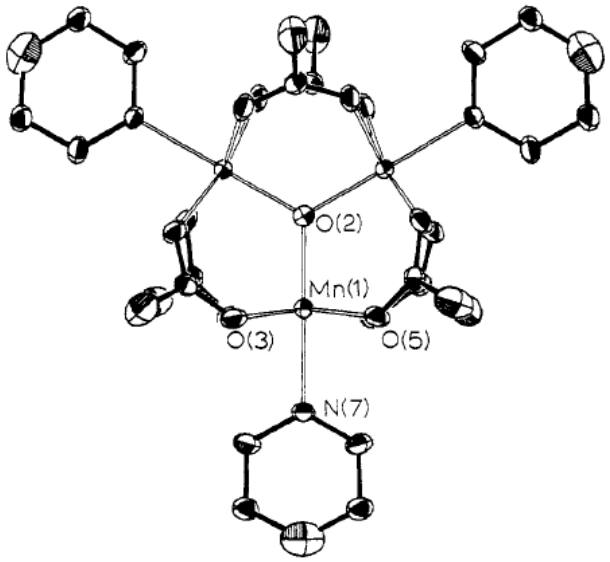

Figure 2.1. ORTEP of $[Mn_3O(O_2CCH_3)_6(py)_3]$ with hydrogen atoms omitted for clarity.

nuclear starting materials were abandoned all together and an even more simplistic synthesis was developed. Pure x-ray quality crystals of **2**, **3**, and **4** were obtained from Mn(II)acetate, $FcCO_2H$, and the chelating amine ligand in a simpler, more efficient, and highly reproducible synthesis.

Interestingly, in the absence of the bulky ferrocene ligand, similar reactions (with only smaller carboxylates present like acetate, propionate, or butyrate) often result in higher nuclearity wheel-shaped [Mn_x] SMMs such as the [Mn_{12}] and [Mn_{16}] wheels reported in previous work from this laboratory (further discussed in Chapter 5).[8,28] Therefore, the resulting topology of **2-4** is speculated to be strongly influenced by the steric effects of the larger ferrocene carboxylate ligand, similar to that observed in the benzoate-substituted analog.[9]

2.3.2. Description of Crystal Structures

The oxo-centered trinuclear Mn complex, **1**, crystallizes in the monoclinic C2/c space group (ORTEP shown in Figure 2.2) with two symmetry-related orientations in the unit cell. (Selected bond distances and angles can be found in Table 2.6.) The mixed-valent compound consists of two Mn(III) ions in a pseudo-octahedral environment with μ_3-oxo and pyridyl ligands bound in the axial positions. The equatorial coordination sites are occupied by oxo-atoms of four bridging $FcCO_2^-$ ligands. The Mn^{II} ion has the same coordination except that it is capped by a coordinated water molecule rather than a pyridine. Intermolecular interactions between this coordinated water molecule and the carboxylate oxo atoms of a neighboring

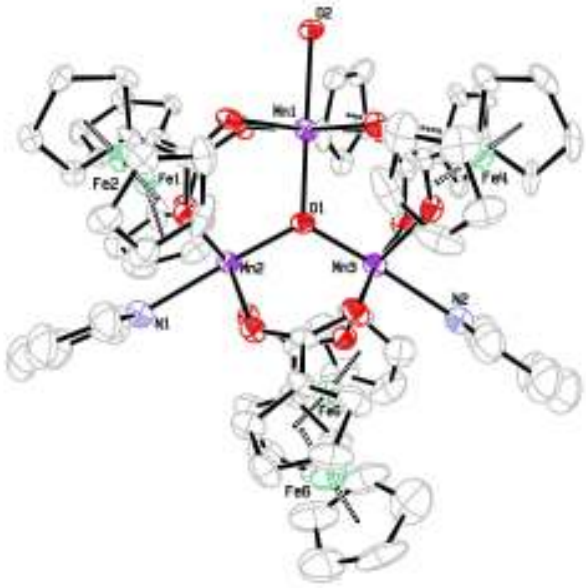

Figure 2.2. ORTEP of $[Mn_3O(O_2CFc)_6(py)_2(H_2O)]$ **(1a)** with thermal ellipsoids drawn at 50% probability level. Solvent and hydrogen atoms omitted for clarity.

Table 2.6. Selected interatomic bond distances [Å] and angles [°] for $[Mn_3O(O_2CFc)_6(py)_2(H_2O)]$ **(1a)**

Mn1-O1	2.034(8)	Mn2-O1	1.847(5)
Mn1-O2	2.170(8)	Mn2-O4	2.008(7)
Mn1-O3	2.157(5)	Mn2-O6	2.005(7)
Mn1-O5	2.233(5)	Mn2-O11	2.043(7)
Mn1-O7	2.142(5)	Mn2-O13	2.031(7)
Mn1-O9	2.213(5)	Mn2-N1	2.243(8)
Mn3-O1	1.836(7)	Mn1-O1-Mn2	119.9(3)
Mn3-O8	2.050(5)	Mn1-O1-Mn3	117.6(3)
Mn3-O10	2.040(6)	Mn2-O1-Mn3	122.5(3)
Mn3-O12	2.060(7)	O1-Mn1-O2	178.3(2)
Mn3-O14	2.061(6)	O1-Mn2-N1	177.6(3)
Mn3-N2	2.21(1)	O1-Mn3-N2	176.5(3)

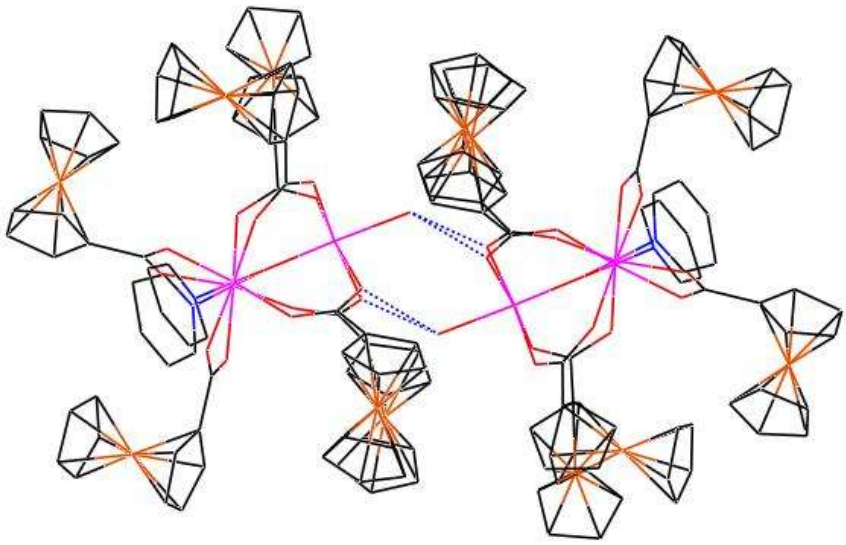

Figure 2.3. Intermolecular H-bonding in $[Mn_3O(O_2CFc)_6(py)_2(H_2O)]$ **(1a).**

trinuclear (O-H···O distances 2.7-2.8 Å) unit leads to the formation of hydrogen-bonded dimers of Mn_3O-Ac triangles in the unit cell (shown in Figure 2.3).

Complex **2** forms large strongly-diffracting plate-shaped crystals leading to a well-ordered structure with no co-crystallized solvate molecules. This complex crystallizes in the monoclinic P2(1)/c space group with only half of the target molecule being crystallographically independent and the other half generated by inversion symmetry (ORTEP in Figure 2.4). The *pseudo*-dicubane core consists of two hexacoordinate Mn(III) ions in the body positions and two heptacoordinate Mn^{II} ions in the wing positions. This is a common topology for manganese SMMs as described in the Introduction Chapter (see Figure 1.2).

The coordination sphere of the Mn(III) ions consists of an apical N-atom from the doubly deprotonated triethanolamine ligand, two μ_3- and two μ_2-alkoxy arms of the amine ligands, and an oxygen atom of a bridging μ_2- ferrocene carboxylate monoanion. For the Mn(II) ions, the singly deprotonated triethanolamine is chelated to the metal ion in the pentagonal plane through the central N atom, and two of the oxo atoms of the ethanol arms. The other equatorial positions are occupied by a μ_3-alkoxide of the other amine ligand and an oxygen atom of the bridging ferrocene carboxylate. The monodentate ferrocene carboxylate coordinates to the Mn(II) ion via a single oxygen atom in an apical position. A μ_2-alkoxide arm in the other axial coordination site completes the coordination sphere of the Mn(II) ions. All four of the triethanolamine ligands bind in a tridentate fashion with one protonated ethanol arm uncoordinated hanging off the periphery of each molecule.

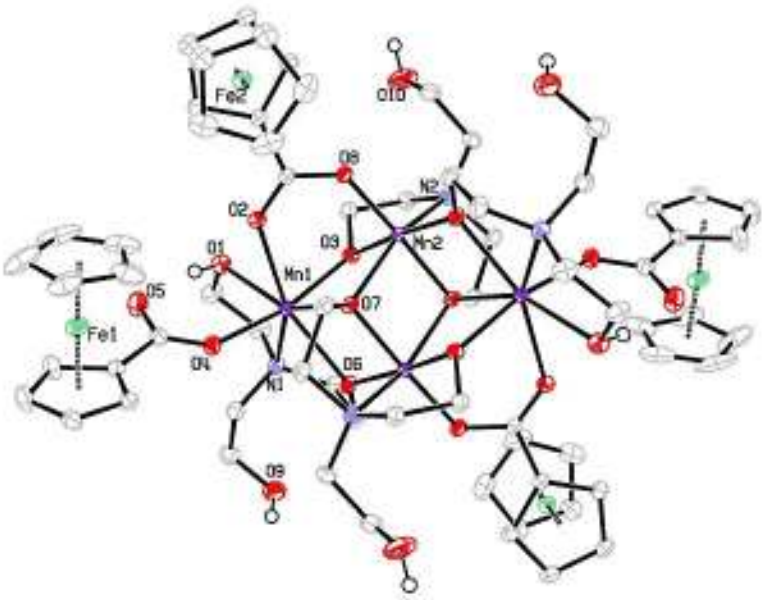

Figure 2.4. ORTEP of $[Mn_4(O_2CFc)_4(teaH_2)_2(teaH)_2]$ **(2)** with hydrogen atoms omitted for clarity and thermal ellipsoids at 30% probability level.

The unit cell of **2** contains two symmetry-related orientations of the molecule. Also, crystal packing diagrams reveal an extensive intermolecular H-bonding network through uncoordinated ethanol arms of the chelating amine ligands. These important crystallographic artifacts may contribute to the smaller $\chi_M T$ value and out-of-phase signal in the ac susceptibility in comparison to **3** and **4** as discussed in the following sections.

Complexes **3** and **4** both crystallize in the triclinic P-1 space group with two halves of the molecule related by inversion symmetry and a single orientation of the [Mn_4] structure in the unit cell. ORTEPs of **3** and **4** are shown in Figures 2.5. Selected bond distances and angles for **2** and **4** are listed in Table 2.7 whereas those for **3** are listed in Table 2.8 (slightly different labeling scheme). Both complexes comprise a $[Mn^{II}_2Mn^{III}_2O_6]^{4+}$ double cuboidal core with two heptacoordinate distorted pentagonal bipyramidal Mn(II) ions, Mn(1), at the wing positions and two hexacoordinate *pseudo*-octahedral Mn(III) ions, Mn(2), at the body positions, very similar to complex **2**. The coordination spheres of the Mn(II) and Mn(III) ions are exactly the same as in complex **2** except for the replacement of a protonated ethanol arm on the coordinated nitrogens with either methyl or ^{n}butyl alkyl groups on the chelating amine ligands. In all three [Mn_4] dicubanes discussed above, the uncoordinated oxygen atom of the monodentate ferrocene carboxylate is involved in an intramolecular H-bond with the protonated ethoxy arm chelated to the wing-position Mn^{II} ion.

The unit cell of both **3** and **4** consists of a single orientation of the molecule which is ideal for single-crystal magnetic and EPR studies. However, co-crystallized acetonitrile solvate molecules in both complexes, though well-ordered, could lead to

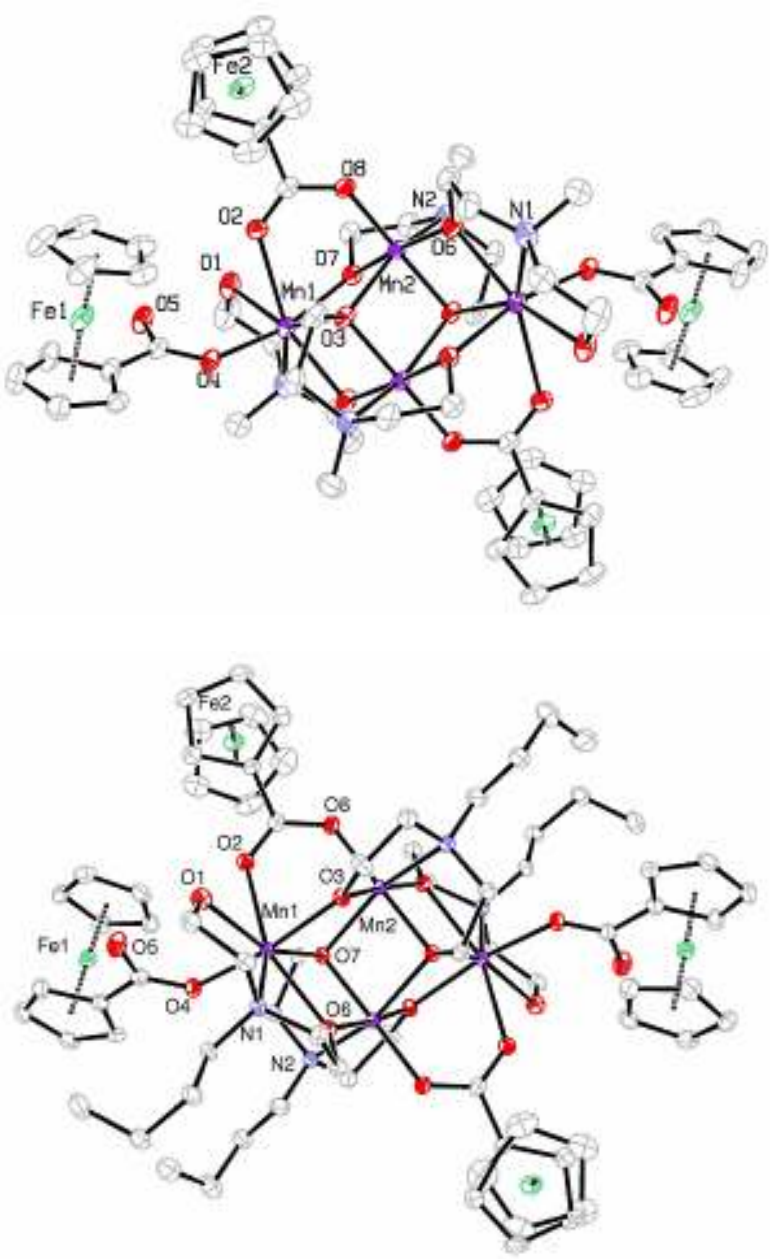

Figure 2.5. ORTEP of $[Mn_4(O_2CFc)_4(mdeaH)_2\ (mdea)_2] \cdot 4MeCN$ (**3**, top) and $[Mn_4(O_2CFc)_4(bdeaH)_2(bdea)_2] \cdot 2MeCN$ (**4**, bottom) with hydrogen and solvate atoms omitted for clarity and thermal ellipsoids drawn at 30% probability level.

Table 2.7. Selected interatomic bond distances [Å] and angles [°] for $[Mn_4(O_2CFc)_4(teaH_2)_2(teaH)_2]$ **(2)** and $[Mn_4(O_2CFc)_4(bdeaH)_2(bdea)_2] \cdot 2MeCN$ **(4)**.

Bonds	2	4
Mn1-O1	2.422(2)	2.354(1)
Mn1-O2	2.400(1)	2.426(2)
Mn1-O3	2.109(1)	2.130(2)
Mn1-O4	2.124(2)	2.133(2)
Mn1-O6	2.294(1)	2.282(2)
Mn1-O7	2.319(1)	2.314(2)
Mn1-N1	2.420(1)	2.427(2)
Mn2-O3	1.910(1)	1.913(2)
Mn2-O6′	1.879(1)	1.874(2)
Mn2-O7	2.217(1)	2.207(2)
Mn2-O7′	1.976(1)	1.972(2)
Mn2-O8	1.945(1)	1.941(2)
Mn2-N2	2.330(2)	2.275(3)

Angles	2	4
O3-Mn1-O4	166.00(5)	165.11(7)
N2-Mn2-O7	154.73(6)	155.56(8)
Mn1-O3-Mn2	105.62(6)	106.39(9)
Mn1-O7-Mn2	89.86(5)	91.50(7)
Mn1-O6-Mn2′	108.15(6)	108.76(9)
Mn1-O7-Mn2′	103.90(6)	104.12(8)

Table 2.8. Selected interatomic bond distances [Å] and angles [°] for $[Mn_4(O_2CFc)_4(mdeaH)_2(mdea)_2] \cdot 4MeCN$ (**3**).

Bonds	
Mn1-O1	2.324(3)
Mn1-O2	2.562(3)
Mn1-O3	2.361(2)
Mn1-O4	2.125(2)
Mn1-O6	2.261(3)
Mn1-O7	2.100(2)
Mn1-N1	2.394(3)
Mn2-O3	2.227(2)
Mn2-O3′	1.956(3)
Mn2-O6′	1.888(2)
Mn2-O7	1.921(2)
Mn2-O8	1.912(3)
Mn2-N2	2.322(4)

Angles	
O4-Mn1-O7	163.2(1)
N2-Mn2-O3	153.9(1)
Mn1-O7-Mn2	109.1(1)
Mn1-O3-Mn2	91.12(9)
Mn1-O6-Mn2′	108.6(1)
Mn1-O3-Mn2′	102.59(1)

intermolecular interactions which may diminish the overall single-molecule magnetic properties of these clusters. It is worth mentioning here that although the core structures of complexes **2-4** are nearly identical, as evident in the bond distances and angles listed in Tables 2.7 and 2.8, they all exhibit very different magnetic properties (as discussed in the following sections). Therefore, the orientation of the molecules in the unit cell, co-crystallized solvate molecules, ligand disorder, intermolecular interactions, etc. must play a major role in the magnetic and quantum dynamics of SMMs; a topic that is revisited many times throughout the course of this thesis.

2.3.3. DC Magnetic Susceptibility

The mixed-valent triangular $[Mn_3(\mu_3\text{-}O)]^{6+}$ core of complex **1** leads to predominately antiferromagnetic coupling between the Mn(III) and Mn(II) centers. The $\chi_M T$ *vs.* T plot in an applied dc field of 1 T and a temperature range of 300-1.8 K can be found in Figure 2.6. The molar susceptibility product is ~10 cm^3 mol^{-1} K at room temperature and steadily decreases as the temperature is lowered from 300-5 K at which point it dramatically drops to a final value of ~2 cm^3 mol^{-1} K at 1.8 K. Variable-field dc measurements were also carried out in temperature range of 4-1.8 K and in applied dc fields of 0.1-5 T and plotted as reduced magnetization $(M/N\mu_B)$ *vs.* H/T in Figure 2.6. The reduced magnetization reaches a value of ~3.6 μ_β but fails to saturate even in a 5 T field. The nearly superimposable isofields imply that there is little to no axial anisotropy in this complex. Therefore, complex **1** is not a single-molecule magnet due to the low magnetization values and ground state spin (S = 1/2 or 3/2) along with the lack of significant magnetoanistropy.

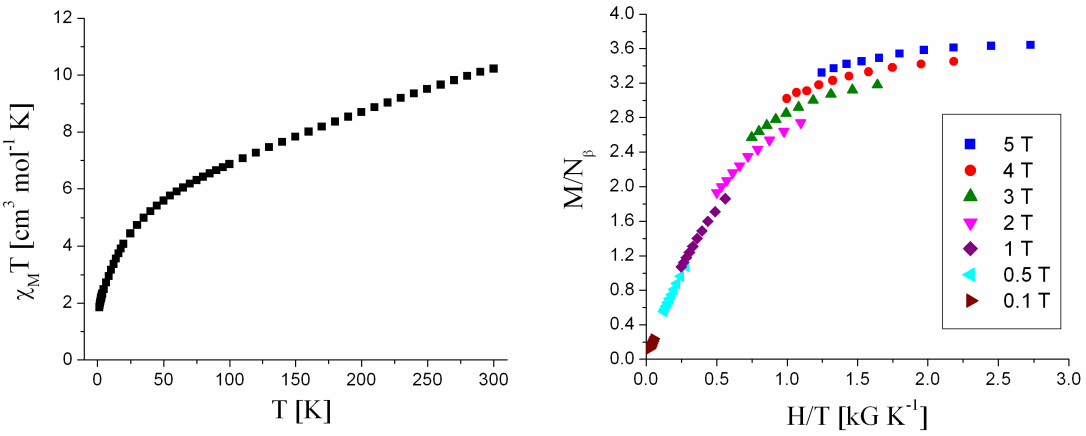

Figure 2.6. (left) $\chi_M T$ *vs.* T in applied dc field of 1 T and (right) reduced magnetization, $M/N\mu_B$ *vs.* H/T for $[Mn_3O(O_2CFc)_6(py)_2(H_2O)]$ **(1)**..

Dc data for complex **2** indicates a much higher spin ground state and also appreciable zero-field splitting as expected for a mixed-valent [Mn_4] dicubane. Figure 2.7 shows a low-temperature field-dependence of the molar susceptibility (collected in applied fields of 0.01, 0.1 and 1 T) with the 0.01 T data reaching the highest $\chi_M T$ of ~26 cm^3 mol^{-1} K at 1.8 K. The 0.1 T data were further analyzed and plotted as $\chi_M T$ *vs.* T in Figure 2.8. The $\chi_M T$ at room temperature is ~14 cm^3 mol^{-1} K which gradually increases as the temperature is decreased from 300 - 50 K. At this point, the $\chi_M T$ rises dramatically to a final maximum value of 24 cm^3 mol^{-1} K. This rise in $\chi_M T$ is indicative of weak intramolecular ferromagnetic coupling between the oxo-bridged Mn(III) and Mn(II) ions.

Using the isotropic exchange ($\hat{H} = -2\sum_{ij} J_{ij}\hat{S}_i \cdot \hat{S}_j$) interactions dictated by the symmetry of this molecule (see Kambe vector coupling[29] scheme in Figure 1.2), the data in Figure 2.8 were least-squares fit to the Van Vleck equation[30] from 300-10 K (solid red curve in Figure 2.9). The theoretical fit gave final optimized parameters of g = 1.9, J_{wb} = 0.12 cm^{-1}, and J_{bb} = 3.9 cm^{-1} where once again J_{wb} represents the exchange interaction between the wing Mn(II) ions and the body Mn(III) ions and J_{bb} represents the exchange interaction between the two body Mn(III) ions. As expected, positive values for both J_{bb} and J_{wb} were obtained, indicating intramolecular ferromagnetic exchange. The value for J_{bb} is an order of magnitude larger than J_{wb} due to the stronger coupling interaction between two Mn(III) ions as opposed to a Mn(II)-Mn(III) interaction. This is do to the fact that the single-ion anisotropy for Mn(II) is about 1/10 that of Mn(III).[31] This fit also indicates a ground state spin of S = 9 which is also typical

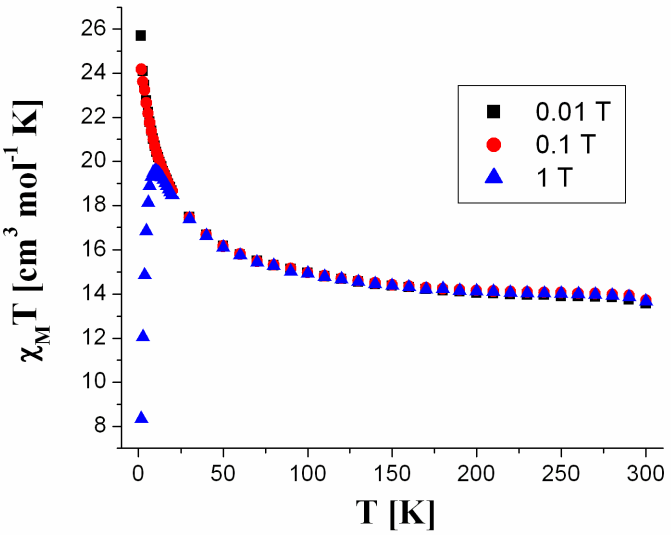

Figure 2.7. Field-dependence of $\chi_M T$ *vs. T* for $[Mn_4(O_2CFc)_4(teaH_2)_2(teaH)_2]$**(2)**.

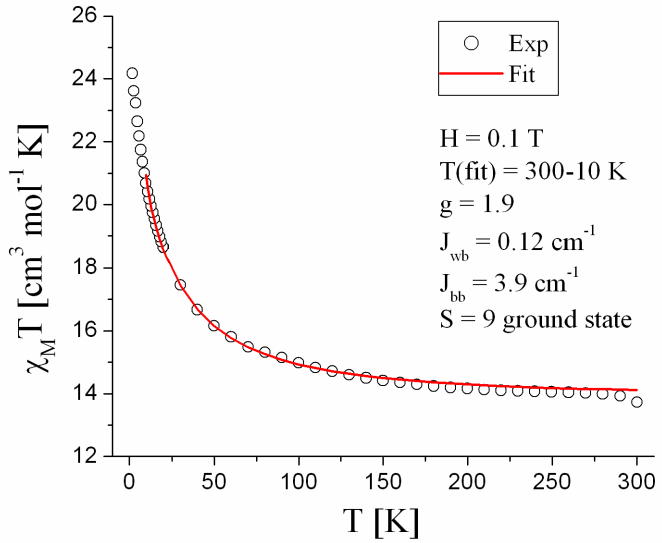

Figure 2.8. $\chi_M T$ *vs. T* for $[Mn_4(O_2CFc)_4(teaH_2)_2(teaH)_2]$ **(2)** in applied dc field of 0.1 T with theoretical fit shown as red curve.

of previously studied [Mn_4] dicubanes and expected from ferromagnetic coupling in a [$Mn^{II}_2Mn^{III}_2$] core. The first excited state (S = 8) is only separated from the ground state by ~1 cm^{-1} which is also expected since many manganese SMMs are known for having many low-lying excited states and is clearly the case in this complex. In fact, complex **2** has 34 spin states within 10 cm^{-1} of the S = 9 ground state.

To further confirm the ground state spin and determine the magnitude of the zero-field splitting parameter, D, field-dependent magnetization data were also collected in applied fields of 5, 4, 3, 2, and 1 T in the 4-1.8 K temperature range (Figure 2.9). Though the magnetization fails to saturate even in higher dc fields, the non-superimposable isofields indicate an appreciable axial-type magnetoanistropy and the magnetization value at 5 T predicts a ground state spin upwards of S = 7. A theoretical least-squares fit to a S = 7 spin Hamiltonian (solid black curves in Figure 2.9), including an isotropic Zeeman interaction ($g\mu_B\hat{S}B$) and an axial zero-field splitting parameter ($D\hat{S}_z^2$), gave parameters of g = 1.96 and a D/k_B = -0.31 cm^{-1}. Though these parameters are reasonable and in line with literature values for similar complexes, it is obvious from the fit shown in Figure 2.9 that this may not be the most accurate depiction of the ground state of **2**.

First, the ground state spin obtained from the fitting of the reduced magnetization is lower than that suggested by the $\chi_M T$ data. Second, the overall quality of the fit is rather poor. Both of these findings can be explained by the fact that the spin states of **2** are extremely close in energy (as indicated by the fitting of the $\chi_M T$ data, *vide supra*). Since the reduced magnetization data are collected at much higher fields than the $\chi_M T$ measurements, it is not unreasonable to assume that excited states may be pop-

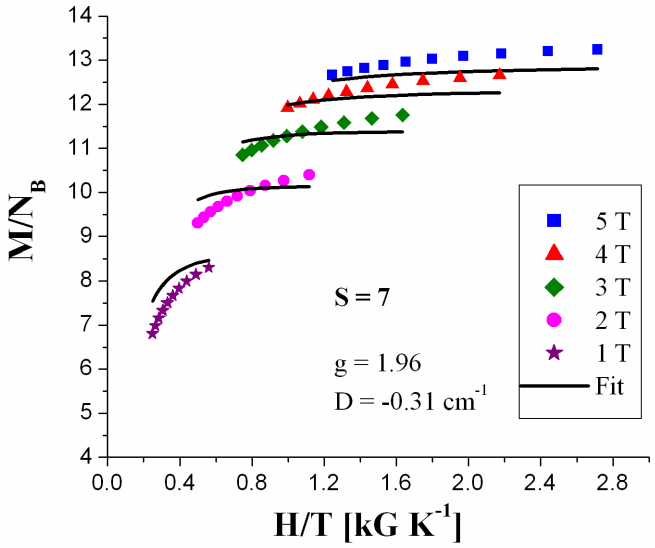

Figure 2.9. Reduced magnetization *vs. H/T* for $[Mn_4(O_2CFc)_4(teaH_2)_2(teaH)_2]$ **(2)** with theoretical fit shown as black curves.

ulated at these fields (increased Zeeman splitting) that were not populated in a 0.1 T field. Furthermore, our fitting model for the reduced magnetization data does not take into account any magnetic exchange interactions and also assumes that only a single ground state is being populated which, as has been established, is not likely the case.

Though the dc magnetic susceptibility for **3** is very similar to **2**, it will be compared directly to that of **4** due to their nearly identical structures. Complexes **3** and **4** also show a field-dependence of the molar susceptibility at low temperatures as shown in Figure 2.10. The 0.1 T $\chi_M T$ *vs.* T data in the temperature range of 300-1.8 K can be found in Figure 2.11. As can be seen from the data, $\chi_M T$ gradually increases as the temperature is lowered from 300 K, again indicating intramolecular ferromagnetic exchange. A maximum $\chi_M T$ value of 27 $cm^3\ mol^{-1}$ K (at 1.8 K) and 34 $cm^3\ mol^{-1}$ K (at 3.8 K) is reached for **3** and **4**, respectively. The $\chi_M T$ of **4** begins to decrease again after the maximum at 3.8 K is reached; most likely due to Zeeman interactions which become stronger as the applied field is increased (see 1 T data in Figure 2.10).

The resulting eigenvalue expression (equation *1.4* of the Introduction) along with the corresponding Van Vleck equation was then used to least-squares fit the experimental data (solid curves in Figure 2.11). Since this model only takes into account the pairwise coupling interactions between the Mn centers and ignores intermolecular interactions and Zeeman effects, fitting attempts were only made for data at temperatures above the maximum $\chi_M T$ value reached. With this approach, reasonable fits were obtained from 300-10 K with final optimized parameters of $g = 1.8$, $J_{wb} = 0.26$ cm^{-1}, $J_{bb} = 4.4$ cm^{-1} for **3** and $g = 2.0$, $J_{wb} = 0.50$ cm^{-1}, $J_{bb} = 4.8$ cm^{-1} for **4**. The fits for both complexes indicate a poorly isolated ground-state spin of $S = 9$ with a first excited

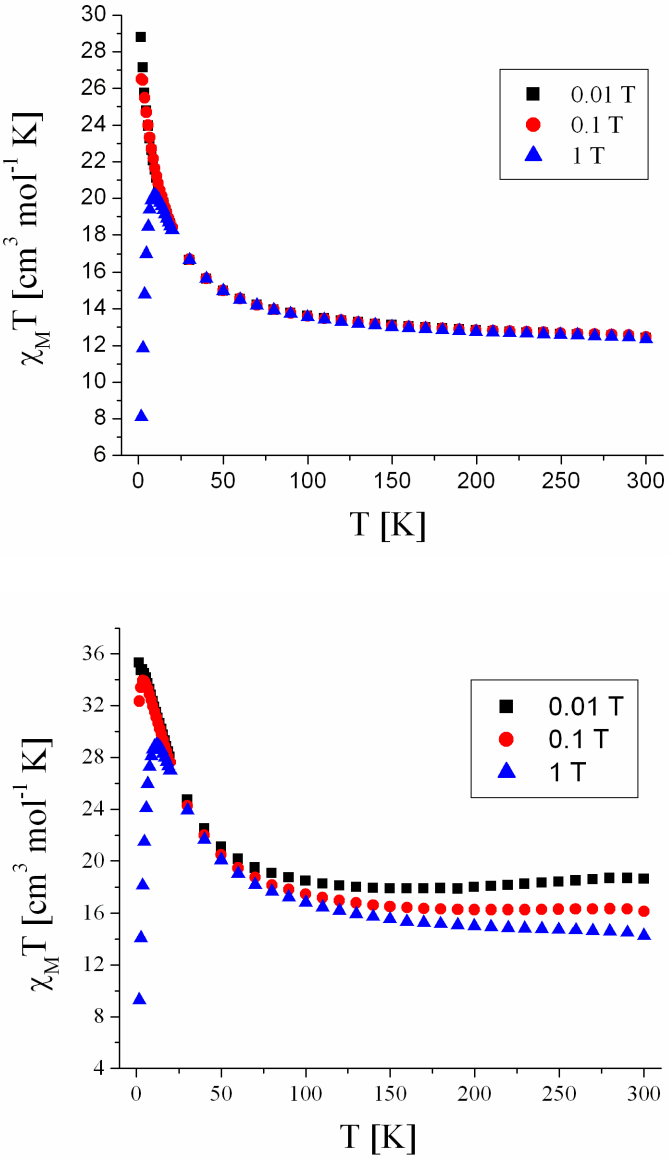

Figure 2.10. Field-dependence of $\chi_M T$ *vs.* T for $[Mn_4(O_2CFc)_4(mdeaH)_2(mdea)_2] \cdot 4MeCN$ (**3**, top) and $[Mn_4(O_2CFc)_4(bdeaH)_2(bdea)_2] \cdot 2MeCN$ (**4**, bottom).

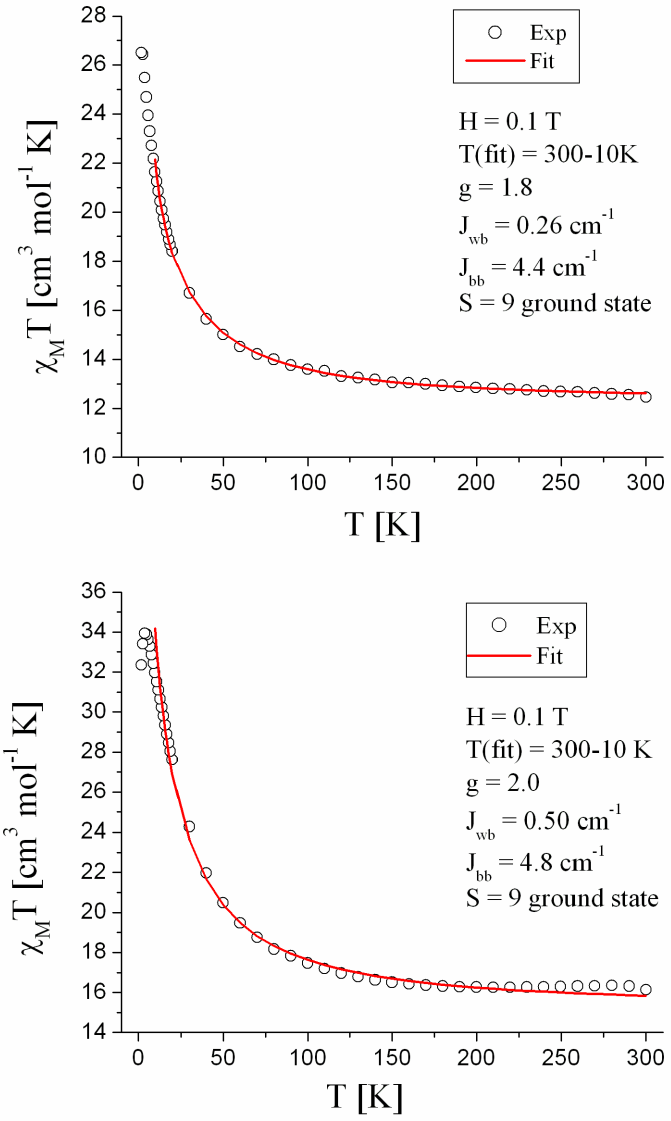

Figure 2.11. $\chi_M T$ *vs.* T in applied dc field of 0.1 T for $[Mn_4(O_2CFc)_4(mdeaH)_2(mdea)_2] \cdot 4MeCN$ (**3**, top) and $[Mn_4(O_2CFc)_4(bdeaH)_2(bdea)_2] \cdot 2MeCN$ (**4**, bottom) with theoretical fits shown as red curves.

state of S = 8 (only 1.7 cm^{-1} and 4.4 cm^{-1} above the ground state for **3** and **4**, respectively).

Reduced magnetization measurements on **3** and **4** were also collected in applied fields of 5, 4, 3, 2, and 1 T in the 4-1.8 K temperature range and are plotted in Figure 2.12. The best theoretical fits (solid curves in Figure 2.12) were found assuming a S = 7 ground state (g fixed at 1.9, D/k_B = -0.35 cm^{-1}) and a S = 8 ground state (g = 1.8, D/k_B = -0.24 cm^{-1}) for **3** and **4**, respectively. Once again, the reduced magnetization data do not fit well to a S = 9 ground state model as suggested by the $\chi_M T$ data which is expected in these [Mn_4] systems with poorly isolated ground states.

In comparison to the previously published [Mn_4] dicubane SMMs, the magnetic parameters determined for complexes **2-4** are comparable as expected due to their structural similarities. All three complexes show non-zero spin ground states (likely S = 8 or 9) and appreciable axial-type anisotropy. The S = 8 and 9 [Mn_4] dicubanes in the literature have exchange coupling constants similar to those found here with J_{wb} ranging from 0.22 to 4.2 cm^{-1} and J_{bb} ranging from 5.3 to 9.9 cm^{-1}, all positive in sign indicating ferromagnetic exchange. The J_{wb} interactions found for **2-4** fall comfortably in this range while those for J_{bb} were just slightly below the lowest reported value at ~4-5 cm^{-1}. Also, the zfs parameter, D, for most [Mn_4] dicubanes is around -0.20 to -0.30 cm^{-1} which again corresponds to the values found for **2-4** which ranged from -0.24 to -0.35 cm^{-1}. Lastly, it is also worth noting that all of the previously reported complexes possess very low-lying excited states as with the complexes discussed here. Typically, the first excited state (S = 8) is located less than 2 cm^{-1} from the S = 9 ground state. The correlation between this energy spacing and the quantum properties of a SMM will be

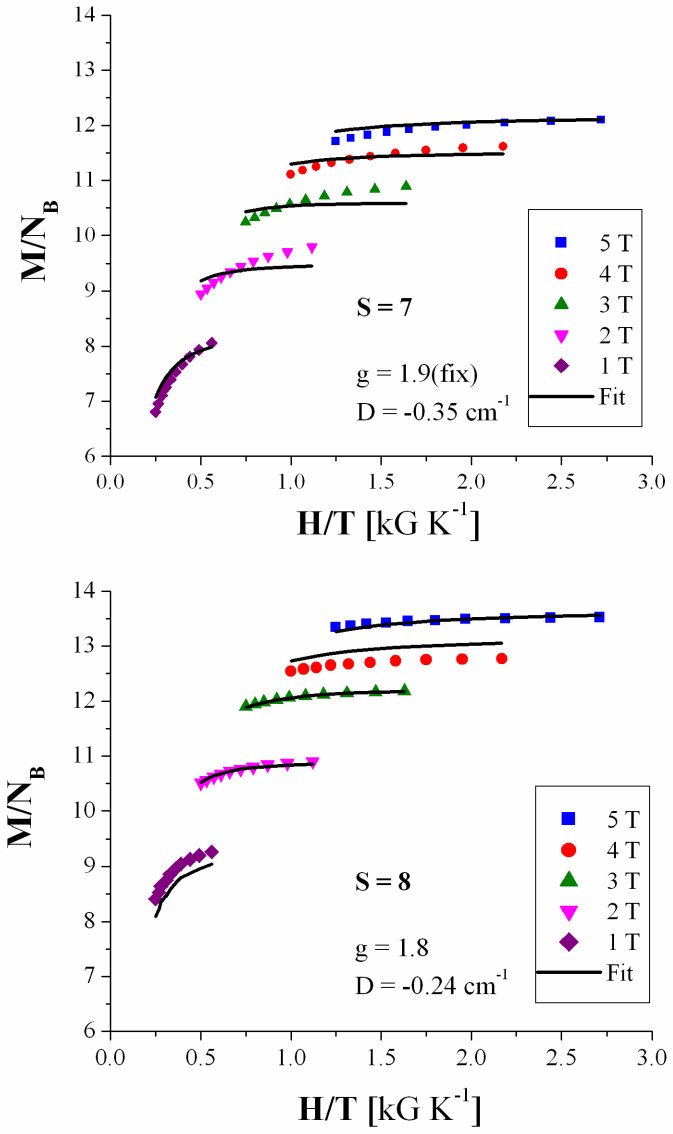

Figure 2.12. Reduced magnetization *vs. H/T* for $[Mn_4(O_2CFc)_4(mdeaH)_2(mdea)_2] \cdot 4MeCN$ (**3**, top) and $[Mn_4(O_2CFc)_4(bdeaH)_2(bdea)_2] \cdot 2MeCN$ (**4**, bottom) with theoretical fits shown as solid black curves.

further discussed in Chapter 3.

2.3.4. AC Magnetic Susceptibility

Ac magnetic susceptibility studies were also conducted for **2**, **3**, and **4** in order to determine the potential-energy barrier for reversal of the magnetization. The data were collected in an oscillating ac field (10-1000 Hz) from 5- 1.8 K and in the absence of an applied dc field. All three ferrocene-substituted [Mn_4] dicubanes show a frequency-dependent out-of-phase signal in the ac susceptibility, indicating slow relaxation of the magnetization. The out-of-phase signal observed in complex **2** (Figure 2.13) only emerges below 2.75 K for the ac fields of highest frequency. Also, the signal is very weak, accounting for only ~6% of the in-phase signal which reaches a maximum of 14 $cm^3\ mol^{-1}$ at 1.8 K.

Though the in-phase ac susceptibility is not much higher than that of **2**, the out-of-phase signal in **3** emerges at 3.25 K and is significantly stronger, accounting for 31% of the in-phase signal (Figure 2.14). In both **2** and **3**, however, no maxima of the out-of-phase signals are observed above the temperature limit of our instrumentation (1.8 K). Also, the magnitude of the out-of-phase signal is quite high in complex **3** despite the fact that only a small portion of it is observed and we cannot see the maximum value. Collecting data at lower temperatures or at higher frequencies of the oscillating field would potentially allow us to locate the out-of-phase peak positions and use them to estimate the energy barrier required for reversal of the magnetization in these complexes.

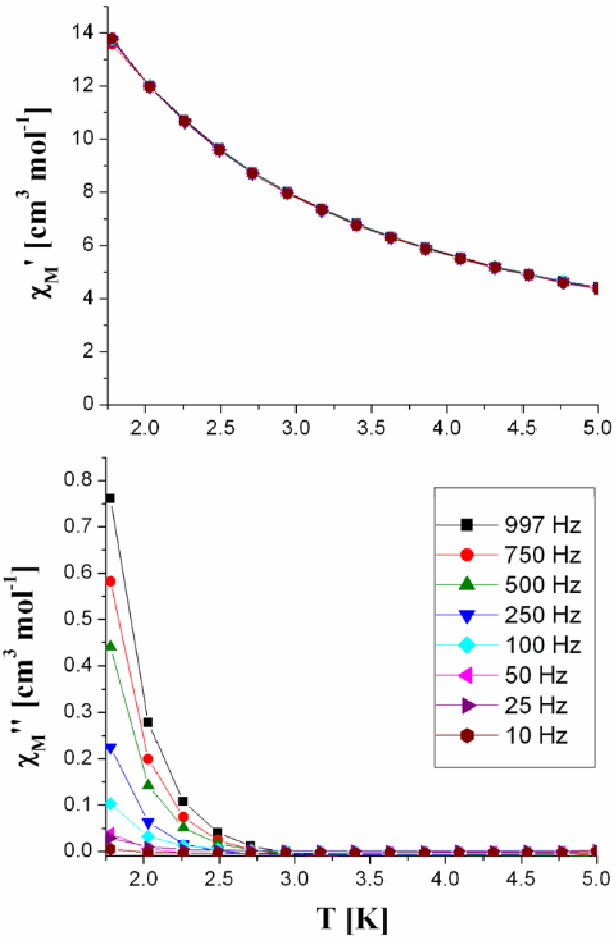

Figure 2.13. In-phase (χ_M') and out-of-phase (χ_M'') ac susceptibility for $[Mn_4(O_2CFc)_4(teaH_2)_2(teaH)_2]$ **(2)**.

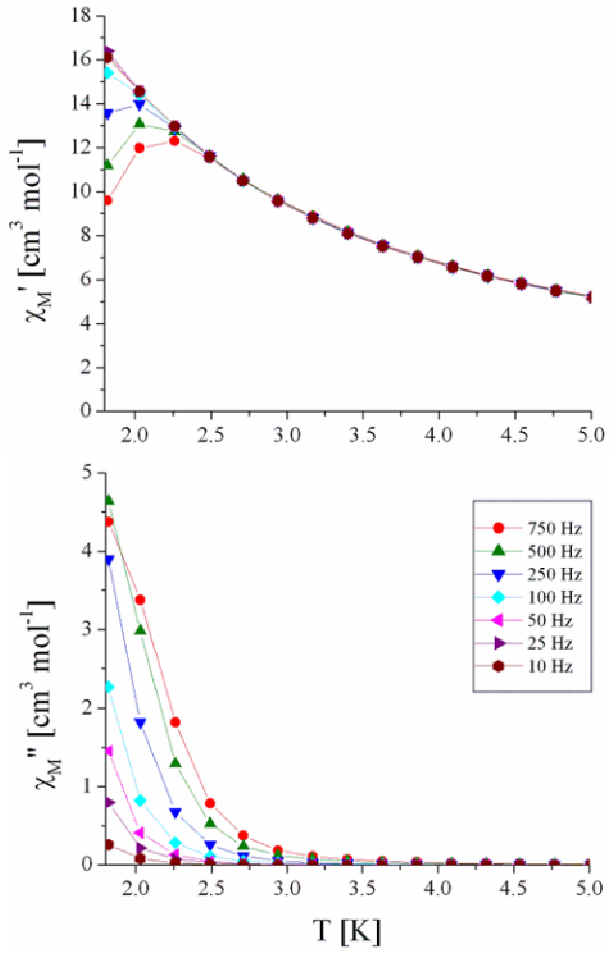

Figure 2.14. In-phase (χ_M') and out-of-phase (χ_M'') ac susceptibility for $[Mn_4(O_2CFc)_4(mdeaH)_2(mdea)_2] \cdot 4MeCN$ **(3)**.

The ac data for complex **4** is quite different from **2** and **3** in that the out-of-phase signal at 1000 Hz emerges around 5 K and peak maxima can be observed down to 50Hz (Figure 2.15). Also, the out-of-phase signal in **4** is much stronger than that observed in **2**, accounting for nearly 44% of the in-phase signal. Using the peak positions at each frequency from 997-50 Hz, the data were fit to the Arrhenius equation $\tau = \tau_0 e^{-Ea(kT)}$, where E_a is the activation energy, k is Boltzman's constant, τ is the relaxation time, and τ_0 is the preexponential factor. A plot of $ln(\tau)$ *vs.* $1/T$ (Figure 2.16) gives a linear correlation from which the E_a was calculated and found to be 15.8 cm^{-1}. This value agrees quite well with the theoretical barrier ($-DS_z^2$) of 15.4 cm^{-1} calculated from the parameters S = 8 and D = -0.24 cm^{-1}, as obtained from the reduced magnetization fitting of **4** discussed in the previous section.

Another useful piece of information gathered from ac susceptibility measurements is an estimate of the ground state spin in the absence of an applied dc field. To do this, the lowest frequency data (10 Hz) were plotted as $\chi_M'T$ *vs.* T, extrapolated to 0 K, and compared to values obtained from the spin-only formula. Extrapolations for **2-4** are plotted together in Figure 2.17 with the spin-only values for S = 6, S = 7, and S = 8 ground states indicated by the black arrows. The extrapolation of the 10 Hz data for **2** indicates a $\chi_M'T$ value of 26 cm^3 mol^{-1} K which is just below the spin-only value for a S = 7 ground state (28 cm^3 mol^{-1} K). For **3**, the extrapolation gave a value of 32 cm^3 mol^{-1} K which lies in between the spin-only values for S = 7 and S = 8 (36 cm^3 mol^{-1} K) ground states. For **4** however, a value of 34 cm^3 mol^{-1} K was calculated which supports a S = 8 ground state as indicated by the reduced magnetization data.

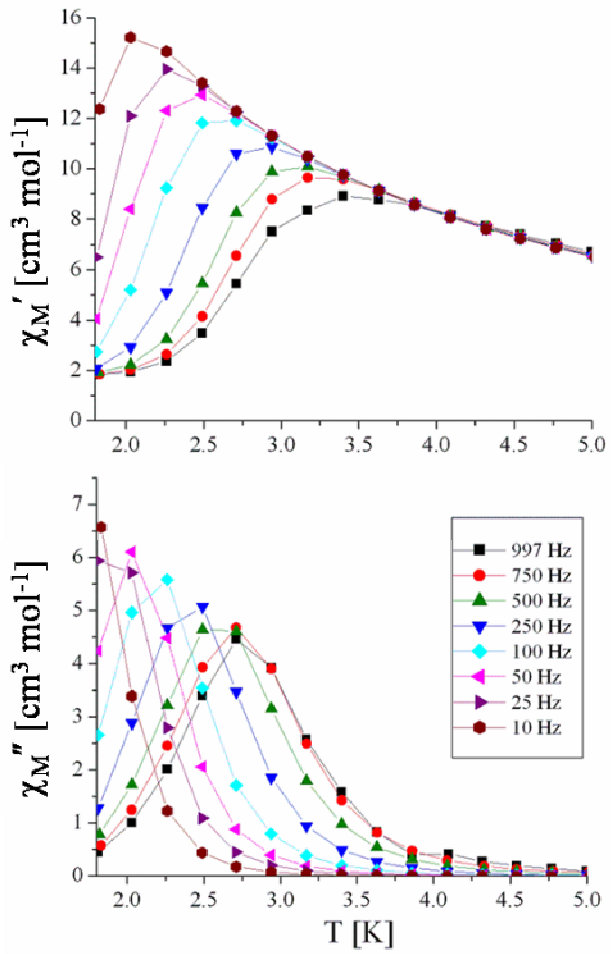

Figure 2.15. In-phase (χ_M') and out-of-phase (χ_M'') ac susceptibility for $[Mn_4(O_2CFc)_4(bdeaH)_2(bdea)_2] \cdot 2MeCN$ **(4)**.

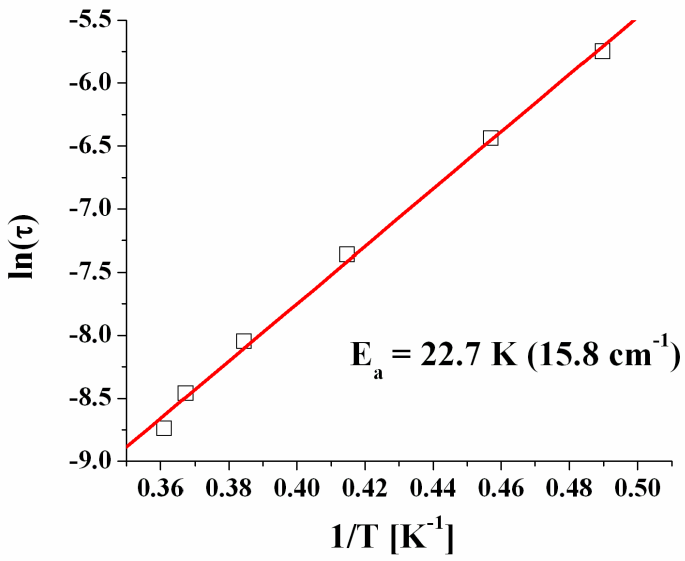

Figure 2.16. Arrhenius plot of out-of-phase ac susceptibility for $[Mn_4(O_2CFc)_4(bdeaH)_2(bdea)_2] \cdot 2MeCN$ **(4)**.

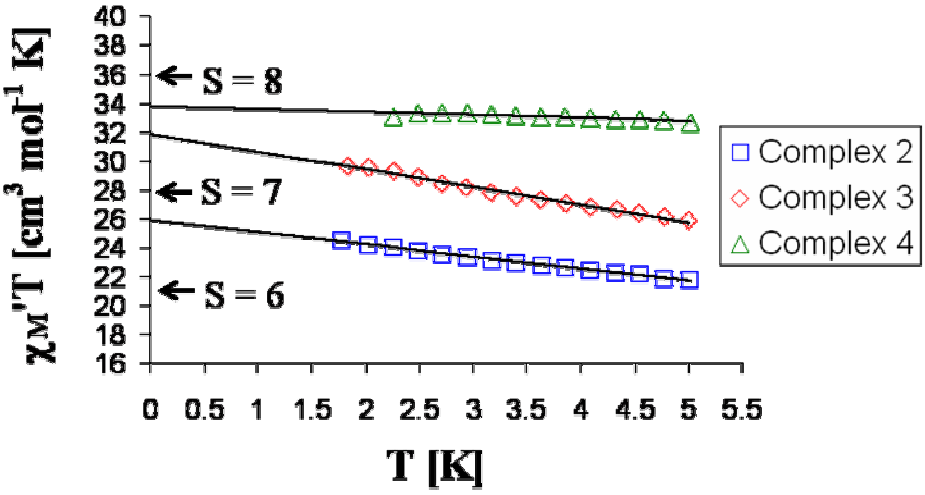

Figure 2.17. Extrapolation of 10 Hz $\chi_M'T$ *vs.* T data for **2-4**. Ground state spin estimates from spin-only formula.

2.3.5. Electrochemistry

Up to this point, the ferrocene-substituted [Mn_4] dicubanes are both structurally and magnetically similar to the previously reported [Mn_4] dicubanes. Here, we explore the electrochemical properties of these new SMMs that make them unique and multi-functional. Electrochemical studies have been carried out to determine the redox properties of **3** and **4** in order to help gauge the feasibility of oxidizing the Fc moieties on the Mn SMMs. The low-solubility of these complexes in typical solvents used for electrochemistry proved to be a difficult challenge. First, the ferrocene-substituted Mn_3 triangle, **1**, was compared to the Mn_3O-Ac triangle starting material as a preliminary study.

Figure 2.18 shows the electrochemistry of these two complexes at a concentration of ~5 mM in DMF. The acetate triangle shows two reductions corresponding to the reduction of one Mn(III) ion followed by the second Mn(III) ion to give an all Mn(II)core as indicated in the top part of Figure 2.18. An irreversible oxidation peak is also evident around +244 mV corresponding to the oxidation of the Mn(II) ion to give the all Mn(III) core. The analogous ferrocene-substituted Mn_3 triangle, **1**, was measured in the bottom portion of Figure 2.18. The irreversible Mn(III) reductions are still observed between -100 and -200 mV though less well-resolved than in the acetate triangle. The main difference is the appearance of the prominent quasi-reversible ferrocene oxidation peak with $E_{1/2}$ = +298 mV. (The oxidation of Fc in the $FcCO_2H$ free ligand in DMF occurs at $E_{1/2}$ = +227 mV.) This peak also contains a shoulder most likely due to the irreversible oxidation of Mn(II) as compared to the acetate triangle.

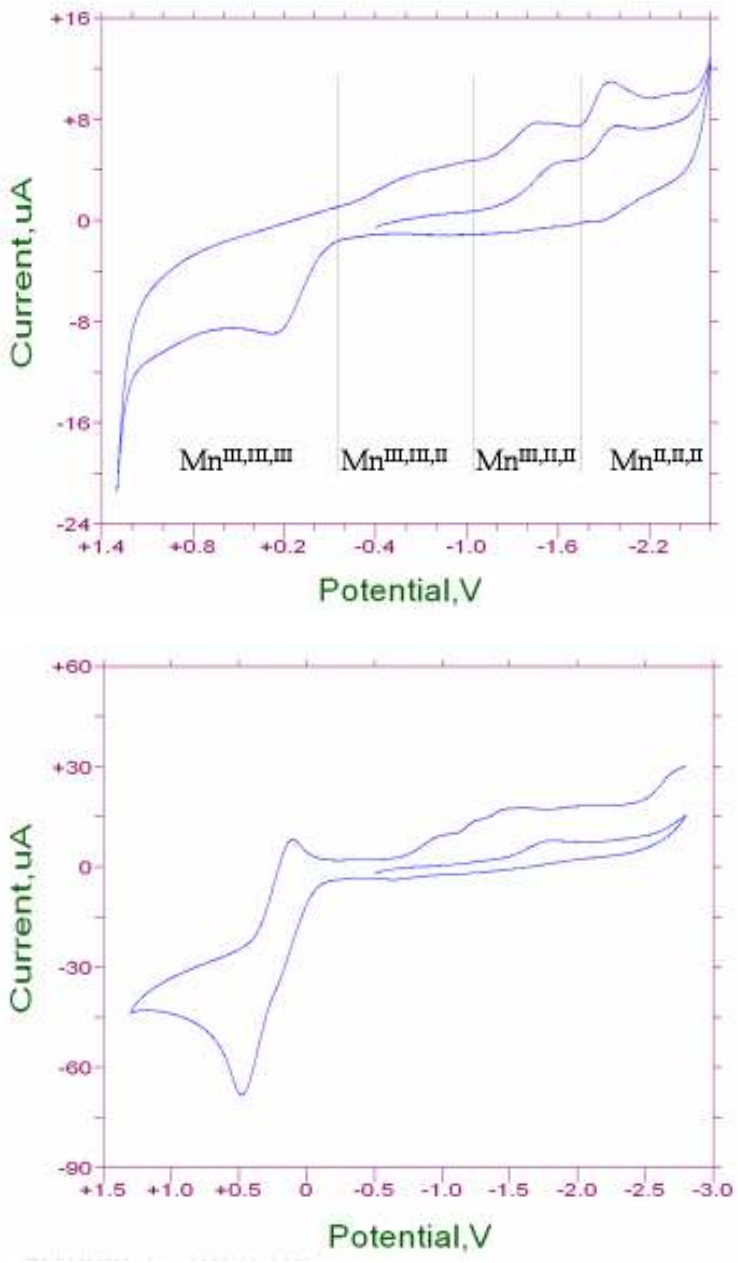

Figure 2.18. Electrochemistry of 5 mM solution of "Mn_3O-Ac" triangle (top) and $[Mn_3O(O_2CFc)_6(py)_2(H_2O)]$ (**1**, bottom) in DMF with 0.1 M TBAH and glassy carbon working, platinum wire counter, and Fc/Fc^+ reference electrodes.

This preliminary study of the Mn_3O-Fc triangle and its simple acetate analog was somewhat disconcerting. First, the oxidation of $FcCO_2H$ will be much harder than that of ferrocene alone, particularly when bound to a metal center as evidenced by the shift in oxidation to higher potential for the Mn_3O-Fc complex. For this reason, ferrocene acetic acid ($FcCH_2CO_2H$) was also synthesized[32] in the hopes that the extra methylene group between the ferrocene and electron-withdrawing carboxylate group would be enough to shift the oxidation to a voltage lower than that of ferrocene.[33] However, no triangle or dicubane complexes were isolated with the ferrocene acetic acid ligand.

The second concern that was realized in this initial study was the overlapping of the ferrocene and Mn(II) oxidation potentials. If our final goal of oxidizing all the Fc ligands on our Mn SMMs was to be achieved, we would want to do so without oxidizing the Mn core. Though having an all Mn(III) core might increase the magnetic coupling and potentially enhance the quantum properties of this molecule, we cannot be certain that it would not destroy the structural integrity of the SMM.

Complexes **3** and **4** were also studied as show in Figures 2.19 and 2.20, respectively. The electrochemistry of both complexes was measured in 1 mM solutions in CH_2Cl_2 and 0.1 mM or 1 mM solutions of THF. In all cases, a strong quasi-reversible oxidation of the ferrocene carboxylate ligand is observed. No peaks are seen corresponding to the reduction of Mn(III) to Mn(II) as was the case in the triangle complexes. However, there is significant peak overlap in the ferrocene region (indicated by the small shoulders seen in Figures 2.19 and 2.20), presumably due to the Mn(III) to Mn(II) reduction which was established in the Mn_3 triangle measurements.

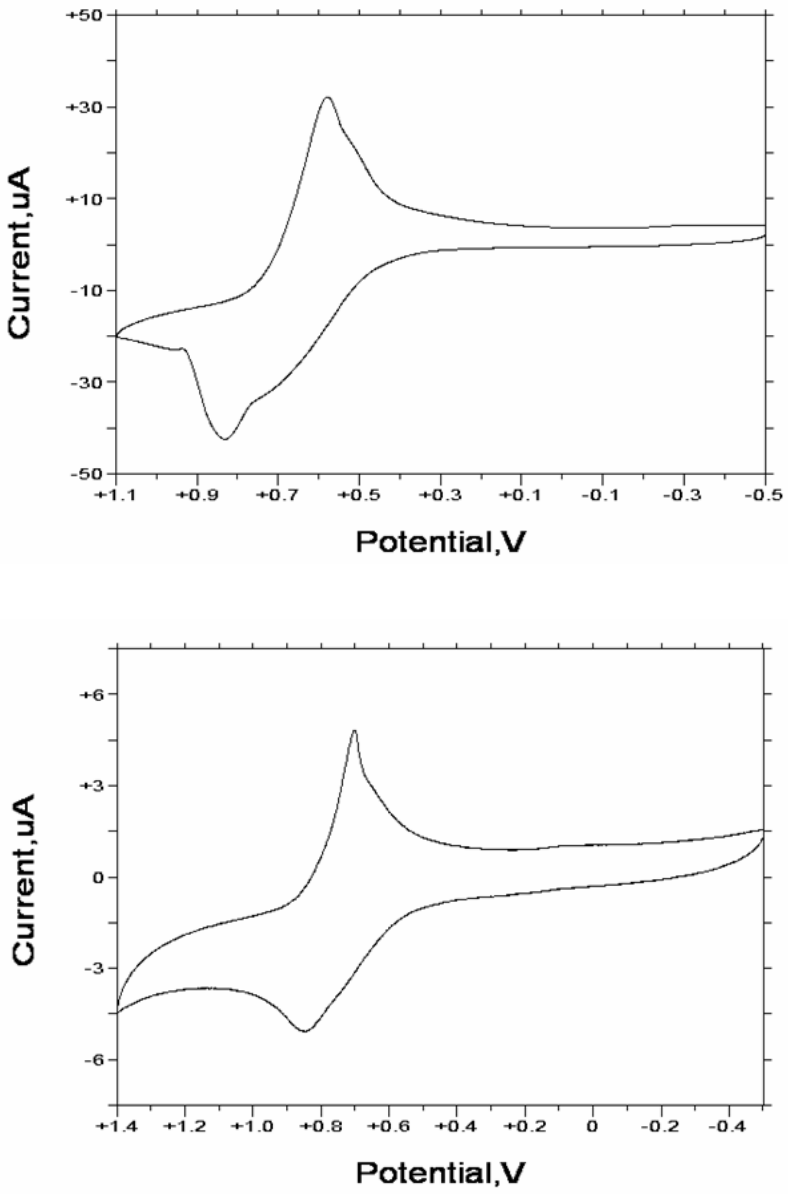

Figure 2.19. Electrochemistry of $[Mn_4(O_2CFc)_4(mdeaH)_2(mdea)_2] \cdot 4MeCN$ (**3**; top, 1 mM solution in CH_2Cl_2; bottom, 0.1 mM solution in THF) with 0.1 M TBAH and glassy carbon working, platinum wire counter, and Fc/Fc^+ reference electrodes.

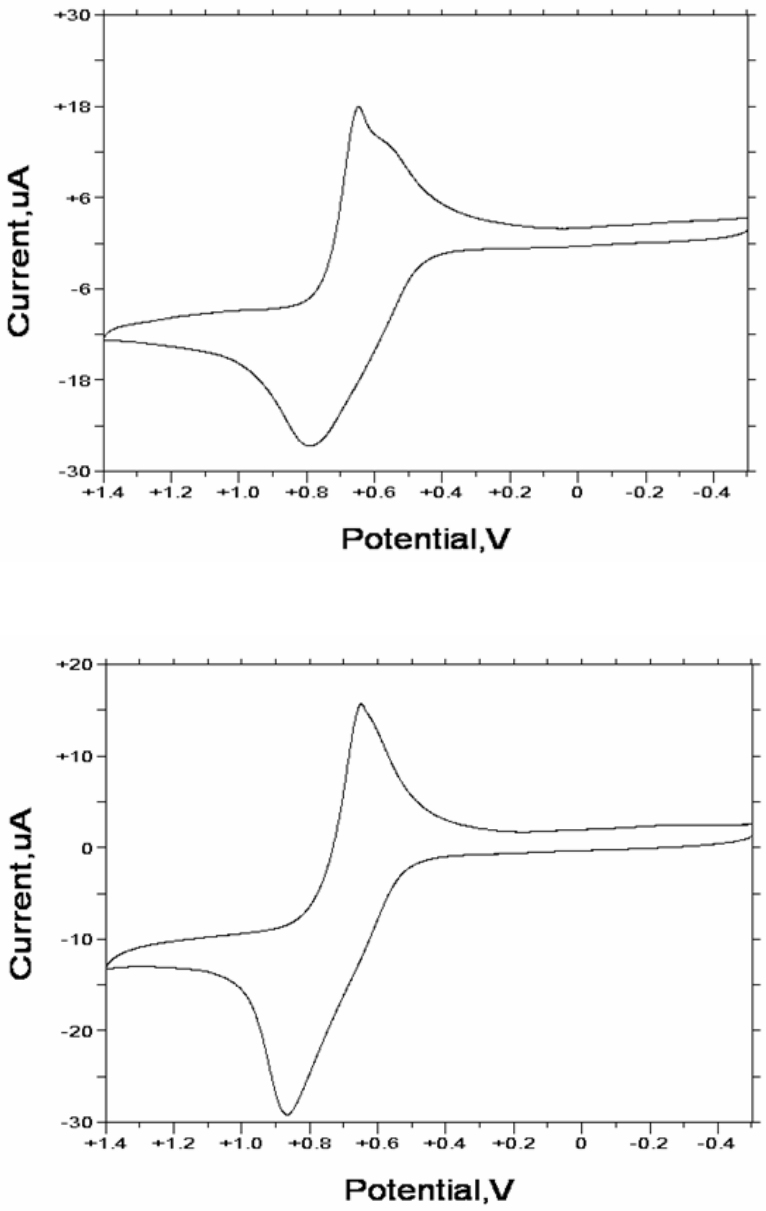

Figure 2.20. Electrochemistry of 1 mM solution of $[Mn_4(O_2CFc)_4(bdeaH)_2\text{-}(bdea)_2] \cdot 2MeCN$ (**4**) in CH_2Cl_2 (top) and THF (bottom) with 0.1 M TBAH and glassy carbon working, platinum wire counter, and Fc/Fc^+ reference electrodes.

There is a strong solvent-dependence on the oxidation potential of ferrocene carboxylate in **3** and **4**. In CH_2Cl_2, the ferrocene carboxylate oxidation occurs at $E_{1/2}$ = +271 mV and +246 mV *vs.* Fc/Fc^+ for **3** and **4**, respectively, which was expected from the Mn_3 triangle results. However, in THF the peak occurs at $E_{1/2}$ = -46 mV and -53 mV *vs*. Fc/Fc^+ for **3** and **4**, respectively. This suggests that the ferrocene carboxylate substituents in these complexes should be easier to oxidize than ferrocene when in THF. These results were a good starting point for chemical oxidation attempts of **3** and **4** in THF solutions. Stoichiometric oxidations using a broad spectrum of chemical oxidants including HCl, Ag^+, $[WCl_6]$, and several quinone complexes were attempted but products were not able to be isolated or fully characterized.

2.4. Conclusions

Several synthetic routes to the common $[Mn_4]$ dicubane family of single-molecule magnets have been discussed. Though oxo-centered triangles have proven to be a useful starting material for higher nuclearity SMMs, the dicubanes reported here were best synthesized from simple metal salts and chelating amines. This approach consistently resulted in well-formed crystals with very little disorder. Also, reducing the amount of side products in the reaction lead to more homogeneous samples with sharp, highly reproducible magnetic data. In methanol- and water-solvated forms of **3** and **4** synthesized from "Mn_3O-Ac" or "Mn_3O-Fc" (**1**) triangles, dc and ac data varied significantly due to solvent-loss and the presence of low-spin impurities.

Three new ferromagnetic $[Mn^{II}_2Mn^{III}_2]$ dicubane complexes have been synthesized and characterized. Though the ground state spins of these complexes are

poorly defined due to low-lying excited states and intermolecular interaction, fitting of the dc magnetic data along with analysis of the low-frequency ac data suggests a ground state of S = 7 for **2** and **3** and a likely S = 8 ground state for **4**. High-spin ground states along with the presence of a significant frequency-dependent out-of-phase signal in the ac susceptibility suggest that all three of these complexes are single-molecule magnets. Furthermore, complexes **2-4** appear to be the first ferrocene-containing complexes to exhibit SMM behavior.

Since the ultimate goal in making these ferrocene-substituted SMMs was to eventually oxidize them to obtain the ferrocenium analogs (making cationic SMMs with a 4+ charge), electrochemical studies were carried out on complexes **1**, **3**, and **4**. Though these preliminary results suggest that the desired ferrocenium analogs of **3** and **4** should be accessible (either chemically or electrochemically), they have not yet been isolated. The highly electron-withdrawing carboxylate group on the ferrocene ligands, along with coordination to Mn ions, should present some difficulties in oxidizing the Fc moieties without also oxidizing the $[Mn_4]$ core. Also, the effect that the resulting S = ½ Fe(III) ions might have on the ferromagnetic $[Mn_4]$ core is still unknown. The unpaired spin may magnetically couple to the $[Mn_4]$ core in such a way that could either enhance or destroy the SMM behavior of the molecule.

This chapter, in part, is a reprint of the material as it appears in: Heroux, K. J.; Rheingold, A. L.; Hendrickson, D. N. "Ferrocene-substituted $[Mn_4]$ dicubane single-molecule magnets", *European Journal of Inorganic Chemistry,* **2009***,* 3541. The dissertation author was the primary investigator and author of this paper.

2.5. References

(1) Christou, G.; Gatteschi, D.; Hendrickson, D. N.; Sessoli, R. *MRS Bulletin* **2000**, *25*, 66-71.

(2) Gatteschi, D.; Sessoli, R. *Angewandte Chemie-International Edition* **2003**, *42*, 268-297.

(3) Wernsdorfer, W.; Sessoli, R.; Caneschi, A.; Gatteschi, D.; Cornia, A. *Journal of the Physical Society of Japan* **2000**, *69*, 375-382.

(4) Leuenberger, M. N.; Loss, D. *Physical Review B* **2000**, *61*, 12200-12203.

(5) Hill, S.; Edwards, R. S.; Aliaga-Alcalde, N.; Christou, G. *Science* **2003**, *302*, 1015-1018.

(6) Hendrickson, D. N.; Yang, E. C.; Isidro, R. M.; Kirman, C.; Lawrence, J.; Edwards, R. S.; Hill, S.; Yamaguchi, A.; Ishimoto, H.; Wernsdorfer, W.; Ramsey, C.; Dalal, N.; Olmstead, M. M. *Polyhedron* **2005**, *24*, 2280-2283.

(7) Beedle, C. C.; Stephenson, C. J.; Heroux, K. J.; Wernsdorfer, W.; Hendrickson, D. N. *Inorganic Chemistry* **2008**, *47*, 10798-10800.

(8) Shah, S. J.; Ramsey, C. M.; Heroux, K. J.; DiPasquale, A. G.; Dalal, N. S.; Rheingold, A. L.; del Barco, E.; Hendrickson, D. N. *Inorganic Chemistry* **2008**, *47*, 9569-9582.

(9) Foguet-Albiol, D.; O'Brien, T. A.; Wernsdorfer, W.; Moulton, B.; Zaworotko, M. J.; Abboud, K. A.; Christou, G. *Angewandte Chemie-International Edition* **2005**, *44*, 897-901.

(10) Ako, A. M.; Mereacre, V.; Hewitt, I. J.; Clerac, R.; Lecren, L.; Anson, C. E.; Powell, A. K. *Journal of Materials Chemistry* **2006**, *16*, 2579-2586.

(11) Brechin, E. K.; Yoo, J.; Nakano, M.; Huffman, J. C.; Hendrickson, D. N.; Christou, G. *Chemical Communications* **1999**, 783-784.

(12) Yoo, J.; Brechin, E. K.; Yamaguchi, A.; Nakano, M.; Huffman, J. C.; Maniero, A. L.; Brunel, L. C.; Awaga, K.; Ishimoto, H.; Christou, G.; Hendrickson, D. N. *Inorganic Chemistry* **2000**, *39*, 3615-3623.

(13) Yang, E. C.; Harden, N.; Wernsdorfer, W.; Zakharov, L.; Brechin, E. K.; Rheingold, A. L.; Christou, G.; Hendrickson, D. N. *Polyhedron* **2003**, *22*, 1857-1863.

(14) Wittick, L. M.; Murray, K. S.; Moubaraki, B.; Batten, S. R.; Spiccia, L.; Berry, K. J. *Dalton Transactions* **2004**, 1003-1011.

(15) Li, G.; Hou, H. W.; Li, L. K.; Meng, X. R.; Fan, Y. T.; Zhu, Y. *Inorganic Chemistry* **2003**, *42*, 4995-5004.

(16) Zhuk, Y.; Strizhakova, N.; Maletin, Y. *Theoretical and Experimental Chemistry* **2000**, *36*, 215-219.

(17) Mereacre, V.; Nakano, M.; Gomez-Segura, J.; Imaz, I.; Sporer, C.; Wurst, K.; Veciana, J.; Turta, C.; Ruiz-Molina, D.; Jaitner, P. *Inorganic Chemistry* **2006**, *45*, 10443-10445.

(18) Chen, Z.; Liang, F.; Zhou, S.; Xia, C.; Hu, R. *Journal of Molecular Structure* **2007**, *827*, 20-24.

(19) Chen, Z.; Ma, Y.; Liang, F.; Zhou, Z. *Journal of Organometallic Chemistry* **2008**, *693*, 646-654.

(20) Zheng, G. L.; Ma, J. F.; Su, Z. M.; Yan, L. K.; Yang, J.; Li, Y. Y.; Liu, J. F. *Angewandte Chemie-International Edition* **2004**, *43*, 2409-2411.

(21) Masello, A.; Murugesu, M.; Abboud, K. A.; Christou, G. *Polyhedron* **2007**, *26*, 2276-2280.

(22) Vincent, J. B.; Chang, H. R.; Folting, K.; Huffman, J. C.; Christou, G.; Hendrickson, D. N. *Journal of the American Chemical Society* **1987**, *109*, 5703-5711.

(23) Wittick, L. M.; Murray, K. S.; Moubaraki, B.; Batten, S. R.; Spiccia, L.; Berry, K. J. *Dalton Transactions* **2004**, 1003-1011.

(24) Manoli, M.; Prescimone, A.; Bagai, R.; Mishra, A.; Murugesu, M.; Parsons, S.; Wernsdorfer, W.; Christou, G.; Brechin, E. K. *Inorganic Chemistry* **2007**, *46*, 6968-6979.

(25) Piligkos, S.; Rajaraman, G.; Soler, M.; Kirchner, N.; van Slageren, J.; Bircher, R.; Parsons, S.; Gudel, H. U.; Kortus, J.; Wernsdorfer, W.; Christou, G.; Brechin, E. K. *Journal of the American Chemical Society* **2005**, *127*, 5572-5580.

(26) Rajaraman, G.; Murugesu, M.; Sanudo, E. C.; Soler, M.; Wernsdorfer, W.; Helliwell, M.; Muryn, C.; Raftery, J.; Teat, S. J.; Christou, G.; Brechin, E. K. *Journal of the American Chemical Society* **2004**, *126*, 15445-15457.

(27) Brechin, E. K.; Soler, M.; Christou, G.; Helliwell, M.; Teat, S. J.; Wernsdorfer, W. *Chemical Communications* **2003**, 1276-1277.

(28) Shah, S. J.; Ramsey, C. M.; Heroux, K. J.; O'Brien, J. R.; DiPasquale, A. G.; Rheingold, A. L.; del Barco, E.; Hendrickson, D. N. *Inorganic Chemistry* **2008**, *47*, 6245-6253.

(29) Kambe, K. *Journal of the Physical Society of Japan* **1950**, *5*, 48.

(30) Van Vleck, J. H. *The Theory of Electric and Magnetic Susceptibilities*; Oxford Univ. Press., 1965.

(31) Krzystek, J.; Ozarowski, A.; Telser, J. *Coordination Chemistry Reviews* **2006**, *250*, 2308-2324.

(32) Lednicer, D.; Lindsay, J. K.; Hauser, C. R. *Journal of Organic Chemistry* **1958**, *23*, 653-655.

(33) Davis, W. L.; Shago, R. F.; Langner, E. H. G.; Swarts, J. C. *Polyhedron* **2005**, *24*, 1611-1616.

Chapter 3:

Sterically-Isolated [Mn_4] Single-Molecule Magnets Exhibiting Novel Quantum Properties

3.1. Introduction

One of the major goals of this thesis research has been to sufficiently isolate the magnetic core of a single-molecule magnet (SMM) in order to reduce environmental coupling effects. Interactions between neighboring SMMs in the crystal lattice, whether through-space (dipole-dipole) or through-bond (magnetic exchange), solvate interactions, and H-bonding, can be detrimental to the magnetic and quantum properties of SMMs. Furthermore, such coupling factors introduce a large number of environmental degrees of freedom which makes these complexes all that more difficult to magnetically characterize. SMMs with significant intermolecular interactions often times have poorly defined magnetic and quantum properties.

In Chapter 2, one strategy to limit intermolecular interactions in SMMs was to use ferrocene carboxylate ligands in the synthesis of well-known tetranuclear manganese SMMs. In addition to the steric bulk provided by the ferrocene moieties, this ligand was chosen for its unique redox properties in the hopes of creating cationic species. With highly-charged SMMs, the magnetic core could potentially be isolated by bulky non-magnetic counterions. Though the ferrocene-substituted SMMs were successfully synthesized, their oxidized ferrocenium analogs were not able to be isolated.

In order to circumvent the electrochemical roadblock encountered in the ferrocene-substituted SMMs, a new strategy utilizing zwitterionic carboxylate ligands was developed. Upon coordination to the metal cluster, the zwitterionic ligand would retain a positive charge thus resulting in cationic SMMs. With this goal in mind,

betaine-type ligands were chosen to replace ferrocene carboxylates in order to create cationic SMMs isolated by bulky couterions in a one-step process.

The original betaine, or trimethylglycine ($O_2CCH_2NMe_3$), is a zwitterionic compound with a free carboxylate group and a quaternary ammonium group (see Figure 3.1) which gives it unique physio-chemical properties. Betaine is commonly found in plant and animal tissues and has been extensively studied over the years in many research areas including chemistry, biology, and materials. For example, betaine has been found to play an integral role as a methyl-transfer agent in amino acid synthesis.[1,2] Betaine derivatives have also been developed for use as surfactants[3] and also as chelating ligands for transition metal coordination complexes.[4-7] Because of the many derivatives of this classic compound synthesized over the years, betaine is now often referred to as glycine betaine in order to distinguish it from closely related compounds.

In materials chemistry, both carboxy- and sulfobetaines have become an important component in the synthesis of many biomimetic materials. Their dual functionality makes them highly resistant to protein adsorption and effective at immobilizing proteins on a surface (shown schematically in Figure 3.2). Also, due to their zwitterionic nature, such betaine-based materials are highly responsive to changes in pH and ionic strength which can be tailored for applications in biosensors and drug delivery.[8,9]

In 2003 and 2004, glycine betaine and various derivatives were used to replace acetate groups on the well-known single-molecule magnet, [Mn_{12}Ac]. Using a previously-developed carboxylate-exchange reaction, 2-electron reduced species of [Mn_{12}Ac] were synthesized with 16 of the acetate groups replaced by betaine-type

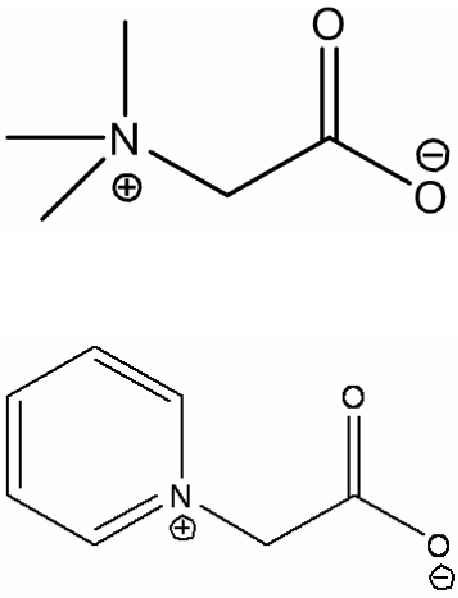

Figure 3.1. Molecular structures of (top) glycine betaine, Bet, and (bottom) pyridyl betaine, pyBet.

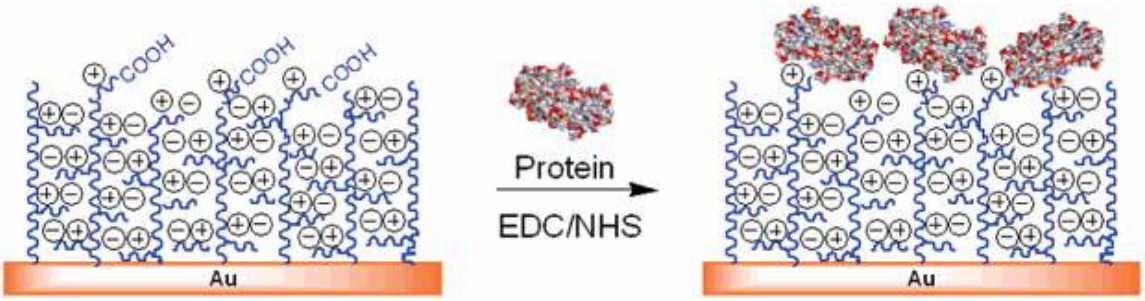

Figure 3.2. Schematic of a polyCBMA-grafted surface (left) with immobilized proteins (right). CBMA is carboxybetaine methacrylate, EDC is 1-ethyl-3-(3 dimethylaminopropyl)-carbodiimide, and NHS is N-hydroxysuccinimide.

ligands. The cationic clusters were isolated by PF_6^- anions[10] or large polyoxometalates[11] of various anionic charges. The Bet-substituted [Mn_{12}] cluster, $[Mn_{12}O_{12}(Bet)_{16}(EtOH)_4](PF_6)_{14} \cdot 4MeCN \cdot H_2O$, is shown in Figure 3.3.[10] For these studies, the [Mn_{12}] SMM was functionalized into a polycationic cluster for self-assembly on soft media or for deposition of monolayers onto chemically-modified metal surfaces.[10,11]

Even though these cationic SMMs were synthesized for a different purpose, the strategy from a synthetic standpoint seemed to be right in line with goals of this project. Since large SMMs like [Mn_{12}Ac] are often subject to ligand and crystal disorder, we chose to employ this new strategy on small well-known SMMs with well-defined structural properties in order to reduce the number of microenvironments. Again, we turned our attention to the [Mn_4] dicubane family of SMMs as described in the Introduction Chapter as well as Chapter 2. Another advantage to working with the [Mn_4] dicubanes is that the betaine-substituted analogs can be synthesized from simple starting materials much like the ferrocene-substituted [Mn_4] SMMs. This method allows us to avoid the often time-consuming and low-yielding carboxylate-exchange reaction.

In this chapter, the synthesis, structure, and magnetic properties of five new cationic [Mn_4] dicubane SMMs will be presented. The complexes prepared are $[Mn_4(Bet)_2(O_2CMe)_2(mdeaH)_2(mdea)_2](BPh_4)_2$ (**5**), $[Mn_4(Bet)_4(mdeaH)_2(mdea)_2](BPh_4)_4$ (**6**), $[Mn_4(Bet)_4(bdeaH)_2(bdea)_2](BPh_4)_4 \cdot Et_2O \cdot 4MeOH$ (**7**), $[Mn_4(pyBet)_2(O_2CMe)_2(mdeaH)_2(mdea)_2](BPh_4)_2 \cdot 2MeCN$ (**8**), and $[Mn_4(pyBet)_4(mdeaH)_2(mdea)_2](BPh_4)_4 \cdot 2MeCN$ (**9**) where $mdeaH_2$ and $bdeaH_2$ are N-methyl- and N-butyldiethanolamine, respectively, and Bet and pyBet are glycine and

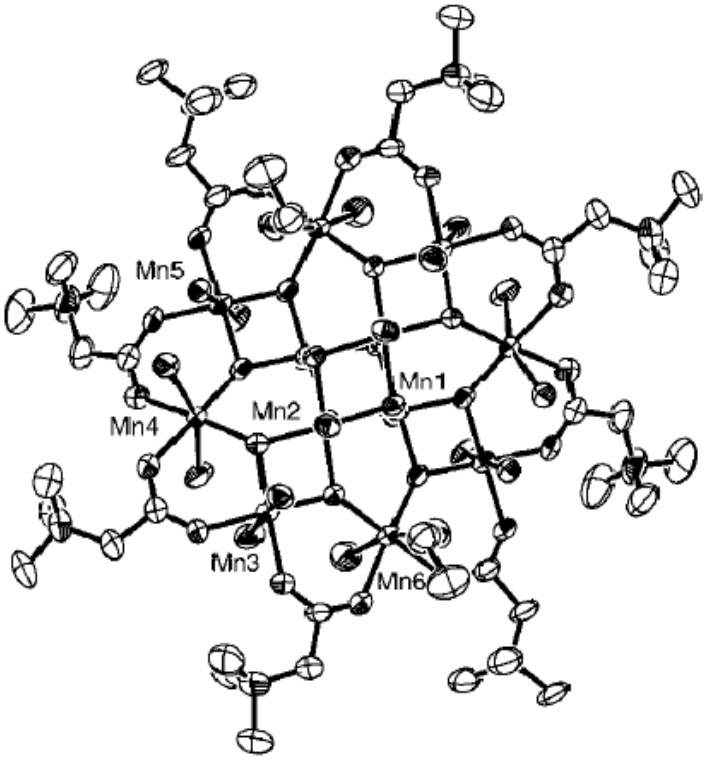

Figure 3.3. Core structure of $[Mn_{12}O_{12}(Bet)_{16}(EtOH)_4](PF_6)_{14} \cdot 4MeCN \cdot H_2O$.

pyridyl betaine ($O_2CCH_2NC_5H_5$), respectively. The previously published neutral benzoate analogs of these complexes, $[Mn_4(O_2CPh)_4(mdeaH)_2(mdea)_2]$[12] and $[Mn_4(O_2CPh)_4(bdeaH)_2(bdea)_2]$[13] (Figure 1.3), will be discussed throughout the chapter for structural and magnetic comparisons.

The resulting betaine-substituted $[Mn_4]$ dicubanes are expected to retain their structural and magnetic integrity just as the ferrocene-substituted analogs displayed in Chapter 2. However, the added steric and electrostatic bulk of the organic counterions in these new compounds should provide some "insulation" of the magnetic core and reduce or possibly eliminate any intermolecular interactions that prevent many SMMs from being fully-characterized. The correlation between steric isolation of the magnetic core and the electronic isolation of the ground state spin in this series of complexes will be closely investigated.

The benefits of such isolation are most clearly demonstrated in the fully-substituted glycine betaine complex, **6**, which has the highest crystal quality and largest intermolecular Mn···Mn separation of all the complexes presented herein. The structural enhancement of this complex leads to well-defined magnetic properties and novel single crystal behavior in HFEPR and magnetization hysteresis studies. Most notably, complex **6** shows complex Berry phase interference due to competing intramolecular anisotropies which has been theorized in the past but never experimentally observed until now.

3.2. Experimental Section

3.2.1. Preparation

All reactions were performed under aerobic conditions. All reagents and ligands were purchased from Sigma Aldrich and used without further purification. The oxo-centered trinuclear species, $[Mn_3(O_2CMe)_6(py)_3]$, was prepared according to a previously published synthesis.[14] The tetraphenylborate salt of glycine betaine ($BetHBPh_4$) was achieved by simple exchange of the chloride ion in commercially available BetHCl in water. Free pyridyl betaine (pyBet) and the intermediate bis(pyBet) were synthesized from chloroacetic acid and pyridine as described by Chen and Mak in 1990.[15]

$[Mn_4(Bet)_2(O_2CMe)_2(mdeaH)_2(mdea)_2](BPh_4)_2$ (5). To a solution of $BetHBPh_4$ (57 mg, 0.13 mmol) in 20 mL MeOH was added $[Mn_3(O_2CMe)_6(py)_3]$ (100 mg, 0.13 mmol) and excess Et_3N. Excess $mdeaH_2$ (0.1 mL, 0.8 mmol) was then added dropwise to the solution. The resulting dark brown solution was stirred and warmed for 1 hour and filtered by gravity. X-ray quality crystals were obtained in 5-7 days from layering the filtrate with pentane with a thin layer of iPr_2O at the interface. Yield: 15 %. Elemental analysis for $C_{82}H_{114}B_2Mn_4N_6O_{16}$ (1681.17), calc'd (found): C 58.58 (57.68), H 6.83 (6.54), N 4.99 (4.95). Selected FT-IR Data (KBr, cm^{-1}): 3431 (w, br), 3059 (w), 3037 (w), 2854 (m), 1612 (s), 1421 (w), 1402 (w), 1329 (m), 1088 (m), 1066 (m), 910 (w), 741 (w), 708 (s).

$[Mn_4(Bet)_4(mdeaH)_2(mdea)_2](BPh_4)_4$ (6). *Method A.* To a solution of $BetHBPh_4$ (175 mg, 0.4 mmol) in 15 mL of MeOH was added $Mn(NO_3)_2 \cdot 4H_2O$ (100 mg, 0.4 mmol) and excess Et_3N. Two equivalents of $mdeaH_2$ (0.1 mL, 0.8 mmol) were

then added dropwise to the milky light brown solution. The solution was refluxed for 1 hour resulting in a deep dark brown solution which was then filtered by gravity. X-ray quality crystals were obtained in 3-5 days from Et_2O or iPr_2O vapor diffusion of the MeOH solution. Yield: 35 %. *Method B.* Same procedure as Method A except $BetHBPh_4$ was dissolved in 15 mL of MeCN followed by the addition of $Mn(NO_3)_2$ and $mdeaH_2$. Excess Et_3N was added dropwise to the reddish-brown solution until the solution became a deep brown, almost black, solution. The resulting solution was stirred at room temperature for 30 min before filtering by gravity. X-ray quality crystals were obtained in 5-7 days from Et_2O vapor diffusion of the MeCN solution. Yield: 10 %. Elemental analysis for $C_{136}H_{170}B_4Mn_4N_8O_{16}$ (2435.80), calc'd (found): C 67.06 (63.89), H 7.03 (7.63), N 4.60 (5.13). Selected FT-IR Data (KBr, cm^{-1}): 3423 (m, br), 3055 (m), 2983 (m), 2866 (m), 1626 (s, br), 1479 (m), 1398 (m), 1309 (m), 1086 (m), 910 (w), 735 (s), 708 (s), 613 (w).

$[Mn_4(Bet)_4(bdeaH)_2(bdea)_2](BPh_4)_4$ · Et_2O · 4MeOH **(7).** To a solution of $BetHBPh_4$ (175 mg, 0.4 mmol) in 15 mL of MeOH was added $Mn(NO_3)_2 \cdot 4H_2O$ (100 mg, 0.4 mmol) and excess Et_3N. Two equivalents of $bdeaH_2$ (0.13 mL, 0.8 mmol) were then added dropwise to the light brown suspension. The solution was refluxed for 1 hour resulting in a deep dark brown solution which was then stirred overnight at room temperature and filtered by gravity (small amount of light brown precipitate). X-ray quality crystals were obtained in 3-5 days from Et_2O vapor diffusion of the MeOH solution. Yield: 40 %. Elemental analysis for $C_{156}H_{220}B_4Mn_4N_8O_{21}$ (2806.40), calc'd (found): C 66.76 (65.25), H 7.90 (6.66), N 3.99 (4.46). Selected FT-IR Data (KBr, cm^{-}

[1]): 3423 (m, br), 3055 (m), 2956 (m), 2864 (m), 1626 (s, br), 1479 (w), 1385 (s), 1306 (w), 1086 (w), 908 (w), 738 (m), 708 (s), 607 (w).

$[Mn_4(pyBet)_2(O_2CMe)_2(mdeaH)_2(mdea)_2](BPh_4)_2 \cdot 2MeCN$ (8). *Method A.* To a solution of pyBet (55 mg, 0.4 mmol) in 15 mL of MeCN was added $Mn(O_2CMe)_2 \cdot 4H_2O$ (100 mg, 0.41 mmol) and excess Et_3N. Two equivalents of $mdeaH_2$ (0.1 mL, 0.8 mmol) were then added dropwise to suspension. The solution was refluxed for 10 minutes, or until a deep brown solution was achieved, and then filtered by gravity. One equivalent of $NaBPh_4$ (137 mg, 0.4 mmol) was dissolved in a minimal amount of MeCN and added dropwise to the filtrate. The solution was stirred at room temperature for additional 10 minutes before being filtered by gravity (small amount of pale precipitate formed). X-ray quality crystals were obtained in 5 days from Et_2O vapor diffusion of the MeCN solution. Yield: 10 %. *Method B.* Same exact procedure as Method A except for the replacement of pyBet with one molar equivalent of bis(pyBet) recrystallized from hot MeOH (113 mg, 0.4 mmol). X-ray quality crystals were obtained in 3 days from Et_2O vapor diffusion of the amber-brown MeCN solution. Yield: 20 %. Elemental analysis for $C_{90}H_{112}B_2Mn_4N_8O_{16}$ (1803.26), calc'd (found): C 59.94 (59.65), H 6.26 (6.95), N 6.21 (3.64).Selected FT-IR Data (KBr, cm^{-1}): 3055 (m), 2860 (m, br), 1579 (s, br), 1425 (m, br), 1400 (m, br), 1336 (w), 1090 (m), 1076 (m), 912 (m), 733 (m), 704 (s).

$[Mn_4(pyBet)_4(mdeaH)_2(mdea)_2](BPh_4)_4 \cdot 2MeCN$ (9). *Method A.* To a solution of pyBet (55 mg, 0.4 mmol) in 10 mL MeCN and 5 mL of MeOH was added $Mn(NO_3)_2 \cdot 4H_2O$ (100 mg, 0.4 mmol) and excess Et_3N. Two equivalents of $mdeaH_2$ (0.1 mL, 0.8 mmol) were then added dropwise to the deep brown solution and warmed for 10

minutes. One equivalent of $NaBPh_4$ (137 mg, 0.4 mmol) was dissolved in a minimal amount of MeCN and added dropwise to the filtrate. The solution was stirred at room temperature for additional 5 minutes before being filtered by gravity (no precipitate). X-ray quality crystals were obtained in 3-5 days from Et_2O vapor diffusion or layering of the MeCN/MeOH solution. Yield: 30 %. *Method B.* Same exact procedure as Method A except for the replacement of pyBet with one equivalent of bis(pyBet) recrystallized from hot MeOH (113 mg, 0.4 mmol). Also, this reaction can be performed in the 2:1 MeCN/MeOH mixture or 100% MeCN. X-ray quality crystals were obtained in 3 days from Et_2O vapor diffusion of the amber-brown filtrate. Yield: 20 %. Elemental analysis for $C_{148}H_{160}B_4Mn_4N_{10}O_{16}$ (2597.86): calc'd (found): C 68.42 (59.22), H 6.21 (6.04), N 5.39 (5.24).Selected FT-IR Data (KBr, cm^{-1}): 3408 (m, br), 3055 (m), 2862 (m), 1633 (m, br), 1485 (w), 1385 (s, br), 1070 (w), 1034 (w), 735 (m), 708 (m).

3.2.2. X-Ray Crystallography

Crystals were mounted on a CryoLoop© with Paratone-N© oil. Diffraction intensity data were collected at 100(2) K on a Bruker Smart Apex CCD diffractometer with Mo Kα radiation (**5**, **7-9**) and with Cu Kα radiation for **6**. Data were integrated using the Bruker SAINT software program and corrected for absorption using the Bruker SADABS program. Crystallographic data and refinement parameters for **5-7** are given in Table 3.1 and those for **8** and **9** are given in Table 3.2.

All complexes were solved by direct methods (SHELXS-97 for **5-8**, SIR-2004 for **9**), developed by successive difference Fourier syntheses, and refined by full matrix least squares on all F^2 data. All non-hydrogen atoms were refined anisotropically by

Table 3.1. Crystallographic data and refinement parameters for **5-7.**

	5	**6**	**7**
Formula	$C_{82}H_{114}B_2Mn_4N_6O_{16}$	$C_{136}H_{170}B_4Mn_4N_8O_{16}$	$C_{156}H_{220}B_4Mn_4N_8O_{21}$
FW	1681.17	2435.80	2806.40
T [K]	100(2)	100(2)	100(2)
λ [Å]	0.71073	1.54178	0.71073
Crystal system	monoclinic	triclinic	triclinic
Space group	P2(1)/c	P-1	P-1
a [Å]	14.030(3)	14.7387(4)	14.1438(12)
b [Å]	19.229(4)	14.8920(4)	15.0432(13)
c [Å]	15.465(3)	16.5865(4)	19.3276(17)
α [deg]	90	71.796(2)	73.6530(10)
β [deg]	99.355(3)	82.316(2)	75.1320(10)
γ [deg]	90	63.118(2)	83.7880(10)
V [Å^3]	4116.7(14)	3084.51(14)	3811.1(6)
Z	2	1	1
D_{calc} [mg m^{-3}]	1.356	1.311	1.223
Abs. coefficient [mm^{-1}]	0.668	3.798	0.390
F(000)	1772	1290	1500
Theta range [deg]	2.10 to 25.03	5.05 to 65.36	1.41 to 28.25
Comp. to theta [25.00°]	99.9 %	98.6 %	99.7 %
Max. and min. transmission	0.9547 and 0.8780	0.8328 and 0.3954	0.9922 and 0.9260
Data / restraints / param.	7282 / 0 / 532	9925 / 0 / 766	17039 / 0 / 829
Goodness-of-fit on F^2	1.061	1.022	1.016
R(F)[a] [I > 2σ(I)]	0.0672	0.0426	0.0545
R(wF^2)[b] [I > 2σ(I)]	0.1840	0.1001	0.1405
Largest diff. peak and hole [e.Å^{-3}]	1.717 and -0.660	1.051 and -0.427	0.817 and -0.501

[a] $R = \Sigma||F_o| - |F_c||/\Sigma|F_o|$. [b] $R(\omega F^2) = \{\Sigma[\omega(F_o^2 - F_c^2)^2]/\Sigma[\omega(F_o^2)^2]\}^{1/2}$;
$\omega = 1/[\sigma^2(F_o^2) + (aP)^2 + bP]$, $P = [2F_c^2 + \max(F_o, 0)]/3$

Table 3.2. Crystallographic data and refinement parameters for **8** and **9.**

	8	**9**
Formula	$C_{90}H_{112}B_2Mn_4N_8O_{16}$	$C_{148}H_{160}B_4Mn_4N_{10}O_{16}$
FW	1803.26	2597.86
T [K]	100(2)	100(2)
λ [Å]	0.71073	0.71073
Crystal system	monoclinic	monoclinic
Space group	P2(1)/c	P2(1)/c
a [Å]	13.881(3)	16.3290(15)
b [Å]	20.656(5)	16.096(15)
c [Å]	15.470(4)	25.298(2)
α [deg]	90	90
β [deg]	96.508(4)	90.256(2)
γ [deg]	90	90
V [Å^3]	4407.0(17)	6649.0(11)
Z	2	2
D_{calc} [mg m^{-3}]	1.359	1.298
Abs. coefficient [mm^{-1}]	0.630	0.440
F(000)	1892	2732
Theta range [deg]	1.65 to 28.41	2.04 to 25.03
Comp. to theta [25.00°]	99.9 %	99.8 %
Max. and min. transmission	0.9692 and 0.9397	0.9913 and 0.9370
Data / restraints / param.	10465 / 30 / 547	11728 / 6 / 921
Goodness-of-fit on F^2	1.007	1.022
R(F)[a] [I > 2σ(I)]	0.0807	0.0496
R(wF^2)[b] [I > 2σ(I)]	0.1869	0.1133
Largest diff. peak and hole [e.Å^{-3}]	0.400 and -0.663	1.325 and -0.505

[a] $R = \Sigma||F_o| - |F_c||/\Sigma|F_o|$. [b] $R(\omega F^2) = \{\Sigma[\omega(F_o^2 - F_c^2)^2]/\Sigma[\omega(F_o^2)^2]\}^{1/2}$;
$\omega = 1/[\sigma^2(F_o^2) + (aP)^2 + bP]$, $P = [2F_c^2 + \max(F_o, 0)]/3$

full-matrix least-squares (SHELXL-97). All hydrogen atoms were placed using a riding model and their positions were constrained relative to their parent atom using the appropriate HFIX command in SHELXL-97. Disordered MeOH, MeCN, and Et_2O solvate molecules in **7** and **8** were treated by the Squeeze method. A positionally disordered N-methyldiethanolamine ligand in **5** was modeled in two parts (Part 1 = C2, C4, C5; Part 2 = C2A, C4A, C5A) and refined to a final occupancy of 48%. The terminal carbon atom of a n-butyl chain in **7** (C14) was disordered over two positions at 65% occupancy. Complex **8** exhibits a significant amount of thermal motion as evidenced by the elongation of all a thermal ellipsoids in the same direction which is highly reproducible. Lastly, complex **9** has a disordered pyridyl ring, BPh_4^- anion, and MeCN solvate molecule which were all modeled and refined anisotropically.

The oxidation states of the Mn ions were determined by charge considerations, the presence of Jahn-Teller distortion around the high-spin Mn(III) ions, and bond valence sum analyses (Tables 3.3-3.5). Also, this pseudo-dicubane mixed-valent core is a well-known topology for Mn SMMs.

3.2.3. Physical Measurements

FT-IR spectra were collected using a Thermo-Nicolet Avatar series spectrometer. Elemental analysis was performed by NuMega Resonance Labs (San Diego, CA). Dc magnetic susceptibility measurements were performed on finely ground polycrystalline samples of complexes **5-9**, restrained in eicosane to prevent torquing of the micro-crystallites in an externally applied magnetic field. Measurements were carried out on a Quantum Design MPMS-5 magnetometer equipped with a 5.5 T

Table 3.3. Bond valence sum analysis for **5**.

Bond	Distance (Å)	Valence
Mn1-O1	2.395	0.175
Mn1-O2	2.203	0.294
Mn1-O3	2.072	0.419
Mn1-O4	2.354	0.196
Mn1-O5	2.459	0.147
Mn1-O7	2.131	0.357
Mn1-N1	2.395	0.236
Mn1 (2+)	**Bond valence sum**	**1.824**
Mn2-O2′	1.894	0.678
Mn2-O3	1.907	0.655
Mn2-O4	2.236	0.269
Mn2-O4′	1.951	0.581
Mn2-O6	1.908	0.653
Mn2-N2	2.304	0.303
Mn2 (3+)	**Bond valence sum**	**3.139**

Table 3.4. Bond valence sum analysis for **9**.

Bond	Distance (Å)	Valence
Mn1-O1	2.329	0.209
Mn1-O2	2.209	0.289
Mn1-O3	2.328	0.21
Mn1-O4	2.082	0.408
Mn1-O5	2.104	0.384
Mn1-O7	2.637	0.091
Mn1-N1	2.365	0.257
Mn1 (2+)	**Bond valence sum**	**1.848**
Mn2-O2	1.868	0.728
Mn2-O3	2.255	0.256
Mn2-O3′	1.959	0.569
Mn2-O4′	1.906	0.657
Mn2-O8	1.946	0.589
Mn2-N2	2.31	0.298
Mn2 (3+)	**Bond valence sum**	**3.097**

Table 3.5. Bond valence sum analysis for **6, 7** and **8**.

Bond	6		7		8	
	Distance (Å)	**Valence**	**Distance (Å)**	**Valence**	**Distance (Å)**	**Valence**
Mn1-O1	2.368	0.188	2.308	0.222	2.382	0.181
Mn1-O2	2.245	0.263	2.235	0.27	2.276	0.242
Mn1-O3	2.104	0.384	2.099	0.39	2.09	0.399
Mn1-O4	2.291	0.232	2.321	0.214	2.349	0.298
Mn1-O5	2.173	0.319	2.124	0.364	2.108	0.38
Mn1-O7	2.614	0.097	2.488	0.136	2.398	0.174
Mn1-N1	2.317	0.293	2.347	0.27	2.419	0.222
Mn1 (2+)		**1.776**		**1.866**		**1.896**
Mn2-O2′	1.861	0.741	1.872	0.72	1.893	0.68
Mn2-O3	1.894	0.678	1.9	0.667	1.904	0.66
Mn2-O4	2.252	0.258	2.28	0.239	2.349	0.194
Mn2-O4′	1.975	0.545	1.944	0.592	1.943	0.594
Mn2-O8	1.954	0.577	1.948	0.586	1.93	0.615
Mn2-N2	2.324	0.287	2.35	0.268	2.347	0.27
Mn2 (3+)		**3.086**		**3.072**		**3.013**

magnet. Magnetic susceptibility measurements were performed in the 1.8-300 K temperature range with applied fields of 0.1-50 kG. Ac magnetic susceptibilities measurements were obtained between 1-5 K with a 3 G ac field, at frequencies in the range of 10-997 Hz, with zero applied dc magnetic field on a Quantum Design MPMS-2 magnetometer. Data were corrected for diamagnetic contributions resulting from the sample rod, capsule and eicosane. Corrections for diamagnetism were estimated from Pascal's constants yielding the overall paramagnetic contribution to the molar magnetic susceptibility. The high-frequency ac magnetic susceptibility data were collected on a Quantum Design PPMS magnetometer at Quantum Design in San Diego, California.

Magnetization hysteresis measurements were carried out on oriented single crystals of complex **6** using a micro-Hall effect magnetometer[16] at the University of Central Florida. Hysteresis measurements were carried out at temperatures as low as 35 mK in an Oxford Instruments ^{3}He cryostat. High-frequency electron paramagnetic resonance (50-290 GHz) measurements were also carried out on single crystals of **6** in the temperature range of 2-20 K using a millimeter-wave vector network analyzer (MVNA) and a high-sensitivity cavity perturbation technique.[17] HFEPR measurements were conducted at the National High Magnetic Field Laboratory in Tallahassee, FL.

3.3. Results and Discussion

3.3.1. Synthesis

The synthesis of betaine-substituted [Mn_4] dicubanes is very similar to that of the ferrocene-substituted SMMs described in Chapter 2. However, it was quickly discovered that the use of any acetate source as a starting material (as in the synthesis of

the ferrocene analogs) leads to only partial-substitution of the carboxylate positions. This is evident in the structures of complexes **5** and **8** (glycine and pyridyl betaine analogs, respectively) which contain only two betaine-type ligands with the other two carboxylate positions occupied by bridging acetate groups. Eliminating the acetate source in these reactions by using manganese(II)nitrate as a starting material allowed for the isolation of the fully-substituted complexes **6**, **7**, and **9**.

Free pyridyl betaine, or pyBet, was easily synthesized from chloroacetic acid and pyridine but resulted in an extremely hygroscopic material that was difficult to purify and handle. Complexes **8** and **9** were first synthesized from this starting material (*Method A*) but the resulting products were not very homogenous and gave inconsistent magnetic data. An intermediate in the synthesis of pyBet was the hydrogen-bonded dimer of pyBetHCl or bis(pyBet) which could be easily recrystallized from MeOH to afford large colorless needles which were pure and easy to handle. *Method B* for complexes **8** and **9** reflects the use of bis(pyBet) instead of free pyBet which resulted in higher quality crystals and magnetic properties. Thus, the magnetic studies on the pyBet-substituted complexes, **8** and **9**, discussed in the following sections reflect only the products obtained from this optimized synthesis (*Method B*).

3.3.2. Description of Crystal Structures

All five complexes discussed herein are [Mn_4] dicubane analogs which have isostructural $[Mn_2^{II}Mn_2^{III}O_6]^{+4}$ cores resembling two face-sharing cubanes missing opposite vertices. ORTEPs of **5-9** can be found in Figures 3.4-3.8 and selected bond

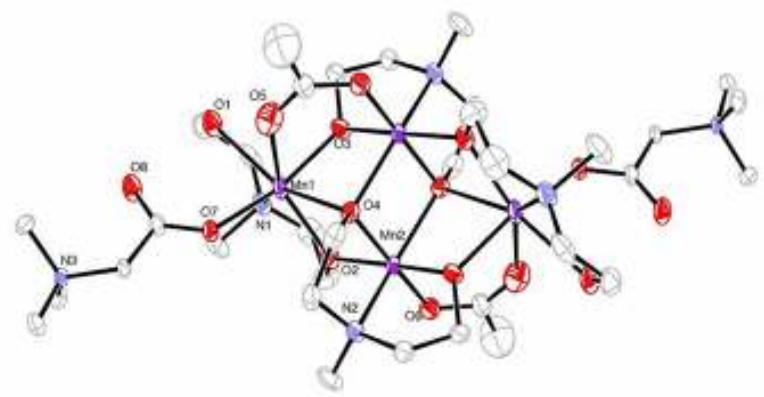

Figure 3.4. ORTEP of $[Mn_4(Bet)_2(O_2CMe)_2(mdeaH)_2(mdea)_2](BPh_4)_2$ **(5)** with BPh_4^- anions and H-atoms omitted for clarity. Thermal ellipsoids drawn at 30% probability level.

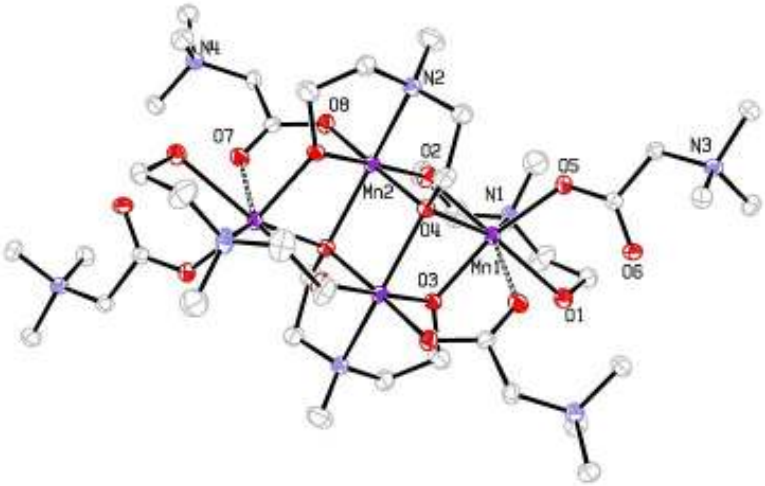

Figure 3.5. ORTEP of $[Mn_4(Bet)_4(mdeaH)_2(mdea)_2](BPh_4)_4$ **(6)** with BPh_4^- anions and H-atoms omitted for clarity. Thermal ellipsoids drawn at 30% probability level.

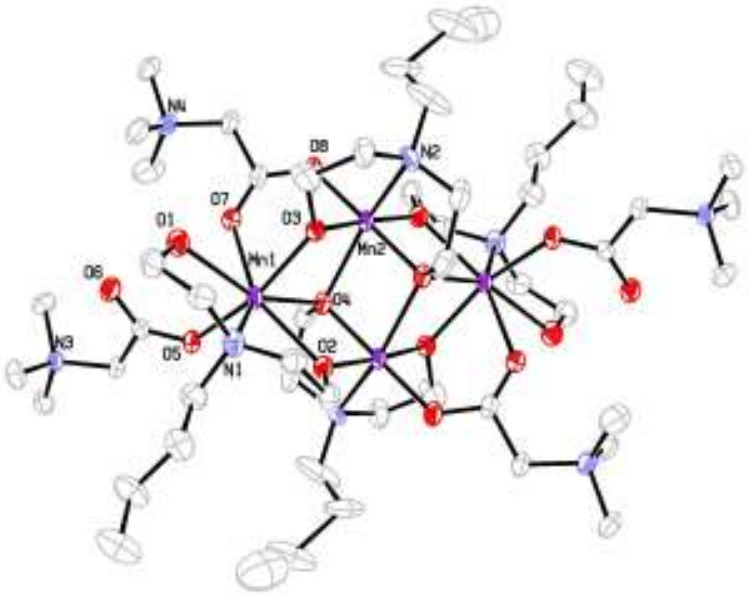

Figure 3.6. ORTEP of $[Mn_4(Bet)_4(bdeaH)_2(bdea)_2](BPh_4)_4 \cdot Et_2O \cdot 4MeOH$ **(7)** with BPh_4^- anions and H-atoms omitted for clarity. Thermal ellipsoids drawn at 30% probability level.

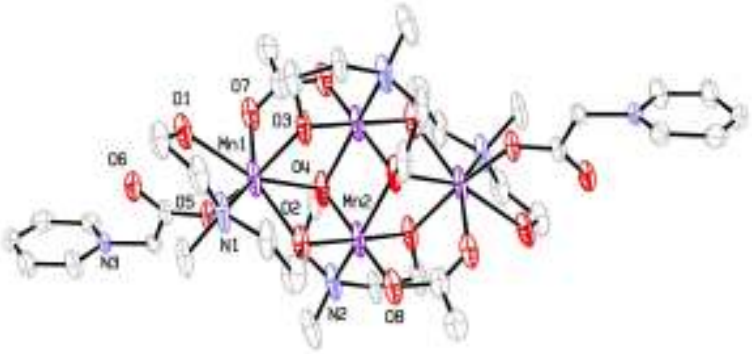

Figure 3.7. ORTEP of $[Mn_4(pyBet)_2(O_2CMe)_2(mdeaH)_2(mdea)_2](BPh_4)_2 \cdot 2MeCN$ **(8)** with BPh_4^- anions and H-atoms omitted for clarity. Thermal ellipsoids drawn at 30% probability level.

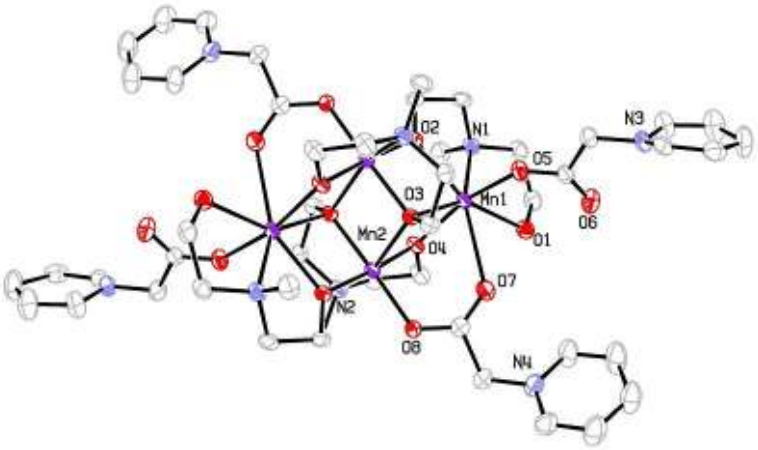

Figure 3.8. ORTEP of $[Mn_4(pyBet)_4(mdeaH)_2(mdea)_2](BPh_4)_4 \cdot 2MeCN$ **(9)** with BPh_4^- anions, H-atoms, and solvate molecules omitted for clarity. Thermal ellipsoids drawn at 30% probability level.

Table 3.6. Selected interatomic bond distances [Å] and angles [°] for $[Mn_4(Bet)_2(O_2CMe)_2(mdeaH)_2(mdea)_2](BPh_4)_2$ **(5).**

Bonds	
Mn1-O1	2.395(4)
Mn1-O2	2.203(5)
Mn1-O3	2.072(4)
Mn1-O4	2.354(4)
Mn1-O5	2.459(6)
Mn1-O7	2.131(4)
Mn1-N1	2.395(6)
Mn2-O2′	1.894(4)
Mn2-O3	1.907(4)
Mn2-O4	2.236(3)
Mn2-O4′	1.951(3)
Mn2-O6	1.908(5)
Mn2-N2	2.304(4)

Angles	
O3-Mn1-O7	158.4(2)
N2-Mn2-O4	151.9(1)
Mn1-O3-Mn2	110.9(2)
Mn1-O4-Mn2	91.1(1)
Mn1-O2-Mn2′	108.6(2)
Mn1-O4-Mn2′	101.1(1)

Table 3.7. Selected interatomic bond distances [Å] and angles [°] for $[Mn_4(Bet)_4(mdeaH)_2(mdea)_2](BPh_4)_4$ **(6)**, $[Mn_4(Bet)_4(bdeaH)_2(bdea)_2](BPh_4)_4 \cdot Et_2O \cdot 4MeOH$ **(7)**, and $[Mn_4(pyBet)_2(O_2CMe)_2(mdeaH)_2(mdea)_2]\ (BPh_4)_2 \cdot 2MeCN$ **(8)**.

	6	**7**	**8**
Mn1-O1	2.368(2)	2.308(2)	2.382(4)
Mn1-O2	2.245(2)	2.235(2)	2.276(5)
Mn1-O3	2.104(2)	2.099(1)	2.090(3)
Mn1-O4	2.291(2)	2.321(2)	2.349(3)
Mn1-O5	2.173(2)	2.124(1)	2.108(3)
Mn1-O7	2.614	2.488	2.398(5)
Mn1-N1	2.317(3)	2.347(3)	2.419(6)
Mn2-O2′	1.861(2)	1.872(2)	1.893(4)
Mn2-O3	1.894(2)	1.900(2)	1.904(3)
Mn2-O4	2.252(2)	2.280(1)	2.349(3)
Mn2-O4′	1.975(2)	1.944(2)	1.943(3)
Mn2-O8	1.954(2)	1.948(2)	1.930(5)
Mn2-N2	2.324(3)	2.350(2)	2.347(4)
O3-Mn1-O5	157.14(8)	158.07(7)	164.1(1)
N2-Mn2-O4	153.07(8)	152.74(7)	153.2(2)
Mn1-O3-Mn2	109.08(9)	109.00(8)	107.9(2)
Mn1-O4-Mn2	91.66(7)	90.17(6)	89.1(1)
Mn1-O2-Mn2′	108.6(1)	107.93(8)	107.2(2)
Mn1-O4-Mn2′	102.83(8)	102.21(7)	102.7(2)

Table 3.8. Selected interatomic bond distances [Å] and angles [°] for $[Mn_4(pyBet)_4(mdeaH)_2(mdea)_2](BPh_4)_4 \cdot 2MeCN$ **(9)**.

Bonds	
Mn1-O1	2.329(2)
Mn1-O2	2.209(2)
Mn1-O3	2.328(2)
Mn1-O4	2.082(2)
Mn1-O5	2.104(2)
Mn1-O7	2.637
Mn1-N1	2.365(3)
Mn2-O2	1.868(2)
Mn2-O3	2.255(2)
Mn2-O3′	1.959(2)
Mn2-O4′	1.906(2)
Mn2-O8	1.946(2)
Mn2-N2	2.310(2)

Angles	
O4-Mn1-O5	165.18(8)
N2-Mn2-O3	152.59(8)
Mn1-O2-Mn2	108.88(9)
Mn1-O3-Mn2	89.81(7)
Mn1-O3-Mn2′	101.25(8)
Mn1-O4-Mn2′	108.38(9)

distances and angles are listed in Tables 3.6, 3.7, and 3.8. Complexes **5**, **8**, and **9** all crystallize in the monoclinic P2(1)/c space group whereas complexes **6** and **7** crystallize in the triclinic P-1 space group. Each complex consists of only half of the molecule (two crystallographically independent Mn ions) in the asymmetric unit with the other half generated by inversion symmetry. The mixed-valent *pseudo*-dicubane core consists of two heptacoordinate Mn(II) ions (Mn1) in the "wing" positions and two hexacoordinate Mn(III) ions (Mn2) in the "body" positions.

For the distorted pentagonal pyramidal Mn(II) ions, the singly deprotonated $mdeaH^-$ (or $bdeaH^-$ for **7**) ligand is tris-chelated to the metal ion in the pentagonal plane through the central N atom, and two of the oxo atoms of the ethanol arms. The other equatorial positions are occupied by a μ_3-alkoxide of the other amine ligand and an oxygen atom of the bridging carboxylate (acetate in **5** and **8**, glycine betaine in **6** and **7**, and pyridyl betaine in **9**). A monodentate carboxylate (glycine betaine in **5-7** and pyridyl betaine in **8** and **9**) coordinates to the Mn(II) ion via a single oxygen atom in an apical position. A μ_2-alkoxide arm in the other axial coordination site completes the coordination sphere of the Mn(II) ions.

The coordination sphere of the *pseudo*-octahedral Mn(III) ions consists of an apical N-atom from the doubly deprotonated $mdea_2^-$ or $bdea_2^-$ ligand, two μ_3- and two μ_2-alkoxy arms of the amine ligands, and an oxygen atom of the bridging carboxylate ligand. In all five [Mn_4] dicubanes discussed above, the uncoordinated oxygen atom of the monodentate betaine ligand is involved in an intramolecular H-bond with the protonated ethoxy arm chelated to the wing-position Mn(II) ion. Also, the Jahn-Teller elongated axes of the Mn(III) ions are nearly parallel in all complexes due to the

inversion symmetry. Lastly, the partially-substituted complexes (**5** and **8**) contain two BPh_4^- anions per $[Mn_4]$ cationic unit whereas the fully-substituted analogs (**6**, **7**, and **9**) contain four BPh_4^- anions per $[Mn_4]$ cation.

3.3.3. Crystal Packing and Intermolecular Interactions

The unit cell of complex **5** contains two symmetry-related orientations of the $[Mn_4]$ dicubane units. However, due to the inversion symmetry, the Jahn-Teller axes are all aligned in the same direction within the unit cell (Figure 3.9). The direction of the Jahn-Teller axes is essentially taken as the direction of the easy axis in the molecule. This is an important observation for the possibility of any single-crystal measurements as will be discussed later.

Figure 3.10 shows the crystal packing of **5** from two different views (down the a-axis and down the b-axis). In both views, two-dimensional sheets of $[Mn_4]$ dicubanes in the bc plane of the unit cell separated by sheets of BPh_4^- anions (highlighted in black) can be clearly seen. The closest Mn···Mn distance within each layer is 8.7 Å whereas the closest interlayer (through the BPh_4^- anions) Mn···Mn distance is 12.4 Å. A stereo-view of the unit cell of **5** can be found in Figure 3.11 which better shows the isolation of the $[Mn_4]$ dicubane layers by the surrounding BPh_4^- counterions.

For a direct comparison, the benzoate analogs of complexes **5** and **7**, $[Mn_4(O_2CPh)_4(mdeaH)_2(mdea)_2]$[12] and $[Mn_4(O_2CPh)_4(bdeaH)_2(bdea)_2]$[13] respectively, were analyzed in terms of their crystal packing. Figure 3.12 shows the crystal packing along the b-axis in both complexes. The $[Mn_4(O_2CPh)_4(mdeaH)_2(mdea)_2]$ dicubane also forms two-dimensional sheets (this time in the ac plane) with the closest Mn···Mn

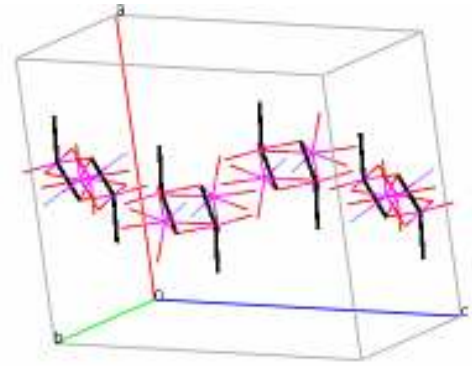

Figure 3.9. Alignment of Jahn-Teller axes in the unit cell of $[Mn_4(Bet)_2(O_2CMe)_2(mdeaH)_2(mdea)_2](BPh_4)_2$ **(5)**. Only the dicubane cores are shown with Jahn-Teller axes highlighted in black.

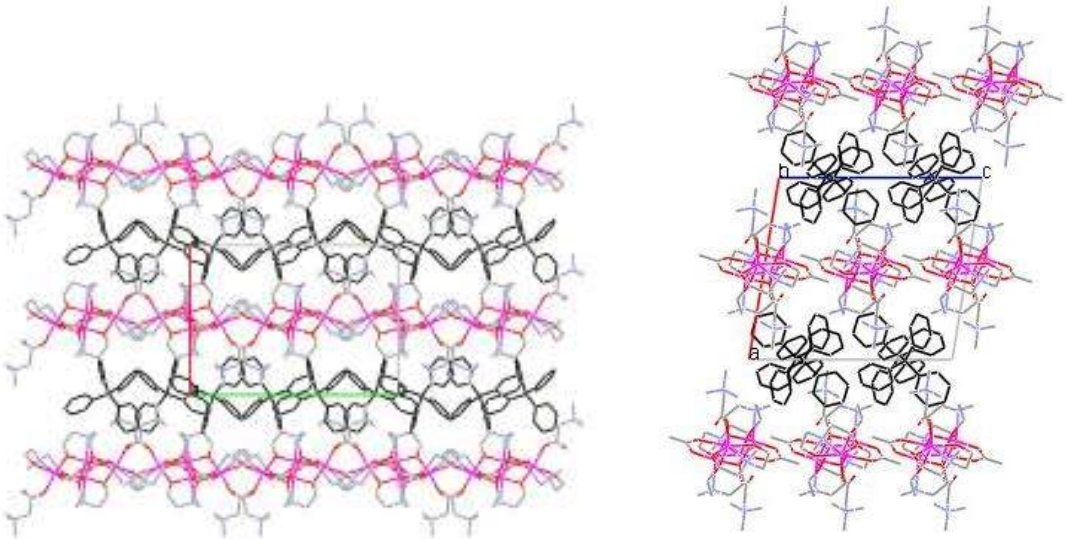

Figure 3.10. Crystal packing of $[Mn_4(Bet)_2(O_2CMe)_2(mdeaH)_2(mdea)_2](BPh_4)_2$ **(5)** as viewed down a-axis (left) and b-axis (right) with BPh_4^- anions highlighted in black.

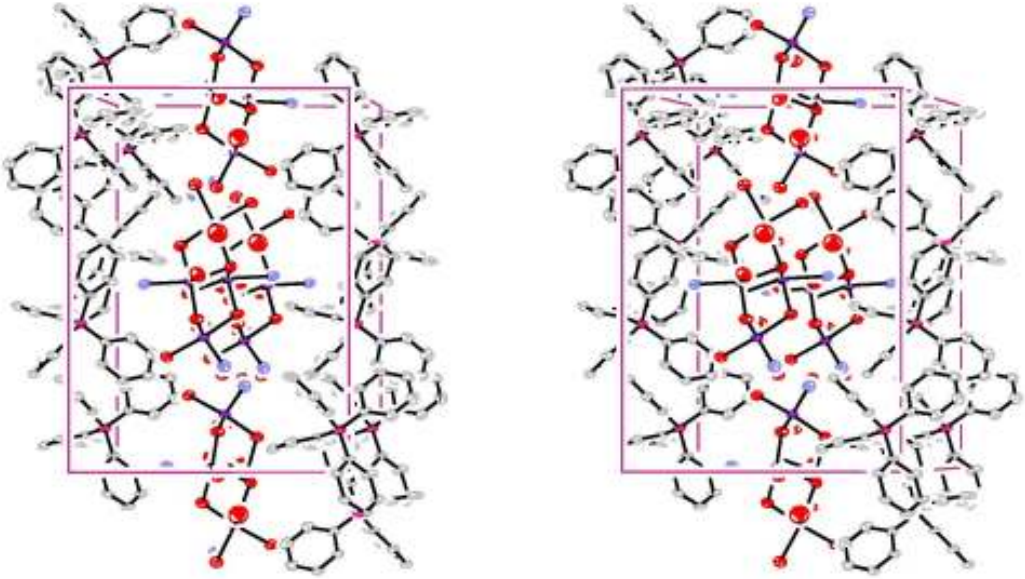

Figure 3.11. Stereo-view of the unit cell of $[Mn_4(Bet)_2(O_2CMe)_2(mdeaH)_2(mdea)_2](BPh_4)_2$ **(5)**.

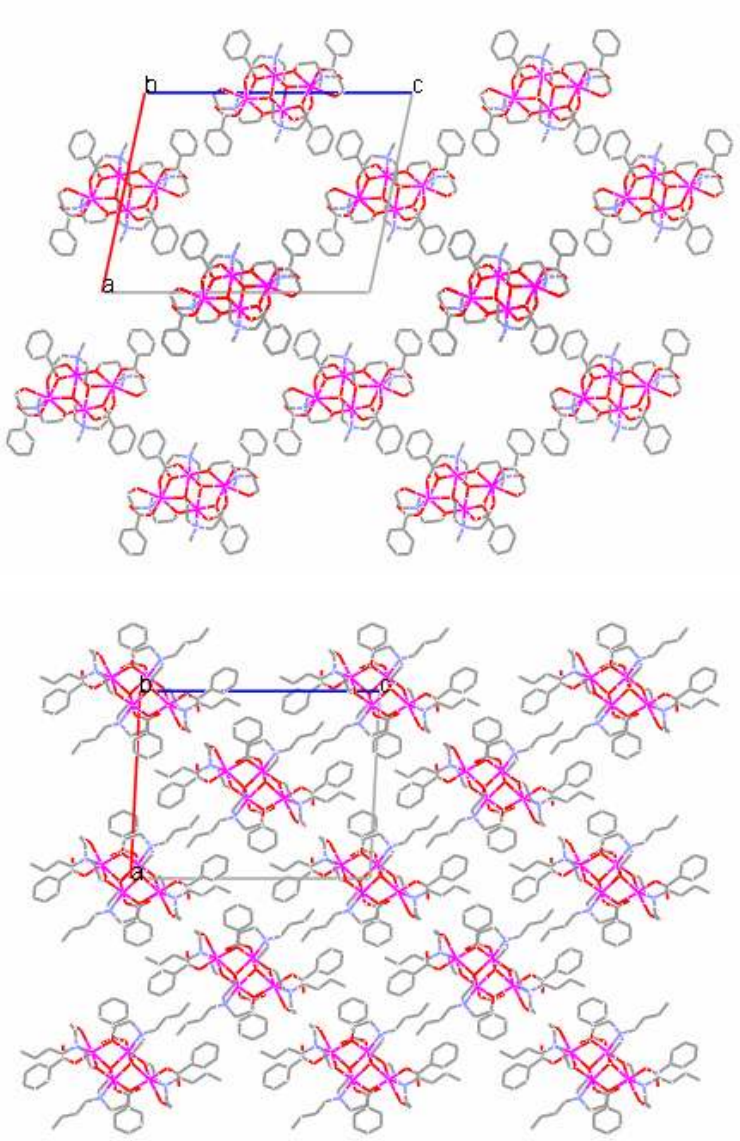

Figure 3.12. Crystal packing of $[Mn_4(O_2CPh)_4(mdeaH)_2(mdea)_2]$ (top) and $[Mn_4(O_2CPh)_4(bdeaH)_2(bdea)_2]$ (bottom) as viewed down the b-axis.

separation within these layers being ~11 Å (due to the steric bulk of the benzoate substituents). However, since this complex is neutral it does not have the added insulation of bulky counterions between the layers of [Mn_4] units. Therefore, the interlayer Mn···Mn separation for this complex is only 8.4 Å. One approach used in the past to increase these separations was to add bulky alkyl groups to the chelating amines. As can be seen in the crystal packing of [$Mn_4(O_2CPh)_4(bdeaH)_2(bdea)_2$] in the bottom portion of Figure 3.12, however, the n-butyl chains actually caused the [Mn_4] units to pack more tightly within the 2D sheets. In this complex, the closest Mn···Mn distances within the layers and between the layers are both around 8-9 Å.

Even the partial substitution of cationic betaine-type ligands on the [Mn_4] core resulted in an increase in the intermolecular Mn···Mn separation in **5**. Thus, the fully-substituted complex **6** should show even more improvement. By doubling the amount of BPh_4^- anions in the unit cell, the Mn···Mn separations are expected to increase significantly. Similarly to **5**, complex **6** is an ideal candidate for single-crystal magnetic and EPR studies since it is free of ligand disorder, has no co-crystallized solvent molecules, and all of its Jahn-Teller axes are aligned in the same direction due to a single orientation of the molecule in the unit cell (see Figure 3.13). Face-indexing of single crystals of this complex (Figure 3.13) also show that the Jahn-Teller axes essentially lie within the ab plane of the unit cell which corresponds to the (0 0 1) crystal face. Also, the Jahn-Teller axes are estimated from crystallographic data to be tilted ~43.5° from the ac plane or (0 1 0) crystal face. This will be important later for orienting a single-crystal of this complex in a magnetic field for magnetization hysteresis studies.

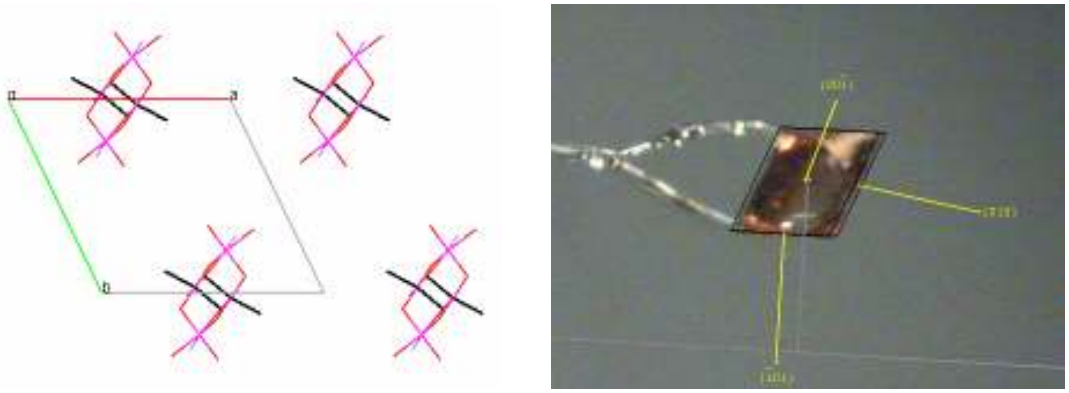

Figure 3.13. (Left) Alignment of Jahn-Teller axes in the unit cell of $[Mn_4(Bet)_4(mdeaH)_2(mdea)_2](BPh_4)_4$ **(6)**, with only the dicubane cores are shown and Jahn-Teller axes highlighted as black sticks. (Right) Face-indexed single crystal of **6** with (0 0 -1), (0 1 0), and (-1 0 1) faces labeled.

The crystal packing of **6** is shown in Figure 3.14 with the BPh_4^- anions highlighted in black. Similarly to **5**, complex **6** packs in two-dimensional sheets, this time in the ab plane of the unit cell. The increased number of bulky counterions surrounding the [Mn_4] units in **6** leads to an increase in the closest intralayer Mn···Mn distance to 10.2 Å. Also, the interlayer Mn···Mn separation is nearly 15 Å which is a significant improvement in [Mn_4] dicubanes. This well-isolated [Mn_4] dicubane core is best conveyed in the stereo plot of the unit cell of **6** and the space-filling model of the BPh_4^- anions surrounding a single molecule of **6** in Figures 3.15 and 3.16, respectively.

The intermolecular dipolar contribution to the zero-field splitting parameter, D_{dd}, can be used as an estimate of the magnitude of the dipole-dipole interaction between two metal centers. The main goal of separating the magnetic cores of SMMs in the crystal lattice is to decrease the likelihood of magnetic exchange and dipole-dipole interactions. Therefore, the increased Mn···Mn separation in **6** should lead to a decrease in the D_{dd} value compared to other [Mn_4] dicubanes. From the simple relationship first employed by Smith and Pilbrow (eqution *3.1*),[18]

$$D_{dd} = 0.65\, g^2/R^3\ , \qquad (3.1)$$

where g is the g_z value from EPR data (or from magnetic susceptibility data), R is the metal-metal distance in Å, and θ is the angle between the magnetic field and R, the dipole-dipole contribution can be calculated. Table 3.9 shows the calculations of D_{dd} when the Mn···Mn distance, R, is increased from 8 to 15 Å. As expected, by doubling

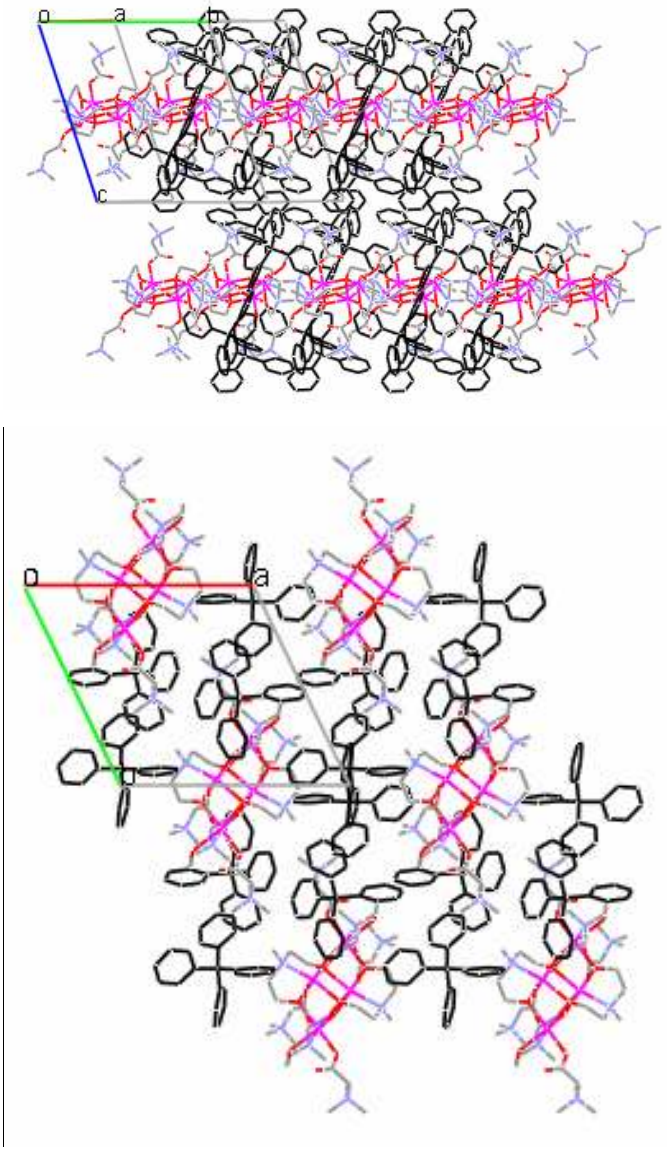

Figure 3.14. Crystal packing of $[Mn_4(Bet)_4(mdeaH)_2(mdea)_2](BPh_4)_4$ **(6)** as viewed down a*-axis (top) and c-axis (bottom). BPh_4^- anions highlighted in black.

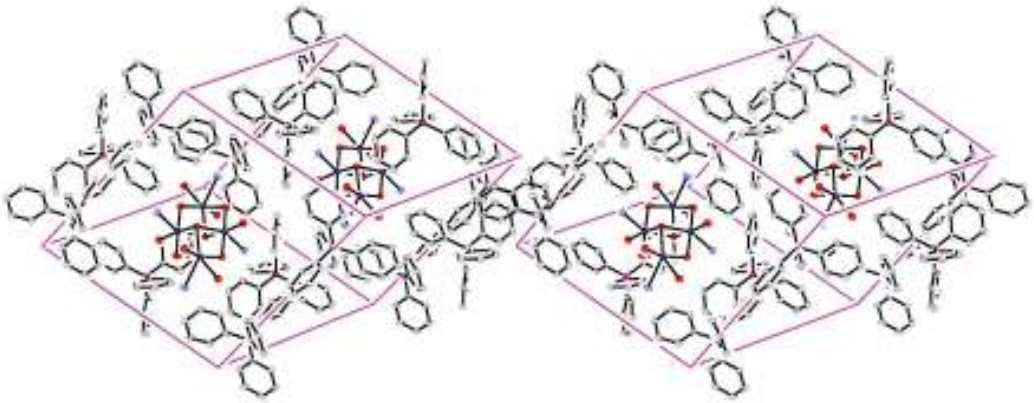

Figure 3.15. Stereo-view of the unit cell of $[Mn_4(Bet)_4(mdeaH)_2(mdea)_2]$-$(BPh_4)_4$ **(6)**.

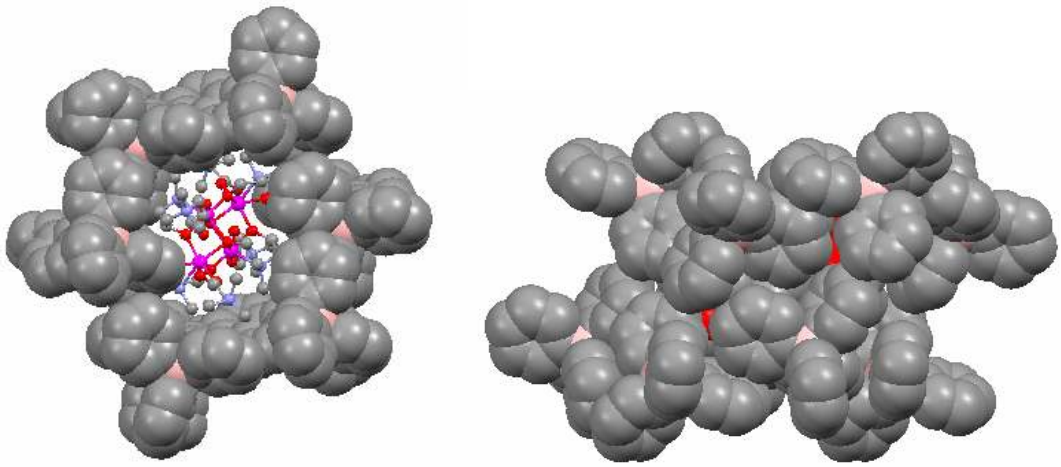

Figure 3.16. Space-filling model of BPh_4^- anions encapsulating a single $[Mn_4]$ unit of $[Mn_4(Bet)_4(mdeaH)_2(mdea)_2](BPh_4)_4$ **(6)**.

the Mn···Mn distance, the dipole-dipole interaction is estimated to decrease by an order of magnitude.

These results are promising in that we have both qualitatively and quantitatively shown that any through-space dipole-dipole interactions should be significantly reduced if not eliminated in complex **6**. Also, the likelihood of any through-bond magnetic exchange interactions between neighboring [Mn_4] units is expected to be very low. This is due to the fact that there are no close-contacts or H-bonding interactions and the tetrahedral symmetry of the BPh_4^- anions does not lend itself to significant orbital overlap with neighboring metal centers needed for magnetic exchange.

As discussed in the Introduction, the [Mn_3Zn_2] complex[19] previously synthesized in our research group also has around a 10 Å Mn···Mn separation in the crystal lattice with no solvate molecules and a single orientation of the molecule. This has been a benchmark molecule in the study of quantum tunneling of the magnetization and resulted in the sharpest EPR signals observed for any SMM.[20] Complex **6** is also of very high crystalline quality with significant intermolecular Mn···Mn separation, thus making it an ideal candidate for single-crystal magnetization hysteresis and EPR studies as will be presented later in this Chapter.

Complex **7** is the n-butyl analog of **6** which is expected to further improve upon the Mn···Mn separation due to the four BPh_4^- anions per molecule in addition to the added bulk of the n-butyl chains. Though we do see significant isolation of the [Mn_4] dicubanes in the unit cell of **7** as can be seen in the stereo-plot in Figure 3.17, the large amounts of ligand and solvent disorder in this complex prevent it from being a very

Table 3.9. Dipole-dipole contributions to the zero-field splitting parameter, D_{dd}, for given Mn···Mn distances and a *g*-value of 1.9.

R_{Mn-Mn} (Å)	D_{dd} (cm^{-1})
8	4.6×10^{-3}
10	2.3×10^{-3}
12	1.4×10^{-3}
15	7.0×10^{-4}

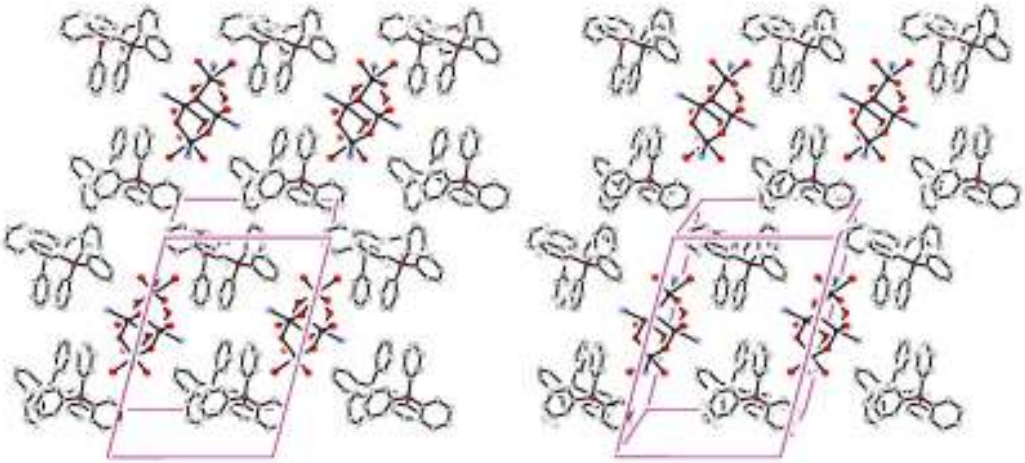

Figure 3.17. Stereo-view of the unit cell of $[Mn_4(Bet)_4(bdeaH)_2(bdea)_2](BPh_4)_4 \cdot Et_2O \cdot 4MeOH$ **(7)**.

useful complex for the purposes of this study. However, this complex is a SMM with rather enhanced properties as will be discussed in the following magnetic susceptibility analyses.

Lastly, complexes **8** and **9** exhibit very similar orientations and crystal packing as seen for their glycine betaine analogs, **5** and **6**. However, because of the co-crystallized solvent molecules and ligand disorder in these complexes, they are not as attractive for single-crystal measurements, as with complex **7**. Also, these crystal packing effects drastically affect the magnetic properties and reduce the SMM behavior of these complexes, as will be evident in the dc and ac magnetic susceptibility studies described later.

3.3.4. DC Magnetic Susceptibility

The following dc magnetic susceptibility data for complexes **5-9** indicate weak intramolecular ferromagnetic coupling between pairs of Mn ions, a non-zero ground state spin, and appreciable axial zero-field splitting typical of mixed-valent [Mn_4] dicubanes. Complex **5** exhibits a field-dependence of the molar susceptibility (collected in applied fields of 0.01, 0.1 and 1 T) at low temperatures as shown in the top portion of Figure 3.18 with the 0.01 T data reaching the highest $\chi_M T$ of 24 cm^3 mol^{-1} K at 1.8 K. The decrease in $\chi_M T_{max}$ with increasing applied dc field is most likely due to Zeeman splitting. The 0.1 T data were further analyzed and plotted separately as $\chi_M T$ *vs.* T in the bottom portion of Figure 3.18. The value of $\chi_M T$ at room temperature is ~12 cm^3 mol^{-1} K which gradually increases as the temperature is lowered from 300 to 50 K. At this point, the $\chi_M T$ rises dramatically to a final maximum value of 23.5 cm^3 mol^{-1} K before

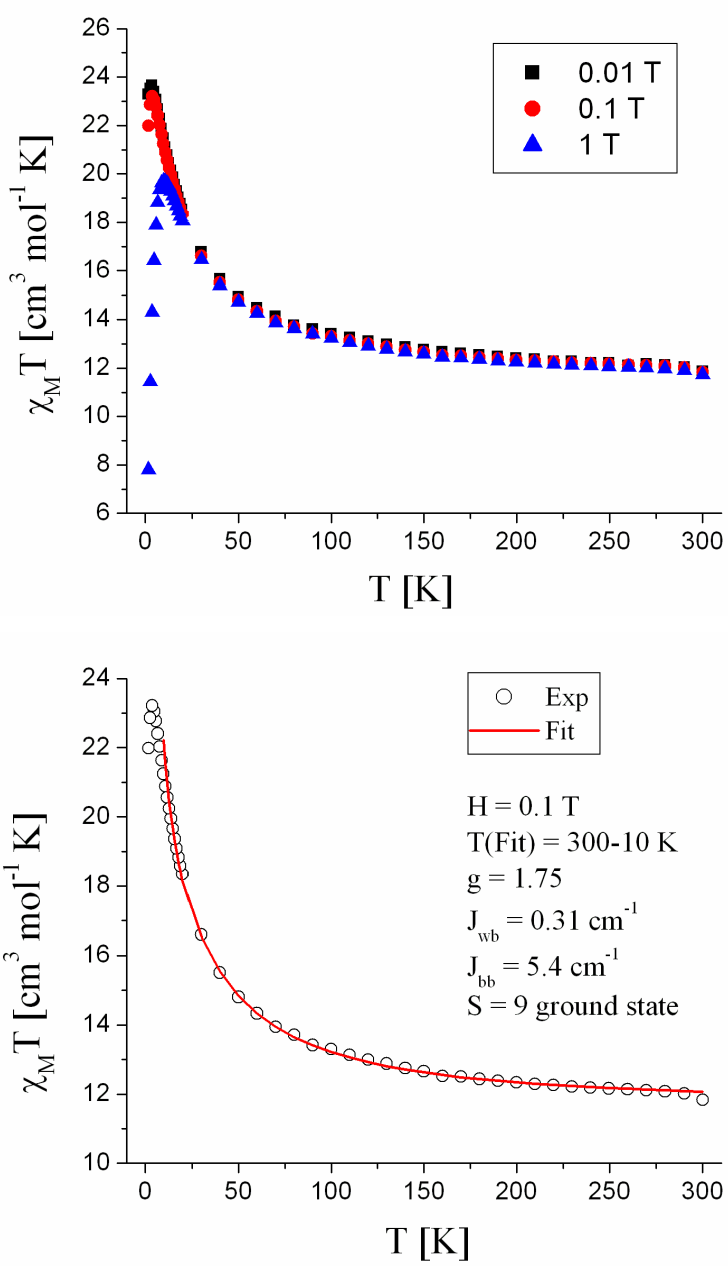

Figure 3.18. $\chi_M T$ *vs.* T at (top) various applied fields and at (bottom) 0.1 T with theoretical fit shown as solid red curve for $[Mn_4(Bet)_2(O_2CMe)_2(mdeaH)_2$-$(mdea)_2](BPh_4)_2$ **(5)**.

dropping to a final value of 22 cm^3 mol^{-1} K at 1.8 K. This characteristic $\chi_M T$ *vs. T* curve is indicative of weak intramolecular ferromagnetic coupling between the oxo-bridged Mn(III) and Mn(II) ions.

The simple two *J*-value (J_{wb} and J_{bb}) coupling scheme described in the Introduction and utilized in the fitting of ferrocene-substituted dicubanes in Chapter 2 was once again employed here followed by a least-squares fit to the Van Vleck equation. The 0.1 T $\chi_M T$ *vs. T* data were fit in the range of 300-10 K (solid red curve in Figure 3.18) to give fitting parameters of g = 1.75, J_{wb} = 0.31 cm^{-1}, and J_{bb} = 5.4 cm^{-1}. (The data are only fit below the $\chi_M T_{max}$ since this model does not account for intermolecular interactions or Zeeman effects). As expected, positive values (ferromagnetic exchange) for both J_{bb} and J_{wb} were obtained with J_{bb} being an order of magnitude larger than J_{wb}. This fit also indicates a ground state spin of S = 9 which is also typical of previously studied [Mn_4] dicubanes and expected from all ferromagnetic coupling in a [$Mn^{II}_2Mn^{III}_2$] core.[12,13,21-23] The first excited state (S = 8) is only separated from the ground state by ~2.5 cm^{-1} with nine other spin states within 10 cm^{-1} of the ground state with spins as low as S = 6.

To further validate the ground state spin and determine the magnitude of the zero-field splitting parameter, D, field-dependent magnetization measurements were also collected in applied fields of 5, 4, 3, 2, and 1 T in the 4-1.8 K temperature range (Figure 3.19). The non-superimposable isofields indicate an appreciable axial-type magnetoanistropy and the magnitude of the magnetization value at 5 T predicts a possible ground state spin of S = 6 or 7. All of the isofields were least-squares fit simultaneously to a S = 7 spin Hamiltonian (solid black curves in Figure 3.19), includ-

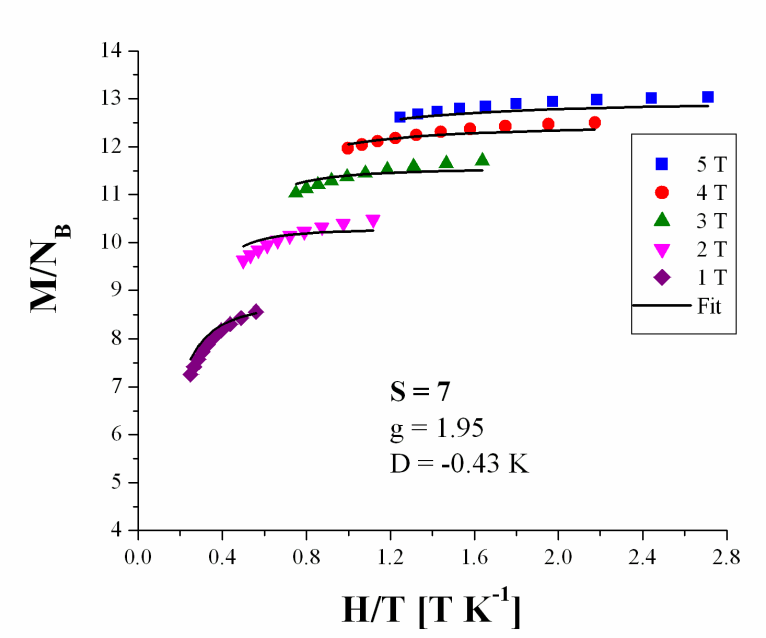

Figure 3.19. Reduced magnetization *vs. H/T* for $[Mn_4(Bet)_2(O_2CMe)_2(mdeaH)_2(mdea)_2](BPh_4)_2$ **(5)** with theoretical fits shown as solid black curves.

ing an isotropic Zeeman interaction and an axial zero-field splitting parameter, to give the parameters of g = 1.95 and a D/k_B = -0.43 cm^{-1}. Once again, this simple model assumes only a single ground state is being populated which, as indicated by the low-lying excited states in the fitting of the $\chi_M T$ *vs. T* data, is not likely the case. Also, at higher dc fields it is reasonable to assume that increased Zeeman splitting could lead to population of a ground state that may have been at a much higher energy in a lower dc field as in the 0.1 T $\chi_M T$ *vs. T* data where a S = 9 ground state was suggested.

Complex **6** exhibits very similar dc magnetic susceptibility as **5** but of much higher magnitude. Figure 3.20 shows the field-dependence of the molar susceptibility at low temperatures (top) and the 0.1 T $\chi_M T$ *vs. T* data in the temperature range of 300-1.8 K (bottom). In this complex, the $\chi_M T_{max}$ in a 0.01 T applied dc field reaches nearly 38 cm^3 mol^{-1} K with the $\chi_M T_{max}$ at 1 T reaching 30 cm^3 mol^{-1} K. For the 0.1 T data, $\chi_M T$ gradually increases as the temperature is lowered from 300 K, again indicating intramolecular ferromagnetic exchange. A maximum $\chi_M T$ value of 36 cm^3 mol^{-1} K is reached before a small drop to ~34 cm^3 mol^{-1} K at 1.8 K.

The theoretical fit for the 0.1 T $\chi_M T$ *vs. T* data in the temperature range of 300-10 K (solid red curve in Figure 3.20) gave reasonable parameters of g = 1.9, J_{wb} = 0.67 cm^{-1}, J_{bb} = 5.7 cm^{-1}. The fit suggests a S = 9 ground state with the first excited state (S = 8) separated by ~5.4 cm^{-1}. This is a better-isolated ground state than the partially-substituted analog, **5**, and only has two spin states within 10 cm^{-1} of the ground state.

Reduced magnetization measurements on **6** were also collected in applied fields of 5, 4, 3, 2, and 1 T in the 4-1.8 K temperature range and are plotted in Figure 3.21. A

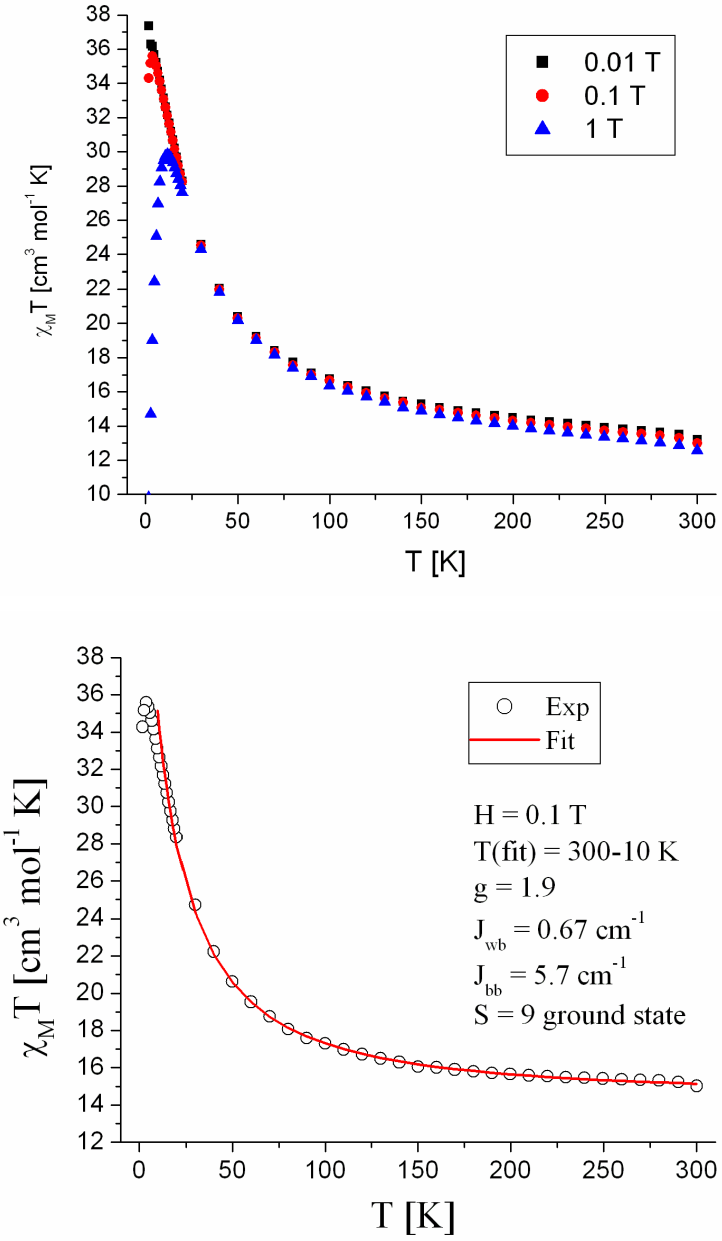

Figure 3.20. $\chi_M T$ *vs.* T at (top) various applied fields and at (bottom) 0.1 T with theoretical fit shown as solid red curve for $[Mn_4(Bet)_4(mdeaH)_2(mdea)_2](BPh_4)_4$ **(6)**.

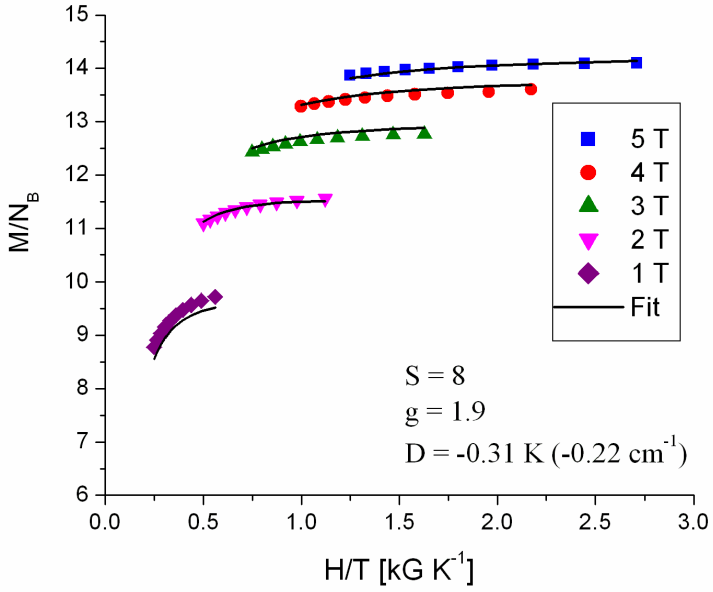

Figure 3.21. Reduced magnetization *vs. H/T* for $[Mn_4(Bet)_4(mdeaH)_2(mdea)_2](BPh_4)_4$ **(6)**, with theoretical fits shown as solid black curves.

ground state spin of S=7 or S=8 is predicted by the magnetization value at 5T (~14 μ_B). The best theoretical fits (solid curves in Figure 3.21) were found assuming a S = 8 ground state (g = 1.9, D/k_B = -0.31 K). As with complex **5**, it is not unreasonable for the reduced magnetization data to be fit to a lower spin ground state than suggested by the $\chi_M T$ data due to low-lying excited states that may be populated at higher fields. Also, the increased isolation of the ground state in **6** allows for the fitting of all fields (1-5 T) to a single spin ground state which is not always possible for [Mn_4] dicubanes as we will see for complexes **7-9** (*vide infra*).

The fully-substituted n-butyl analog, complex **7**, has an even higher $\chi_M T_{max}$ than **6**. The top portion of Figure 3.22 shows the low temperature field-dependence of $\chi_M T$ at 0.01, 0.1, and 1 T with the $\chi_M T$ reaching nearly 40 cm^3 mol^{-1} K at the lowest field. Again there is a significant amount of Zeeman effects in a 1 T field as indicated by the drop-off in $\chi_M T$ to ~10 cm^3 mol^{-1} K at 1.8 K. The bottom portion of Figure 3.22 shows 0.1 T $\chi_M T$ *vs.* T data along with the theoretical fit (solid red curve). The $\chi_M T$ rises gradually from 16 cm^3 mol^{-1} K at 300 K to ~20 cm^3 mol^{-1} K around 50 K before dramatically increasing to a maximum value of 37 cm^3 mol^{-1} K. The data were fit from 300-10 K giving parameters of g = 1.9, J_{wb} = 0.51 cm^{-1}, J_{bb} = 6.0 cm^{-1} which are very close to those determined for complex **6**. Though a S = 9 ground state was also estimated from the fit, there are four other spin states within 10 cm^{-1} of the ground state ranging from S = 6 to S = 8 with the first excited state 4 cm^{-1} above the ground state.

The reduced magnetization of **7** (plotted as M/N_B *vs.* H/T in Figure 3.23) reaches a value of ~15 μ_B at 5 T but does not saturate. This suggests a ground state spin of at

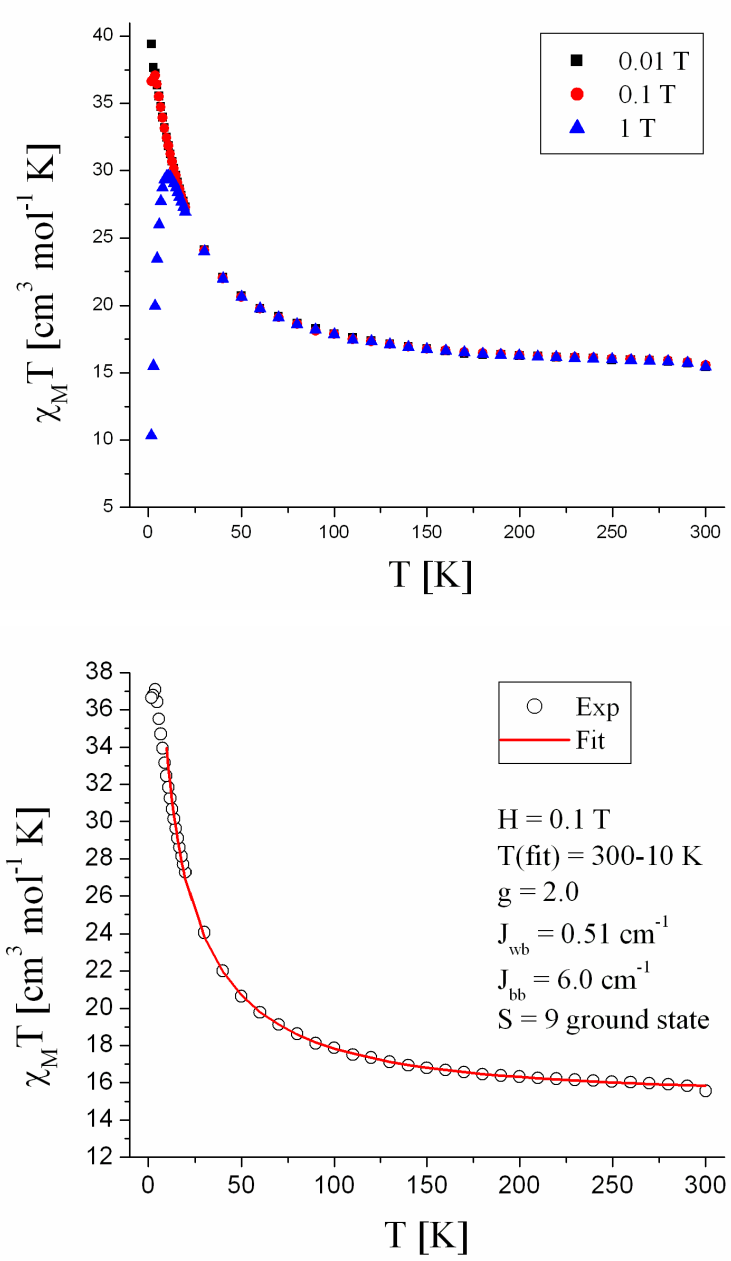

Figure 3.22. $\chi_M T$ *vs.* T at (top) various applied fields and at (bottom) 0.1 T with theoretical fit shown as solid red curve for $[Mn_4(Bet)_4(bdeaH)_2(bdea)_2](BPh_4)_4 \cdot Et_2O \cdot 4MeOH$ **(7)**.

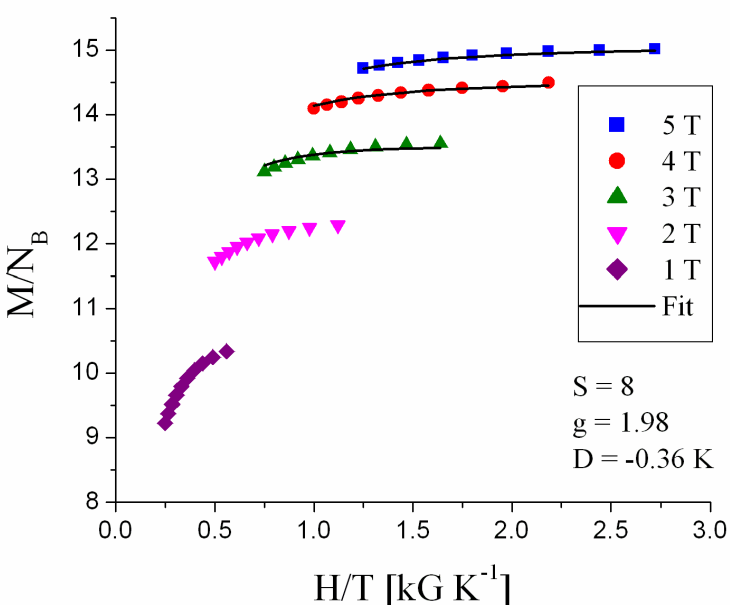

Figure 3.23. Reduced magnetization *vs. H/T* for $[Mn_4(Bet)_4(bdeaH)_2(bdea)_2](BPh_4)_4 \cdot Et_2O \cdot 4MeOH$ **(7)** with theoretical fits shown as solid black curves.

least S =7 or 8 but yet the data cannot be easily fit to either of these spins. The best fit (shown as black solid curves in Figure 3.23) was found for a S = 8 ground state with g = 1.98 and D/k_B = -0.36 K. Only the highest fields (5, 4, and 3 T) were able to be fit to these parameters due to the poorly-isolated ground state at lower fields as indicated by the $\chi_M T$ *vs.* T fit.

The partially- and fully-substituted pyridyl betaine analogs, **8** and **9**, show similar magnetic properties as their glycine betaine analogs. However, these complexes have very poorly-isolated ground states, most likely due to a significant amount of solvent and ligand disorder which is not present in complexes **5** and **6**. The same field-dependence of the $\chi_M T$ at low temperatures is seen in Figure 3.24 with the 0.01 T data reaching maximum values of 26 and 34 cm^3 mol^{-1} K for **8** and **9**, respectively. Once again there are significant field effects as indicated by the dramatic drop in $\chi_M T$ at low temperatures as the field is increased.

Figure 3.25 contains the 0.1 T $\chi_M T$ *vs.* T data for **8** and **9** which show a rise in $\chi_M T$ as the temperature is lowered from 300 K to 1.8 K, characteristic of ferromagnetic coupling. The $\chi_M T$ reaches maximum values of 25 cm^3 mol-1 K and 31 cm^3 mol^{-1} K for **8** and **9**, respectively. Theoretical fits (solid red curves in Figure 3.25) of the data from 300-10 K give parameters of g = 2.0, J_{wb} = 0.17 cm^{-1}, J_{bb} = 5.9 cm^{-1} for **8** and g = 1.8, J_{wb} = 0.35 cm^{-1}, J_{bb} = 4.6 cm^{-1} for **9**. In both cases, a S = 9 ground state was suggested but with very closely lying excited states. For **8**, the first excited state (S = 8) is located only 1.3 cm^{-1} from the ground state. Furthermore, there are 25 spin states within 10 cm^{-1} of the ground state ranging in spin from S = 2 to S = 9. For **9**, the S = 8 first excited state is

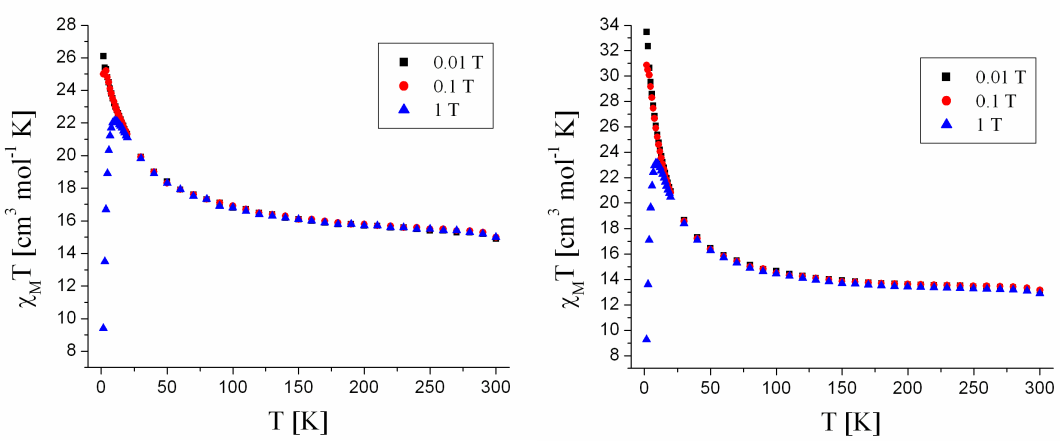

Figure 3.24. Field-dependence of $\chi_M T$ *vs.* T for $[Mn_4(pyBet)_2(O_2CMe)_2(mdeaH)_2(mdea)_2](BPh_4)_2 \cdot 2MeCN$ (**8**, left) and $[Mn_4(pyBet)_4(mdeaH)_2(mdea)_2](BPh_4)_4 \cdot 2MeCN$ (**9,** right).

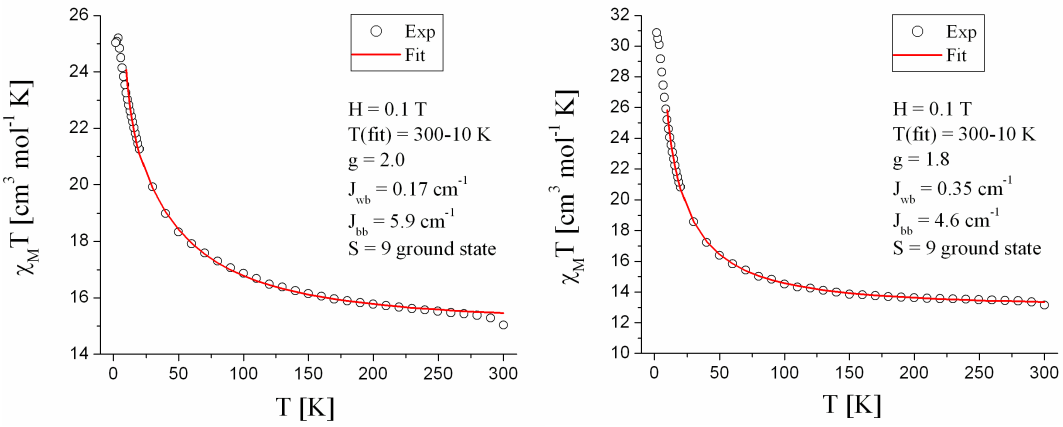

Figure 3.25. $\chi_M T$ *vs.* T in applied field of 0.1 T for $[Mn_4(pyBet)_2(O_2CMe)_2(mdeaH)_2(mdea)_2](BPh_4)_2 \cdot 2MeCN$ (**8**, left) and $[Mn_4(pyBet)_4(mdeaH)_2(mdea)_2](BPh_4)_4 \cdot 2MeCN$ (**9,** right) with theoretical fits shown as solid red curves.

~2.8 cm^{-1} above the ground state with only 7 spin states (S = 6 to S = 9) within 10 cm^{-1} of the ground state. This close energy spacing of spin states is more in line with the ferrocene-substituted [Mn_4] dicubanes discussed in Chapter 2 than the analogous glycine betaine [Mn_4] complexes in this chapter.

The many low-lying excited states in **8** and **9** are also clearly evident in the fitting of the reduced magnetization data as shown in Figure 3.26. Though the magnetization does not saturate at 5 T, the spacing of the isofields clearly indicates appreciable zero-field splitting, particularly in complex **8**. Similar to complex 7, only the three highest fields (5, 4, and 3 T) were reasonably fit to a single spin ground state due to the closely spaced excited states. Both complexes were best fit to a S = 7 spin Hamiltonian with g = 1.99 and D/k_B = -0.68 K for **8** and g = 1.96 and D/k_B = -0.38 K for **9**. It is worth noting here that surprisingly the partially-substituted dicubanes 5 and 8 have the largest axial anisotropy terms. In fact, the D-value for complex **8** is nearly double that of its fully-substituted analog, **9**.

In summary, the $\chi_M T$ *vs.* T data for **5-9** suggests weak intramolecular ferromagnetic coupling with positive value for both J_{wb} and J_{bb} and a S = 9 ground state. However, multiple excited states lying very close in energy to the ground state leads to difficulties in fitting the reduced magnetization data which relies upon the population of a single ground state spin. Reduced magnetization for all five complexes were fit to either S = 7 or S = 8 ground states which are often close in energy to the S = 9 ground state determined from the $\chi_M T$ data. Table 3.10 summarizes the low-lying excited states present in each complex as determined from the fitting of the $\chi_M T$ *vs.* T data. It is clear

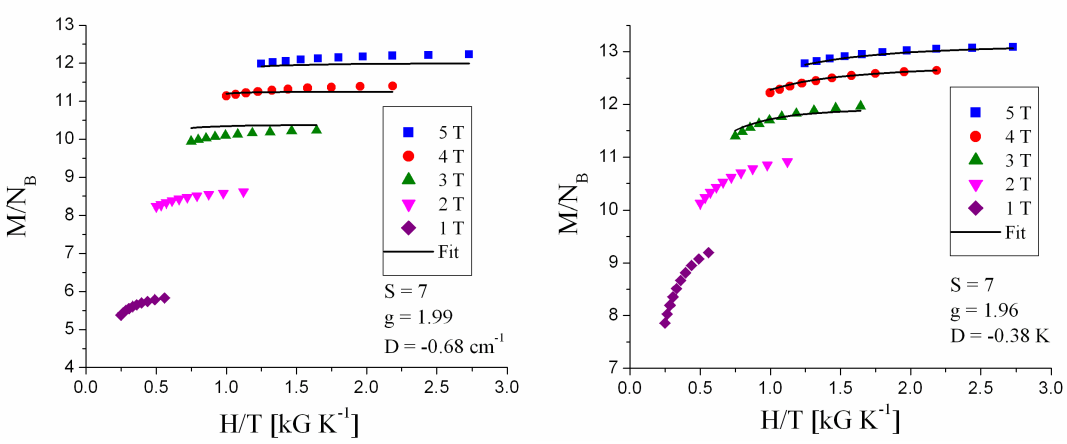

Figure 3.26. Reduced magnetization *vs. H/T* for $[Mn_4(pyBet)_2(O_2CMe)_2(mdeaH)_2(mdea)_2](BPh_4)_2 \cdot 2MeCN$ (**8**, left) and $[Mn_4(pyBet)_4(mdeaH)_2(mdea)_2](BPh_4)_4 \cdot 2MeCN$ (**9,** right) with theoretical fits shown as solid black curves.

Table 3.10. Summary of low-lying spin states from fitting of $\chi_M T$ *vs. T* data for **5-9**.

Complex	Energy to 1st excited state [cm^{-1}]	Number of spin states within 10 cm^{-1} of ground state	Low-lying spin states
5	2.5	10	$S = 5$ to $S = 9$
6	5.4	3	$S = 7$ to $S = 9$
7	4.0	5	$S = 6$ to $S = 9$
8	1.3	25	$S = 2$ to $S = 9$
9	2.8	7	$S = 6$ to $S = 9$

from this table that the fully-substituted complex **6** has the most well-isolated ground state while the partially-substituted [Mn_4] dicubanes, **5** and **8**, have very poorly-isolated ground states. This explains why the reduced magnetization fit of complex **6** is the most consistent with its $\chi_M T$ *vs. T* data while the closely-spaced spin states of **8** and **9** prevent reasonable and consistent fits using our simple model. This correlation between low-lying excited states and enhancement of magnetic properties will be seen again in the following ac magnetic susceptibility studies.

Since the fully-substituted glycine betaine complex, **6**, shows reasonable fits of the $\chi_M T$ *vs. T* and reduced magnetization data and the most well-isolated ground state, the dc susceptibility data for this compound were also analyzed via a full Hamiltonian matrix diagonalization approach as described in the Introduction Chapter. Here, all of the data from the $\chi_M T$ and M/N_B studies can be fit simultaneously to the single-ion spin Hamiltonian which includes terms for isotropic exchange, both axial and rhombic zero-field splitting, and Zeeman interactions (see equations *1.8-1.12*). The inversion symmetry of **6** precludes and Dzyaloshinsky-Moriya interactions thus it is not included in this study. Two different isotropic exchange models were used for this analysis: one is the same two *J*-value model (J_{bb} and J_{wb}) used in the HDVV fitting the $\chi_M T$ *vs. T* data (*vide supra*) while the other employs three *J*-values based on the symmetry of the molecule where an additional Mn(III)-Mn(II) interaction, J_{wb}', is accounted for. Both coupling schemes are shown in Figure 3.27. The Jahn-Teller axes of the Mn(III) ions were assumed to be parallel to one another due to the center of inversion.

Figure 3.28 shows dc susceptibility for **6** collected in applied fields of 1-5 T and in the temperature range of 330-1.8 K least-squares fit (solid black curves) to the spin

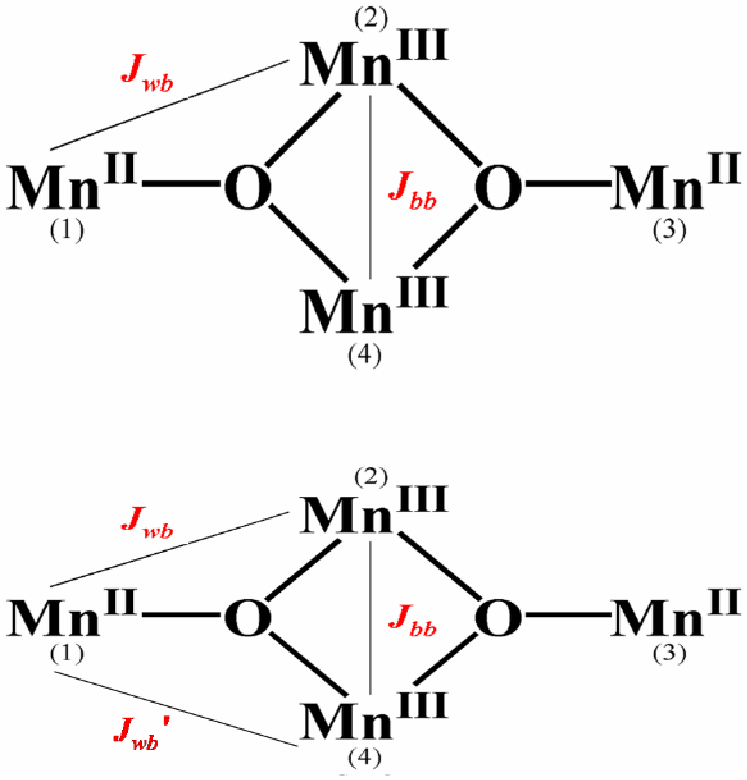

Figure 3.27. (Top) Two *J*-value and (bottom) three *J*-value coupling schemes for complex $[Mn_4(Bet)_4(mdeaH)_2(mdea)_2](BPh_4)_4$ **(6)**.

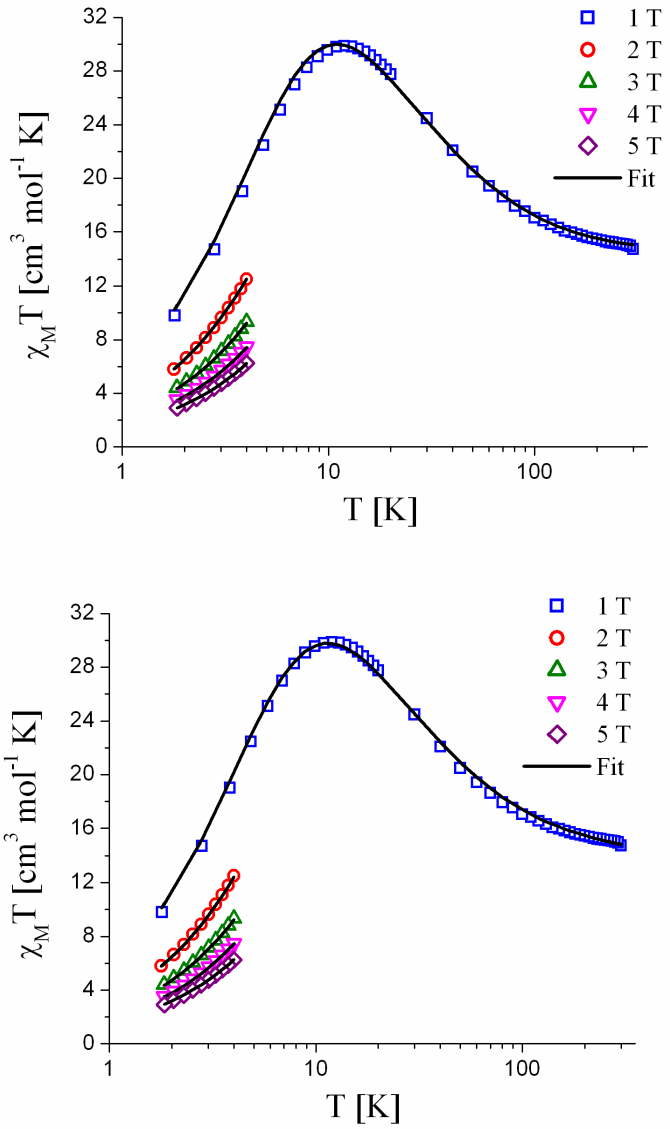

Figure 3.28. Dc magnetic susceptibility for $[Mn_4(Bet)_4(mdeaH)_2(mdea)_2](BPh_4)_4$ **(6)**, in applied fields of 1-5 T and a temperature range of 300-1.8 K. Least-squares fit to the spin Hamiltonian (by full-matrix diagonalization) represented by solid black curves for two J-value model (top) and three J-value model (bottom).

Hamiltonian employing the two *J*-value and three *J*-value models. In both cases, the single-ion anisotropy (d_{ion}) for the Mn(II) ions was assumed to be zero and the *g*-value was fixed at 1.9. The best fit with the two *J*-value model gave optimized parameters of $S = 9$, d = -9.5 K (-6.6 cm^{-1}), J_{bb} = 9.1 K (6.3 cm^{-1}), and J_{wb} = 1.1 K (0.8 cm^{-1}). The rhombic zfs parameter, *E*, was fixed at zero for the two *J*-value model and a temperature independent paramagnetism (TIP) was included and optimized to a final value of 1.6 x 10^{-3} cgsu.

The data in Figure 1.28 also fit nicely to the three *J*-value model with final parameters of S = 9, d = -9.1 K (-6.3 cm^{-1}), J_{bb} = 8.1 K (5.6 cm^{-1}), and J_{wb} = 5.0 K (3.5 cm^{-1}), J_{wb}' = -1.48 K (-1.0 cm^{-1}), E = 2.97 K, and TIP = 3.15 x 10^{-4} cgsu with the most notable difference being the Mn(III)-Mn(II) interactions as expected. The single J_{wb} interaction in the two *J*-value model is small and ferromagnetic in nature while the J_{wb} interaction in the three *J*-value model consists of a larger ferromagnetic J_{wb} and a small antiferromagnetic J_{wb}' (roughly the same magnitude as the J_{wb} interaction in the two *J*-value fit). Both fits, however, suggest a $S = 9$ ground sate and dominant ferromagnetic exchange between the Mn(III) ions which corroborates the results of the HDVV fits of the $\chi_M T$ *vs. T* data which did not account for zfs and Zeeman interactions. The single-ion anisotropy for the Mn(III) ions in **6** is rather large at -9.5 K (or 6.6 cm^{-1}). Typical *d*-values for high-spin Mn(III) ions obtained from HFEPR techniques range from -1 to -5 cm^{-1}.[24]

The zero-field eigenvalue spectrum of **6** for the parameters determined from the two J-value fit are shown in Figure 3.29. As suggested by the earlier fits of the $\chi_M T$ and reduced magnetization data, complex **6** possess very low-lying excited states. Though

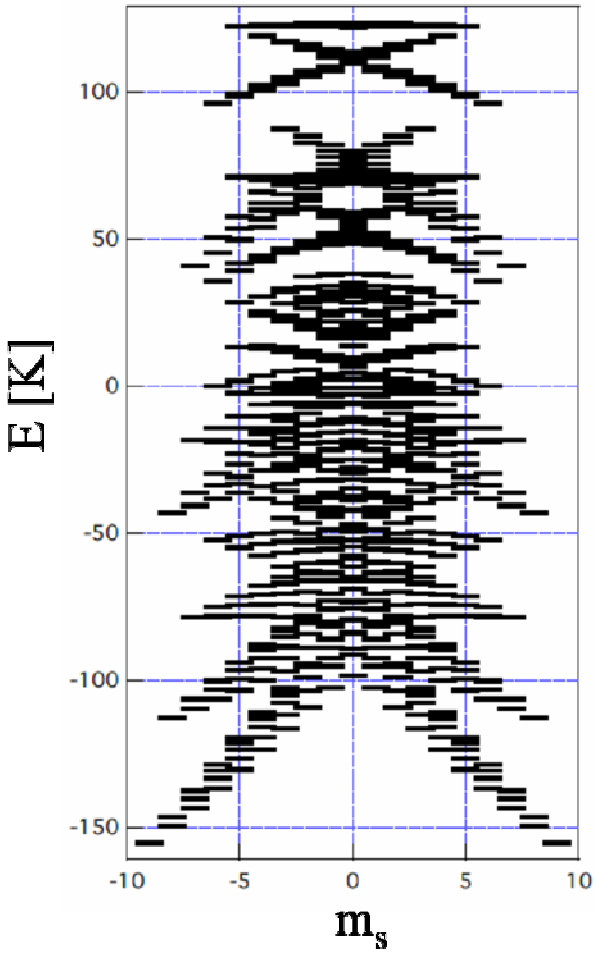

Figure 3.29. Zero-field eigenvalue spectrum of $[Mn_4(Bet)_4(mdeaH)_2(mdea)_2](BPh_4)_4$ **(6)**, for parameters from two J-value fit as discussed in the text.

slightly better isolated than in the other betaine-substituted [Mn_4] complexes, the S = 9 ground state of **6** is only slightly lower in energy than the first excited state (<10 K). In Figure 3.29 it is clear that the lowest lying S = 8 and S = 7 spin manifolds are nested quite close in energy to the S = 9 ground state. This supports the findings of the earlier reduced magnetization fits which suggested ground state spins closer to S = 7 or 8 for this family of SMMs. These excited states are very likely to be populated at higher magnetic fields based on their proximity to the S = 9 ground state in the eigenvalue spectrum, an issue that was not accounted for in the simple reduced magnetization fits.

It is difficult to estimate the axial anisotropy, D, of complex **6** from the single-ion anisotropy, d, for the high-spin Mn(III) ions determined in the above mentioned full matrix diagonalization fits. Projection of the single-ion value on a giant spin via the classical vector model gives a value of ~25 K for each Mn(III) ion, which seems to be somewhat overestimated in comparison to that obtained under the strong-coupling approximation with the Wigner-Eckart theorem.[25] However, quantum mechanical treatment of this projection reduces the overall barrier height to ~30 K for the complex which is much more reasonable.

3.3.5. AC Magnetic Susceptibility

In order to determine a more accurate description of the ground state spin as well as identify a potential energy barrier to the reversal of magnetization, ac magnetic susceptibility studies were also conducted. The data were collected in an oscillating ac field (0.01-10 kHz) from 5- 1.8 K and in the absence of an applied dc field. All five

complexes show a frequency-dependent out-of-phase signal in the ac susceptibility, indicative of SMM behavior.

The in-phase (χ_M') and out-of-phase (χ_M'') ac susceptibility for **5** in an oscillating field of 0.01-1 kHz is shown in Figure 3.30. The out-of-phase signal accounts for ~25 % of the in-phase signal and begins to emerge around 3.5 K. Unfortunately, the peak maxima for the out-of-phase signals are not visible above 1.8 K at these frequencies. In order to see these maxima, data were also collected in an oscillating field of 0.1-10 kHz as shown in Figure 3.31. The high-frequency data now starts to shown an out-of-phase signal (~37 % of the in-phase signal) above 4 K which allows for the peak positions to be located and fit to the Arrhenius equation, $\tau = \tau_0 e^{-Ea(kT)}$. A plot of $ln(\tau)$ *vs.* $1/T$ (Figure 3.32) gives a linear correlation from which the activation energy to reversal of the magnetization, E_a, was calculated and found to be 19.8 K. This value is in good agreement with the theoretical barrier, $|DS_z^2|$, of 21 K calculated from the parameters $S = 7$ and $D = -0.43$ K, as obtained from the reduced magnetization fitting of **5** discussed in the previous section. However, because a consistent ground state spin could not be determined from dc susceptibility fits, the theoretical barrier is likely much higher (if $S = 8$ or 9)

The ac susceptibility for **6** in an oscillating field of 0.01-1 kHz is shown in Figure 3.33. The in-phase susceptibility reaches a maximum of nearly 20 $cm^3\ mol^{-1}$ at 10 Hz which gradually drops off to ~12 $cm^3\ mol^{-1}$ as the frequency of the oscillating field is increased to 1000 Hz. This decrease in susceptibility is accompanied by the growth of a significant frequency-dependent out-of-phase signal which accounts for ~35 % of the in-phase signal. The peak maxima for the four highest frequencies (1000, 750,

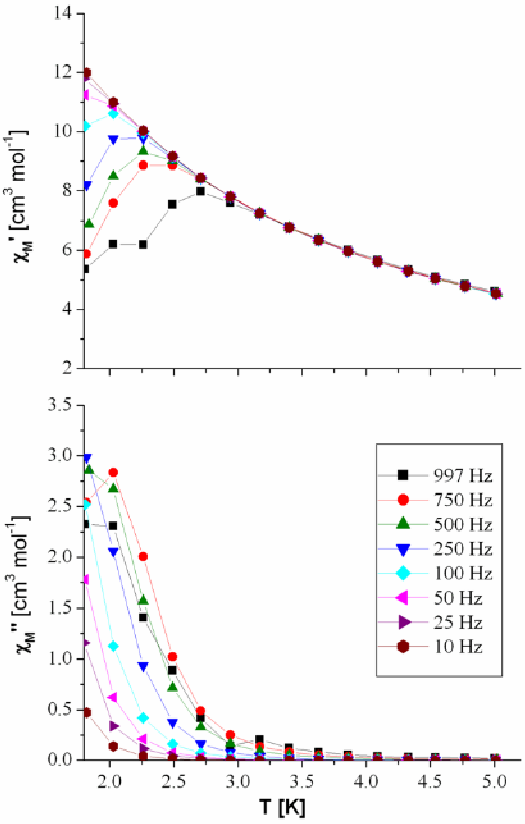

Figure 3.30. In-phase (χ_M') and out-of-phase (χ_M'') ac susceptibility for $[Mn_4(Bet)_2(O_2CMe)_2(mdeaH)_2(mdea)_2](BPh_4)_2$ **(5)** in an oscillating field up to 1 kHz.

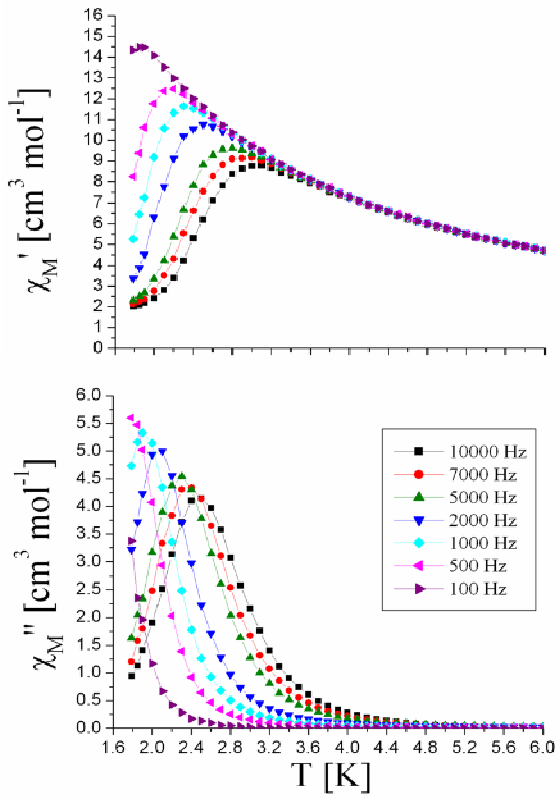

Figure 3.31. In-phase (χ_M') and out-of-phase (χ_M'') ac susceptibility for $[Mn_4(Bet)_2(O_2CMe)_2(mdeaH)_2(mdea)_2](BPh_4)_2$ **(5)** in an oscillating field up to 10 kHz.

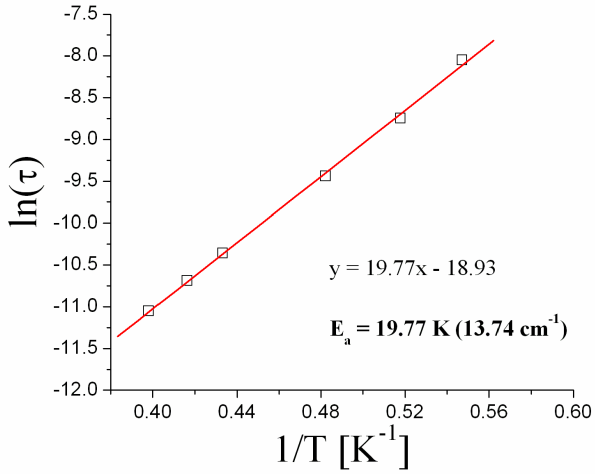

Figure 3.32. Arrhenius plot of high-frequency ac susceptibility for **5**.

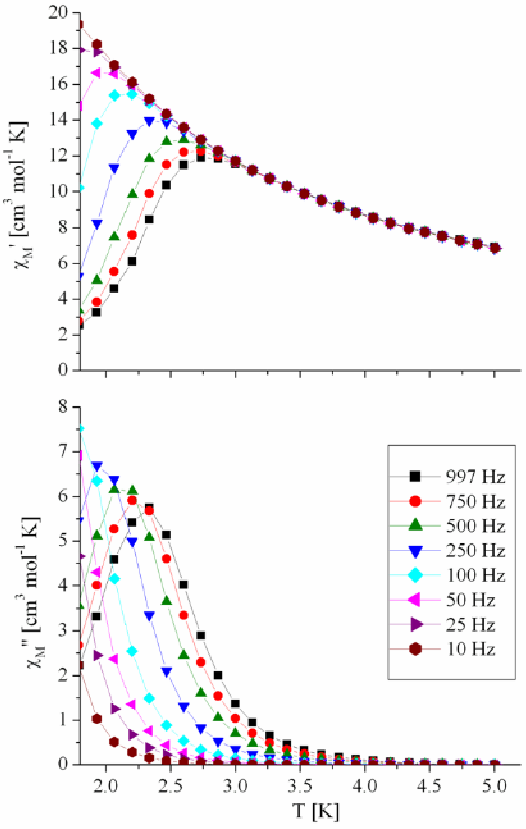

Figure 3.33. In-phase (χ_M') and out-of-phase (χ_M'') ac susceptibility for $[Mn_4(Bet)_4(mdeaH)_2(mdea)_2](BPh_4)_4$ **(6)** in an oscillating field up to 1 kHz.

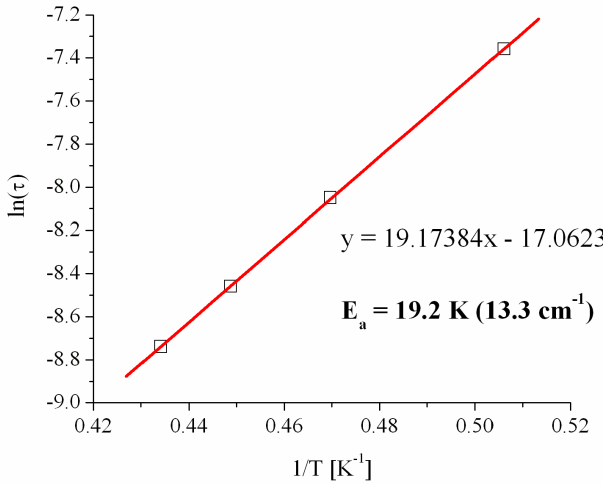

Figure 3.34. Arrhenius plot of low-frequency ac susceptibility for **6**.

500, and 250 Hz) are observed above 1.8 K and are plotted as *ln(τ) vs. 1/T* in Figure 3.34. The activation energy extracted from this Arrhenius plot is 19.2 K which is nearly identical to the barrier found in **5**. Also, with an estimated barrier height of ~30 K from the full-matrix diagonalization fits of the dc susceptibility for **6**, the lower experimental activation energy calculated here suggests that quantum tunneling may be a significant pathway for magnetization relaxation in this complex. Magnetization hysteresis measurements were performed on single crystals of **6** in order to confirm this hypothesis, the results of which are presented later in this chapter.

Ac measurements up to 10 kHz were collected for **6** and are shown in Figure 3.35. Here, the out-of-phase signal accounts for 42% of the in-phase signal (which reaches a maximum value of 20 cm^3 mol^{-1} at 10 Hz) and begins to emerge around 5.2 K. This allows for all of the frequencies above 100 Hz to be plotted in an Arrhenius manner as their peak positions can be easily observed above 1.8 K. The linear Arrhenius plot (Figure 3.36) gives an E_a value of 20.5 K which again agrees with the value calculated from the low-frequency data for **6**.

The ac magnetic susceptibility for **7** in an oscillating field of 0.01-1 kHz is shown in Figure 3.37. Complex **7** shows a beautiful frequency-dependent out-of-phase signal in the ac susceptibility at frequencies as low as 100 Hz so there was little need to measure this complex at frequencies higher than 1000 Hz. The out-of-phase signal which is ~38% of the maximum in-phase signal (24 cm^3 mol^{-1}) emerges around 4 K. Peak maxima are observed at frequencies of 1000, 750, 500, 250, and 100 Hz and plotted as *ln(τ) vs. 1/T* in Figure 3.38. Using the Arrhenius equation, the energy required

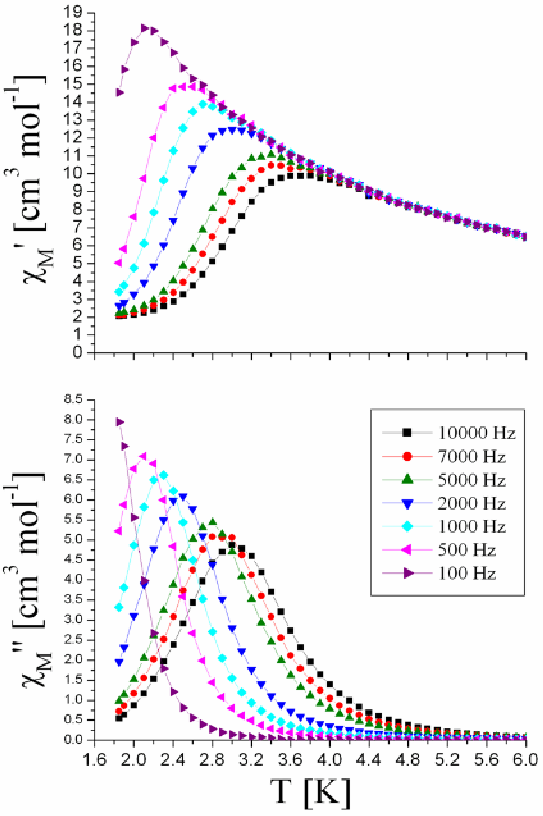

Figure 3.35. In-phase (χ_M') and out-of-phase (χ_M'') ac susceptibility for [Mn_4-$(Bet)_4(mdeaH)_2(mdea)_2$]$(BPh_4)_4$ **(6)** in an oscillating field up to 10 kHz.

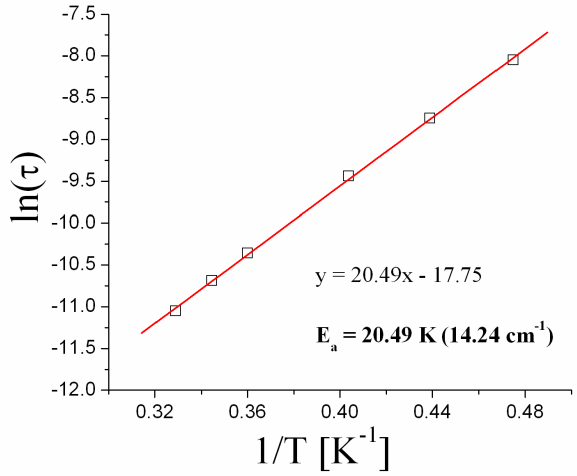

Figure 3.36. Arrhenius plot of high-frequency ac susceptibility for **6**.

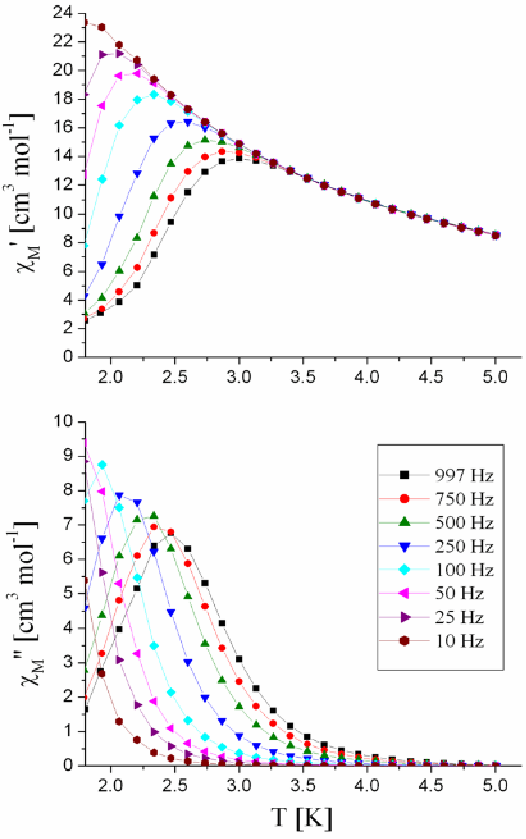

Figure 3.37. In-phase (χ_M') and out-of-phase (χ_M'') ac susceptibility for $[Mn_4(Bet)_4(bdeaH)_2(bdea)_2](BPh_4)_4 \cdot Et_2O \cdot 4MeOH$ **(7)**.

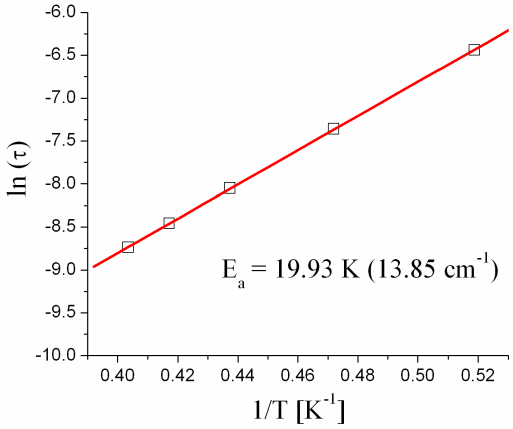

Figure 3.38. Arrhenius plot of out-of-phase ac susceptibility for **7**.

for reversal of the magnetization, E_a, was found to be 19.9 K which, as expected, is very close to the values obtained for **5** and **6**. The experimental barrier height for **7** is slightly lower than the theoretical barrier height, $|DS_z^2|$, of 23 K calculated for $S = 8$ and $D = -0.36$ K, again suggesting quantum tunneling of the magnetization.

As expected from the dc magnetic susceptibility results and the close spacing of energy states in the pyridyl betaine complexes, the ac magnetic susceptibility of **8** and **9** is mediocre compared to that of their glycine betaine analogs (*vide supra*). The ac susceptibility in an oscillating field of 0.01-1 kHz is shown for both **8** and **9** in Figure 3.39. In both complexes, there is definitely a frequency-dependent out-of-phase signal in the ac susceptibility, indicating SMM-like behavior. This signal accounts for 12% and 14% of the in-phase ac susceptibility for **8** and **9**, respectively. However, the out-of-phase signal does not emerge until the temperature is lowered to 3 K therefore no peak positions can be determined above 1.8 K.

In order to observe the peak maxima of the out-of-phase signals, the measurements would need to be made at lower temperatures or higher frequencies of the ac field. Since 1.8 K is already the lower temperature limit of our instrumentation, complexes **8** and **9** were measured again in an ac field oscillating at frequencies of 0.1-10 kHz. The higher frequency ac susceptibility measurements are plotted in Figure 3.40 where the out-of-phase signal now accounts for 18% and 20% of the in-phase signal for **8** and **9**, respectively. However, even at higher frequencies, no peak maxima for the out-of-phase signal are observed above 1.8 K thus the activation energy could not be determined from the ac susceptibility of complexes **8** and **9**.

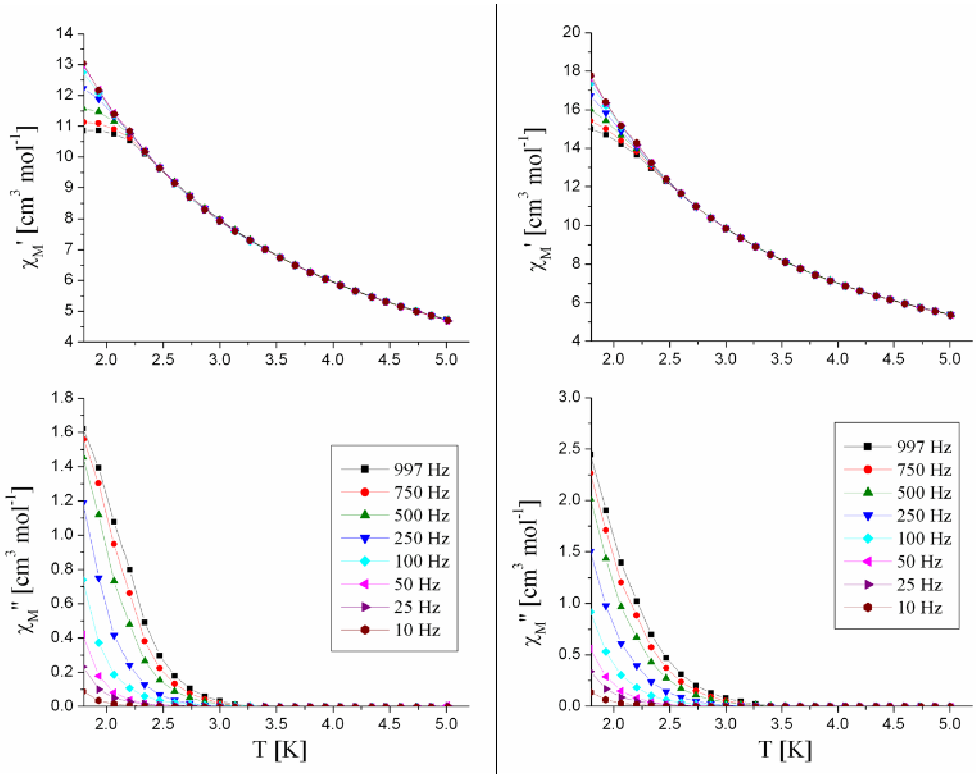

Figure 3.39. In-phase (χ_M') and out-of-phase (χ_M'') ac susceptibility for $[Mn_4(pyBet)_2\text{-}(O_2CMe)_2(mdeaH)_2(mdea)_2](BPh_4)_2 \cdot 2MeCN$ (**8**, left) and $[Mn_4(pyBet)_4(mdeaH)_2\text{-}(mdea)_2](BPh_4)_4 \cdot 2MeCN$ (**9,** right) in oscillating ac fields up to 1 kHz.

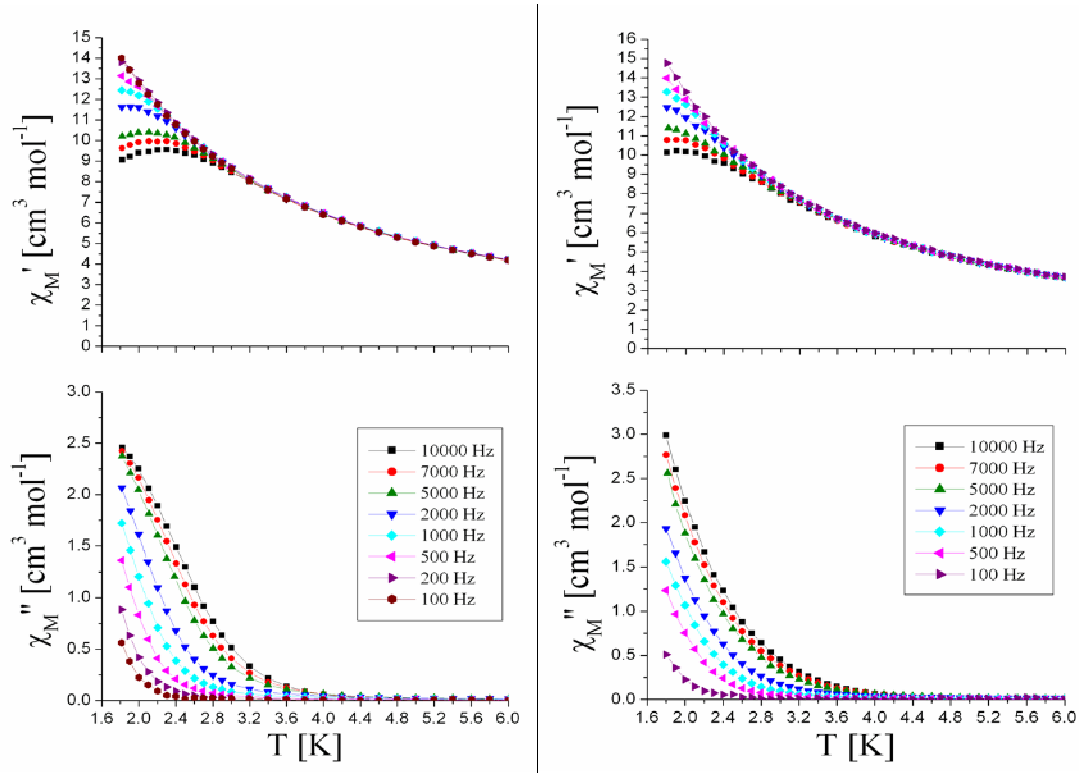

Figure 3.40. In-phase (χ_M') and out-of-phase (χ_M'') ac susceptibility for $[Mn_4(pyBet)_2\text{-}(O_2CMe)_2(mdeaH)_2(mdea)_2](BPh_4)_2 \cdot 2MeCN$ (**8**, left) and $[Mn_4(pyBet)_4(mdeaH)_2\text{-}(mdea)_2](BPh_4)_4 \cdot 2MeCN$ (**9,** right) in oscillating ac fields up to 10 kHz.

While the high frequency ac magnetic susceptibility data is very useful for determining the energy barrier to the reversal of the magnetization in SMMs, the lower frequency data can also provide valuable information. Since the ac measurements are collected in the absence of an applied dc field, a good estimate of the ground state spin can often be determined. Figure 3.41 shows the 10 Hz in-phase ac data for complexes **5-9** plotted as $\chi_M'T$ *vs.* T. These data were then extrapolated to 0 K and compared to $\chi_M T$ values for specific spin ground states calculated from the spin-only formula. The spin-only $\chi_M T$ values for $S = 6$, $S = 7$, $S = 8$, and $S = 9$ ground states are indicated by the black arrows.

From Figure 3.41 it is easy to see that the partially-substituted glycine and pyridyl betaine complexes **5** and **8**, respectively, are likely to have a ground state spin of $S = 6$ or 7. The fully-substituted analogs, **6** and **9**, are expected to have a ground state spin of $S = 8$. In fact, the extrapolated $\chi_M'T$ value of 36 cm^3 mol^{-1} K for complex **6** matches exactly with the spin-only value for a $S = 8$ ground state which is also the ground state spin suggested by the reduced magnetization fit for this complex. Finally, complex **7** appears to have a $\chi_M'T$ value closest to that of the spin-only value for a $S = 9$ ground state which agrees with the result of the $\chi_M T$ *vs.* T fit which makes sense since both of these measurements were made in little to no dc field. When a higher field is applied, Zeeman splitting increases causing closely-spaced energy states to cross which may explain why complex **7** fits better to a $S = 8$ ground state in the reduced magnetization where a lower spin ground state may be populated in applied fields of 3, 4 , and 5 T.

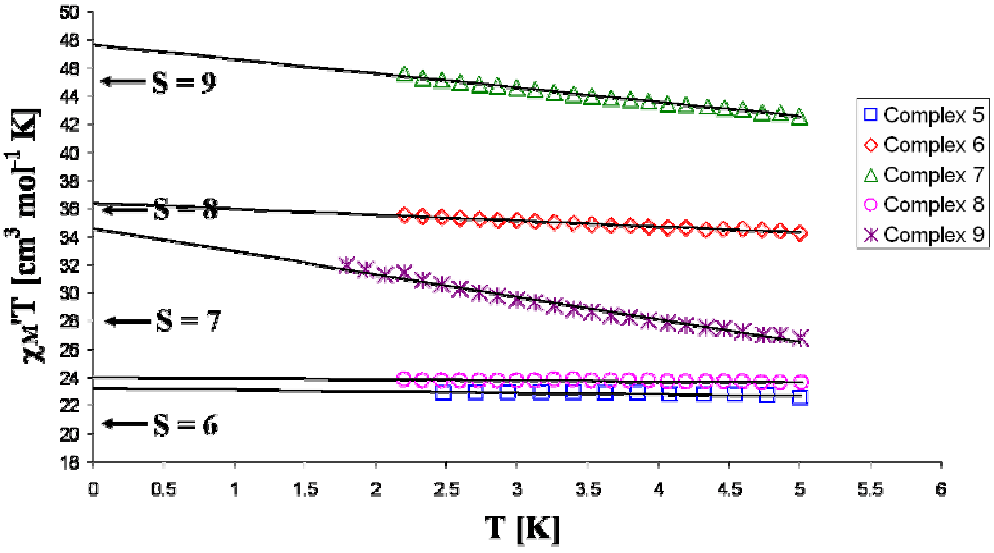

Figure 3.41. Extrapolation of 10 Hz χ_M'T vs. T data. Ground state spin estimates from spin-only formula.

Table 3.11. Summary of ground state spin determination for **5-9**.

Complex	$\chi_M T$ *vs. T*	M/N_B *vs. H/T*	Extrapolation of ac data (spin-only formula)
5	$S = 9$	$S = 7$	$S = 6$ or 7
6	$S = 9$	$S = 8$	$S = 8$
7	$S = 9$	$S = 8$	$S = 9$
8	$S = 9$	$S = 7$	$S = 6$ or 7
9	$S = 9$	$S = 7$	$S = 8$

Furthermore, the fact that consistent ground state spins for **6** were determined in both low and high dc field measurements further confirms that complex **6** has the most well-isolated ground state of this family of [Mn_4] dicubanes. Table 3.11 summarizes the ground state spins determined by the three methods discussed above. This table shows that the fully-substituted glycine betaine complexes **6** and **7** have the most consistent ground states in low and high dc fields. This result could have already been predicted by the data summarized in Table 3.10 which showed that complexes **6** and **7** also have the most well-defined ground states with minimal low-lying excited states. Since the full-matrix diagonalization of the dc susceptibility for **6** suggests a higher, $S = 9$, ground state, this will be further analyzed in the following high-frequency EPR measurements.

3.3.6. Single Crystal HFEPR Studies

The high crystalline quality of complex **6** and fairly well-isolated ground state as determined from dc and ac susceptibility studies make this molecule an ideal candidate for single crystal high-frequency electron paramagnetic resonance (HFEPR). This highly-sensitive technique has become increasingly useful for the unambiguous determination of the spin ground state (S), magnitude and absolute sign of the axial anisotropy (D), and transverse zero-field splitting terms which play an integral role in the quantum tunneling exhibited in SMMs.[19,24,26-32]

In order to determine the absolute sign of D, temperature-dependent EPR measurements were obtained both along the easy axis and hard plane of **6** at various frequencies and in the temperature range of 2-20 K. Single-molecule magnets require a negative D-value in order for the energy barrier between the “spin-up” and “spin-down”

states to exist.[33-35] However, the absolute sign of the *D*-value obtained from fitting of the magnetic susceptibility data is somewhat ambiguous, with reasonable fits often obtained for both positive and negative values. Thus, HFEPR provides a more definitive method for determining this important parameter.

The peaks observed in EPR spectra represent the magnetic-dipole transitions between the 2*S*+1 ground spin states differing in m_s by ±1 (*i.e.* -9 to -8, -8 to -7…etc.). For a well-isolated $S = 9$ ground state, the lowest energy transition (when measured along the easy axis) is expected to be from $m_s = -9$ to $m_s = -8$ and will occur at lower magnetic fields. When measured in the hard plane, the opposite is expected, making the -8 to -9 transition the highest in energy and thus observed at higher magnetic fields. With this in mind, Figure 3.42 shows the temperature-dependent spectra for **6** with the field aligned parallel to the easy axis of the molecule and at a frequency of 139.5 GHz. As the temperature is decreased, the Boltzman distribution of the spectra clearly shifts toward the transitions occurring at lower magnetic fields, indicating a negative *D*-value. The 20 K spectrum is also enlarged in Figure 3.42 to show the increased number (and distribution) of transitions occurring at higher temperatures as more excited states become thermally populated. To further confirm a negative *D*-value in **6**, the same temperature-dependent measurements were made in the hard plane of the molecule at a frequency of 67.3 GHz as shown in Figure 3.43. For a negative *D*-value, the distribution of spectra should shift toward the transitions occurring at higher magnetic fields when measured in the hard plane. As expected from the easy axis results, this behavior in the hard plane is exactly what is observed experimentally in Figure 4.43.

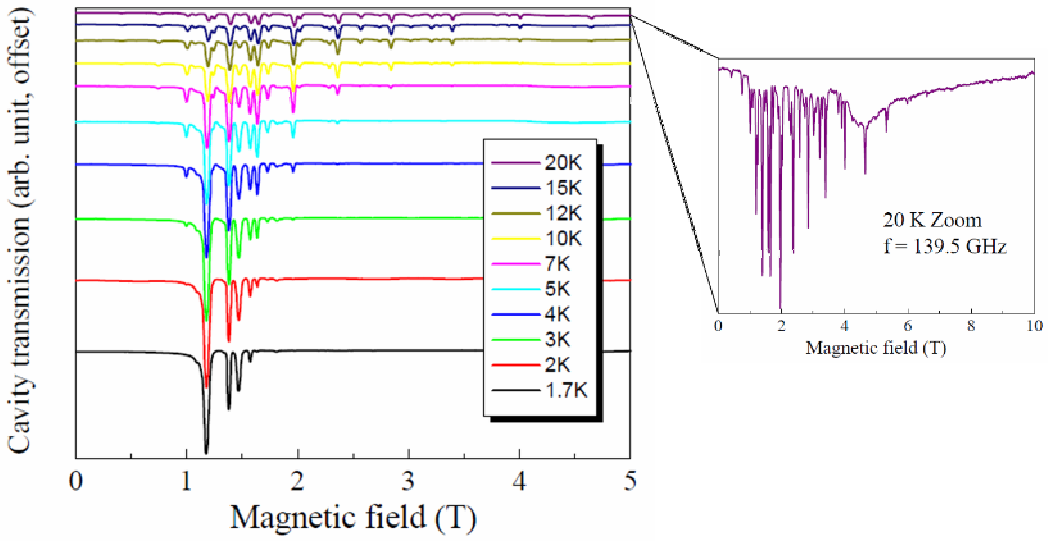

Figure 3.42. (Left) Temperature-dependent HFEPR spectra measured along the easy axis of $[Mn_4(Bet)_4(mdeaH)_2(mdea)_2](BPh_4)_4$ **(6)** in the temperature range of 1.7-20 K and a frequency of 139.5 GHz. (Right) Enlargement of 20 K spectrum.

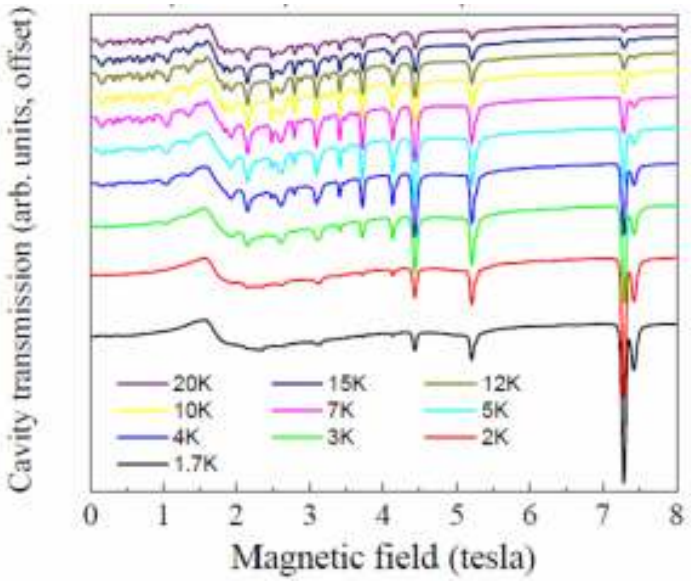

Figure 3.43. Temperature-dependent HFEPR spectra measured in the hard plane of $[Mn_4(Bet)_4(mdeaH)_2(mdea)_2](BPh_4)_4$ **(6)** in the temperature range of 1.7-20 K and a frequency of 67.3 GHz.

Frequency-dependent HFEPR experiments were also performed on complex **6** in order to determine the intramolecular coupling constant *J*, the magnitude of single-ion *d*-values, the rhombic zfs term *E*, and any higher-order transverse terms in the spin Hamiltonian (see equation *1.15* in the Introduction Chapter). Frequency-dependent EPR of **6** with the field aligned close to the easy axis of the molecule at frequencies of 128-290 GHz and at a temperature of 3 K were measured. A similar experiment was performed with the field aligned in the hard plane of **6** at frequencies of 50-211 GHz and a temperature of 10 K. Both sets of spectra are found in Figure 3.44. As the frequency is increased, the transitions shift to higher magnetic fields in both the easy axis and hard plane cases.

For these preliminary EPR studies of complex **6**, a three-spin trimer model was employed in order to simplify calculations while still obtaining reasonable estimates for *d*, *E*, and *J*. The trimer model is shown in Figure 3.45 with a central spin, A**,** representing a pair of high-spin Mn(III) ions with $S = 4$ and two outer spins, B, each representing the high-spin Mn(II) ions with $S = 5/2$. The Jahn-Teller (JT) or anisotropy axis for each ion is tilted from the easy axis (z-direction) by the angles ϕ and θ. However, due to inversion symmetry, the JT axes were assumed to be parallel to one another and aligned with the easy axis of the molecule (ϕ and $\theta = 0$). The intramolecular coupling interaction between A and B is represented by *J*. Also due to inversion symmetry, the *d*-values for both outer spins, B, are assumed to be equivalent and smaller in magnitude than that for A since Mn(II) ions are known to have much smaller anisotropy than Mn(III) ions as previously discussed.[24] The zfs tensors, *d*, are also taken to be parallel to one another.

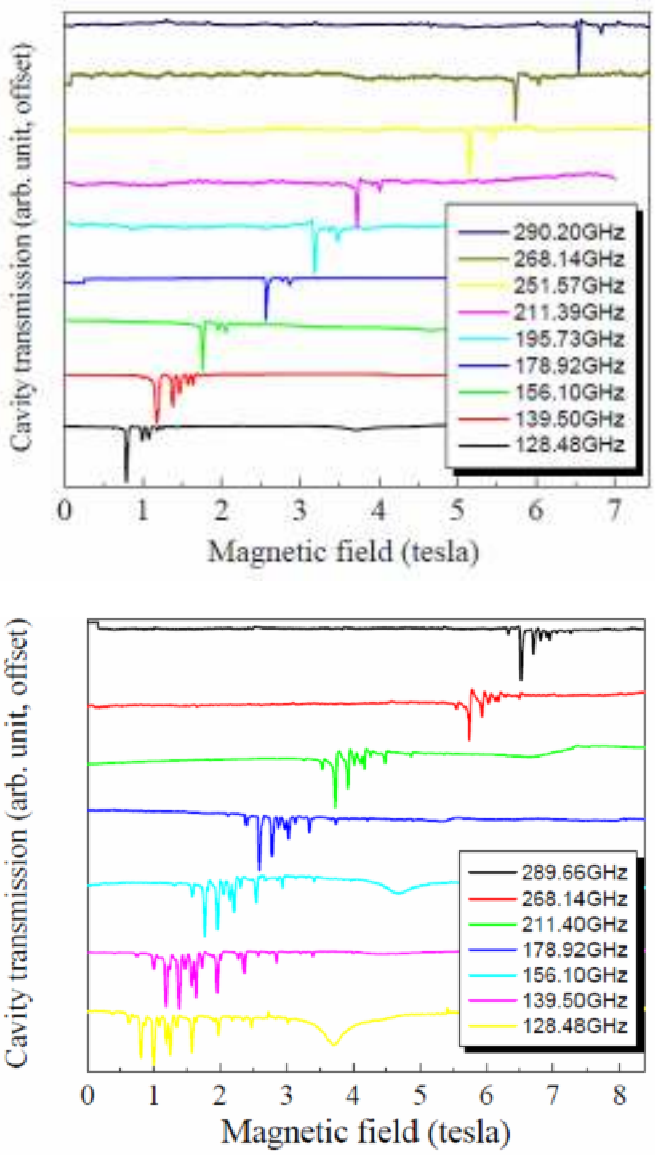

Figure 3.44. Frequency-dependent HFEPR spectra of $[Mn_4(Bet)_4(mdeaH)_2(mdea)_2](BPh_4)_4$ **(6)** measured (top) along the easy axis at 3 K and 128-290 GHz and (bottom) in the hard plane at 10 K and 50-211 GHz.

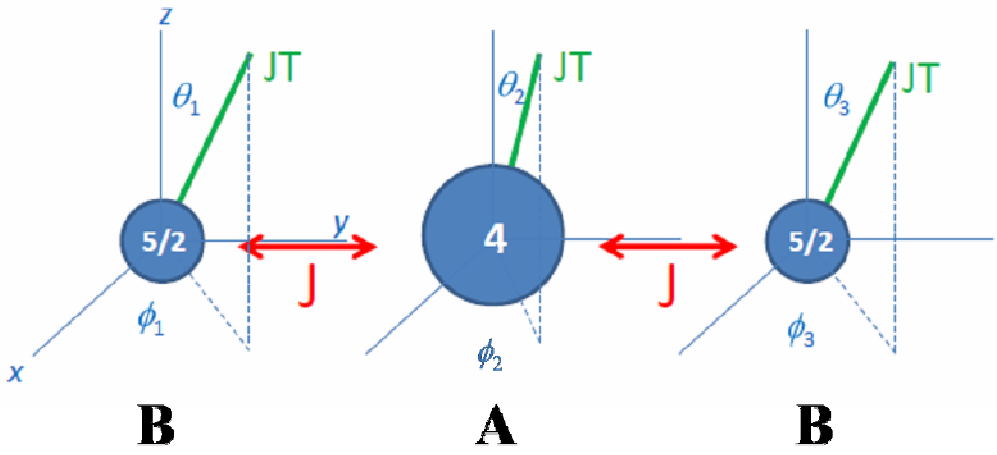

Figure 3.45. Trimer model used to simulate frequency-dependent EPR data for $[Mn_4(Bet)_4(mdeaH)_2(mdea)_2](BPh_4)_4$ **(6)** where **A** and **B** represent S = 4 and S = 5/2 spins, respectively, *J* is the coupling interaction between **A** and **B**, and *JT* is the Jahn-Teller axis of each ion tilted from the easy axis (z-axis) by angles ϕ and θ.

Figure 3.46 is a plot of the peak positions for the major transitions observed in Figure 3.44 at each frequency measured. Each transition can then be fit across the entire frequency range by exact diagonalization of the extended Hamiltonian in equation *1.15*. The resulting simulations of the data, taking into account the trimer model in Figure 3.45, are represented by the solid curves in Figure 3.46. The best simulation of the 3 K easy axis data gave optimized Hamiltonian parameters of d_A = -2.1 K (-1.5 cm^{-1}), E_A = 0.34 K (0.23 cm^{-1}), $B_4^0{}_A$ = 4.8 x 10^{-4} K (3.3 x 10^{-4} cm^{-1}), d_B = -0.14 K (-0.10 cm^{-1}), and J = -3.4 K (-2.3 cm^{-1}). These same parameters were then used to also simulate the 10 K hard plane data which agrees reasonably well as shown in Figure 3.46.

The single-ion anisotropy for Mn(II) is indeed ~1/10 the *d*-value for Mn(III) as expected and both zfs parameters, d_A and d_B, are comparable to the values reported in the literature[24] as opposed to the large value obtained for Mn(III) in the full-matrix diagonalization of the dc susceptibility data for **6**. It is worth noting that the negative *J*-value here implies ferromagnetic coupling between spins A and B leading to an overall S = 9 system. The magnitude of J is also fairly consistent with the intramolecular exchange parameters determined from the dc susceptibility measurements. Lastly, anisotropic transverse terms were included in these simulations giving a small 2nd order rhombic zfs parameter, E, and a 4th order B_4^0 term which is on the same order of magnitude (10^{-5}-10^{-4} K) as those measured in some recently studied [Mn_4] cubane complexes[36] and the [Mn_3Ni_2] complexes[19] discussed in the Introduction Chapter.

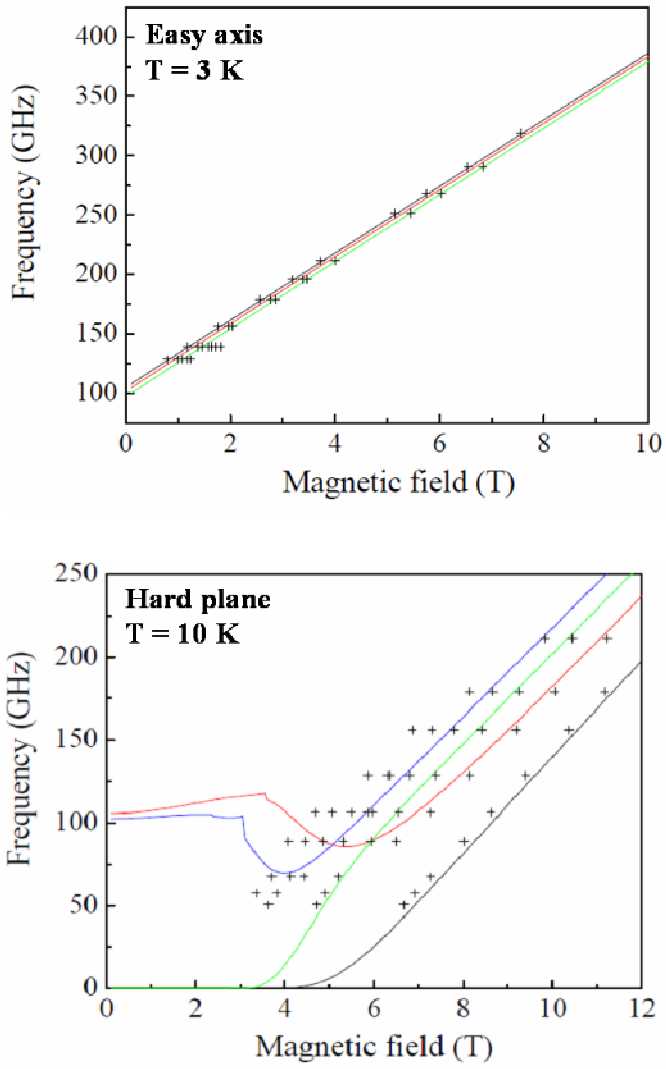

Figure 3.46. Simulation of easy axis (top) and hard plane (bottom) EPR spectra from Figure 3.44. All zfs tensors are parallel.

3.3.7. Single Crystal Magnetization Hysteresis

From the magnetic susceptibility and EPR experiments discussed above, complex **6** clearly has a large spin ground state, a negative magnetoanisotropy, and an appreciable energy barrier toward the reversal of the direction of magnetization, all of which strongly suggest that **6** is a single-molecule magnet. However, in order to definitely classify this complex as a SMM, we must show that it exhibits quantum tunneling relaxation of the magnetization. For this purpose, magnetization *vs.* field experiments were performed on oriented single crystals of **6**. The face-indexing of **6** (see Figure 3.13) was used as a guide to properly align the assumed easy axis (Jahn-Teller axes of the high-spin Mn(III) ions) of the molecule with the applied magnetic field as shown in Figure 3.47. The actual position of the easy axis was found to be in good agreement with that determined from crystallographic data.

The top portion of Figure 3.48 shows the temperature-dependent magnetization, M/M_s, *vs.* longitudinal field, H_z, data collected in the temperature range of 35-1200 mK and at a field sweep rate, α, of 0.02 T/min. The data clearly show evenly spaced vertical steps in the hysteresis loops, indicative of quantum tunneling of the magnetization (QTM). The hysteresis is essentially temperature-independent below ~300 mK where pure ground state tunneling is presumed to be taking place. Thermally-assisted quantum tunneling is shown as the temperature is increased until the blocking temperature of ~1.2 K is reached, at which point the hysteresis loop collapses.

The vertical steps in the hysteresis plots at H_z = 0, 0.2, and 0.4 T can be assigned to the quantum tunneling transitions between the m_s = -10 and m_s = 10-k states (where k = 0, 1, and 2) or m_s = -10 to +10, -10 to +9, and -10 to +8, respectively. In the temper-

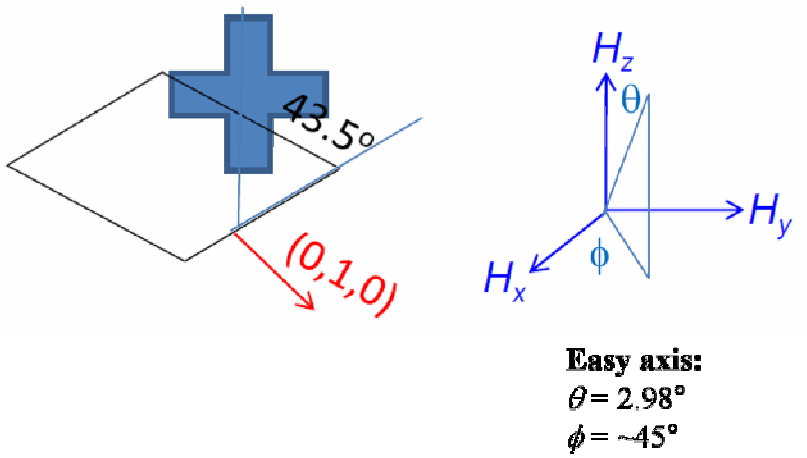

Figure 3.47. (Left) Alignment of a single-crystal of $[Mn_4(Bet)_4(mdeaH)_2(mdea)_2](BPh_4)_4$ **(6)** with respect to Jahn-Teller orientation from crystallographic data and (right) the actual position of the easy axis.

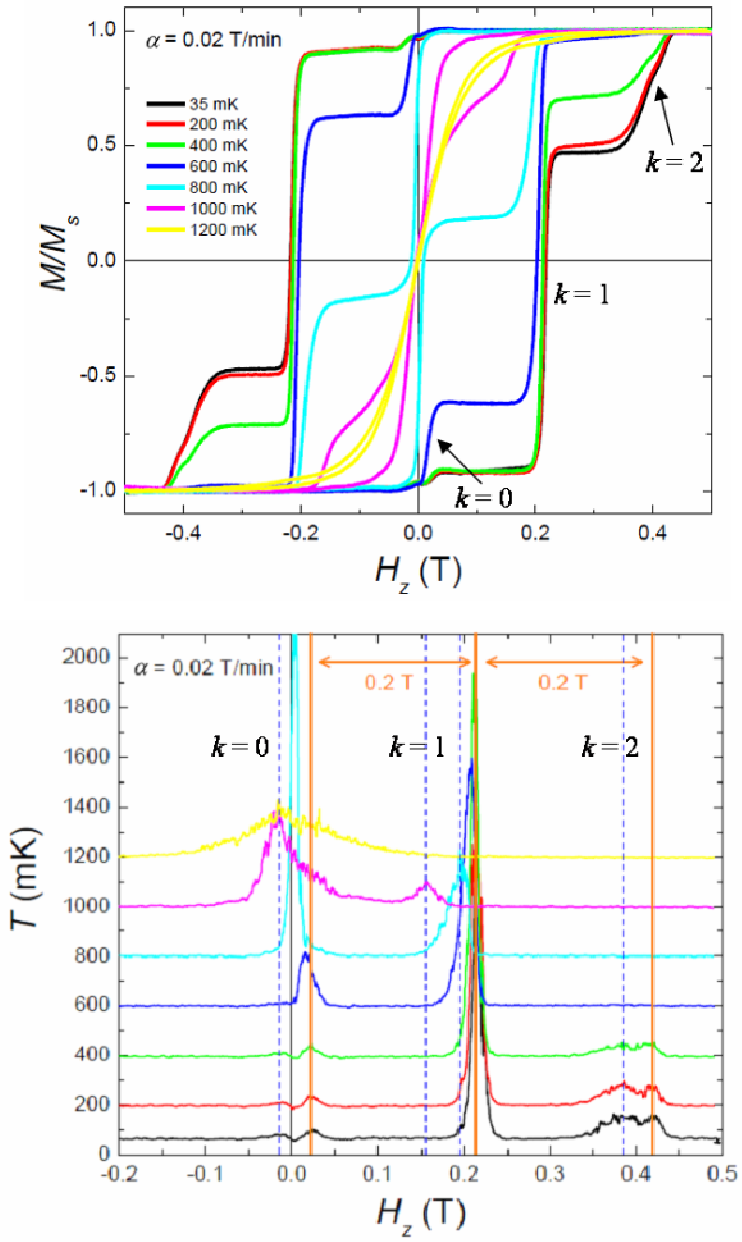

Figure 3.48. (Top) Temperature-dependence of the magnetization (M/M_s) *vs.* longitudinal field (H_z) at a sweep rate of 0.02 T/min. (Bottom) First-derivative of M/M_s *vs.* H_z plot showing QTM resonances regularly spaced 0.2 T apart.

ature-dependent range, the quantum tunneling relaxation increases with increasing temperature which is most notable in the $k = 0$ and $k = 1$ steps. The position of these QTM resonances is more easily seen in the first-derivative plot *vs.* applied field which is shown in the bottom portion of Figure 3.48. The three QTM resonances occur at a regular interval of 0.2 T (ΔH). There is a small shift of ~0.02 T for all resonances as well as some other minor peaks (mostly in the $k = 2$ resonance and at higher temperatures) which is likely due to intermolecular interaction and/or small dipolar effects. The $k = 2$ resonance is only observed at low temperatures and is not as defined as $k = 0$ and $k = 1$ with smaller features present.

From $\Delta H = 0.2$ T, the zero-field splitting parameter, D, was found to be 0.258 K from equation 3.1,

$$\Delta H = k|D| / g\mu_0\mu_B cos(\alpha) \qquad (3.1)$$

Where α is the bisecting angle between the applied dc field and the easy axis of the molecule which is close to 0° for **6**. Recall that the D-value determined from the giant-spin model of the dc susceptibility data for **6** was 0.31 K for a $S = 8$ ground state. However, now that full-matrix diagonalization fits as well as EPR measurements have confirmed a S = 9 ground state for this complex, the D-value is estimated to be closer to 0.26 K. Furthermore, the effective energy barrier calculated from the ac susceptibility of **6** was determined to be ~21 K which, assuming $S = 9$, also gives $D = 0.26$ K from $|DS_z^2|$. Both of these values agree exactly with that extracted from the hysteresis data.

The inversion symmetry of **6** should also give rise to a 2nd-order transverse anisotropy term in the spin Hamiltonian, $E(S_x^2-S_y^2)$, of which the single-ion value for the central Mn(III) was determined to be ~0.34 K from the fitting of the HFEPR data. In order to characterize the hard plane of this molecule, M/M_s *vs.* H_z measurements were also taken with a small transverse field, H_T, of 0.2 T applied at different angles, ϕ, in the hard anisotropy plane. These data were collected at a temperature of 35 mK and with H_T applied at ϕ = 0 - 360° in 15° increments. Figure 3.49 shows two different views of the quantum tunneling probability, P, of the k = 0 resonance as a function of the transverse field angle, ϕ. The two-fold modulation of the tunneling probability at k = 0 follows the inversion symmetry of this molecule and once again suggests the presence of a 2nd-order transverse term in the Hamiltonian. Also, the two minima observed in the left part of Figure 3.49 occur at angles of 123° and 303° which are assigned to the hard axis of the molecule (as shown in the 360° view on the right side of Figure 3.49). Thus, the angle-dependence and symmetry of the k = 0 QTM resonance allowed for the determination of the direction of the hard axis at essentially zero applied field.

The effects of a transverse field on the k = 1 resonance becomes slightly more involved since this also requires an applied longitudinal field, H_z. The tunneling probability, P, of both the k = 0 and k = 1 QTM resonances was plotted as a function of the transverse field, H_T, applied at an angle, ϕ, in the hard plane ranging from 110°-145°. These data are plotted in Figure 3.50 with the results for k = 0 on the top and those for k = 1 on the bottom. Both QTM resonances show a clear demonstration of quantum mechanical Berry phase (as discussed in the Introduction Chapter) resulting from the constructive and destructive interference of competing tunneling trajectories.

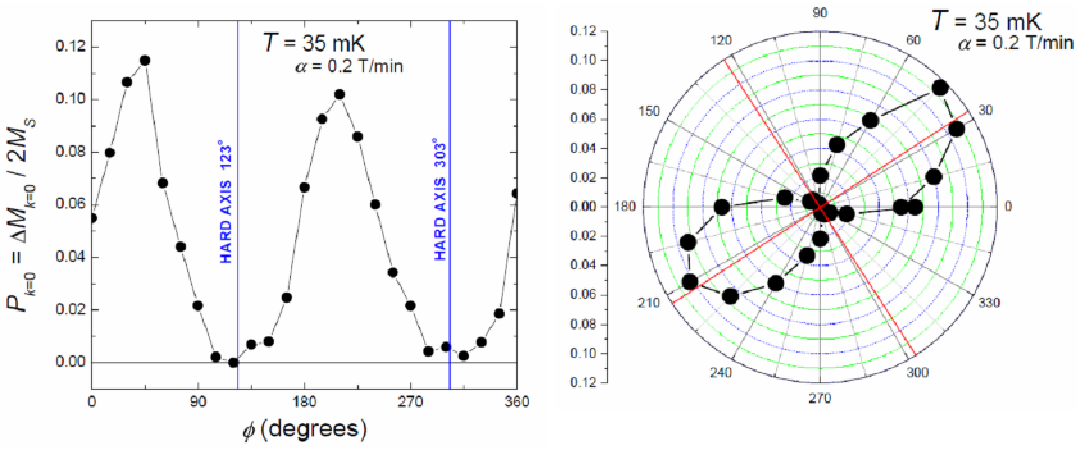

Figure 3.49. Two different views of the tunneling probability, P, at resonance $k = 0$ as a function of the angle, ϕ, of the applied transverse field. The hard axis is assigned along the 123°-303° direction.

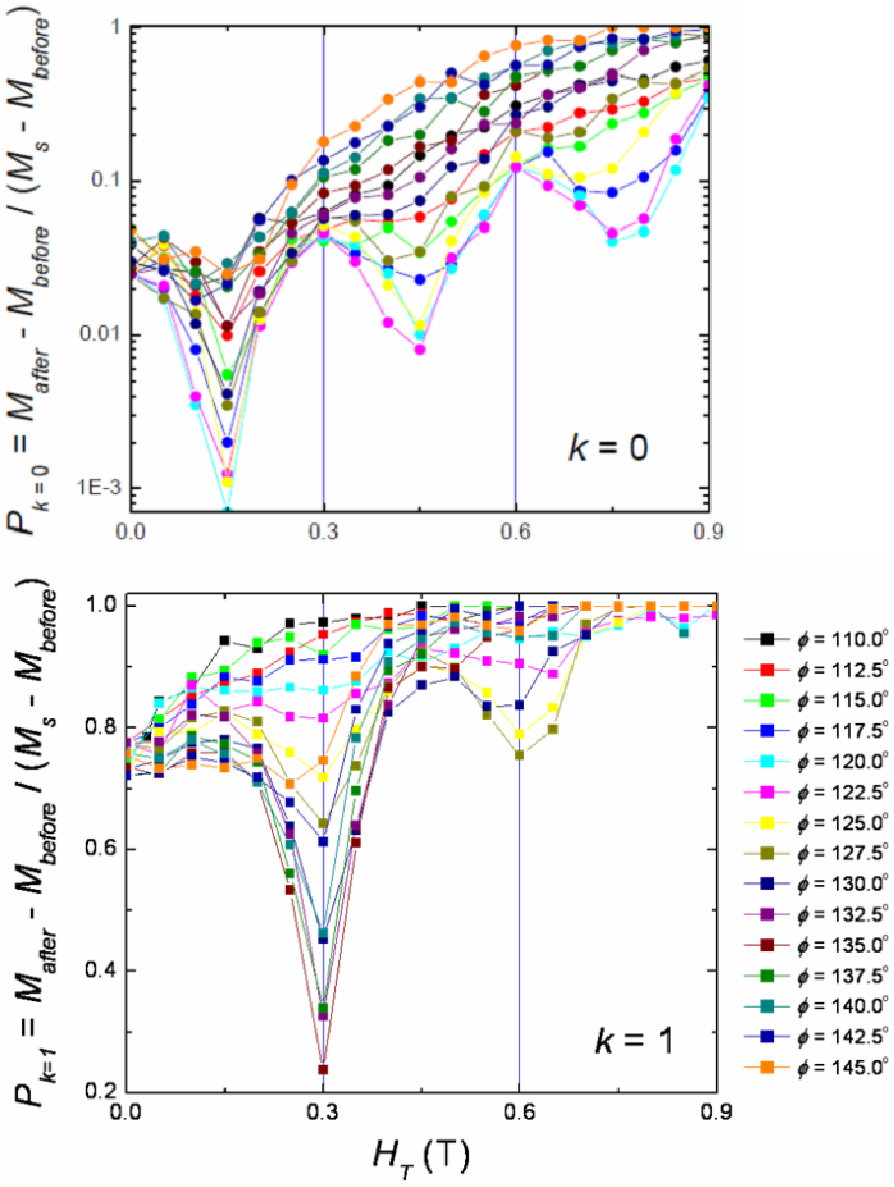

Figure 3.50. Tunneling probability, P, at resonance $k = 0$ (top) and $k = 1$ (bottom) as a function of transverse field, H_T, applied at angle, ϕ, in the hard plane.

The probability minima in both sets of data occur at regularly spaced intervals of H_T = 0.3 T. Equation *3.2* allows for the determination of the transverse anisotropy term, *E*, from

$$\Delta H_T = 2k_B / g\mu_B[2E(E+D)]^{1/2} , \qquad (3.2)$$

where *D* is the axial zfs parameter determined experimentally from the separation of QTM resonances in the hysteresis data (equation *3.1*) which was found to be 0.258 K for **6**. A small *E*-value of 58 mK was determined from the data in Figure 3.50.

The interesting observation in the Berry phase exhibited by complex **6** is that the minima do not all occur at the same angle, ϕ, in k = 1 as they do in k = 0. At the k = 0 QTM resonance, the three observed minima in the transverse field range of 0 - 0.9 T all occur at ϕ = 120-122° which is expected based on the assignment of the hard axis along the ϕ = 123°, 303° direction from the symmetry of the k = 0 resonance in Figure 3.49. However, at the k = 1 resonance, the first minimum at H_T = 0.3 T occurs at ϕ = 135° (significantly shifted from the presumed hard axis of the molecule) whereas the second minimum at 0.6 T is observed at 125-127°. These data are more clearly depicted in the contour plots in Figure 3.51 with the previously determined hard axis delineated by the white dotted line at ϕ = 122°. The top portion of Figure 3.51 clearly shows how the three minima all fall along the dotted line for the k = 0 QTM resonance even as the magnitude of the transverse field increases. Contrarily, for k = 1 in the bottom portion of Figure 3.51, neither minima fall along the dotted line. Furthermore, the minima for

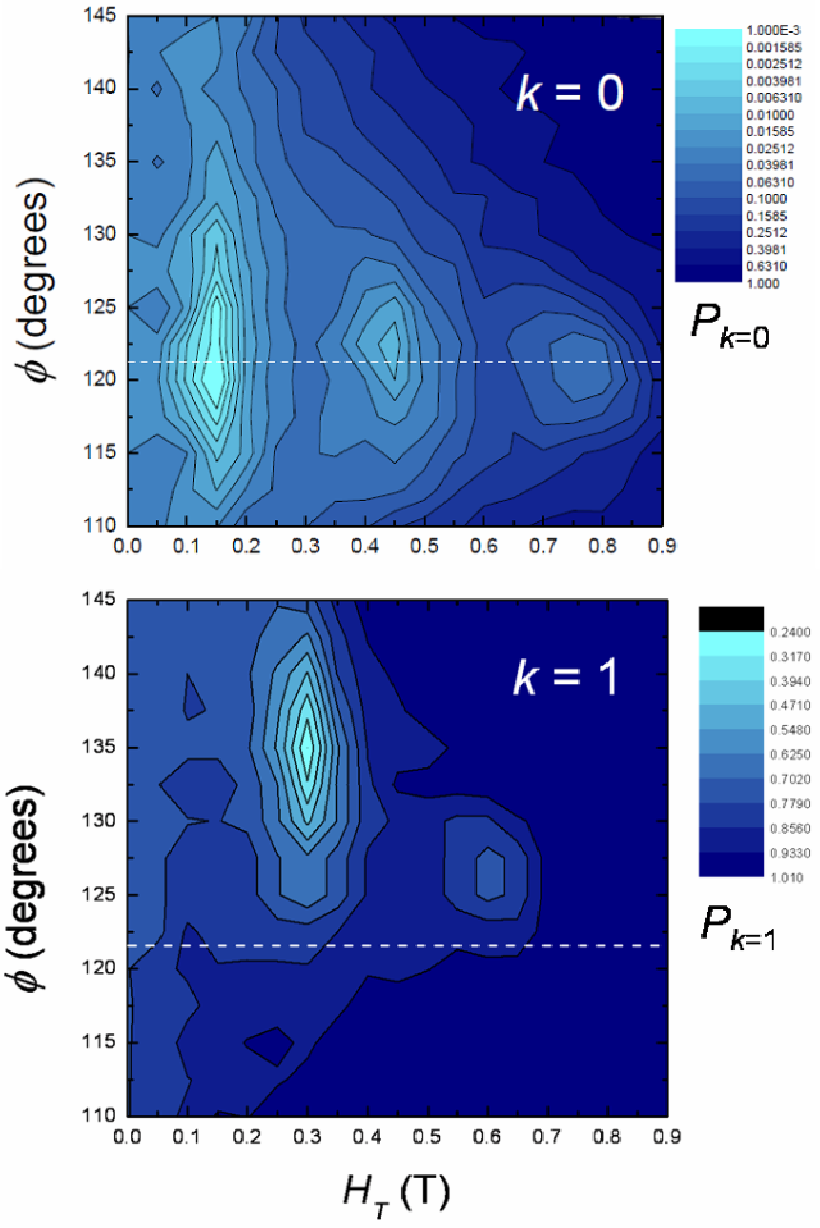

Figure 3.51. Contour plots of the data in Figure 3.49 for $k = 0$ (top) and $k = 1$ (bottom). The hard axis is represented by the dotted line at $\phi = 122°$ in both plots.

k = 1 occur at different angles as the magnitude of the transverse field increase from 0 to 0.9 T.

In order to explain this observation, let us go back to the three-spin model employed in the HFEPR data simulation found in Figure 3.45. When the zfs tensors of the outer spins, Mn(II) ions, are oriented away from the zfs tensor of the central spin, Mn(III) ion, there is a projection of the Mn(II) anisotropy onto the hard plane at an angle, β, from the x-axis. This results in competition between the two interactions (zfs projection from Mn(III) and from Mn(II) ions) to assign the direction of the hard anisotropy axis for the whole molecule. There is no definitive "hard" axis when this happens, resulting in Berry phase minima occurring along different directions of application of the transverse field depending also on the magnitude of the field.

This effect is clearly shown in k = 1 (see Figure 3.51) and should be observed in k = 0 but to a lesser extent. The reason for this is that the 2nd-order zfs term of the central Mn(III) ion imposes a transverse anisotropy projected onto the x-axis which mainly affects QTM resonances where k is a multiple of two (i.e. k = 0, k = 2, k = 4, etc.). Therefore, regardless of the magnitude of H_T, the Berry phase minima at k = 0 all occur along the direction of the hard axis (ϕ = ~122°) as imposed by the projection of the transverse anisotropy of the central Mn(III) ion onto the x-axis. This interference between intramolecular anisotropies oriented in different directions has been speculated previously in hysteresis studies on Mn_{12}Ac. The idea that competing intramolecular 2nd and 4th-order anisotropies could lead to Berry phase minima occurring at different angles of the application of the transverse field in Mn_{12}Ac had been calculated before, but never observed in a SMM.[37-40]

Another interesting observation differentiating the Berry phase exhibited at k =0 and k = 1 is the presence of an asymmetric Berry phase pattern at the k = 1 QTM resonance. The top portion of Figure 3.52 shows the Berry phase response at k = 0 and k =1 as the polarity of the transverse field is reversed. The Berry phase is symmetric for both positive and negative values of H_T at resonance k = 0 but asymmetric for k = 1. This is easily explained by the fact that a longitudinal field is also applied at k = 1 which distorts the anisotropy barrier out of the hard plane in a particular direction. At the same time, the transverse field is also distorting the anisotropy barrier in a different direction, where simply reversing the polarity of the transverse field will not elicit the same response. In k = 0, however, there is no longitudinal field to perturb the barrier out of the hard plane. Therefore, the anisotropy axes do not have direction, leading to a symmetric response upon reversal of the transverse field.

Interestingly, if the total magnetic field is reversed, both H_z and H_T, then the symmetry in the Berry phase response is restored as shown in the bottom portion of Figure 3.52. (Here of course the transverse field is applied at ϕ = 135° where the first Berry phase minimum was observed for k = 1 in Figures 3.50 and 3.51.) This behavior is observed as a result of the inversion symmetry of complex **6** which makes the two outer spins of the three-spin model equivalent and thus the angle at which their anisotropy axes are projected onto the hard plane also equivalent. Therefore, the requirement of a total magnetic field reversal in order to maintain a centrosymmetric response is a clear manifestation of the inversion symmetry of this molecule. Asymmetric Berry phase patterns have been observed in other SMMs (such as the Mn_{12}-allyl wheel discussed in Chapter 4) but are most likely due to a transverse

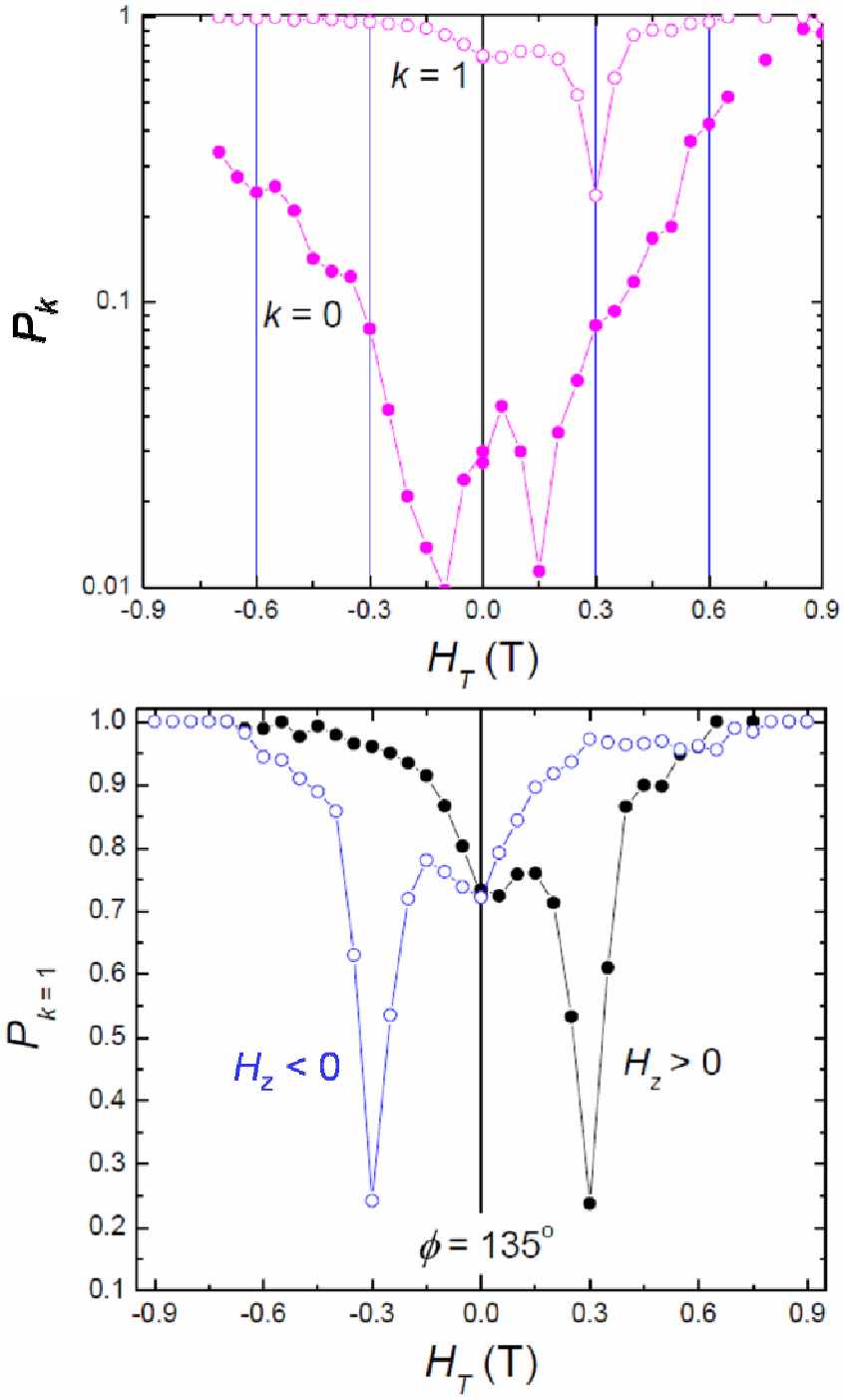

Figure 3.52. Symmetry of the Berry phase upon reversal of the transverse field, H_T, for $k = 0$ and $k = 1$ (top) and upon reversal of both H_T and the longitudinal field, H_z, for $k = 1$ (bottom).

Dzyaloshinsky-Moriya term in the Hamiltonian, provided that the inversion symmetry is broken, and is obviously not the case in complex **6**.[41]

3.4. Conclusions

A new family of [Mn_4] dicubane single-molecule magnets with zwitterionic betaine-type ligand substituents has been synthesized and magnetically characterized. These cationic SMMs, isolated by bulky tetraphenylborate anions, have increased steric isolation of their magnetic cores. This is important for future application in quantum computing and information storage devices where even the slightest environmental coupling to the magnetic core can be detrimental to the system. All five complexes presented in this chapter show promise as SMMs with a large spin ground state (S = 8 or 9), appreciable axial-type anisotropy, and an effective energy barrier toward the reversal of the direction of magnetization, all supported by dc and ac magnetic susceptibility studies.

The magnetic studies herein have shown that there is a direct correlation between the steric isolation of the magnetic core of these SMMs and the electronic isolation of their ground state spin. Complex **6**, in particular has a well-isolated core with intermolecular Mn···Mn separations of 10-15 Å. Decreased potential for magnetic exchange and dipolar interactions within the crystal lattice, along with high crystalline quality, made **6** an ideal complex for single crystal HFEPR and magnetization hysteresis studies. HFEPR signals for **6** were extremely well-defined and allowed for the unambiguous determination of the ground state spin (S = 9), the absolute sign of the

zero-field splitting parameter D, and confirmed the presence of 2^{nd}-order transverse anisotropy terms in the spin Hamiltonian.

Oriented single crystal magnetization hysteresis measurements on **6** revealed sharp quantum tunneling of the magnetization (QTM) resonances from which D was determined to be 0.258 K (in excellent agreement with magnetic susceptibility data). Complex **6** was also shown to exhibit Berry phase interference at both $k = 0$ and $k = 1$ QTM resonances. Two important observations were made from the hysteresis data. (1) Complicated Berry phase patterns were observed due to the presence of competing intramolecular single-ion anisotropies oriented at different direction. (2) Asymmetric Berry phase response upon reversal of the transverse field polarity was observed at $k = 1$ retained its symmetry at $k = 0$. A total magnetic field reversal (transverse as well as longitudinal) was required in order to recover the symmetry in the Berry phase response at $k = 1$, a clear manifestation of the inversion symmetry of this molecule. This behavior in Berry phase interference had been theoretically predicted but not yet observed in a SMM.

The steric isolation of well-known [Mn_4] dicubanes through a bottom-up synthetic approach has lead to the discovery of a new SMM of very high quality. Complex **6** exhibits significantly enhanced magnetic and quantum properties as compared to other complexes within this family of SMMs. The small structural changes and high crystalline quality of **6** have resulted in some of the most novel and intriguing single crystal HFEPR and hysteresis data ever observed for a single-molecule magnet.

3.5. References

(1) Blunden, G.; Gordon, S. M. *Prog. Phycol. Res.* **1986**, *4*, 39-80.

(2) Ciszewska, R. *Postepy Nauk Roln.* **1981**, *28*, 55-69.

(3) Allen, J. C.; Humphries, C. *FEBS Letters* **1975**, *57*, 158-162.

(4) Chen, X. M.; Mak, T. C. W. *Journal of Chemical Crystallography* **1991**, *21*, 21-25.

(5) Chen, X.-M.; Mak, T. C. W. *Inorganica Chimica Acta* **1991**, *182*, 139-144.

(6) Chen, X.-M.; Aubin, S. M. J.; Wu, Y.-L.; Yang, Y.-S.; Mak, T. C. W.; Hendrickson, D. N. *Journal of the American Chemical Society* **1995**, *117*, 9600-9601.

(7) Ramos Silva, M. M. B., A.; Paixao, J. A.; Alte da Veiga, L.; Martin-Gil, J. *Acta Crystallographica Section C* **2001**, *57*, 542-545.

(8) Zhang, Z.; Chen, S.; Jiang, S. *Biomacromolecules* **2006**, *7*, 3311-3315.

(9) Li, G.; Cheng, G.; Xue, H.; Chen, S.; Zhang, F.; Jiang, S. *Biomaterials* **2008**, *29*, 4592-4597.

(10) Coronado, E.; Torment-Aliaga, A.; Gaita-Arino, A.; Giminez-Saiz, C.; Romero, F. M.; Wernsdorfer, W. *Angewandte Chemie-International Edition* **2004**, *43*, 6152-6156.

(11) Forment-Aliaga, A.; Coronado, E.; Feliz, M.; Gaita-Arino, A.; Llusar, R.; Romero, F. M. *Inorganic Chemistry* **2003**, *42*, 8019-8027.

(12) Foguet-Albiol, D.; O'Brien, T. A.; Wernsdorfer, W.; Moulton, B.; Zaworotko, M. J.; Abboud, K. A.; Christou, G. *Angewandte Chemie-International Edition* **2005**, *44*, 897-901.

(13) Ako, A. M.; Mereacre, V.; Hewitt, I. J.; Clerac, R.; Lecren, L.; Anson, C. E.; Powell, A. K. *Journal of Materials Chemistry* **2006**, *16*, 2579-2586.

(14) Vincent, J. B.; Chang, H. R.; Folting, K.; Huffman, J. C.; Christou, G.; Hendrickson, D. N. *Journal of the American Chemical Society* **1987**, *109*, 5703-5711.

(15) Chen, X.-M.; Mak, T. C. W. *Journal of Molecular Structure* **1990**, *221*, 265-269.

(16) Kent, A. D.; Vonmolnar, S.; Gider, S.; Awschalom, D. D. *Journal of Applied Physics* **1994**, *76*, 6656-6660.

(17) Mola, M.; Hill, S.; Goy, P.; Gross, M. *Review of Scientific Instruments* **2000**, *71*, 186-200.

(18) Smith, T. D.; Pilbrow, J. R. *Coordination Chemistry Reviews* **1974**, *13*, 173-278.

(19) Feng, P. L.; Koo, C.; Henderson, J. J.; Nakano, M.; Hill, S.; del Barco, E.; Hendrickson, D. N. *Inorganic Chemistry* **2008**, *47*, 8610-8612.

(20) Henderson, J. J.; Koo, C.; Feng, P. L.; del Barco, E.; Hill, S.; Tupitsyn, I. S.; Stamp, P. C. E.; Hendrickson, D. N. *Physical Review Letters* **2009**, *103*, 017202.

(21) Yang, E. C.; Harden, N.; Wernsdorfer, W.; Zakharov, L.; Brechin, E. K.; Rheingold, A. L.; Christou, G.; Hendrickson, D. N. *Polyhedron* **2003**, *22*, 1857-1863.

(22) Wittick, L. M.; Murray, K. S.; Moubaraki, B.; Batten, S. R.; Spiccia, L.; Berry, K. J. *Dalton Transactions* **2004**, 1003-1011.

(23) Beedle, C. C.; Stephenson, C. J.; Heroux, K. J.; Wernsdorfer, W.; Hendrickson, D. N. *Inorganic Chemistry* **2008**, *47*, 10798-10800.

(24) Krzystek, J.; Ozarowski, A.; Telser, J. *Coordination Chemistry Reviews* **2006**, *250*, 2308-2324.

(25) McWeeny, R.; John Wiley & Sons Ltd.: 2003; Vol. 1, p 161-175.

(26) Gatteschi, D.; Sessoli, R. *Angewandte Chemie-International Edition* **2003**, *42*, 268-297.

(27) Hill, S.; Edwards, R. S.; Jones, S. I.; Dalal, N. S.; North, J. M. *Physical Review Letters* **2003**, *90*, -.

(28) Hill, S.; Datta, S.; Liu, J.; Inglis, R.; Milios, C. J.; Feng, P. L.; Henderson, J. J.; Barco, E. d.; Brechin, E. K.; Hendrickson, D. N. *Dalton Transactions*, *39*, 4693-4707.

(29) Hill, S.; Maccagnano, S.; Park, K.; Achey, R. M.; North, J. M.; Dalal, N. S. *Physical Review B* **2002**, *65*, 224410.

(30) Edwards, R. S.; Hill, S.; Bhaduri, S.; Aliaga-Alcalde, N.; Bolin, E.; Maccagnano, S.; Christou, G.; Hendrickson, D. N. *Polyhedron* **2003**, *22*, 1911-1916.

(31) Rumberger, E. M.; Hill, S.; Edwards, R. S.; Wernsdorfer, W.; Zakharov, L. N.; Rheingold, A. L.; Christou, G.; Hendrickson, D. N. *Polyhedron* **2003**, *22*, 1865-1870.

(32) Feng, P. L.; Beedle, C. C.; Koo, C.; Lawrence, J.; Hill, S.; Hendrickson, D. N. *Inorg. Chim. Acta* **2008**, *361*, 3465-3480.

(33) Sessoli, R.; Tsai, H. L.; Schake, A. R.; Wang, S. Y.; Vincent, J. B.; Folting, K.; Gatteschi, D.; Christou, G.; Hendrickson, D. N. *Journal of the American Chemical Society* **1993**, *115*, 1804-1816.

(34) Eppley, H. J.; Tsai, H. L.; Devries, N.; Folting, K.; Christou, G.; Hendrickson, D. N. *Journal of the American Chemical Society* **1995**, *117*, 301-317.

(35) Tsai, H. L.; Eppley, H. J.; DeVries, N.; Folting, K.; Christou, G.; Hendrickson, D. N. *Molecular Crystals and Liquid Crystals Science and Technology Section a-Molecular Crystals and Liquid Crystals* **1995**, *273*, A167-A173.

(36) Feng, P. L.; Beedle, C. C.; Koo, C.; Wernsdorfer, W.; Nakano, M.; Hill, S.; Hendrickson, D. N. *Inorganic Chemistry* **2008**, *47*, 3188-3204.

(37) del Barco, E.; Kent, A. D.; Rumberger, E. M.; Hendrickson, D. N.; Christou, G. *Physical Review Letters* **2003**, *91*, 047203.

(38) del Barco, E.; Kent, A. D.; Chakov, N. E.; Zakharov, L. N.; Rheingold, A. L.; Hendrickson, D. N.; Christou, G. *Physical Review B* **2004**, *69*, -.

(39) del Barco, E.; Kent, A. D.; Hill, S.; North, J. M.; Dalal, N. S.; Rumberger, E. M.; Hendrickson, D. N.; Chakov, N.; Christou, G. *Journal of Low Temperature Physics* **2005**, *140*, 119-174.

(40) Park, K.; Pederson, M. R.; Baruah, T.; Bernstein, N.; Kortus, J.; Richardson, S. L.; del, B. E.; Kent, A. D.; Hill, S.; Dalal, N. S. *J. Appl. Phys.* **2005**, *97*, 10M505/1-10M505/3.

(41) Ramsey, C. M.; del Barco, E.; Hill, S.; Shah, S. J.; Beedle, C. C.; Hendrickson, D. N. *Nat Phys* **2008**, *4*, 277-281.

Chapter 4:

Single-Stranded Manganese Wheels

4.1. Introduction

4.1.1. Wheel-Shaped SMMs

Though the focus of Chapters 2 and 3 was on the well-known family of tetranuclear manganese dicubane complexes, single-molecule magnets (SMMs) have been synthesized in a wide variety of topologies and nuclearities over the years. Other common topologies encountered in SMMs include triangles, cubanes, squares, rods, wheels, chains, etc. ranging in nuclearity from two[1] to eighty-four[2] metal centers. Wheel-shaped complexes of various transition metals including Ni, Fe, and Mn are of particular interest, not only for their aesthetic appeal, but also for their often fascinating magnetic properties.[3]

For example, odd-numbered molecular wheels, such as the [Cr_8Ni] species studied by Winpenny *et al.,* [4] are of interest for studying spin frustration. This phenomenon occurs when all interactions between spin pairs cannot be optimized simultaneously.[5] This has been extensively studied in polynuclear transition metal complexes that exhibit geometric frustration leading to the competition between ferromagnetic and antiferromagnetic interactions.[6] However, the simplest systems where spin frustration could be observed are odd-membered rings of antiferromagnetically coupled spins.[5]

Antiferromagnetic molecular wheels are also of great interest as they show quantum tunneling of the Néel vector which is not normally observed in extended antiferromagnets since the lowest lying excitations are spin waves. In antiferromagnetic wheels, however, the lowest lying excitations correspond to rotation of the Néel

vector.[7-9] These magnetic and quantum phenomena make wheel-shaped SMMs some of the most promising candidates for use as qubits in quantum computation devices. [10]

The family of wheel-shaped manganese SMMs is steadily growing and ranges in nuclearity from the smallest [Mn_4] wheel reported by Beedle *et al*.[11] to the [Mn_{84}] wheel[2] which is the largest SMM known to date. Other manganese wheels include a [Mn_{24}] complex,[12] a series of [Mn_{22}] wheels,[13] and a [Mn_{16}] wheel, [$Mn_{16}O_2(OMe)_{12}(tmp)_8(O_2CMe)_{10}$] where $tmpH_3$ is tris-hydroxymethyl propane, which boasts the largest reported spin ground state for a wheel-shaped SMM at S = 14.[14]

The larger molecular wheels listed above are constructed of smaller subunits such as triangles or cubanes which are linked together by various bridging ligands and/or metal ions. However, a smaller sub-set of the family of molecular wheels is the so-called "single-stranded wheels" which are constructed of a single continuous loop of oxo-bridged metal ions. The first reported single-stranded wheel is the well-studied Ni species[15,16] that consists of twelve ferromagnetically-coupled Ni(II) ions. This complex possesses a S = 12 ground state and exhibits magnetization hysteresis below 0.4 K.

Since the [Ni_{12}] wheel, a large number of manganese single-stranded molecular wheels have been synthesized including a large family of [Mn_{12}][17-20] wheels and several [Mn_{16}][21,22] wheels. These particular manganese wheels exhibit SMM behavior and have been extensively studied in our laboratory as detailed below.

4.1.2. [Mn_{12}] Single-Stranded Wheels

In 2005, a series of [Mn_{12}] single-stranded wheels were reported by Rumberger *et al.*[17,18] The three complexes described re [$Mn_{12}(O_2CMe)_{14}(bdea)_8$], [$Mn_{12}(O_2CMe)_{14}(edea)_8$] and [$Mn_{12}(O_2CMe)_{14}(mdea)_8$], where $mdeaH_2$, $edeaH_2$, and $bdeaH_2$ are N-methyl-, N-ethyl-, and N-butyldiethanolamine, respectively. In 2009, Shah *et al.*[19] reported three additional single-stranded [Mn_{12}] wheels which are isostructural to the previously reported wheels. These new wheels are [$Mn_{12}(O_2CMe)_{14}(adea)_8$], [$Mn_{12}(O_2CCH_2CH_3)_{14}(edea)_8$], and [$Mn_{12}(O_2CMe)_2(O_2CCH_2CH_3)_{12}(edea)_8$] where $adeaH_2$ is N-allyldiethanolamine.

Each of these wheels consists of six Mn(II) and six Mn(III) ions arranged in an alternating, single-stranded wheel topology with inversion site symmetry. An ORTEP [$Mn_{12}(O_2CMe)_{14}(adea)_8$], henceforth denoted as [Mn_{12}-allyl], is shown in Figure 4.1.[18,19] Our attention was focused on the study of this particular [Mn_{12}] wheel due to the fact that, despite having a similar structure and magnetic susceptibility compared to the other wheels in this family, the [Mn_{12}-allyl] wheel exhibits unique magnetization vs. magnetic field hysteresis properties.

The dc magnetic susceptibility data for [Mn_{12}-allyl] in the temperature range of 300-1.8 K in applied fields of 0.01, 0.1., and 1 T (Figure 4.2) shows a typical field-dependence below 15 K, as was observed in all of the [Mn_{12}] wheels. Also, the reduced magnetization data for [Mn_{12}-allyl] shows a significant axial-type anisotropy and was fit at high fields to $S = 9$, $g = 1.9$ and $D/k_B = -0.47$ K while data collected at lower fields were fit with the parameters $S = 9$, $g = 2$ and $D/k_B = -0.33$ K as shown in Figure 4.3.[19]

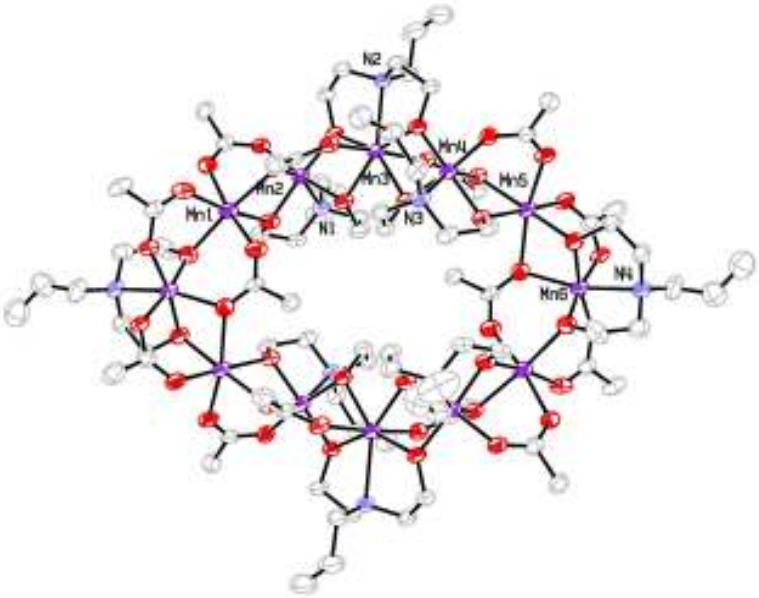

Figure 4.1. ORTEP of [Mn_{12}-allyl] with hydrogen atoms omitted for clarity and thermal ellipsoids at 50% probability level.

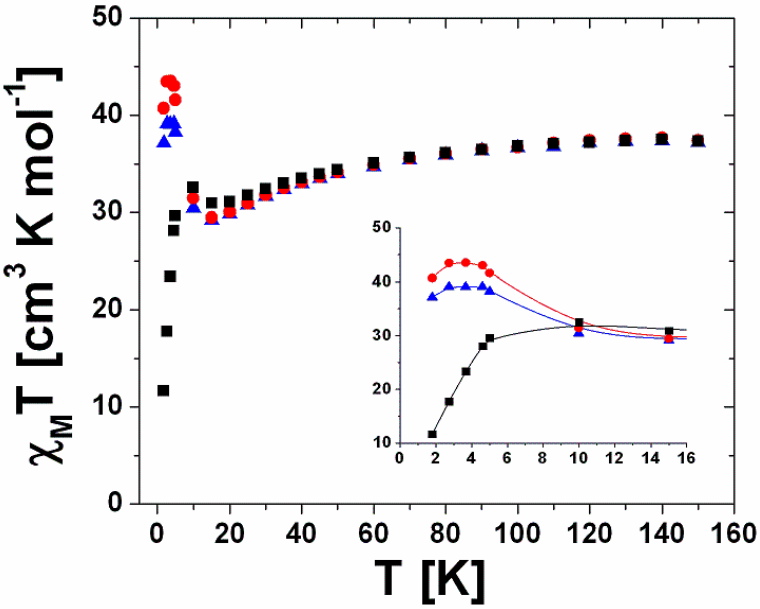

Figure 4.2. $\chi_M T$ *vs.* T for [Mn_{12}-allyl] collected at applied fields of 1T (■), 0.1T (▲) and 0.01T (●) and in the temperature range of 300-1.8 K.

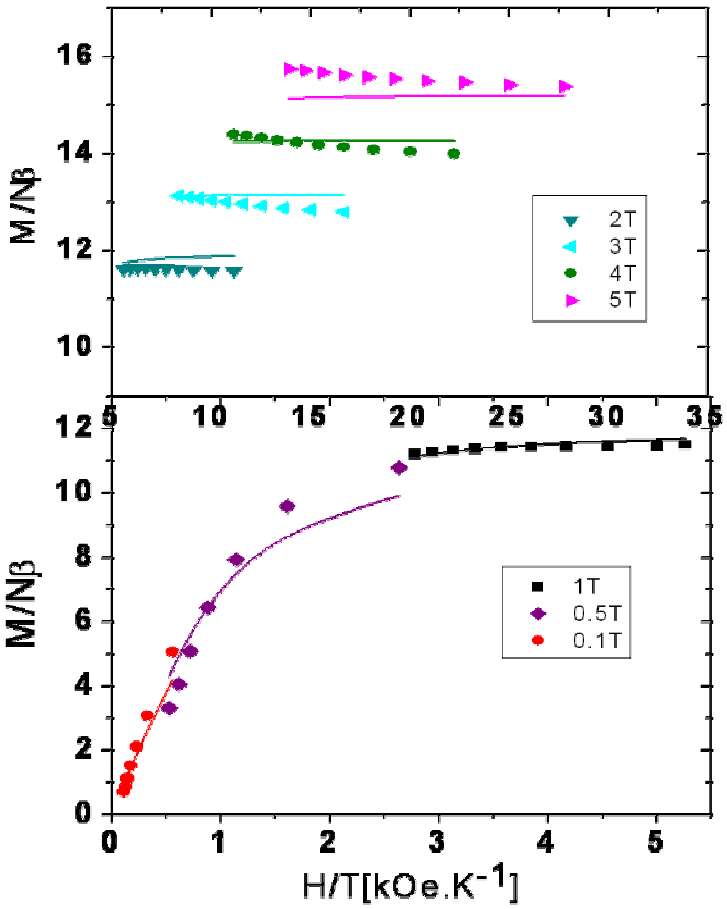

Figure 4.3. Reduced magnetization (M/N_β) vs. H/T for [Mn_{12}-allyl] collected in applied fields of 5, 4, 3, and 2 T (top) and 1, 0.5, and 0.1 T (bottom) in the temperature range of 1.8 to 10 K. Theoretical fits are shown as solid curves with parameters (top) $S = 9$, $g = 1.9$ and $D/k_B = -0.47$ K (-0.33 cm^{-1}) and (bottom) $S = 9$, $g = 2$, $D/k_B = -0.33$ K (-0.23 cm^{-1}).

All of the [Mn_{12}] single-stranded wheels show a frequency-dependent out-of-phase signal in the ac susceptibility indicating slow magnetization relaxation relative to the frequency of the oscillating ac field at low temperatures. However, since a full peak in the out-of-phase signal cannot be seen above the lower temperature limit of the measurements (1.8 K), the activation barrier (E_a) to this magnetization reversal cannot be quantified from these data. Figure 4.4 shows the in-phase and out-of-phase ac susceptibility for [Mn_{12}-allyl]. Extrapolation of the low frequency ac data suggests a S = 7 ground state as predicted by the spin-only formula and will later be substantiated by the hysteresis data.[19]

Magnetization hysteresis measurements were carried out in the laboratory of Professor Enrique del Barco at the University of Central Florida using a high-sensitivity micro-Hall effect magnetometer. These data can provide valuable information such as the spin ground state, blocking and crossover temperatures, and the anisotropy parameters that characterize the spin Hamiltonian for complexes. These measurements made on this family of [Mn_{12}] wheels, in particular [Mn_{12}-allyl], have produced interesting data which has lead to a benchmark study in the field of SMMs.

Magnetization hysteresis measurements on a single crystal of [Mn_{12}-allyl] in the temperature range of 0.27-0.9 K were measured. The hysteresis loops collected at 270 mK at sweep rates of 0.1, 0.2, and 0.4 T/min are shown in the top portion of Figure 4.5. It is clear from the figure that steps due to quantum tunneling of the direction of magnetization (QTM) are observed at regular intervals in the hysteresis loops.[23,24] The bottom portion of Figure 4.5 shows the first derivative of magnetization (*dM/dH*)

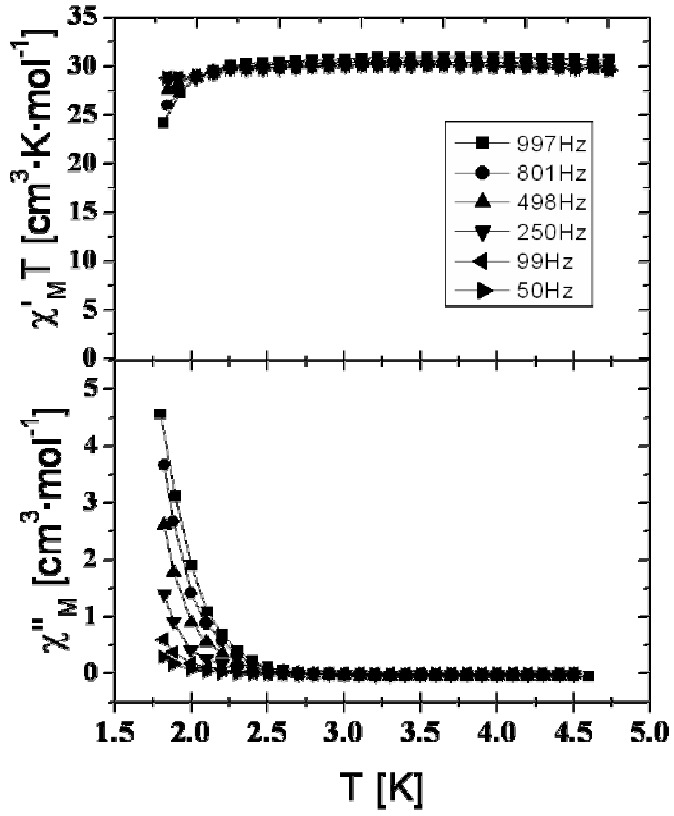

Figure 4.4. In-phase (χ_M') and out-of-phase (χ_M'') ac magnetic susceptibility for [Mn_{12}-allyl] collected in an ac field of 3 Oe oscillating at frequencies of 50-1000 Hz.

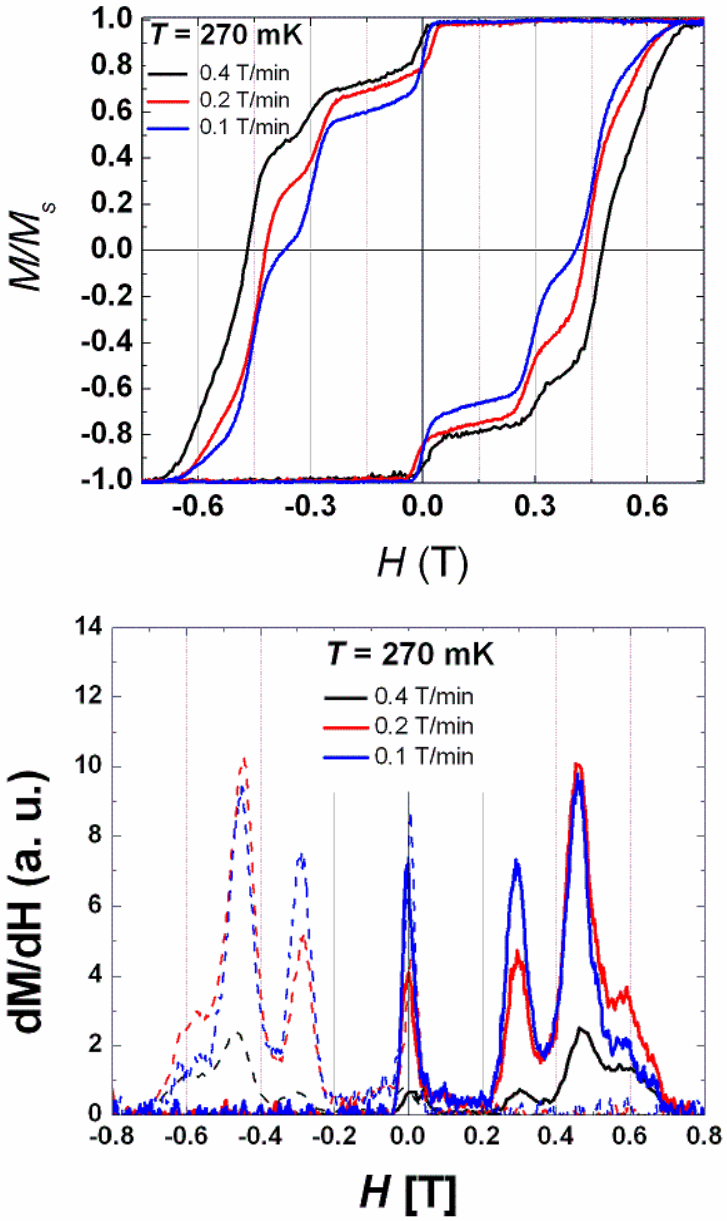

Figure 4.5. (Top) Single-crystal magnetization vs. applied magnetic field hysteresis loops for [Mn_{12}-allyl] collected at 0.27 K and sweep rates of 0.1, 0.2 and 0.4 T/min. (Bottom) First derivative (*dM/dH*) plotted vs. applied field (*H)*.

plotted vs. the field (*H)* where the peaks correspond to the fields at which QTM resonances are observed in the hysteresis data.[19]

Resonances observed at 0.0 T, 0.29 T, and 0.58 T can be explained in terms of QTM between opposite projections of a rigid spin S = 7 along the easy magnetic axis of the molecule (using the parameters given above and H_k = k×0.29 T, with k = 0, 1 and 2). The rigid spin model assumes that the wheel as a whole acts as a ferromagnetically coupled entity with a total spin of S = 7. The spin projection of the lowest energy spin states for a rigid S = 7 complex (shown in Figure 4.6) show the three possible QTM resonances corresponding to k = 0, 1, and 2. However, there are two extra resonances observed in the hysteresis measurements that cannot be explained by this model; one at 0.15 T which is only observed above 0.5 K (not shown in Figure 4.5) and the other at 0.45 T only observed at low temperatures.[19]

Further studies on this complex by Ramsey *et al.*[25] explain these extra QTM resonances with a "dimer" model of the complex in which the wheel behaves as two rigid S = 7/2 halves ferromagnetically coupled together to give an overall S = 7 complex (see Figure 4.7). A closer look at the bond distances and angles in [Mn_{12}-allyl] as compared to the other [Mn_{12}] wheels suggested a weaker exchange coupling between the Mn5 and Mn6 ions at opposite sides of the wheel was entirely possible since the ions are separated by a larger distance at these sites than anywhere else in the molecule. The average Mn···Mn distance throughout the [Mn_{12}-allyl] wheel is slightly shorter (d_{av} = 3.173Å) than that of the analogous wheels reported in the same publication (d_{av} = 3.1988 and 3.1956 Å) Furthermore, the ratio between the weak contact point in each

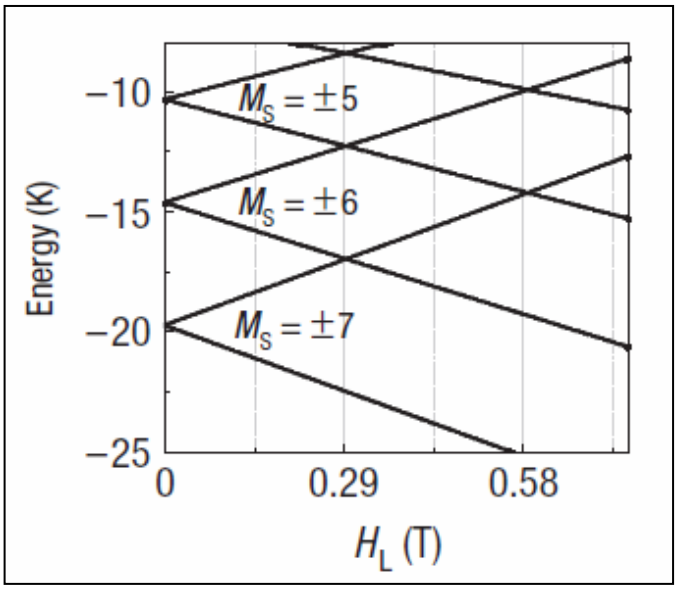

Figure 4.6. Magnetic field behavior of lowest-lying energy states for a rigid S = 7 spin system.

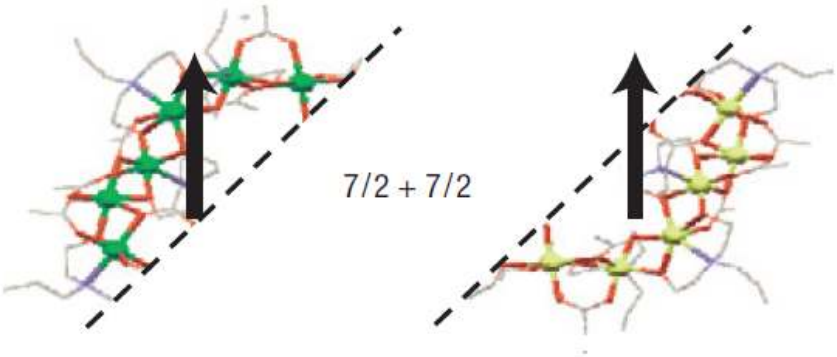

Figure 4.7. Schematic representation of two ferromagnetically coupled S = 7/2 halves of the [Mn_{12}-allyl] wheel.

wheel (between Mn5 and Mn6) with the average Mn···Mn distance is slightly larger in [Mn_{12}-allyl].[19]

Consequently, the molecule behaves as a dimer of two ferromagnetically exchange-coupled S = 7/2 halves giving rise to both M_S = 7 and M_S = 6 entangled spin states at low temperature whose avoided level crossings with magnetic field generate the observed extra resonances as depicted in Figure 4.8.[25] Part *a* of Figure 4.8 shows the lowest energy levels of the coupled spin system which result from linear combinations of the (7/2, 7/2), (7/2, 5/2), and (5/2, 7/2) states. Furthermore, transverse interactions (J_x and J_y>0) break the degeneracy of the M_S = 6 energy level giving rise to both symmetric and antisymmetric states. Figure 4.8*c* shows the magnetic field behavior of the energy levels as a result of the exchange-coupled model which clearly predicts the three QTM resonances also explained by the rigid S=7 model (shown again in Figure 4.8b for comparison) as well as the three additional QTM resonances. The two k = 1 resonances clearly correspond to the transitions between the ground state and either the symmetric or antisymmetric M_S = 6 excited state with the antisymmetric transition occurring at 0.45 T. The other two extra resonances are linked to QTM from excited states only populated at high temperatures.[25]

Another interesting consequence of the symmetric and antisymmetric nature of energy levels of the exchange-coupled dimer model is that they exhibit Berry phase intereference,[26-28] as described in detail in the Introduction Chapter. The study of the [Mn_{12}-allyl] wheel has provided yet another example of the importance of entanglement of states for coherent manipulation of individual spin states. In the case of two interacting SMMs (as in the two halves of [Mn_{12}-allyl]), it also possible that the observ-

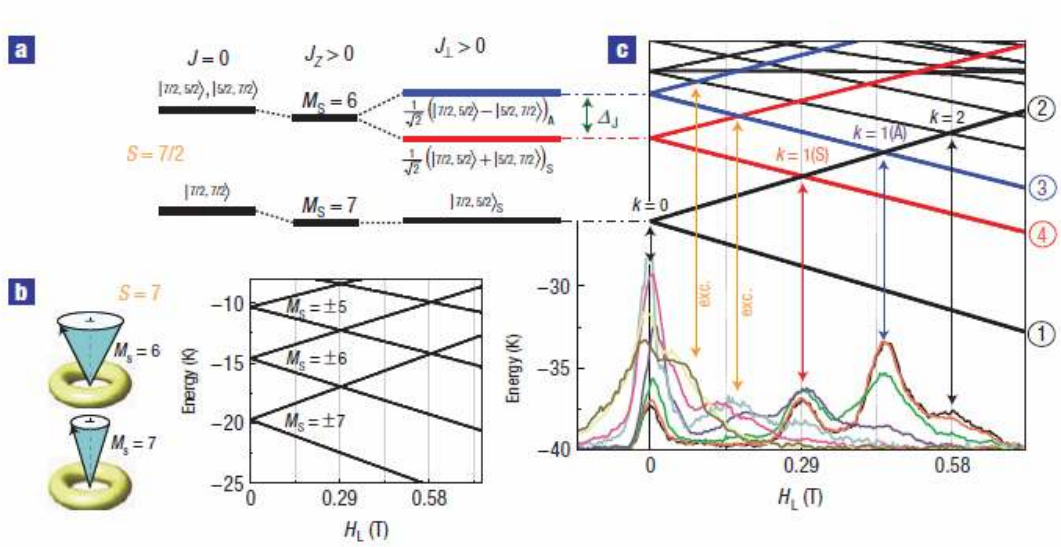

Figure 4.8. (a) Lowest-lying energy levels of exchange-coupled dimer model for [Mn_{12}-allyl] showing how transverse interactions lift the degeneracy in the M_S = 6 excited state. (b) Magnetic field behavior of the lowest energy levels assuming rigid spin S = 7. (c) Magnetic field behavior of the energy levels assuming the exchange-coupled model showing correlation to the first derivative of the hysteresis plot for [Mn_{12}-allyl].

ed oscillation of the tunneling probability may be attributed to two competing Berry phases. Thus, this SMM is a remarkable system for experimental and theoretical studies of such topological effects.[25]

4.1.3. [Mn_{16}] Single-Stranded Wheels

The first single-stranded [Mn_{16}] wheel was reported by Murugesu *et al*. in 2005.[21] Since then, two structurally analogous wheels have been synthesized and studied by our group. These two complexes, reported in 2009, are shown as ORTEPs in Figure 4.9 with the formulas $[Mn_{16}(O_2CCH_3)_8(O_2C(CH_2)_2CH_3)_8(teaH)_{12}] \cdot 10$ MeCN (abbreviated [Mn_{16}]-MeCN) and $[Mn_{16}(O_2CCH(CH_3)_2)_{16}(teaH)_{12}] \cdot 4CHCl_3$ (abbreviated [Mn_{16}]-$CHCl_3$) where $teaH_3$ is the triethanolamine ligand.[22]

These complexes comprise a [Mn_{16}] wheel with a closed sinusoidal or saddle-shaped topology with eight Mn(II) and eight Mn(III) ions alternating in a single-stranded arrangement. The orientation of the Jahn-Teller axes around the high-spin Mn(III) ions is shown in Figure 4.10. This figure also shows the differing H-bonding interactions (also shown in Figure 4.10) involved in these two structurally similar complexes.[22] Both wheels exhibit intramolecular H-bonding between the protonated alcohol arm of the $teaH^{2-}$ ligand, which is bound to a seven-coordinate Mn(II) ion, and a neighboring oxygen atom of a bridging acetate ligand. The free alcohol arms on the outsides of either wheel are involved in intermolecular H-bonding with acetate and *n*-butyrate oxygen atoms or other unbound alcohol arms of adjacent wheels.[22]

The main difference in the H-bonding of these two wheels comes with the four additional unbound alcohol arms located on the interior of the wheel. In [Mn_{16}]-MeCN,

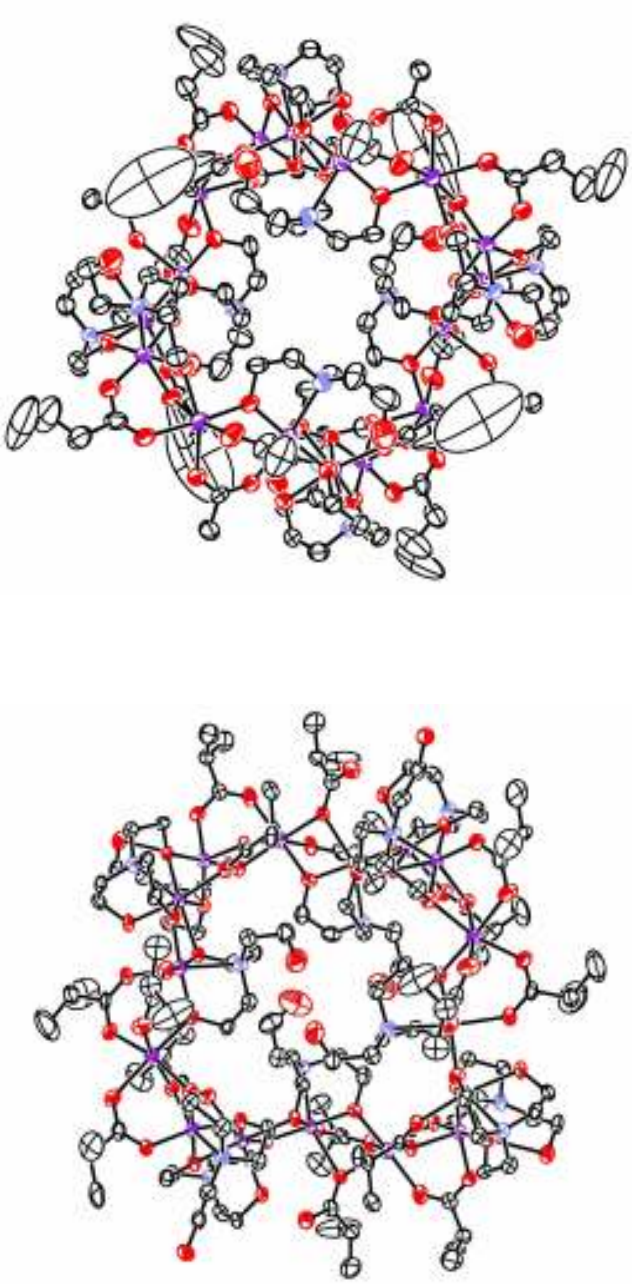

Figure 4.9. ORTEP of $[Mn_{16}]$-MeCN (top) and $[Mn_{16}]$-$CHCl_3$ (bottom) with thermal ellipsoids drawn at 30% probability level and hydrogen atoms omitted for clarity.

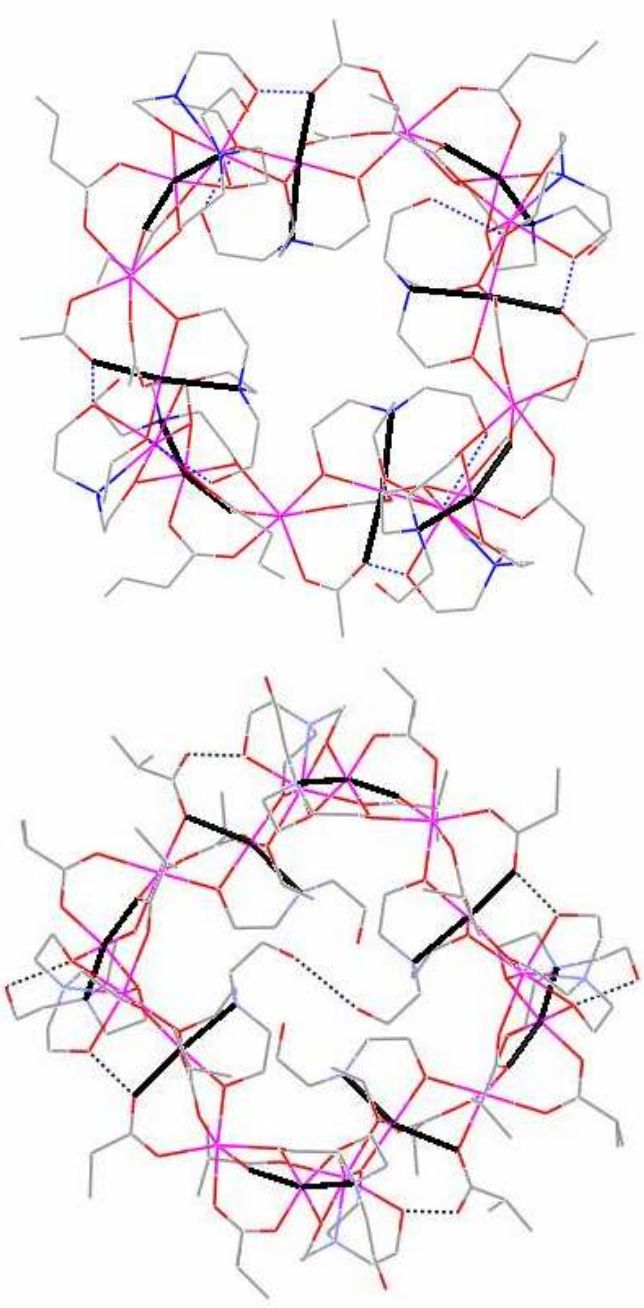

Figure 4.10. Intramolecular H-bonding in [Mn_{16}]-MeCN (top) and [Mn_{16}]-$CHCl_3$ (bottom) with Jahn-teller axes highlighted in black.

all of these free alcohol arms arm folded back in towards the wheel and H-bonded to nearby bridging alkoxide oxygen atoms. However, in $[Mn_{16}]$-$CHCl_3$, the free alcohol arms are bent outward into the central void space of the wheel, two of which are H-bonded to each other forming a weak interaction (~2.7 Å) across the interior of the wheel.[22]

The dc magnetic susceptibility data for both $[Mn_{16}]$ wheels were collected at fields of 0.01, 0.1, and 1 T from 300-1.8 K. Plots of the $\chi_M T$ *vs.* T data (Figure 4.11) show a similar field-dependence below 15 K as observed in the $[Mn_{12}]$ single-stranded wheels (see Figure 4.2). Fitting of high- and low-field M/N_B *vs.* H/T data (Figures 4.12 and 4.13) gave S = 13 and S = 14 ground state for $[Mn_{16}]$-MeCN and $[Mn_{16}]$-$CHCl_3$, respectively.[22]

The in-phase and out-of-phase ac susceptibility data for both complexes are shown in Figure 4.14. Both clearly show the emergence of a weak frequency-dependent out-of-phase signal in the ac susceptibility around 2.5 K at oscillating field frequencies of 250-10,000 Hz, indicative of an energy barrier to the reversal of the direction of magnetization.[22] The low-frequency in-phase data was extrapolated to zero K in order to determine a better estimate of the spin ground state in the absence of an applied dc field. This analysis suggested a S = 12 and S = 11 ground state predicted by the spin-only formula for $[Mn_{16}]$-MeCN and $[Mn_{16}]$-$CHCl_3$, respectively.[22]

So far, the magnetic properties of these $[Mn_{16}]$ wheels are similar to that of other single-stranded wheels. However, the magnetization hysteresis data is quite intriguing. The absence of steps in a hysteresis loop is common for large SMMs which are more susceptible to step-broadening effects. Such effects arise from the presence of low-lying

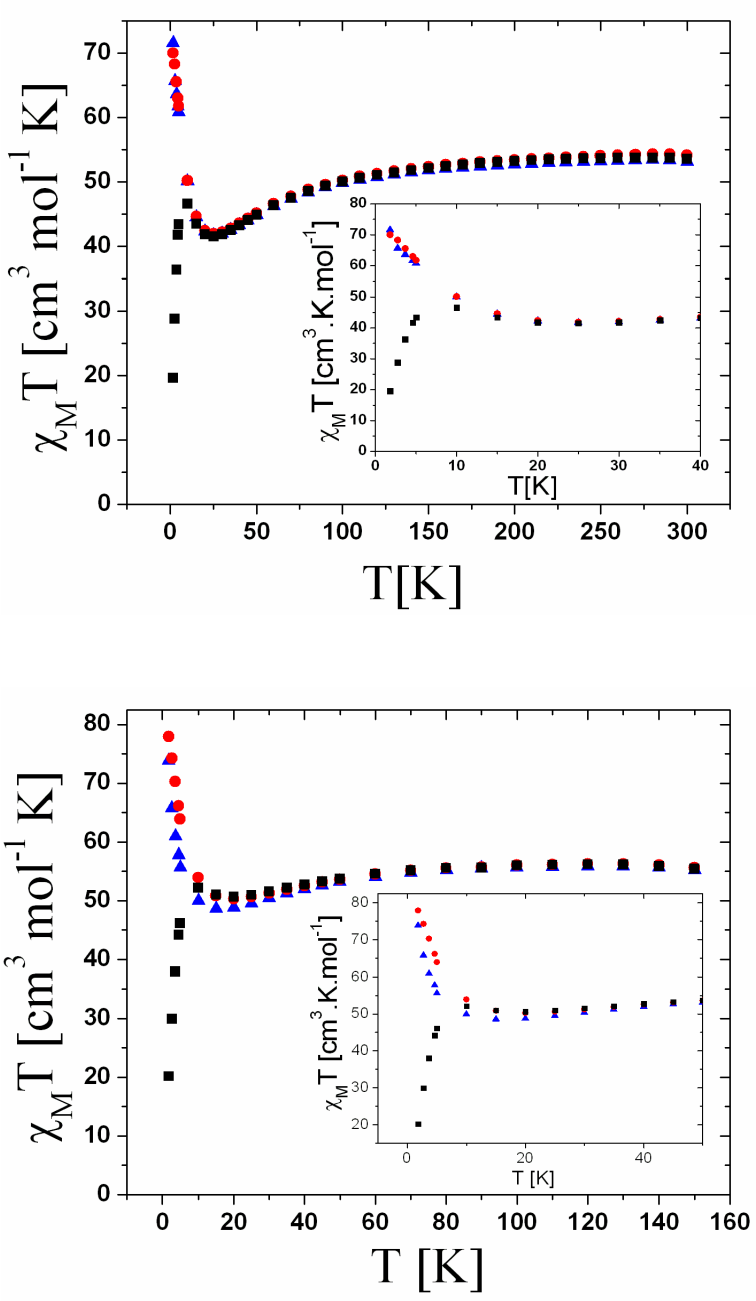

Figure 4.11. $\chi_M T$ *vs.* T for $[Mn_{16}]$-MeCN (top) and $[Mn_{16}]$-$CHCl_3$ (bottom) collected in applied fields of 1T (■), 0.1T (▲) and 0.01T (●).

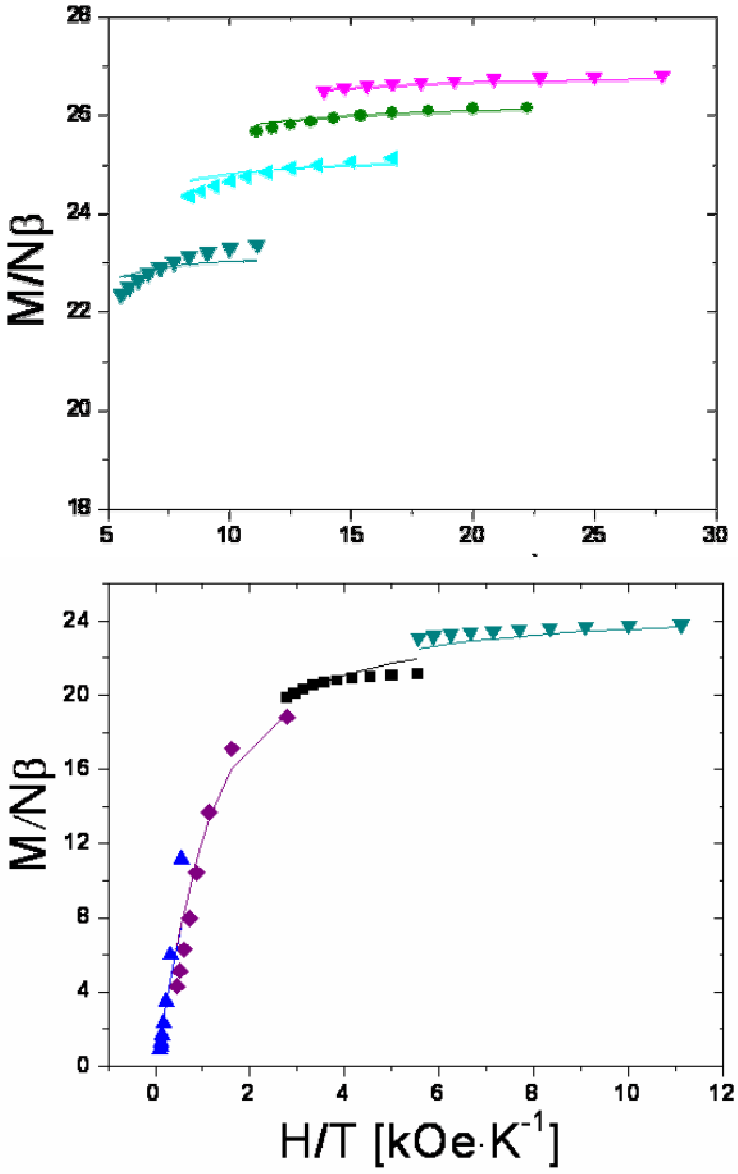

Figure 4.12. Reduced magnetization (M/N_β) vs. H/T for [Mn_{16}]-MeCN collected in applied fields of (top) 5T (▼), 4T (●), 3T (◀), 2T (▼) and (bottom) 2T (▼), 1T (■), 0.5T (♦), 0.1T (▲) in the temperature range of 1.8 to 10 K. Theoretical fits are shown as solid curves with parameters (top) S = 13, g = 2.1 and D/k_B = -0.19 K (-0.13 cm^{-1}) and (bottom) S = 13, g = 1.8, D/k_B = -0.04 K (-0.03 cm^{-1}).

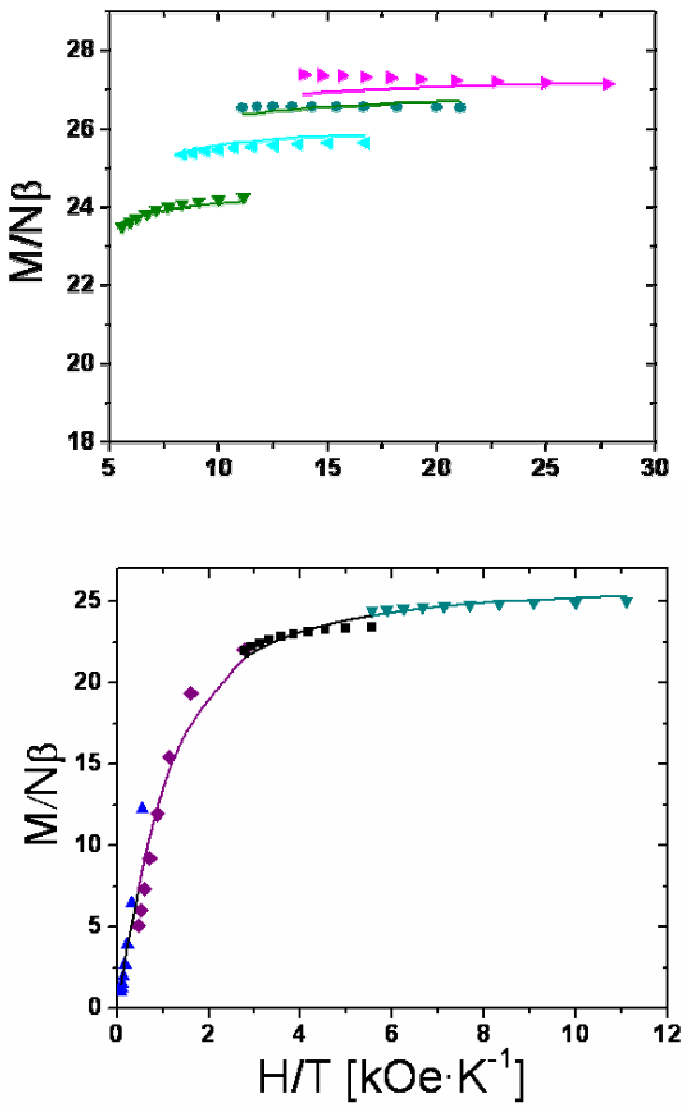

Figure 4.13. Reduced magnetization (M/N_β) vs. H/T for $[Mn_{16}]$-$CHCl_3$ collected in applied fields of (top) 5T (▶), 4T (●), 3T (◀), 2T (▼) and (bottom) 2T (▼), 1T (■), 0.5T (♦), 0.1T (▲) in the temperature range of 1.8 to 10 K. Theoretical fits are shown as solid curves with parameters (top) $S = 14$, $g = 2.0$ and $D/k_B = -0.12$ K (-0.08 cm^{-1}) and (bottom) $S = 13$, $g = 1.9$, $D/k_B = -1.21$ K (-0.84 cm^{-1}).

excited states as well as a greater distribution of molecular environments. Even the smallest changes in local environments can have significant effects on the magnetic properties of SMMs. The numerous chelating ligands and solvate molecules in these larger complexes often impart disorder in the crystal structure which leads to this distribution of environments.

Some large SMMs which demonstrate this behavior include the $[Mn_{22}]$[14] and $[Mn_{84}]$[2] wheels discussed earlier as well as several other Mn clusters.[29-32] For the $[Mn_{84}]$ wheel, the absence of QTM steps in the hysteresis loops was attributed to the large number of disordered solvate molecules (water and chloroform) located in the interior of the wheel.[2] The $[Mn_{16}]$ wheel reported by Murugesu *et al.*[21] shows magnetization hysteresis at temperatures below 0.8 K but is also absent of any QTM steps, including a step at H = 0. Since all of the $[Mn_{16}]$ single-stranded wheels are similar in structure and magnetic properties, all of them were expected to exhibit this same behavior in their magnetization hysteresis.

However, the magnetization hysteresis measurements on a single crystal of $[Mn_{16}]$-$CHCl_3$ in the temperature range of 0.04 K to 1 K and a sweep rate of 0.2 T/ min (Figure 4.15) shows a prominent step due to QTM at H = 0.[22] This observation clearly indicates that $[Mn_{16}]$-$CHCl_3$ is indeed a SMM and, furthermore, is the largest SMM to show a step in the hysteresis loop due to QTM. The reason for the enhanced quantum behavior in this $[Mn_{16}]$ wheel is believed to be the smaller amount of disorder and co-crystallized solvate molecules as compared to the other $[Mn_{16}]$ wheels which reduces the number of microenvironments and lessens any step-broadening effects.[22] Once again, this study has shown the impact that small differences in intermolecular interact-

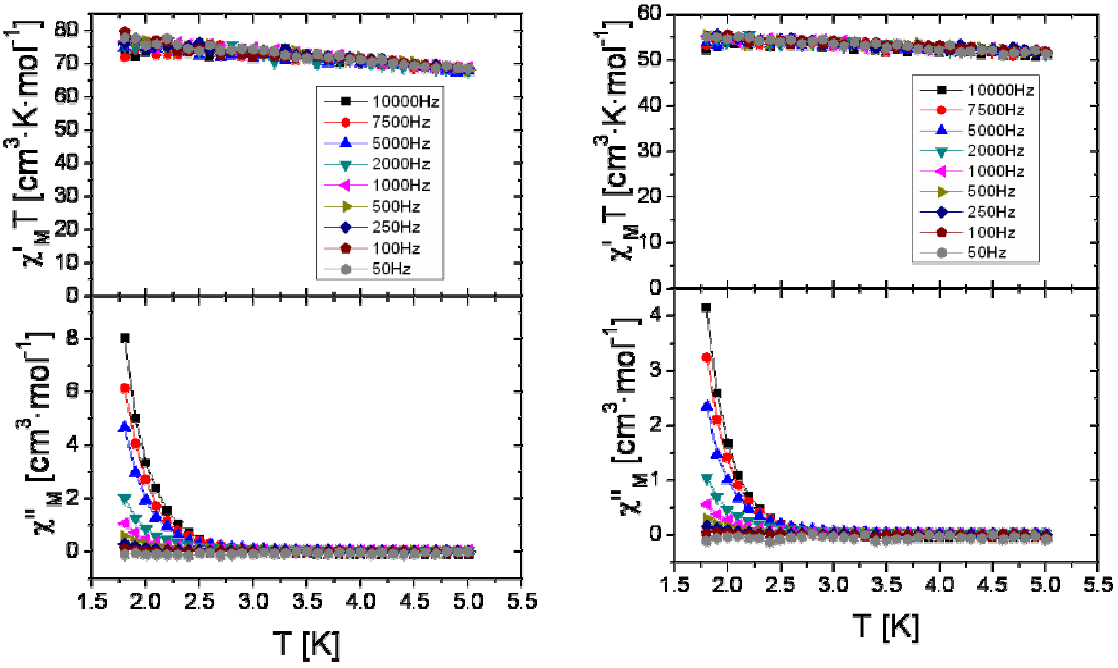

Figure 4.14. Ac magnetic susceptibility for $[Mn_{16}]$-MeCN (left) and $[Mn_{16}]$-$CHCl_3$ (right) collected in an applied ac field of 0.99 Oe oscillating at frequencies of 50-10,000 Hz.

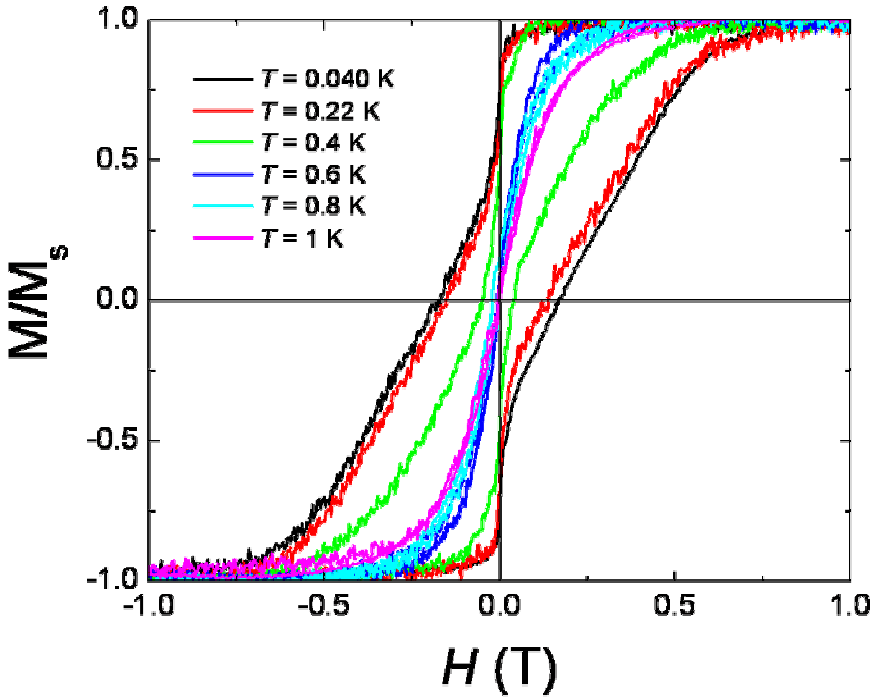

Figure 4.15. Temperature-dependent single-crystal magnetization hysteresis plot for $[Mn_{16}]$-$CHCl_3$ in the temperature range of 0.04-1 K and a sweep rate of 0.2 T/ min.

ions and environmental coupling factors can have on the magnetic and quantum properties of SMMs. In this chapter, a new single-stranded manganese wheel will be presented. This [Mn_{24}] wheel is the largest single-stranded wheel synthesized to date. Also, preliminary magnetic susceptibility studies suggest that it may have the highest ground state spin of any single-stranded molecular wheel to date.

4.2. Experimental Section

4.2.1. Preparation

All reactions were performed under aerobic conditions. All reagents and ligands were purchased from Sigma Aldrich and used without further purification.

[$Mn_{24}(O_2CMe)_{24}(mdea)_{18}$] · $5CH_2Cl_2$ (**10**). To a suspension of $Mn(O_2CMe)_2$ · $4H_2O$ (100 mg, 0.4 mmol) in 20 mL CH_2Cl_2 was added an excess of NEt_3 followed by two equivalents of H_2mdea (0.1 mL, 0.8 mmol). The solution was stirred at room temperature for approx. 4 hours or until all Mn(II) acetate dissolved. The resulting orange-brown solution was filtered by gravity, layered with pentane, and allowed to slowly evaporate. Dark brown block-shaped crystals were obtained after 1 month in <2% yield (35 mg). Elemental analysis for $C_{143}H_{280}Mn_{24}N_{18}O_{84}Cl_{10}$ (5268.91), % calc'd (found): C 32.60 (27.97), H 5.36 (6.06), N 4.79 (4.01). Selected IR data (KBr, cm^{-1}) 3416 (s, br), 1584 (s), 1491 (s), 1329 (w), 1277 (m), 1074 (m), 748 (w), 696 (w), 621 (w), 502 (w).

4.2.2. X-Ray Crystallography

Crystals were mounted on a CryoLoop© with Paratone-N© oil. Diffraction intensity data were collected at 100 K for complex **10** on a Bruker Smart Apex CCD diffractometer with Mo Kα radiation, integrated using the Bruker SAINT software program, and corrected for absorption using the Bruker SADABS program. The structure of complex **10** was solved by direct methods (SHELXS-97), developed by successive difference Fourier syntheses, and refined by full matrix least squares on all F^2 data. All non-hydrogen atoms were refined anisotropically by full-matrix least-squares techniques (SHELXL-97). All hydrogen atoms were placed using a riding model. Disordered solvate molecules (CH_2Cl_2) were treated by the Squeeze method, the details of which can be found in the CIF files. Crystallographic data and refinement parameters are found in Table 4.1.

4.2.3. Physical Measurements

FT-IR spectra were collected using a Thermo-Nicolet Avatar series spectrometer. Elemental analysis was performed by NuMega Resonance Labs (San Diego, CA). Dc magnetic susceptibility measurements were performed on a finely ground polycrystalline sample of complex **10**, restrained in eicosane to prevent torquing of the micro-crystallites in an externally applied magnetic field. Measurements were carried out on a Quantum Design MPMS-5 magnetometer equipped with a 5.5 T magnet. Magnetic susceptibility measurements were performed in the 1.8-300 K temperature range with applied fields of 0.1-50 kG. Ac magnetic susceptibilities measurements were obtained in the temperature range of 1-5 K, with a 3 Oe ac field

Table 4.1. Crystallographic data and refinement parameters for $[Mn_{24}(O_2CMe)_{24}(mdea)_{18}] \cdot 5CH_2Cl_2$ **(10)**.

Formula	$C_{143}H_{280}Cl_{10}Mn_{24}N_{18}O_{84}$
FW	5268.91
T [K]	100(2)
λ [Å]	0.71073
Crystal system	rhombohedral
Space group	R-3
a [Å]	25.063(5)
b [Å]	25.063(5)
c [Å]	33.459(7)
α [deg]	90
β [deg]	90
γ [deg]	120
V [Å^3]	18201(7)
Z	3
D_{calc} [mg m^{-3}]	1.442
Abs. coefficient [mm^{-1}]	1.387
F(000)	8118
Theta range [deg]	2.24 to 25.02
Comp. to theta [25.00°]	98.1 %
Max. and min. transmission	0.8737 and 0.7689
Data / restraints / param.	7032 / 0 / 404
Goodness-of-fit on F^2	1.069
R(F)[a] [I > 2σ(I)]	0.0828
R(wF^2)[b] [I > 2σ(I)]	0.2352
Largest diff. peak and hole [e.Å^{-3}]	1.476 and -0.746

[a] $R = \Sigma||F_o| - |F_c||/\Sigma|F_o|$. [b] $R(\omega F^2) = \{\Sigma[\omega(F_o^2 - F_c^2)^2]/\Sigma[\omega(F_o^2)^2]\}^{1/2}$; $\omega = 1/[\sigma^2(F_o^2) + (aP)^2 + bP]$, $P = [2F_c^2 + \max(F_o, 0)]/3$

oscillating at frequencies of 0.01-1 kHz, and a zero applied dc magnetic field employing a Quantum Design MPMS-2 magnetometer. Data were corrected for diamagnetic contributions resulting from the sample rod, capsule and eicosane. Corrections for diamagnetism were estimated from Pascal's constants yielding the overall paramagnetic contribution to the molar magnetic susceptibility.

4.3. Results and Discussion

4.3.1. Synthesis and Structure

A new single-stranded manganese wheel complex, $[Mn_{24}(O_2CMe)_{24}(mdea)_{18}] \cdot 5CH_2Cl_2$ (**10**) where H_2mdea is N-methyldiethanolamine, has been synthesized and characterized. This complex was synthesized from a 1:2 ratio of $Mn(O_2CMe)_2 \cdot 4H_2O$, and mdeaH_2 with an excess of triethylamine (NEt_3) in CH_2Cl_2. A similar synthesis was reported by Foguet-Albiol *et al.*[20] in 2005 in which $Mn(O_2CMe)_2$, H_2mdea, and NEt_3 were combined in a 1:1:1 ratio in MeCN. Interestingly, the resulting product was a single-stranded $[Mn_{12}]$ wheel, identical to Rumberger's complex[18] reported earlier in the same year. This shows just how easily new topologies of transition metal complexes can be discovered. By simply doubling the equivalence of the chelating amine in this reaction, the resulting wheel essentially doubled in size as well, $[Mn_{12}]$ to $[Mn_{24}]$. Also, if one were to use larger carboxylate ligands in place of acetate in a similar reaction, the common $[Mn_4]$ dicubane topology often results, most likely due to steric constraints. This type of result is observed in the syntheses of the benzoate, ferrocene, and betaine-substituted $[Mn_4]$ dicubanes described in Chapters 2 and 3.

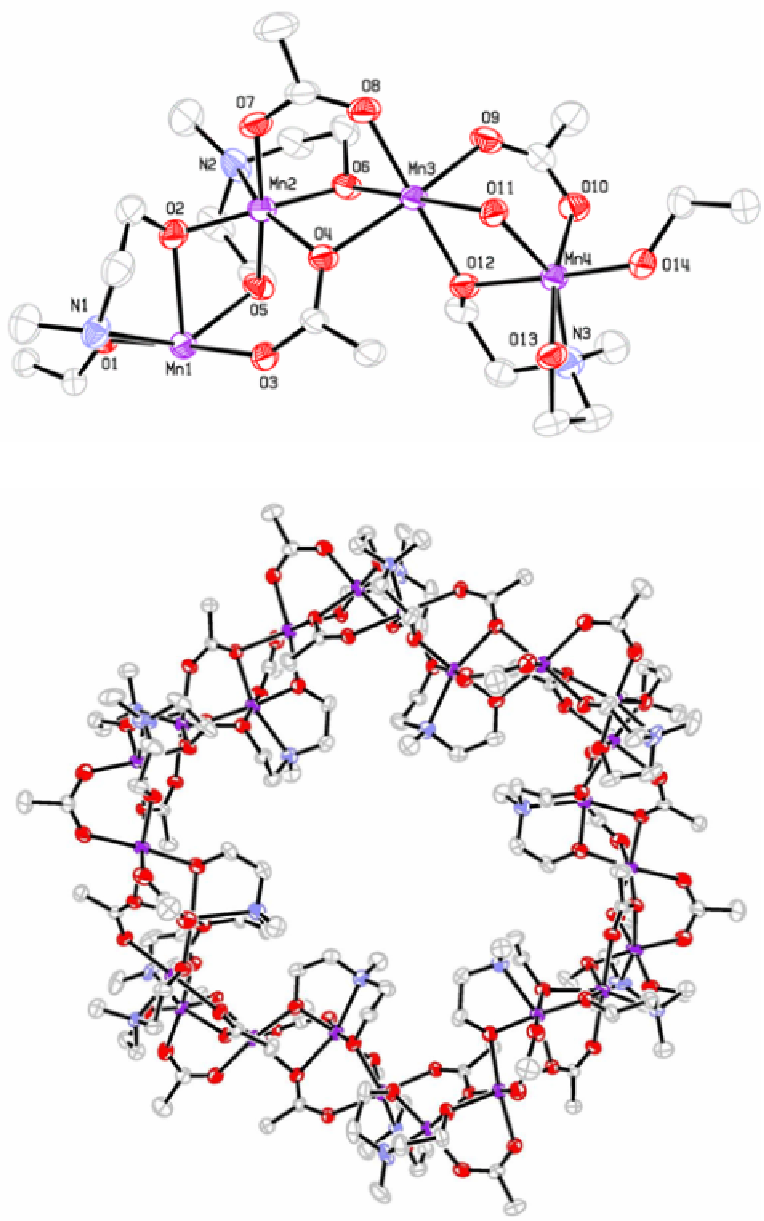

Figure 4.16. ORTEP of (top) asymmetric unit with labeling scheme and (bottom) full structure of $[Mn_{24}(O_2CMe)_{24}(mdea)_{18}] \cdot 5CH_2Cl_2$ **(10)** with thermal ellipsoids drawn at 50% probability level and hydrogen atoms omitted for clarity.

Table 4.2. Selected bond distances and bond valence sum analyses for **10**.

Bond	**Distance (Å)**	**Valence**	**Bond**	**Distance (Å)**	**Valence**
Mn2-O5	2.216	0.284	Mn2-O2	1.884	0.697
Mn1-O3	2.219	0.282	Mn2-O5	1.898	0.671
Mn1-O14	2.223	0.279	Mn2-O6	1.919	0.634
Mn1-O1	2.226	0.276	Mn2-O7	1.969	0.554
Mn1-O13	2.236	0.269	Mn2-O4	2.21	0.289
Mn1-O2	2.273	0.243	Mn2-N2	2.34	0.275
Mn1-N1	2.413	0.226			
Mn1	**Bond valence sum**	**1.859**	**Mn2**	**Bond valence sum**	**3.12**
Mn3-O12	2.124	0.364	Mn4-O14'	1.877	0.71
Mn3-O8	2.135	0.354	Mn4-O12	1.911	0.648
Mn3-O6	2.138	0.351	Mn4-O13'	1.912	0.646
Mn3-O9	2.164	0.327	Mn4-O10	1.972	0.549
Mn3-O11	2.205	0.293	Mn4-O11	2.236	0.269
Mn3-O4	2.215	0.285	Mn4-N3	2.36	0.261
Mn3	**Bond valence sum**	**1.974**	**Mn4**	**Bond valence sum**	**3.083**

Complex **10** crystallizes in the rhombohedral, R-3 space group with four independent Mn ions in the asymmetric unit as depicted in the ORTEP representation in Figure 4.16. The wheel consists of 12 Mn(II) ions (Mn1, Mn3, and their symmetry equivalents) and 12 Mn(III) ions (Mn2, Mn4, and their symmetry equivalents) alternating in a single-stranded fashion by means of bridging acetate and alkoxy ligands. The oxidation states of the Mn ions were determined by charge considerations, the presence of Jahn-Teller distortion around the high-spin Mn(III) ions, and bond valence sum analyses. Selected bond distances and corresponding bond valence sum analysis can be found in Table 4.2.

All of the doubly deprotonated $mdea^{2-}$ ligands chelate the Mn ions in a tridentate, μ_3-bridging mode. Half of the acetate ligands are found in the $\eta^1:\eta^1:\mu_2$-bridging mode whereas the other half adopts a $\eta^1:\eta^2:\mu_3$-bridging mode. Mn1 possesses heptacoordinate, pentagonal bipyramidal geometry with all of the coordination sites in the pentagonal plane occupied by the chelating $mdea^{2-}$ ligands (four alkoxy oxygen atoms and one nitrogen atom) and both axial sites occupied by an oxygen atom of a bridging acetate ligand. Mn3 is a hexacoordinate, distorted octahedron surrounded by six oxygen atoms (four from bridging acetate ligands and two from $mdea^{2-}$ ligands). The high-spin Mn(III) ions (Mn2 and Mn4) both adopt distorted octahedral geometries with the square planar coordination sites occupied by three alkoxy arms of $mdea^{2-}$ ligands and one bridging acetate. The axial sites are occupied by another acetate oxygen and the nitrogen atom of $mdea^{2-}$ giving rise to the Jahn-Teller axes N2-Mn2-O4 and N3-Mn4-O11 for Mn2 and Mn4, respectively.

The central cavity of each wheel is surrounded by six $mdea^{2-}$ ligands and is occupied by five disordered CH_2Cl_2 solvate molecules. The $C_3(S_6)$ rotation axis through the center of **10** is taken as the easy axis (z-axis) of the molecule and is co-linear with c-axis of the unit cell. The crystal packing of **10** is shown in Figure 4.17 down the a-axis (left) and c-axis (right) of the unit cell. The wheels stack along the c-direction forming layers of wheels in the ab-plane with all of their easy axes aligned parallel to one another. Figure 4.18 shows a space-filling model of **10** in which the entire structure is nearly 27 Å across with a central void space of ~12 Å in diameter.

To compare the shape and symmetry of this molecular wheel to the $[Mn_{12}]$ and $[Mn_{16}]$ members of this family of single-stranded wheels, wire-frame models of the top and side-on view of each type of wheel are shown in Figures 4.19-4.21. The nearly "football" shaped $[Mn_{12}$-allyl] complex is shown in Figure 4.19 with carbon atoms highlighted to emphasize the inversion symmetry. This molecular wheel is essentially planar and possesses very low C_i (S_2) site symmetry. Figure 4.20 shows two views of the "saddle-shaped" $[Mn_{16}]$ wheel which possess S_4 site symmetry as indicated by the highlighted atoms in the figure. Lastly, the $[Mn_{24}]$ wheel, **10**, has much higher symmetry than its lower nuclearity analogs, as depicted in Figure 4.21. The S_6 improper rotation axis lies in the center of the staggered triangles in the top-view of **10**. Symmetry and structure play an integral role in determining the magnetic and quantum properties observed for a molecular magnet.

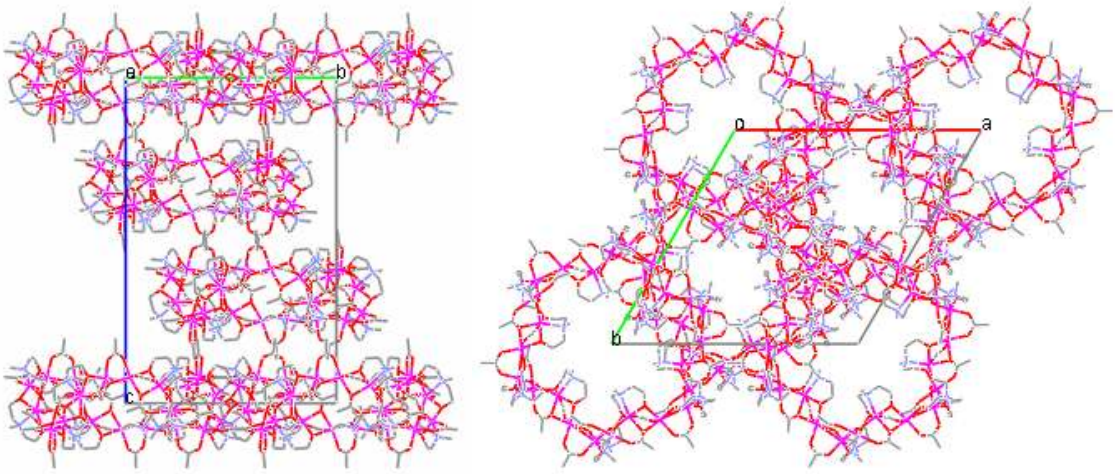

Figure 4.17. Crystal packing of $[Mn_{24}(O_2CMe)_{24}(mdea)_{18}] \cdot 5CH_2Cl_2$ **(10)** as viewed down the a-axis (left) and c-axis (right) of the unit cell.

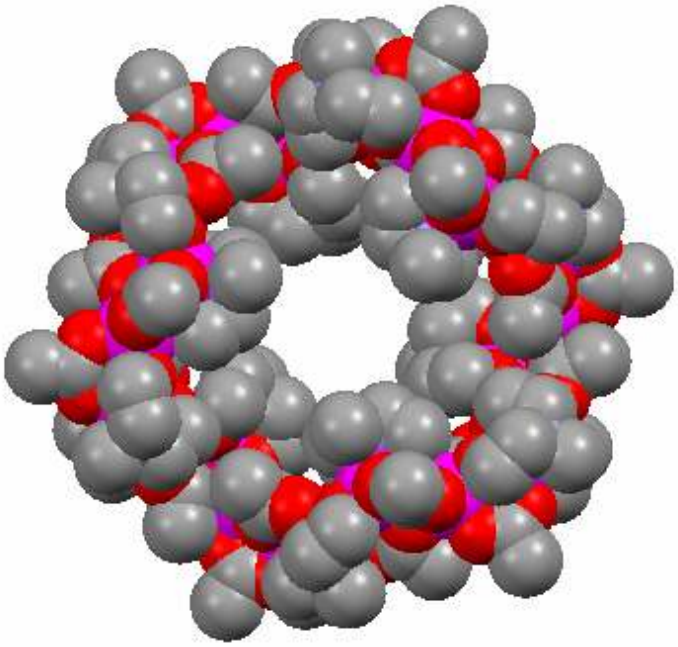

Figure 4.18. Space-filling model of $[Mn_{24}(O_2CMe)_{24}(mdea)_{18}] \cdot 5CH_2Cl_2$ **(10)**

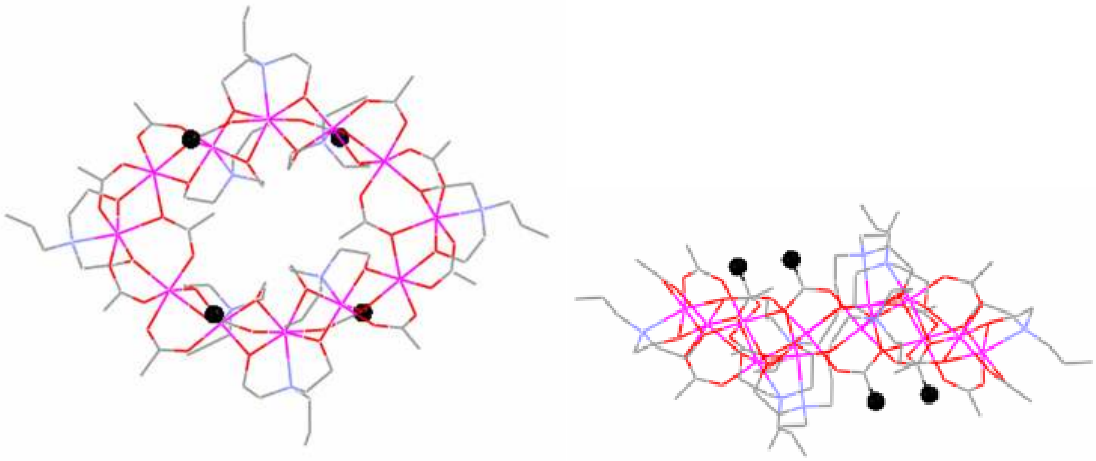

Figure 4.19. Top (left) and side (right) views of a [Mn_{12}] single-stranded wheel emphasizing the C_i symmetry. Highlighted carbon atoms represent four of the η^1,η^2,μ_3-acetate bridges.

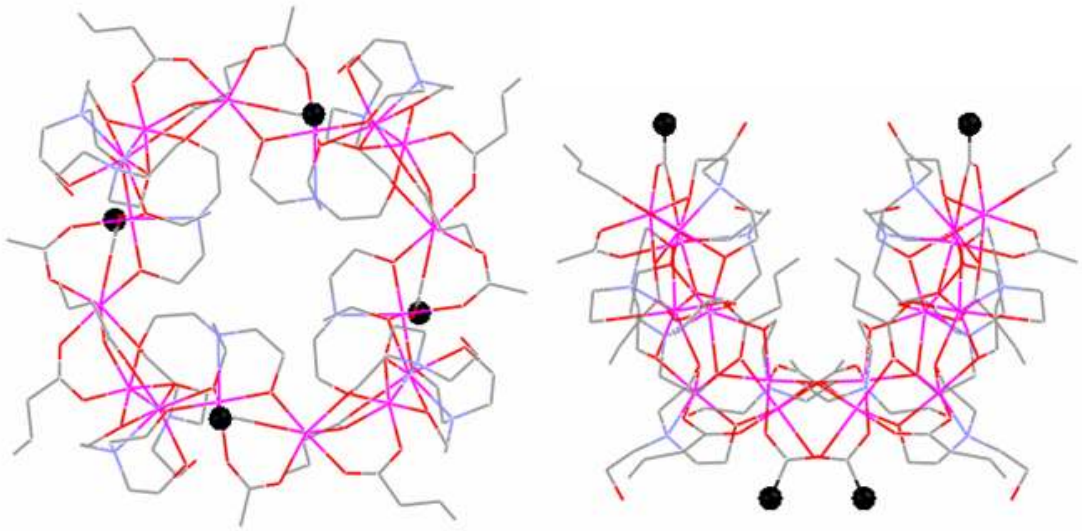

Figure 4.20. Top (left) and side (right) views of a [Mn_{16}] single-stranded wheel emphasizing the S_4 symmetry. Highlighted carbon atoms represent four of the η^1,η^1,μ_2-acetate bridges between Mn1 and Mn4 ions.

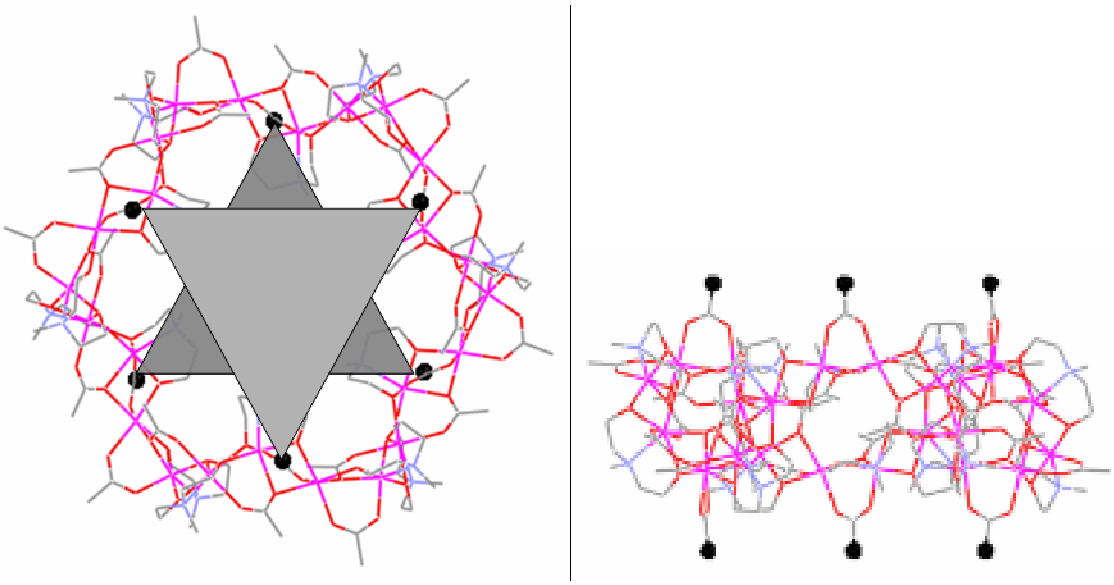

Figure 4.21. Top (left) and side (right) views of a [Mn_{24}] single-stranded wheel (**10**) emphasizing the S_6 symmetry. Highlighted carbon atoms represent four of the η^1,η^1,μ_2-acetate bridges between Mn3 and Mn4 ions.

4.3.2. Magnetic Susceptibility Studies

Direct current (dc) magnetic susceptibility data of a microcrystalline sample of complex **10** were measured from 300-1.8 K in applied dc fields of 0.01, 0.1, and 1 T, as shown in Figure 4.22 (low-temperature enlarged in Figure 4.22 inset). The $\chi_M T$ for **10** at 300 K is ~74 cm^3 mol^{-1} K which is lower than the spin-only value of 88.5 cm^3 mol^{-1} K calculated for twelve Mn(II) and twelve Mn(III) non-interacting ions. The data at all three fields are essentially superimposable as the temperature is lowered and the $\chi_M T$ gradually decreases. At 13 K, both the 0.01 and 0.1 T data reach a minimum $\chi_M T$ value of ~53 cm^3 mol^{-1} K before rising again to a maximum value of 74.2 and 69.5 cm^3 mol^{-1} K at 1.8 K for 0.01 and 0.1 T, respectively.

The $\chi_M T$ of **10** in a 1 T field, however, reaches a small plateau at ~52 cm^3 mol^{-1} K in the 13-7 K temperature range before plummeting to a minimum value of 26.3 cm^3 mol^{-1} K at 1.8 K. The dramatic drop in $\chi_M T$ is largely due to Zeeman effects (which increase with increasing field). This same field-dependence of the low-temperature $\chi_M T$ data was also observed for the single-stranded $[Mn_{12}]$[18-20] and $[Mn_{16}]$[21,22] wheels discussed in the introduction.

Field-dependent magnetization studies (called "reduced magnetization") were also carried out on **10** to determine the ground state spin and the axial zero-field splitting parameter, *D*. Measurements were taken at applied dc fields of 5, 4, 3, 2, and 1 T in the temperature range of 4-1.8 K The data for **10** (Figure 4.23) are plotted as reduced magnetization ($M/N_{\mu B}$) vs. H/T, where *M* is the magnetization, *N* is Avogadro's number, μ_B is the Bohr magneton, and *H* is the magnetic field. The isofields are non-

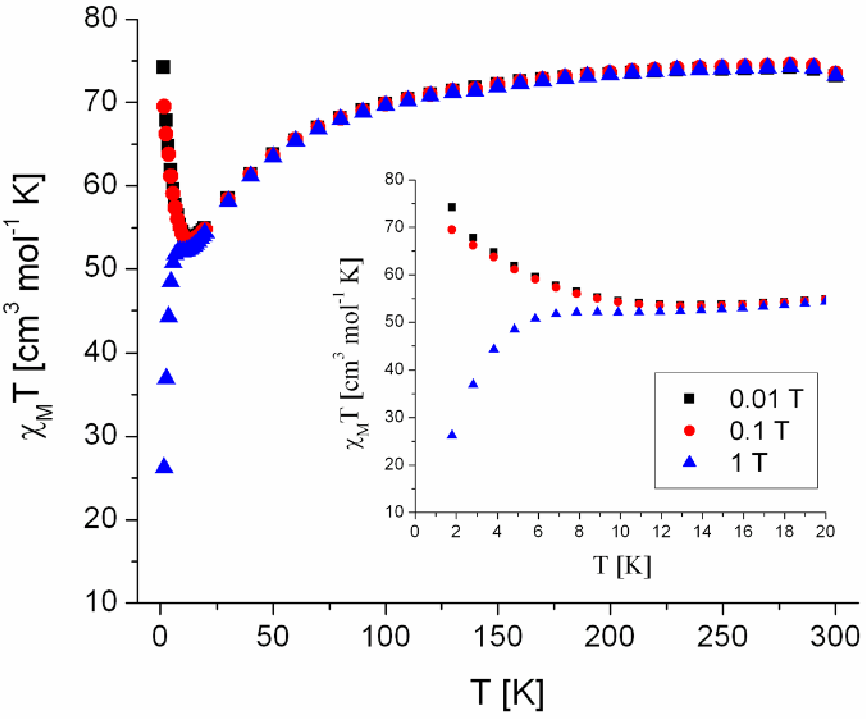

Figure 4.22. $\chi_M T$ vs. T for $[Mn_{24}(O_2CMe)_{24}(mdea)_{18}] \cdot 5CH_2Cl_2$ **(10)** at applied dc fields of 0.01, 0.1, and 1 T in the temperature range 300-1.8 K.

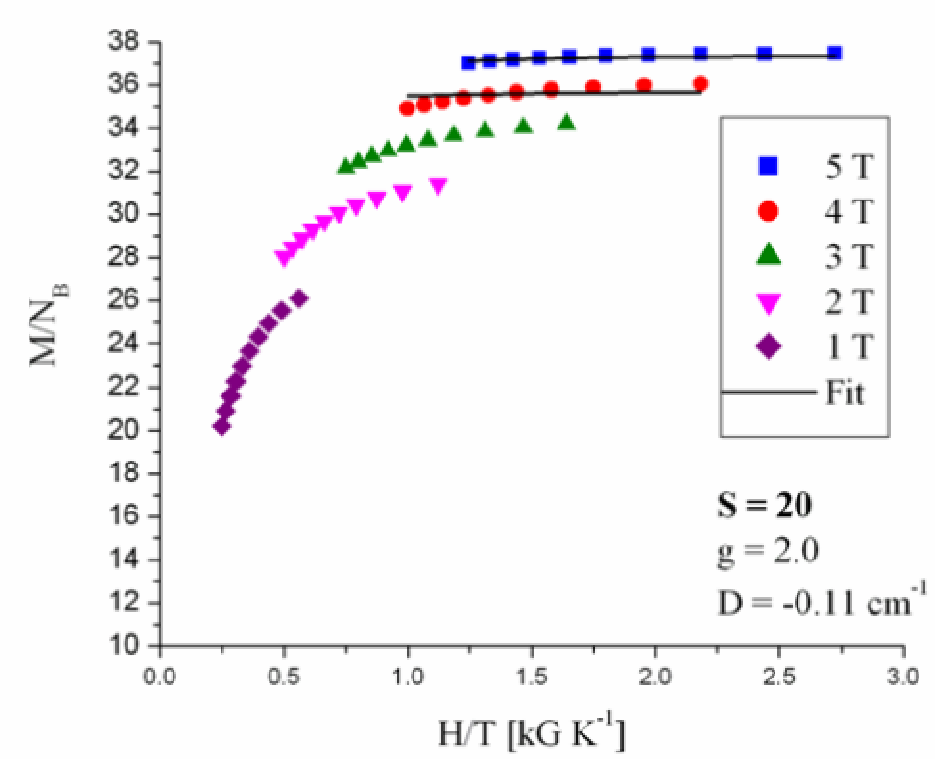

Figure 4.23. Reduced magnetization (M/N_B) vs. H/T for $[Mn_{24}(O_2CMe)_{24}(mdea)_{18}] \cdot 5CH_2Cl_2$ **(10)** at applied dc fields of 5, 4, 3, 2, and 1 T in the temperature range of 4-1.8 K. Theoretical fit shown as solid black curve.

superimposable, indicating some degree of zero-field splitting in the complex. The data were least-squares fit to a spin Hamiltonian including an isotropic Zeeman interaction and an axial zero-field splitting parameter (DS_z^2). The highest fields were best fit (solid lines in Figure 4.22) to a ground state spin of $S = 20$ with $g = 2.0$ and $D/k_B = -0.11$ cm^{-1} (-0.16 K). Fitting of all the fields proved problematic since the spin Hamiltonian assumes only one spin state is populated when in actuality there may be many excited states lying very close in energy to the ground state. Therefore, only the highest fields (5 and 4 T) were fit to this model where a single ground state is more likely to be populated as Zeeman splitting increases.

To determine if **10** possesses a potential energy barrier toward the reversal of the magnetization, alternating current (ac) magnetic susceptibility measurements were conducted in a 3 Oe ac field oscillating at frequencies of 997, 750, 500, 250, 100, 50, 25, and 10 Hz and in the absence of an applied dc field. The in-phase ac susceptibility (χ_M') reaches a maximum value of ~34 cm^3 mol^{-1} at 1.8 K but there is no frequency-dependent out-of-phase (χ_M'') signal detected (Figure 4.24). It is still possible, however, that the barrier to magnetization reversal may be observed at higher frequencies of the oscillating ac field (as in the case of Shah's [Mn_{16}] wheels)[22] or at temperatures below the lower limit of our instrument.

The lack of out-of-phase signal in the ac susceptibility may also be due to the high-symmetry of this molecular wheel. As was shown in the previous section, complex **10** crystallizes in a rhombohedral space group with S_6 site symmetry. In most manganese SMMs, the direction of magnetoanisotropy (or easy axis) is taken as the average direction of the Jahn-Teller distorted axes of the high-spin Mn(III) ions. In very

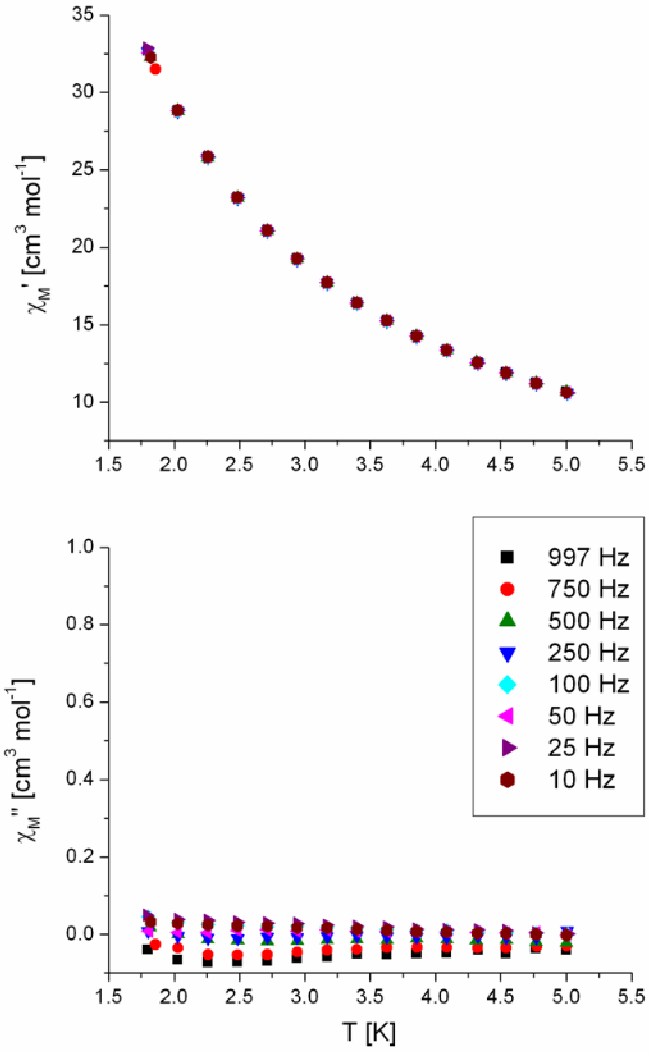

Figure 4.24. In-phase (χ_M') and out-of-phase (χ_M'') ac magnetic susceptibility for $[Mn_{24}(O_2CMe)_{24}(mdea)_{18}] \cdot 5CH_2Cl_2$ **(10)** collected in an ac field of 3 Oe oscillating at frequencies of 50-1000 Hz.

high-symmetry systems, the Jahn-Teller axes are often aligned orthogonal to one another and essentially "cancel" each other out leading to a diminution of the overall anisotropy of the molecule. Since the energy barrier to the reversal of magnetization between the "spin-up" and "spin-down" energy wells scales with $D\hat{S}_z^2$, even with a large spin ground state such as in **10**, this barrier height will not increase significantly if the *D*-value is very small. This is evident in the lower symmetry [Mn_{12}] single-stranded wheels in which the inversion center leads to parallel alignment of the Jahn-Teller axes of the molecule, maximizing the anisotropy. The *D*-value calculated from the reduced magnetization fits of [Mn_{12}-allyl] (see Figure 4.3) was nearly 3-times that of the *D*-value found for **10** despite the fact that the ground state spin is nearly half that of **10**.

The 10 Hz in-phase data from the ac susceptibility measurements were plotted as $\chi_M'T$ *vs.* *T*, fit to a linear regression line, and extrapolated to 0 K in order to provide an estimate of the ground state spin of **10** in zero field. The extrapolation (shown in Figure 4.25) gives a value of 62.2 cm^3 mol^{-1} K which corresponds closest to the spin-only value calculated for a $S = 11$ ground state (66 cm^3 mol^{-1} K). This result is much lower than the $S = 20$ ground state obtained from the fits of the reduced magnetization data. However, this discrepancy can most likely be explained by the presence of low-lying excited states. At low temperatures and in the absence of a dc field (as in the ac susceptibility measurements) the $S = 11$ spin state is likely populated. At higher fields and/or temperatures (as in the dc experiments, particularly at 4 and 5 T) higher energy spin-states, including $S = 20$, can be stabilized due to increased Zeeman splitting and subsequent mixing/crossing of energy levels.

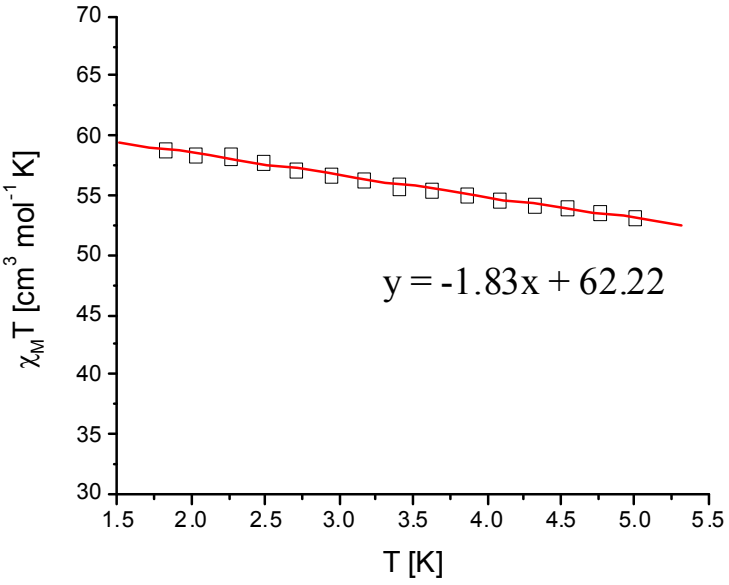

Figure 4.25. Extrapolation of 10 Hz $\chi_M'T$ *vs.* T data for $[Mn_{24}(O_2CMe)_{24}(mdea)_{18}] \cdot 5CH_2Cl_2$ **(10)** to zero K suggesting a ground state spin of $S = 11$ from the spin-only formula.

4.4. Conclusions

In summary, a new high-symmetry [Mn_{24}] wheel-shaped molecule (**10**) has been synthesized as well as structurally and magnetically characterized. This complex is the first single-stranded [Mn_{24}] wheel and is also the largest of this family of molecular wheels. The dc magnetic susceptibility data suggests that **10** could likely possess single-molecule magnet behavior based on the magnitude of its molar susceptibility as well as the appearance of a high-spin ground state appreciable zero-field splitting in the reduced magnetization data.

Though a frequency-dependent out-of-phase signal was not observed in the ac susceptibility, this does not necessarily preclude a barrier to the reversal of magnetization in **10**. Together, the dc and ac magnetic data suggest that **10** likely possesses an $S = 11$ ground state with spin-states as high as $S = 20$ (the highest for any single-stranded wheel) also being stabilized at higher fields. Higher-frequency ac susceptibility measurements or single-crystal magnetization hysteresis studies may reveal the potential SMM-like properties of **10**. This study has also shown the effects that symmetry can have on magnetic and quantum properties. In the series of [Mn_{12}] to [Mn_{16}] to [Mn_{24}] single-stranded wheels, there is a systematic increase in size, symmetry, and ground state spin of these molecular wheels which is inversely proportional to the magnetoanisotropy and overall SMM-like behavior of these molecules.

This chapter includes material currently being prepared for submission for publication: Heroux, K. J.; Hendrickson, D. N. “A single-stranded [Mn_{24}] wheel:

synthesis, crystal structure, and magnetic properties". The dissertation author was the primary investigator and author of this paper.

4.5. References

(1) Oshio, H.; Nihei, M.; Yoshida, A.; Nojiri, H.; Nakano, M.; Yamaguchi, A.; Karaki, Y.; Ishimoto, H. *Chemistry-a European Journal* **2005**, *11*, 843-848.

(2) Tasiopoulos, A. J.; Vinslava, A.; Wernsdorfer, W.; Abboud, K. A.; Christou, G. *Angewandte Chemie-International Edition* **2004**, *43*, 2117-2121.

(3) Hoffmann, R. *Scientific American* **1993**, *268*, 66-73.

(4) Cador, O.; Gatteschi, D.; Sessoli, R.; Larsen, F. K.; Overgaard, J.; Barra, A.-L.; Teat, S. J.; Timco, G. A.; Winpenny, R. E. P. *Angewandte Chemie International Edition* **2004**, *43*, 5196-5200.

(5) Cador, O.; Gatteschi, D.; Sessoli, R.; Barra, A.-L.; Timco, G. A.; Winpenny, R. E. P. *Journal of Magnetism and Magnetic Materials* **2005**, *290-291*, 55-60.

(6) Hendrickson, D. N.; World Sci.: 1993, p 87-108.

(7) Waldmann, O.; Gudel, H. U. *Physical Review B* **2005**, *72*.

(8) Waldmann, O.; Dobe, C.; Mutka, H.; Furrer, A.; Güdel, H. U. *Physical Review Letters* **2005**, *95*, 057202.

(9) Waldmann, O. *Coordination Chemistry Reviews* **2005**, *249*, 2550-2566.

(10) Affronte, M.; Casson, I.; Evangelisti, M.; Candini, A.; Carretta, S.; Muryn, C. A.; Teat, S. J.; Timco, G. A.; Wernsdorfer, W.; Winpenny, R. E. P. *Angewandte Chemie International Edition* **2005**, *44*, 6496-6500.

(11) Beedle, C. C.; Heroux, K. J.; Nakano, M.; DiPasquale, A. G.; Rheingold, A. L.; Hendrickson, D. N. *Polyhedron* **2007**, *26*, 2200-2206.

(12) Scott, R. T. W.; Milios, C. J.; Vinslava, A.; Lifford, D.; Parsons, S.; Wernsdorfer, W.; Christou, G.; Brechin, E. K. *Dalton Transactions* **2006**, 3161-3163.

(13) Murugesu, M.; Raftery, J.; Wernsdorfer, W.; Christou, G.; Brechin, E. *Inorganic Chemistry* **2004**, *43*, 4203-4209.

(14) Manoli, M.; Prescimone, A.; Bagai, R.; Mishra, A.; Murugesu, M.; Parsons, S.; Wernsdorfer, W.; Christou, G.; Brechin, E. K. *Inorganic Chemistry* **2007**, *46*, 6968-6979.

(15) Cadiou, C.; Murrie, M.; Paulsen, C.; Villar, V.; Wernsdorfer, W.; Winpenny, R. E. P. *Chemical Communications* **2001**, 2666-2667.

(16) Andres, H.; Basler, R.; Blake, A. J.; Cadiou, C.; Chaboussant, G.; Grant, C. M.; Gudel, H. U.; Murrie, M.; Parsons, S.; Paulsen, C.; Semadini, F.; Villar, V.; Wernsdorfer, W.; Winpenny, R. E. P. *Chemistry-a European Journal* **2002**, *8*, 4867-4876.

(17) Rumberger, E. M.; Zakharov, L. N.; Rheingold, A. L.; Hendrickson, D. N. *Inorganic Chemistry* **2004**, *43*, 6531-6533.

(18) Rumberger, E. M.; Shah, S. J.; Beedle, C. C.; Zakharov, L. N.; Rheingold, A. L.; Hendrickson, D. N. *Inorganic Chemistry* **2005**, *44*, 2742-2752.

(19) Shah, S. J.; Ramsey, C. M.; Heroux, K. J.; DiPasquale, A. G.; Dalal, N. S.; Rheingold, A. L.; del Barco, E.; Hendrickson, D. N. *Inorganic Chemistry* **2008**, *47*, 9569-9582.

(20) Foguet-Albiol, D.; O'Brien, T. A.; Wernsdorfer, W.; Moulton, B.; Zaworotko, M. J.; Abboud, K. A.; Christou, G. *Angewandte Chemie-International Edition* **2005**, *44*, 897-901.

(21) Murugesu, M.; Wernsdorfer, W.; Abboud, K. A.; Christou, G. *Angewandte Chemie International Edition* **2005**, *44*, 892-896.

(22) Shah, S. J.; Ramsey, C. M.; Heroux, K. J.; O'Brien, J. R.; DiPasquale, A. G.; Rheingold, A. L.; del Barco, E.; Hendrickson, D. N. *Inorganic Chemistry* **2008**, *47*, 6245-6253.

(23) Gatteschi, D.; Sessoli, R. *Angewandte Chemie-International Edition* **2003**, *42*, 268-297.

(24) Friedman, J. R.; Sarachik, M. P.; Tejada, J.; Maciejewski, J.; Ziolo, R. *Journal of Applied Physics* **1996**, *79*, 6031-6033.

(25) Ramsey, C. M.; del Barco, E.; Hill, S.; Shah, S. J.; Beedle, C. C.; Hendrickson, D. N. *Nat Phys* **2008**, *4*, 277-281.

(26) Wernsdorfer, W.; Sessoli, R. *Science* **1999**, *284*, 133-135.

(27) del Barco, E.; Kent, A. D.; Rumberger, E. M.; Hendrickson, D. N.; Christou, G. *Physical Review Letters* **2003**, *91*, 047203.

(28) del Barco, E.; Kent, A. D.; Hill, S.; North, J. M.; Dalal, N. S.; Rumberger, E. M.; Hendrickson, D. N.; Chakov, N.; Christou, G. *Journal of Low Temperature Physics* **2005**, *140*, 119-174.

(29) Soler, M.; Rumberger, E.; Folting, K.; Hendrickson, D. N.; Christou, G. *Polyhedron* **2001**, *20*, 1365-1369.

(30) Soler, M.; Wernsdorfer, W.; Folting, K.; Pink, M.; Christou, G. *Journal of the American Chemical Society* **2004**, *126*, 2156-2165.

(31) Sanudo, E. C.; Brechin, E. K.; Boskovic, C.; Wernsdorfer, W.; Yoo, J.; Yamaguchi, A.; Concolino, T. R.; Abboud, K. A.; Rheingold, A. L.; Ishimoto, H.; Hendrickson, D. N.; Christou, G. *Polyhedron* **2003**, *22*, 2267-2271.

(32) Jones, L. F.; Brechin, E. K.; Collison, D.; Harrison, A.; Teat, S. J.; Wernsdorfer, W. *Chemical Communications* **2002**, 2974-2975.

Chapter 5:

Hexanuclear Manganese Rod-Shaped Single-Molecule Magnets

5.1. Introduction

Since the discovery of the first SMM (Mn_{12}-acetate) in 1993,[1] a large number of polynuclear manganese clusters of various topologies and nuclearities have been found to behave as SMMs. In addition to the cubanes, dicubanes, and wheel-shaped SMMs discussed in previous chapters, rod-shaped complexes are also a common topology seen in manganese clusters. The tris-hydroxymethyl ethane ($thmeH_3$) and tris-hydroxymethyl propane ($tmpH_3$) ligands have proven to be useful synthetic tools in the synthesis of rod-shaped manganese complexes of various nuclearities, some of which show SMM-like characteristics. Heptanuclear and octanuclear manganese rods such as $[Mn_7O_2(O_2CPh)_9(thme)_2(py)_3]$ and $[Mn_8O_4(O_2CCMe_3)_{10}(thme)_2(py)_2]$ were reported by Rajaraman *et al.*[2] in 2004 but do not function as SMMs. However, the dodecanuclear manganese rod $[Mn_{12}O_4(OH)_2(O_2CPh)_{12}(thme)_4(py)_2]$, also reported in 2004,[2] has a S = 7 ground state and shows magnetization hysteresis at low temperatures, indicative of SMM behavior.

Other rod-shaped SMMs utilizing the $thmeH_3$ and $tmpH_3$ ligands include the mixed-valent hexanuclear manganese clusters $[Mn_6(O_2CCMe_3)_8(tmp)_2(py)_2]$ also reported by Rajaraman *et al.*[2] in 2004 and $[Mn_6(O_2CMe)_8(thme)_2(py)_4] \cdot 2py$ and $[Mn_6(O_2CMe)_8(tmp)_2(py)_4] \cdot 2py$ reported by Milios *et al.*[3] in 2006. All three complexes have S = 4 ground states and the latter two complexes show magnetization hysteresis at low temperatures.[3] Various derivatives of the salicylaldoxime ligand have also been used in the synthesis of a similar family of hexanuclear rods including $[Mn_6O_2(Et\text{-}sao)_6(O_2CCMe_3)_2(EtOH)_5]$ and $[Mn_6O_2(Me\text{-}sao)_6(O_2C\text{-}th)_2(EtOH)_4(H_2O)_2]$.[4] However,

unlike the mixed-valent hexanuclear rods discussed above, these complexes contain only Mn(III) ions and exhibit very different magnetic properties.

Interestingly, though all of these [Mn_6] complexes are grouped together in this family of "rod-shaped" SMMs, they do not all possess the same core connectivity. For example, the four complexes reported in 2006 consist of three different core structures as depicted in Figure 5.1.[3] In this chapter, the structure and magnetic properties of four new hexanuclear rod-shaped SMMs will be presented and discussed. All of the complexes were synthesized using the $tmpH_3$ ligand along with either N-substituted diethanolamine ligands ($RdeaH_2$) or triethanolamine ($teaH_3$). The core structure adopted by all four of these complexes differs slightly from all previously studied [Mn_6] rods, representing yet another structural form of hexanuclear manganese rods.

5.2. Experimental Section

5.2.1. Preparation

All manipulations were performed under aerobic conditions. The chemicals Mn(II)acetate tetrahydrate, triethylamine (Et_3N), N-ethyl diethanolamine ($edeaH_2$), N-methyl diethanolamine ($mdeaH_2$), triethanolamine ($teaH_3$) and *tris*-hydroxymethyl propane ($tmpH_3$) were purchased from Sigma Aldrich. Mn(II) triflouroacetate and $[Mn_3O(PhCOO)_6(py)_3(H_2O)] \cdot 0.5$ MeCN were prepared as previously described.[5,6]

$[Mn_6(O_2CCH_3)_6(edeaH)_2(tmp)_2]$ (11). To a solution of $Mn(O_2CMe)_2 \cdot 4H_2O$ (1.22 g, 5 mmol) in 50 mL CH_2Cl_2 was added $edeaH_2$ (0.332 g, 2.5 mmol) in 25 mL CH_2Cl_2. To this solution, a 25 mL MeOH solution of $tmpH_3$ (0.335 g, 2.5 mmol) was then added. Addition of Et_3N (0.69 mL, 5 mmol) caused the solution to turn a deep

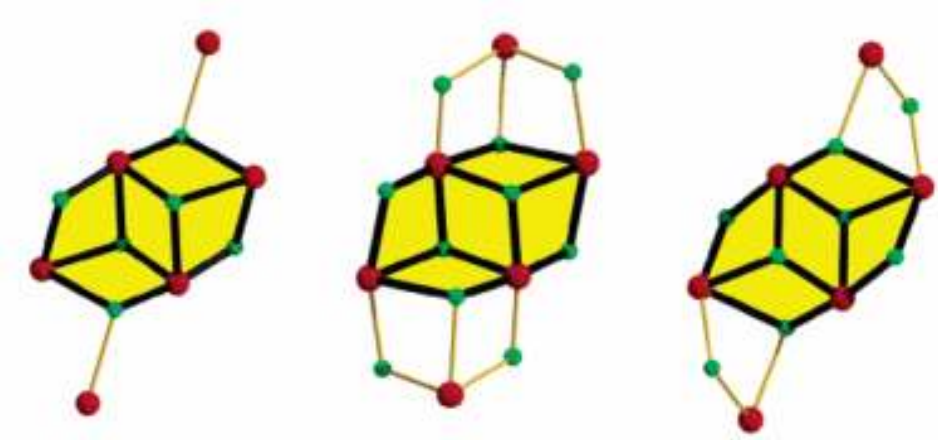

Figure 5.1. Comparison of metal-oxygen cores of some [Mn_6] rods.

brown color. This solution was allowed to stir overnight then filtered and evaporated by vacuum distillation to yield an oil. The oil was dissolved in 80 mL of MeCN and allowed to slowly evaporate. Red-brown block-shaped crystals of **11** were obtained after two days in 2.5% yield. Elemental analysis calc'd (found) for $C_{36}H_{66}Mn_6N_2O_{22}$: C 35.7 (33.29); H 5.5 (5.52); N 2.31 (2.45). Selected IR data (KBr, cm^{-1}): 3500 (m, br), 2900 (m), 1600 (s), 1400 (s), 1150 (s), 1100 (s), 600 (s).

$[Mn_6(O_2CCH_3)_6(mdeaH)_2(tmp)_2]$ (12). To a solution of $Mn(O_2CMe)_2 \cdot 4H_2O$ (1.22 g, 5 mmol) in 20 mL MeOH and 10 mL pyridine was added a solution of $mdeaH_2$ (0.297 g, 2.5 mmol) in 20 mL MeOH. To this was added $tmpH_3$ (0.335 g, 2.5 mmol) in 20 mL MeOH. Addition of Et_3N (0.69 mL, 5 mmol) to the solution yielded a dark brown solution which was stirred overnight and filtered. Crystals of **12** were obtained in 47 % yield after two days by vapor diffusion of diethyl ether into the filtrate. Elemental analysis calc'd (found) for $C_{34}H_{62}Mn_6N_2O_{22}$: C 34.5 (34.2); H 5.25 (5.28); N 2.37 (2.32). Selected IR data (KBr, cm^{-1}): 3500 (m, br), 2900 (m), 1600 (s), 1400 (s), 1100 (s), 700 (m), 600 (m).

$[Mn_6(O_2CCF_3)_6(teaH_2)_2(tmp)_2] \cdot 2MeCN$ (13). To a solution of $Mn(O_2CCF_3)_2$ (1.765 g, 5 mmol) in 50 mL CH_2Cl_2 was added $tmpH_3$ (0.335 g, 2.5 mmol) in 20 mL MeOH. To this solution was added $teaH_3$ (0.37 g, 2.5 mmol) in 25 mL CH_2Cl_2, followed by addition of Et_3N (0.69 mL, 5 mmol). The solution was allowed to stir overnight then evaporated by vacuum distillation to yield an oil. The oil was dissolved in 100 mL of MeCN and allowed to slowly evaporate. Crystals of **13** were obtained after three days in 6% yield. Elemental analysis calc'd (found) for $C_{40}H_{52}F_{18}Mn_6N_4O_{24}$:

C 29.16 (29.2); H 3.28 (3.49); N 3.40 (3.48). Selected IR data (KBr, cm^{-1}): 3400 (m, br), 2900 (m), 1700 (s), 1650 (s), 1200 (s), 1100 (s), 700 (m).

$[Mn_6(O_2CPh)_6(EdeaH)_2(tmp)_2] \cdot 2Et_2O$ (14). To a solution of $[Mn_3O(O_2CPh)_6(py)_3(H_2O)]$ (0.54 g, 0.5 mmol) in 40 mL MeCN was added $edeaH_2$ (0.332 g, 2.5 mmol) in 25 mL CH_2Cl_2. To this solution was added $tmpH_3$ (0.335 g, 2.5 mmol) in 25 mL MeOH. The solution was allowed to stir overnight and then filtered. Diethyl ether diffusion of the filtrate resulted in crystals of **14** after one week in 3.8% yield. Elemental analysis calc'd (found) for $C_{74}H_{100}Mn_6N_2O_{24}$: C 50.1 (50.46); H 4.9 (5.39); N 1.7 (2.0). Selected IR data (KBr, cm^{-1}): 3400 (m, br), 1600 (s), 1400 (s), 1100 (m), 700 (m).

5.2.2. X-Ray Crystallography

Crystals were mounted on a CryoLoop© with Paratone-N© oil. Diffraction intensity data were collected at 208 K for all complexes except for **12** which were collected at 100 K on a Bruker Smart Apex CCD diffractometer with Mo Kα radiation, integrated using Bruker SAINT software program, and corrected for absorption using the Bruker SADABS program. Crystallographic data and refinement parameters are given in Tables 5.1 (**11** and **12**) and 5.2 (**13** and **14**).

Solution by direct methods (SHELXS-97 for **11** and **12**, SIR-2004 for **13** and **14**) produced a complete heavy-atom phasing model consistent with the proposed structures. All non-hydrogen atoms were refined anisotropically by full-matrix least-squares (SHELXL-97). All hydrogen atoms were placed using a riding model and their positions were constrained relative to their parent atom using the appropriate HFIX

Table 5.1. Crystallographic data and refinement parameters for $[Mn_6(O_2CCH_3)_6(edeaH)_2(tmp)_2]$ **(11)** and $[Mn_6(O_2CCH_3)_6$ mdeaH$)_2(tmp)_2]$ **(12).**

	11	**12**
formula	$C_{36}H_{66}Mn_6N_2O_{22}$	$C_{34}H_{62}Mn_6N_2O_{22}$
formula weight	1208.55	1180.50
temp [K]	208(2)	100(2)
wavelength [Å]	0.71073	0.71073
crystal system	monoclinic	monoclinic
space group	$P2_1/c$	$P2_1/c$
a [Å]	10.284(2)	10.0974(13)
b [Å]	16.199(4)	15.4559(19)
c [Å]	18.489(4)	18.957(2)
α [deg]	90	90
β [deg]	100.075(4)	102.671(2)
γ [deg]	90	90
V [Å^3]	3032.6(11)	2886.4(6)
Z	2	2
D_{calc} (Mg m^{-3})	1.324	1.358
abs. coefficient [mm^{-1}]	1.275	1.338
F(000)	1244	1212
theta range	1.68 to 28.25°	1.72 to 28.27°
comp. to theta [25.00°]	94.3 %	100.0 %
Max. / min. trans.	0.7328 and 0.6711	0.8779 and 0.8453
Data / restraints / param.	6555 / 0 / 302	6706 / 0 / 294
Goodness-of-fit on F2	1.076	1.070
R1 ($I > 2\sigma(I)$)	0.0367	0.0308
R1 (all data)	0.0402	0.0346
Largest diff. peak / hole	0.876 and -0.384 e.Å^{-3}	0.752 and -0.310 e.Å^{-3}

[a] $R = \Sigma||F_o| - |F_c||/\Sigma|F_o|$. [b] $R(\omega F^2) = \{\Sigma[\omega(F_o^2 - F_c^2)^2]/\Sigma[\omega(F_o^2)^2]\}^{1/2}$; $\omega = 1/[\sigma^2(F_o^2) + (aP)^2 + bP]$, $P = [2F_c^2 + \max(F_o, 0)]/3$.

Table 5.2. Crystallographic data and refinement parameters for $[Mn_6(O_2CCF_3)_6(teaH_2)_2(tmp)_2] \cdot 2MeCN$ **(13)** and $[Mn_6(O_2CPh)_6(EdeaH)_2(tmp)_2] \cdot 2Et_2O$ **(14).**

	13	**14**
formula	$C_{40}H_{52}F_{18}Mn_6N_4O_{24}$	$C_{74}H_{100}Mn_6N_2O_{24}$
formula weight	1644.50	1731.20
temp [K]	208(2)	208(2)
wavelength [Å]	0.71073	0.71073
crystal system	triclinic	monoclinic
space group	P-1	$P2_1/c$
a [Å]	10.522(2)	10.500(3)
b [Å]	11.826(3)	17.970(5)
c [Å]	13.546(3)	20.850(6)
α [deg]	73.314(4)	90
β [deg]	71.092(4)	95.084(6)°
γ [deg]	82.370(4)	90
V [Å^3]	1526.0(6)	3918.6(19)
Z	1	2
D_{calc} (Mg m^{-3})	1.789	1.467
abs. coefficient [mm^{-1}]	1.337	1.013
F(000)	824	1800
theta range	1.65 to 28.26°	1.50 to 28.32°
comp. to theta [25.00°]	99.4 %	100.0 %
Max. / min. trans.	0.9738 and 0.8247	0.9899 and 0.9511
Data / restraints / param.	6981 / 0 / 473	9289 / 0 / 483
Goodness-of-fit on F2	1.022	1.031
R1 ($I > 2\sigma(I)$)	0.0536	0.0492
R1 (all data)	0.0859	0.0778
Largest diff. peak / hole	0.713 and -0.444 e.Å^{-3}	0.581 and -0.445 e.Å^{-3}

[a] $R = \Sigma||F_o| - |F_c||/\Sigma|F_o|$. [b] $R(\omega F^2) = \{\Sigma[\omega(F_o^2 - F_c^2)^2]/\Sigma[\omega(F_o^2)^2]\}^{1/2}$;
$\omega = 1/[\sigma^2(F_o^2) + (aP)^2 + bP]$, $P = [2F_c^2 + \max(F_o, 0)]/3$.

command in SHELXL-97. In complex **13**, the disordered fluorine atoms of C8, C16, and their symmetry equivalents were treated using a rotational disorder model.

5.2.3. Physical Measurements

Infrared spectra were recorded as KBr pellets using a Thermo-Nicolet Avatar series spectrophotometer. The AC magnetic susceptibility data were collected on a Quantum Design PPMS SQUID magnetometer at Quantum Design in San Diego, California. The DC magnetic susceptibility data were collected on a Quantum Design MPMS SQUID magnetometer equipped with a 5 T magnet at the University of California at San Diego. Microcrystalline samples were restrained using eicosane to prevent torquing. Diamagnetic corrections were applied to the magnetic susceptibility data using Pascal's constants. Elemental analyses were performed by Numega Resonance Labs in San Diego, CA.

5.3. Results and Discussion

5.3.1. Description of Crystal Structures

Complexes **11**, **12**, and **14** crystallize in the monoclinic, $P2_1/c$ space group with two molecules in the unit cell (Z = 2). Complex **13** crystallizes in the triclinic, P-1 space group with Z = 1. Each complex comprises the same rod-like $[Mn^{II}_4Mn^{III}_2(\mu_2\text{-}OR)_4(\mu_3\text{-}OR)_4]^{6+}$ unit (Figure 5.2) with the two Mn(III) ions located in the center of the core. The oxidation state of each Mn atom was determined by charge considerations, the presence of Jahn-Teller (JT) distortion around the high-spin Mn(III) ions, and bond valence sum

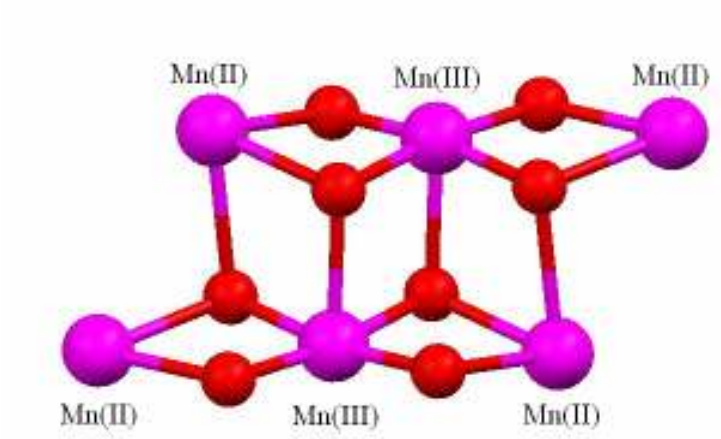

Figure 5.2. Mn-oxo core connectivity for complexes **11-14**.

Table 5.3. Bond valence sum analysis for **11** and **12**.

11		**12**	
Bond	**Valence**	**Bond**	**Valence**
Mn1-O4	0.311	Mn1-O1	0.281
Mn1-O5	0.302	Mn1-O2	0.298
Mn1-O6	0.351	Mn1-O3	0.331
Mn1-O7	0.164	Mn1-O4	0.344
Mn1-O8	0.395	Mn1-O5	0.278
Mn1-O10	0.4	Mn1-N1	0.298
Mn1	**1.92**	**Mn1**	**1.83**
Mn2-O2	0.699	Mn2-O2	0.689
Mn2-O3	0.294	Mn2-O5	0.601
Mn2-O5	0.591	Mn2-O6	0.583
Mn2-O6	0.651	Mn2-O7	0.641
Mn2-O7	0.614	Mn2-O8	0.289
Mn2-O5′	0.259	Mn2-O6′	0.265
Mn2	**3.11**	**Mn2**	**3.07**
Mn3-O1	0.309	Mn3-O6	0.294
Mn3-O2	0.311	Mn3-O7	0.355
Mn3-O7	0.275	Mn3-O9	0.316
Mn3-O9	0.37	Mn3-O10	0.39
Mn3-O11	0.334	Mn3-O11	0.396
Mn3-N1	0.236	Mn3-O5′	0.191
Mn3	**1.84**	**Mn3**	**1.94**

Table 5.4. Bond valence sum analysis for **13** and **14**.

13		**14**	
Bond	**Valence**	**Bond**	**Valence**
Mn1-O1	0.284	Mn1-O1	0.365
Mn1-O3	0.252	Mn1-O2	0.388
Mn1-O6′	0.247	Mn1-O3	0.342
Mn1-O10′	0.233	Mn1-O5	0.333
Mn1-O12′	0.367	Mn1-O6	0.302
Mn1-N1	0.28	Mn1-O10	0.161
Mn1	**1.66**	**Mn1**	**1.89**
Mn2-O3	0.726	Mn2-O4	0.302
Mn2-O4	0.289	Mn2-O5	0.658
Mn2-O6′	0.607	Mn2-O6	0.589
Mn2-O7	0.648	Mn2-O7	0.701
Mn2-O8	0.572	Mn2-O6	0.265
Mn2-O8′	0.276	Mn2-O10′	0.607
Mn2	**3.12**	**Mn2**	**3.12**
Mn3-O5	0.309	Mn3-O7′	0.33
Mn3-O6	0.181	Mn3-O8	0.276
Mn3-O7	0.354	Mn3-O9	0.38
Mn3-O8	0.326	Mn3-O10	0.304
Mn3-O9	0.393	Mn3-O11	0.346
Mn3-O11	0.355	Mn3-N1	0.288
Mn3	**1.92**	**Mn3**	**1.92**

analyses (BVS) which can be found in Tables 5.3 and 5.4. The six Mn ions lie in the same plane forming four edge-sharing triangles. There are only three crystallographically independent Mn ions in each complex with the other three generated by inversion symmetry. Complexes **11-14** most closely resemble the family of [Mn_6] compounds reported by Rajaraman *et al.*[2] in 2004 and Milios *et al.*[3] in 2006. These previously reported [Mn_6] complexes, however, all possess a slightly different core structure, none of which have exactly the same connectivity as the complexes reported here. This point is emphasized in Figure 5.3 which shows core structures of the two published [Mn_6] rods whose magnetic properties most closely resemble those of the complexes presented herein.[3]

[$Mn_6(O_2CCH_3)_6(EdeaH)_2(tmp)_2$] (11). The structure of complex **1** is shown in Figure 5.4 with selected bond distances and angles given in Table 5.5. Each Mn ion exhibits 6-coordinate, distorted octahedral geometry except for the outermost Mn atoms (Mn3) which adopt a 6-coordinate, trigonal prismatic geometry. The Mn(III) ions are Mn2 and its symmetry equivalent ion which have JT-elongated Mn-O bonds of 2.20 and 2.25 Å which are significantly longer than the Mn-O bonds making up the square plane of the octahedron (~1.9 Å). The JT axes lie parallel to one another and form an angle of ~35° with the effective plane of the Mn ions.

The two tripodal *tris*-hydroxymethyl propane ligands are fully deprotonated (tmp^{3-}) and located directly above and below the [Mn_6] plane. Both ligands bind in the $\eta^3:\eta^3:\eta^2:\mu_5$ bridging mode across five metal centers occupying three edge-sharing triangles. All six of the acetate ligands bind in the usual $\eta^1:\eta^1:\mu_2$ bridging mode; two form a bridge between the Mn(III) ion and an adjacent Mn(II) ion (Mn1) while the

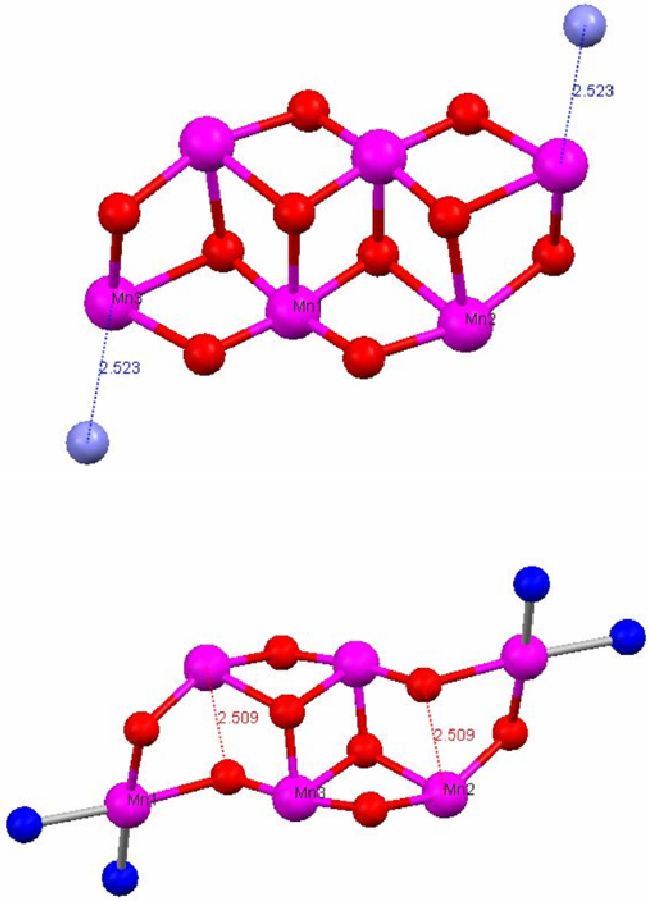

Figure 5.3. Mn-oxo core connectivity for $[Mn_6(O_2CMe)_6(teaH_2)_2(tmp)_2]$ · 2MeCN (top) and $[Mn_6(O_2CMe)_8(thme)_2(py)_4]$ · 2py (bottom).

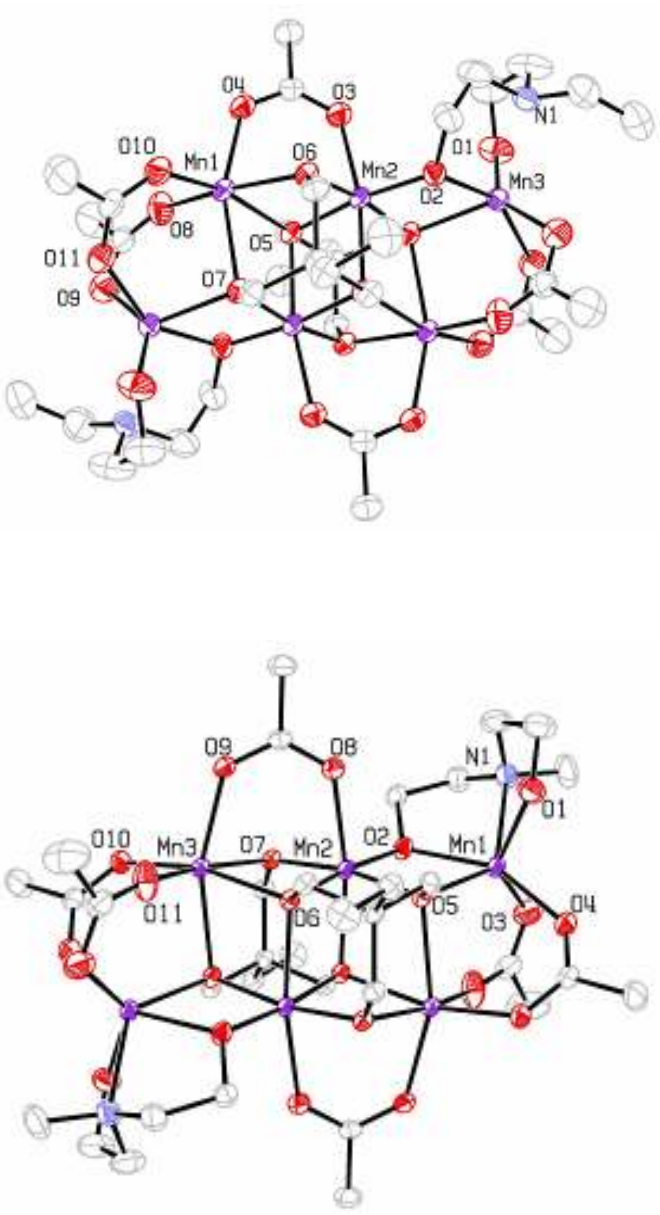

Figure 5.4. ORTEP of $[Mn_6(O_2CCH_3)_6(EdeaH)_2(tmp)_2]$ (**11**, top) and $[Mn_6(O_2CCH_3)_6(mdeaH)_2(tmp)_2]$ (**12**, bottom) with thermal ellipsoids drawn at 50% probability level. Hydrogen atoms omitted for clarity.

Table 5.5. Selected interatomic bond distances [Å] and angles [°] for $[Mn_6(O_2CCH_3)_6(EdeaH)_2(tmp)_2]$ **(11)**.

Mn1-O4	2.1823(15)	Mn2-O6	1.9091(14)	Mn2-O2-Mn3	105.01(6)
Mn1-O5	2.1932(14)	Mn2-O7	1.9309(13)	Mn1-O5-Mn2	96.10(5)
Mn1-O6	2.1385(14)	Mn2-O5′	2.2497(13)	Mn1-O5-Mn2′	99.66(5)
Mn1-O7	2.4197(14)	Mn3-O1	2.1852(18)	Mn2-O5-Mn2′	99.38(6)
Mn1-O8	2.0942(17)	Mn3-O2	2.1824(15)	Mn1-O6-Mn2	99.04(6)
Mn1-O10	2.0893(15)	Mn3-O7	2.2275(14)	Mn1-O7-Mn2	102.01(6)
Mn2-O2	1.8833(15)	Mn3-O9	2.1179(18)	Mn1-O7-Mn3	94.06(5)
Mn2-O3	2.2034(14)	Mn3-O11	2.1559(16)	Mn2-O7-Mn3	101.74(6)
Mn2-O5	1.9453(14)	Mn3-N1	2.3955(18)		

Table 5.6. Selected interatomic bond distances [Å] and angles [°] for $[Mn_6(O_2CCH_3)_6mdeaH)_2(tmp)_2]$ **(12)**.

Mn1-O1	2.2198(14)	Mn2-O7	1.9146(11)	Mn1-O2-Mn2	103.65(5)
Mn1-O2	2.1981(12)	Mn2-O8	2.2097(12)	Mn1-O5-Mn2	101.04(5)
Mn1-O3	2.1385(14)	Mn2-O6′	2.2423(11)	Mn2-O5-Mn3′	103.49(5)
Mn1-O4	2.1455(12)	Mn3-O6	2.2034(11)	Mn1-O5-Mn3′	93.49(4)
Mn1-O5	2.2239(11)	Mn3-O7	2.1335(11)	Mn2-O6-Mn3	95.21(5)
Mn1-N1	2.3096(16)	Mn3-O9	2.1768(12)	Mn2-O6-Mn2′	100.18(5)
Mn2-O2	1.8885(12)	Mn3-O10	2.0993(12)	Mn3-O6-Mn2′	99.30(4)
Mn2-O5	1.9391(11)	Mn3-O11	2.0933(13)	Mn2-O7-Mn3	98.60(5)
Mn2-O6	1.9504(11)	Mn3-O5′	2.3624(11)		

remaining four acetate ligands are located between Mn(II) ions (Mn1 and Mn3). Finally, the coordination sphere of the outer Mn(II) ion (Mn3) is capped by a singly deprotonated ethyldiethanolamine ligand ($edeaH^{1-}$) which binds in a $\eta^2:\eta^1:\eta^1:\mu_2$ mode linking Mn3 and Mn2.

There are two symmetry-related orientations of the molecule in the unit cell packing diagram of **11** (Figure 5.5). The molecules form layers on the crystallographic c-axis with each row comprising molecules of the same orientation and stacked in an alternating manner along the b-axis. The [Mn_6] planes of the two different orientations are tilted ~44° from one another. There are no solvent molecules present in the crystal lattice as well as no significant intra- or intermolecular H-bonding or van der Waals interactions.

$[Mn_6(O_2CCH_3)_6(mdeaH)_2(tmp)_2]$ (12). The ORTEP of complex **2** is also shown in Figure 5.4 and selected bond distances and angles are given in Table 5.6. The oxidation states and geometry of the six Mn ions are identical to that found in **11**. The two fully deprotonated tmp^{3-} ligands, as well as the six acetate ligands, all bind analogously to those in **11,** *vide supra*. The only structural difference between **11** and **12** is that the outermost Mn atoms in **2** (Mn1 and its symmetry equivalent) are chelated by a singly deprotonated N-methyl diethanolamine ligand ($MdeaH^{1-}$) rather than the ethyldiethanolamine monoanion. However, the ligand still binds in a $\eta^2:\eta^2:\eta^1:\mu_2$ mode linking Mn1 to the trivalent Mn2 ion. The Mn(III) ions (Mn2 and its symmetry equivalent) have JT-elongated Mn-O bonds of 2.21 and 2.24 Å which are comparable to those found in **1**. The JT axes lie parallel to one another and form an angle of ~38° with the effective plane of the Mn ions.

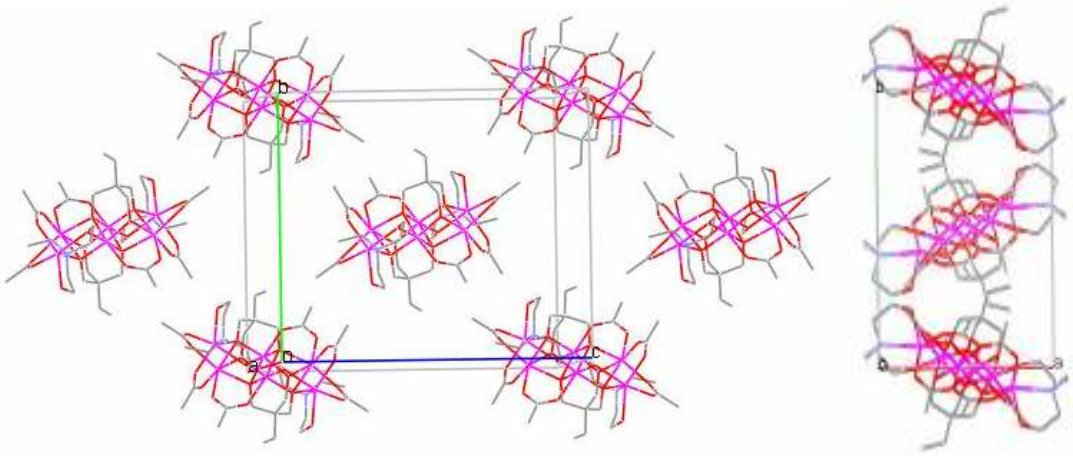

Figure 5.5. Unit cell of $[Mn_6(O_2CCH_3)_6(EdeaH)_2(tmp)_2]$ **(11)** as viewed down the a-axis (left) and the c-axis (right).

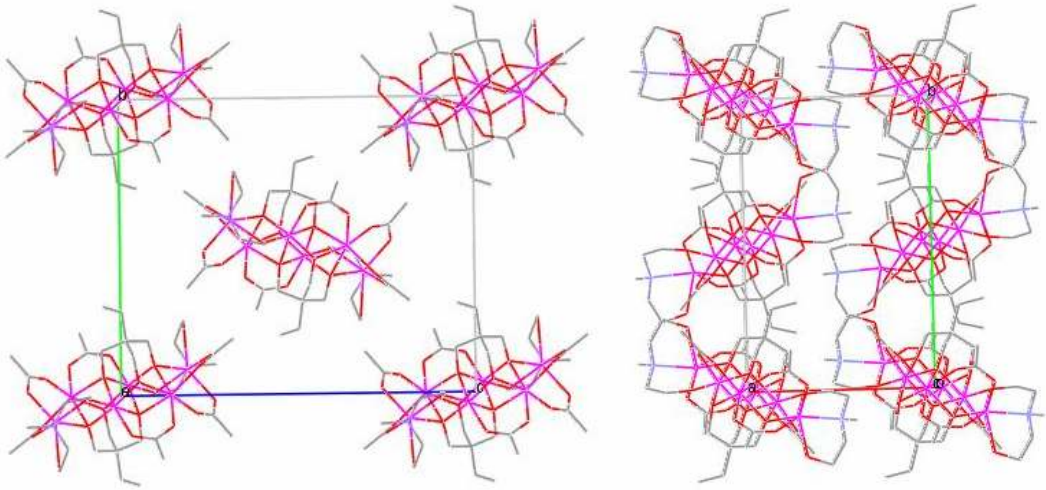

Figure 5.6. Unit cell of $[Mn_6(O_2CCH_3)_6mdeaH)_2(tmp)_2]$ **(12)** as viewed down the a-axis (left) and the c-axis (right).

There are also two symmetry-related orientations of the molecule in the unit cell packing diagram of **12** (Figure 5.6). The molecules pack similarly to those in the unit cell of **11**, forming rows of molecules with the same orientation stacked in an alternating manner with rows of molecules in the other orientation along the b-axis. As found for complex **11**, the [Mn_6] planes of the two different molecular orientations in **12** are also tilted ~44° from one another. Also, there are no solvent molecules or intra- or intermolecular interactions present in the crystal lattice.

[$Mn_6(O_2CCF_3)_6(teaH_2)_2(tmp)_2$] · 2MeCN (13). The structure of complex **13** is shown in Figure 5.7 with selected bond distances and angles given in Table 5.7. Complex **13** exhibits the same $[Mn^{II}_4Mn^{III}_2(\mu_2\text{-OR})_4(\mu_3\text{-OR})_4]^{6+}$ core unit as **11** and **12** with the two trivalent Mn ions located in the center of the core. The Mn(III) ions (Mn2 and its symmetry equivalent) have JT-elongated Mn-O bonds of 2.20 and 2.23 Å which comprise a JT-axis that forms an angle of ~38° with the effective [Mn_6] plane.

The [Mn_6] unit is capped on either end with a singly deprotonated triethanolamine ligand ($teaH_2^{1-}$) which binds to the divalent Mn1 ions through the nitrogen atom and two of the alcohol arms, forming a single oxygen bridge between Mn1 and the adjacent trivalent Mn2. The nature of the triethanolamine ligand leads to a 6-coordinate, distorted trigonal prismatic geometry around the outer Mn(II) ions with a very long Mn-O contact of 2.57 Å between Mn1 and the uncoordinated alcohol arm of the ligand. This protonated arm of the $teaH_2^{1-}$ ligand also forms an intramolecular H-bond to each of the neighboring trifluoroacetate ligands between Mn1 and Mn3. The two fully deprotonated tmp^{3-} ligands occupy analogous positions and binding modes to

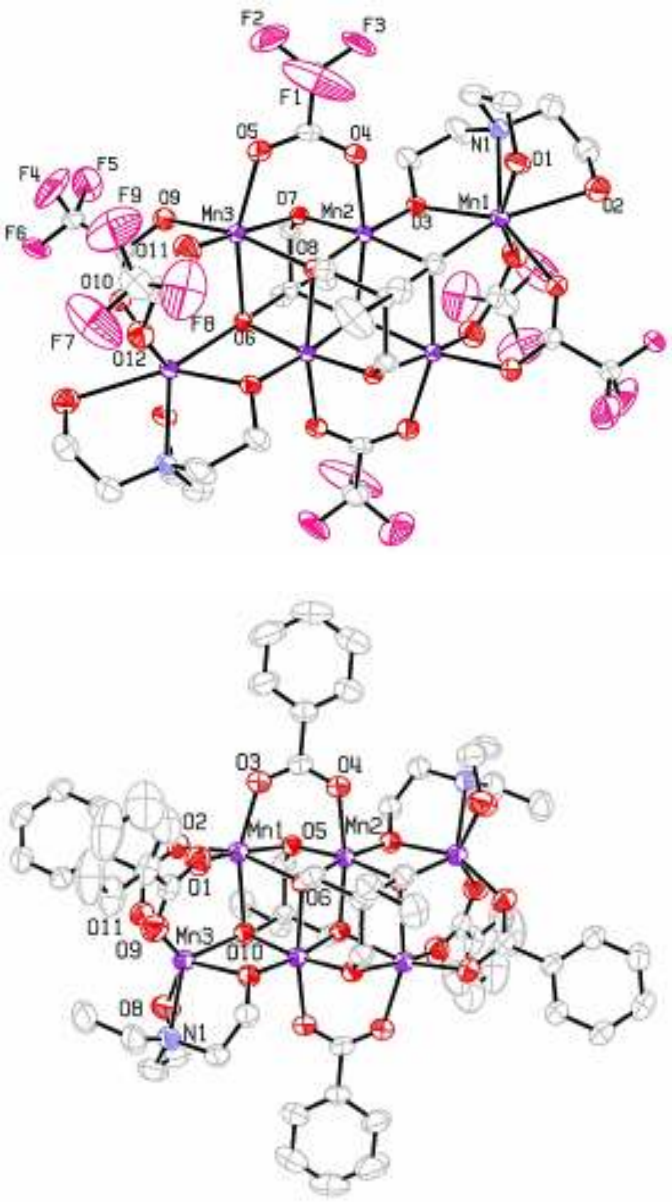

Figure 5.7. ORTEP of $[Mn_6(O_2CCF_3)_6(teaH_2)_2(tmp)_2] \cdot 2MeCN$ (**13**, top) and $[Mn_6(O_2CPh)_6(EdeaH)_2(tmp)_2] \cdot 2Et_2O$ (**14**, bottom) with thermal ellipsoids drawn at 50% probability level. Hydrogen atoms and solvate molecules omitted for clarity.

Table 5.7. Selected interatomic bond distances [Å] and angles [°] for $[Mn_6(O_2CCF_3)_6(teaH_2)_2(tmp)_2] \cdot 2MeCN$ **(13)**.

Mn1-O1	2.216(3)	Mn2-O7	1.911(2)	Mn1-O3-Mn2	105.16(11)
Mn1-O3	2.260(3)	Mn2-O8	1.957(2)	Mn1-O6′-Mn2	102.67(10)
Mn1-O6′	2.267(2)	Mn2-O8′	2.227(2)	Mn2-O6-Mn3′	99.75(10)
Mn1-O10′	2.290(3)	Mn3-O5	2.185(3)	Mn1-O6-Mn3′	102.10(9)
Mn1-O12′	2.121(3)	Mn3-O6	2.382(2)	Mn2-O7-Mn3	99.03(10)
Mn1-N1	2.334(3)	Mn3-O7	2.134(3)	Mn2-O8-Mn3	96.56(10)
Mn2-O3	1.869(2)	Mn3-O8	2.165(2)	Mn2-O8-Mn1′	99.33(10)
Mn2-O4	2.208(3)	Mn3-O9	2.096(3)	Mn3-O8-Mn2′	97.94(9)
Mn2-O6′	1.935(2)	Mn3-O11	2.135(3)		

Table 5.8. Selected interatomic bond distances [Å] and angles [°] for $[Mn_6(O_2CPh)_6(EdeaH)_2(tmp)_2] \cdot 2Et_2O$ **(14)**.

Mn1-O1	2.123(2)	Mn2-O7	1.8821(19)	Mn1-O5-Mn2	98.52(8)
Mn1-O2	2.101(2)	Mn2-O6	1.9465(19)	Mn1-O6-Mn2	96.05(7)
Mn1-O3	2.147(2)	Mn2-O10′	1.9355(19)	Mn1-O6-Mn2′	101.00(7)
Mn1-O5	2.1569(19)	Mn3-O7′	2.161(2)	Mn2-O6-Mn2′	99.47(8)
Mn1-O6	2.1927(18)	Mn3-O8	2.227(8)	Mn2-O7-Mn3′	105.02(8)
Mn1-O10	2.4619(19)	Mn3-O9	2.108(2)	Mn3-O10-Mn2′	102.07(8)
Mn2-O4	2.193(2)	Mn3-O10	2.1906(19)	Mn1-O10-Mn2′	101.50(8)
Mn2-O5	1.9046(19)	Mn3-O11	2.143(2)	Mn1-O10-Mn3	95.06(7)
Mn2-O6	1.9465(19)	Mn3-N1	2.410(3)		

those found in **11** and **12**. The six trifluoroacetate ligands in **13** all bind in the same fashion (η^1:η^1:μ_2) as the acetate ligands in **11** and **12.**

The crystal packing of **13** (Figure 5.8) differs in that there is only one orientation of the molecule in the unit cell and all molecules are related only by a center of inversion. The molecules do, however, form similar layers on the crystallographic c-axis which then stack along the b-axis. The effective plane of the [Mn_6] unit lies nearly perpendicular the crystallographic b-axis (1 0 0 Miller plane) and forms an angle of ~37° with the c-axis (0 1 0 plane).

There is one MeCN solvate molecule co-crystallized with each [Mn_6] unit. The solvate molecules form an extensive H-bonding network between [Mn_6] units as shown in Figure 5.9. The carbon end of the MeCN molecule interacts with an oxygen atom of a neighboring trifluoroacetate ligand (bridging Mn2 and Mn3) while the nitrogen end of the solvate molecule is H-bonded to the unbound alcohol arm of the $teaH_2^{1-}$ ligand. There are further intermolecular short contacts between the uncoordinated alcohol arm and the $teaH_2^{1-}$ ligand on an adjacent molecule as well as between fluorine atoms of adjacent molecules. All of the intermolecular contacts expand within the plane of the [Mn_6] units. The closest intermolecular Mn···Mn distance is ~6.2 Å.

$[Mn_6(O_2CPh)_6(EdeaH)_2(tmp)_2] \cdot 2Et_2O$ (14). The ORTEP of complex **14** is also shown in Figure 5.7 and selected bond distances and angles are given in Table 5.8. This complex also consists of the same $[Mn^{II}_4Mn^{III}_2(\mu_2\text{-}OR)_4(\mu_3\text{-}OR)_4]^{6+}$ core with the Mn(III) ions located in the center of the unit. The ancillary ligands, as well as their binding modes, are identical to those found in **11** with the exception of six benzoate ligands instead of acetates. The benzoate ligands, however, still bind in the same η^1:η^1:

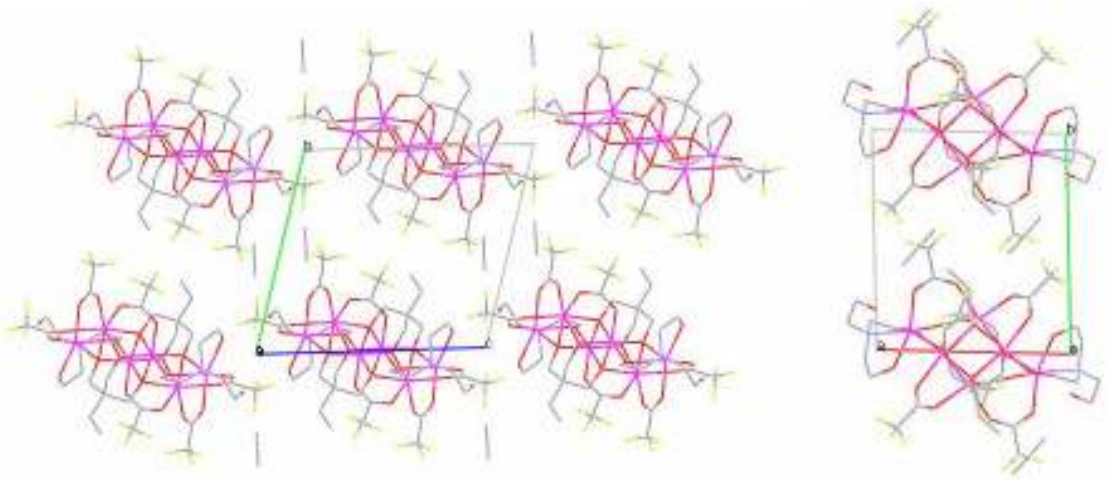

Figure 5.8. Unit cell of $[Mn_6(O_2CCF_3)_6(teaH_2)_2(tmp)_2] \cdot 2MeCN$ **(13)** as viewed down the a-axis (left) and the c-axis (right).

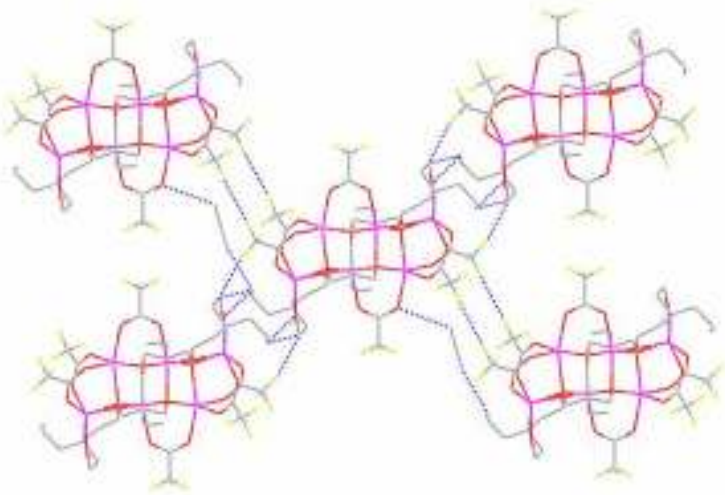

Figure 5.9. Intermolecular interactions in the crystal packing of $[Mn_6(O_2CCF_3)_6(teaH_2)_2(tmp)_2] \cdot 2MeCN$ **(13)**.

μ_2 bridging mode as the acetate groups in **11**. The Mn(III) ions (Mn2 and its symmetry equivalent) have JT-elongated Mn-O bonds of 2.19 and 2.24 Å which are also comparable to those found in **11**. The JT axes lie parallel to one another and form an angle of ~37° with the effective plane of the [Mn_6] unit

There are also two symmetry-related orientations of the molecule in the unit cell packing diagram of **14** (Figure 5.10). The molecules pack similarly to those in the unit cell of **11** but form a much more severe angle of ~78° between the effective [Mn_6] planes of the two different orientations. Furthermore, there is one well-ordered diethyl ether solvate molecule per [Mn_6] unit co-crystallized in the unit cell. The protonated alcohol arm of each edeaH^{1-} ligand is H-bonded to the oxygen atom of a neighboring ether solvate molecule.

5.3.2. DC Magnetic Susceptibility

Dc magnetic susceptibility data for complexes **11-14** collected in an applied field of 1 T are plotted as $\chi_M T$ *vs.* T as shown in Figures 5.11 and 5.12. All four complexes show similar magnetic behavior in the temperature range of 300-1.8 K. The $\chi_M T$ value at 300 K is around 20 cm^3 mol^{-1} K for complexes **11-13** and 23 cm^3 mol^{-1} K for complex **14**. These values are only slightly lower than the spin-only value of 24 cm^3 mol^{-1} K which was calculated for four Mn(II) and two Mn(III) non-interacting ions. As the temperature is lowered, the magnetic susceptibility remains fairly constant until about 100 K at which point a dramatic decrease in $\chi_M T$ is observed. At 1.8 K, the χ_MT reaches minimum values around 1, 4, 2, and 3 cm^3 mol^{-1} K for **11-14**, respectively. This behavior is indicative of weak antiferromagnetic exchange and is also consistent with

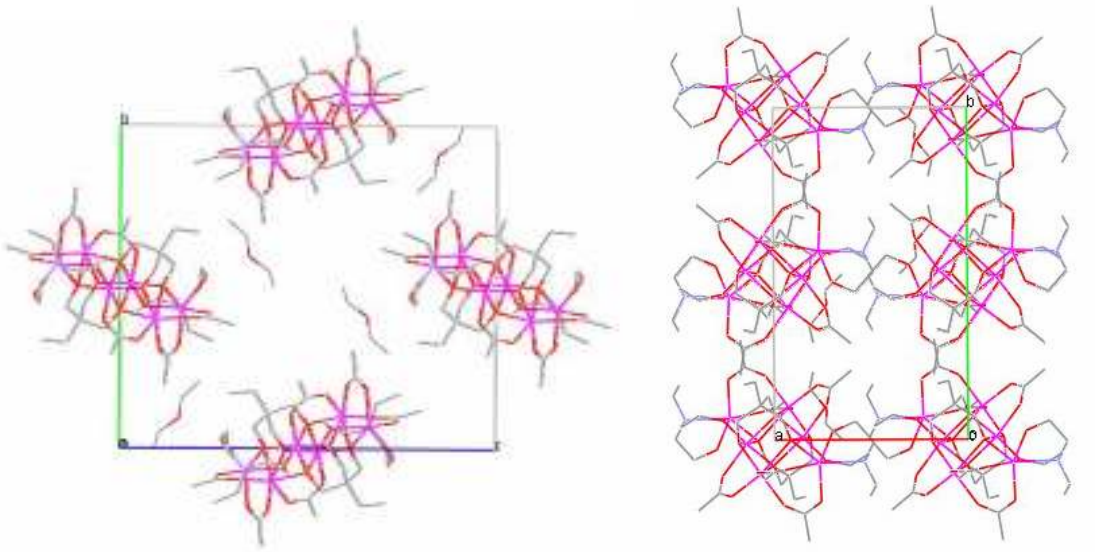

Figure 5.10. Unit cell of $[Mn_6(O_2CPh)_6(EdeaH)_2(tmp)_2] \cdot 2Et_2O$ **(14)** as viewed down the a-axis (left) and the c-axis (right). Only the *ipso* carbon atoms of the benzoate ligands are shown.

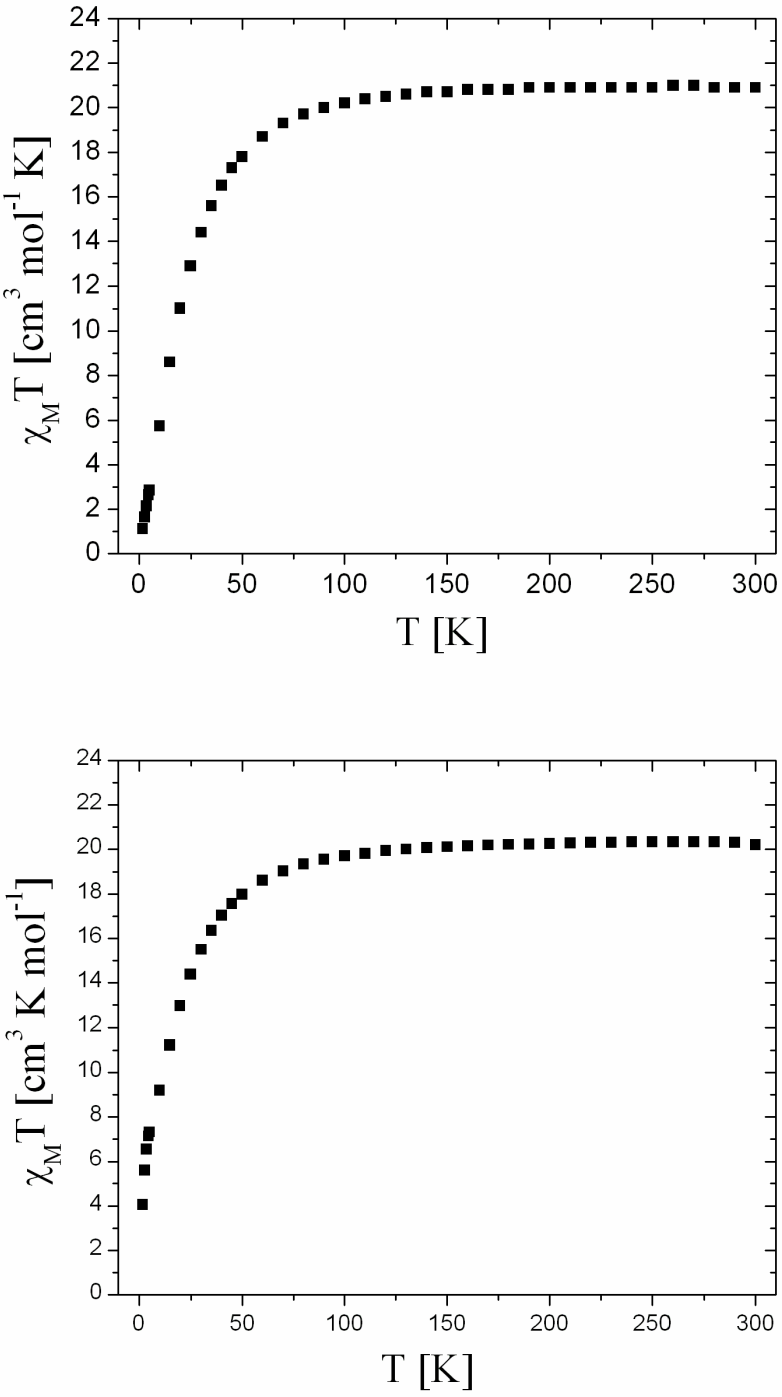

Figure 5.11. Plot of $\chi_M T$ *vs. T* for $[Mn_6(O_2CCH_3)_6(EdeaH)_2(tmp)_2]$ (**11**, top) and $[Mn_6(O_2CCH_3)_6mdeaH)_2(tmp)_2]$ (**12**, bottom) in an applied dc field of 1 T.

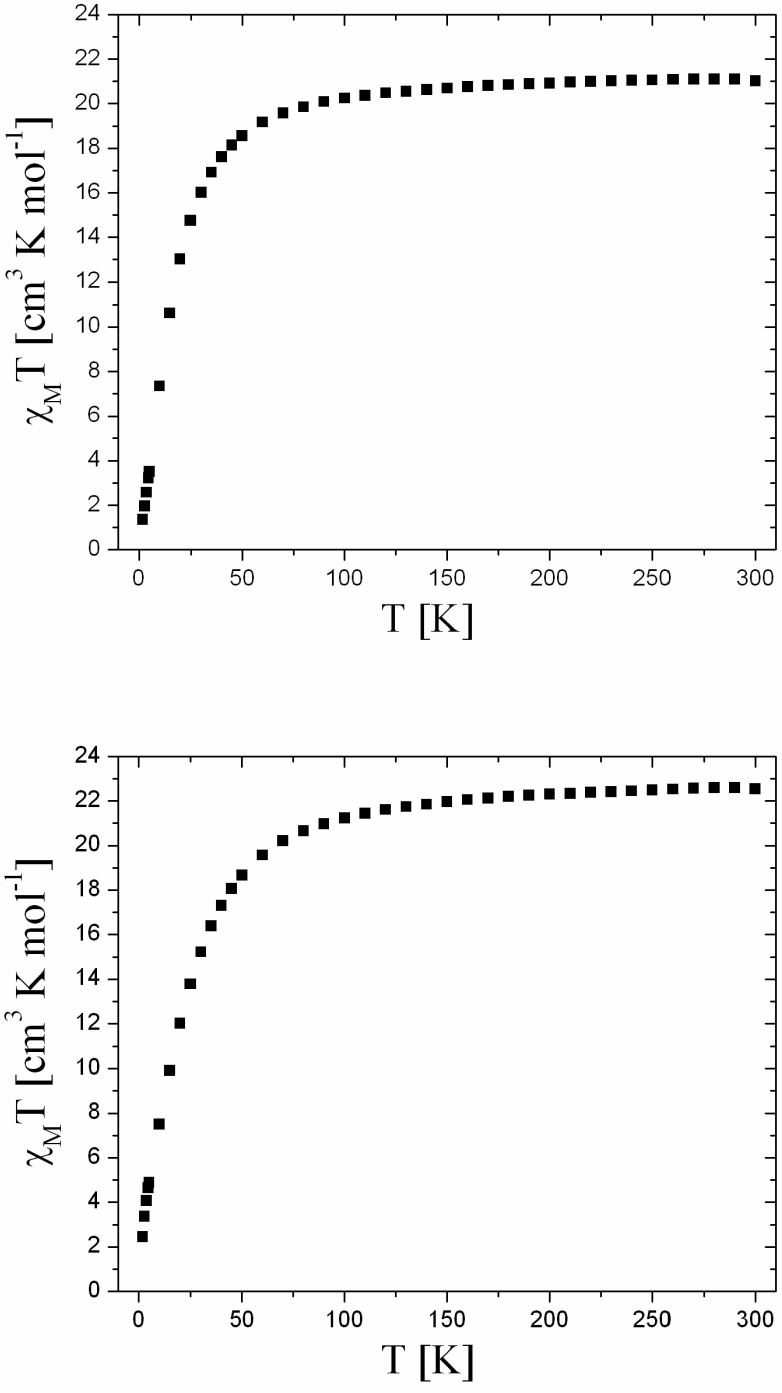

Figure 5.12. Plot of $\chi_M T$ *vs. T* for $[Mn_6(O_2CCF_3)_6(teaH_2)_2(tmp)_2] \cdot 2MeCN$ (**13**, top) and $[Mn_6(O_2CPh)_6(EdeaH)_2(tmp)_2] \cdot 2Et_2O$ (**14**, bottom) in an applied dc field of 1 T.

the $\chi_M T$ data observed for the previously studied mixed-valent [Mn_6] SMMs.[6, 7] Data were also collected at applied fields of 0.01 T and 0.1 T but no significant field-dependence was observed in 11, 13, or 14. However, in 12, the low-field data exhibit a small plateau at 5 K which is not present at 1 T.

The coupling scheme for this [$Mn^{III}_2Mn^{II}_4$] core is shown in Figure 5.13. The coupling constants (J_a, J_b, J_c, J_d and J_e) represent the five different magnetic exchange pathways between neighboring Mn ions. More specifically, J_a represents the Mn(III)-Mn(III) interaction; J_b, J_d, and J_e represent the Mn(III)-Mn(II) interactions; and J_c represents the Mn(II)-Mn(II) interaction. The Hamiltonian representing the pairwise exchange interactions is given in equation *5.1*. The total degeneracy of the [$Mn^{III}_2Mn^{II}_4$] complex is 32,400.

$$H = -2J_d[\hat{S}_1\hat{S}_5+\hat{S}_3\hat{S}_4]-2J_c[\hat{S}_1\hat{S}_2 + \hat{S}_3\hat{S}_6]-2J_b[\hat{S}_2\hat{S}_5+\hat{S}_4\hat{S}_6]-2J_e[\hat{S}_2\hat{S}_4+\hat{S}_5\hat{S}_6]-2J_a[\hat{S}_4\hat{S}_5] \qquad (5.1)$$

Due to entangled exchange paths that do not allow the whole system to be split into partial spin sums, the Kambe vector coupling method cannot be employed to determine the appropriate eigenvalue expression from the spin Hamiltonian. The alternative approach of block diagonalization was used, which is based on the fact that the Hamiltonian preserves the z-component of the total spin *S*, as shown in equation *5.2*.

$$S_z = \sum_i S_z(i) \qquad (5.2)$$

The largest block matrix is constructed in $S_z = 0$ for integer spin systems and S_z = -½ for half-integer systems, starting with the decoupled basis vectors $\prod_i |s_Z(i)\rangle$. $S^+ \mid Sz\rangle$ is evaluated for each eigenstate because the square of the total spin, S^2, should be a good quantum number, which we need to assign to an eigenstate along with S_z.

$$\langle S_Z + 1|\hat{S}^+|S_Z\rangle = \sqrt{(S - S_Z)(S + S_Z + 1)} \qquad (5.3)$$

From equation *5.3* above, equation *5.4* is derived for $S_z = 0$ and equation *5.5* is derived for $S_z = -½$

$$S = \frac{1}{2}\left(\sqrt{1 + 4\langle S_Z + 1|\hat{S}^+|S_Z\rangle^2} - 1\right) \qquad (5.4)$$

$$S = \langle S_Z + 1|\hat{S}^+|S_Z\rangle - \frac{1}{2} \qquad (5.5)$$

The energy eigenvalues, E (S, S_z), are obtained and the Van-Vleck equation (equation *5.6*) is used to calculate the magnetic susceptibilities as a function of the temperature.

$$\mu_{\text{eff}} = g\mu_{\text{B}}\sqrt{\frac{\sum_S S(S+1)(2S+1)\exp[-E(S,S_Z)/k_{\text{B}}T]}{\sum_S (2S+1)\exp[-E(S,S_Z)/k_{\text{B}}T]}} \qquad (5.6)$$

Figure 5.14 shows the μ_{eff} *vs.* T data (fit shown as solid curves) collected at 0.1 T for complexes **11-14**. The data collected from 1.8-300 K were fit with the following parameters: J_d = 0.87 cm^{-1}, J_c = -2.11 cm^{-1}, J_b = 2.36 cm^{-1}, J_e = 1.71 cm^{-1}, J_a = -4.17 cm^{-}

[1], and g = 1.8 for **11**; J_d = 1.84 cm^{-1}, J_c = -1.25 cm^{-1}, J_b = 2.06 cm^{-1}, J_e = -1.32 cm^{-1}, J_a= -3.45 cm^{-1}, and g = 1.8 (for T > 9 K) for **12**; J_d = -0.08 cm^{-1}, J_c = -1.67 cm^{-1}, J_b = 1.44 cm^{-1}, J_e = 0.94 cm^{-1}, J_a = -1.64 cm^{-1}, and g = 1.9 for **13**; J_d = 4.65 cm^{-1}, J_c = -1.92 cm^{-1}, J_b = 3.27 cm^{-1}, J_e = -0.88 cm^{-1}, J_a = -7.26 cm^{-1} and g = 1.89 for **14**.

The exchange interactions for the mixed-valent [Mn_6] complexes (with $S > 0$) reported by Rajaraman and Manoli *et al.,* [2,3] were determined by DFT calculations utilizing the same coupling scheme shown in Figure 5.13 except that J-values of J_1, J_2, J_3, J_4, and J_5 are used in place of J_d, J_c, J_b, J_e, *and* J_a, respectively. Table 5.9 shows a comparison of these J-values for the previously reported [Mn_6] complexes compared to those found for **11-14**.

Interestingly Mn(II)-Mn(II) and Mn(II)-Mn(III) interactions (J_1 and J_2) are found to be antiferromagnetic ($J < 0$) for all of the previously studied complexes whereas Mn(II)-Mn(III) and Mn(III)-Mn(III) interactions (J_3-J_5) are all ferromagnetic ($J > 0$) in nature.[2,3] Complexes **11-14** do not behave as similarly in their magnetic exchange parameters, however. The Mn(II)-Mn(II) interactions in **11-14** are also antiferromagnetic as expected but surprisingly, the Mn(III)-Mn(III) interaction was also found to be antiferromagnetic in all four complexes. The only mixed-valent [Mn_6] complexes with an antiferromagnetic Mn(III)-Mn(III) interaction are the previously studied $S = 0$ complexes which do not function as SMMs.[2,3] It is also important to note that complex **13** appears to have the weakest exchange interactions of all the [Mn_6] complexes with J-values ranging from -1.67 to +1.44 cm^{-1} as opposed to complex **14**, for instance, which has a J-value range of -7.26 to +4.56 cm^{-1}.

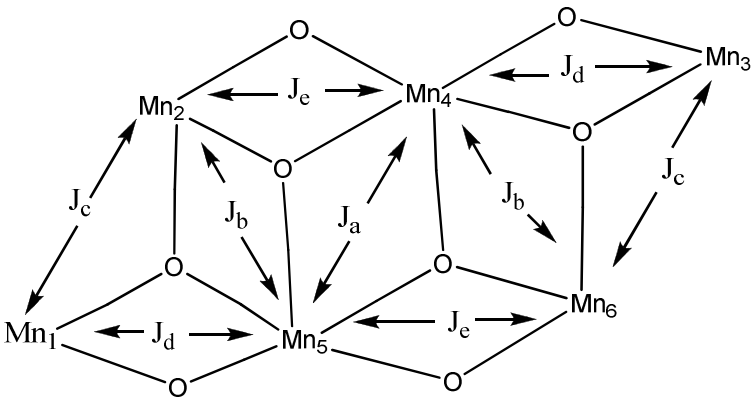

Figure 5.13. Coupling scheme for $[Mn^{III}_2Mn^{II}_4]$ complexes, where Mn1, Mn2, Mn3, and Mn6 are in the +2 oxidation state and Mn4 and Mn5 are in the +2 oxidation state.

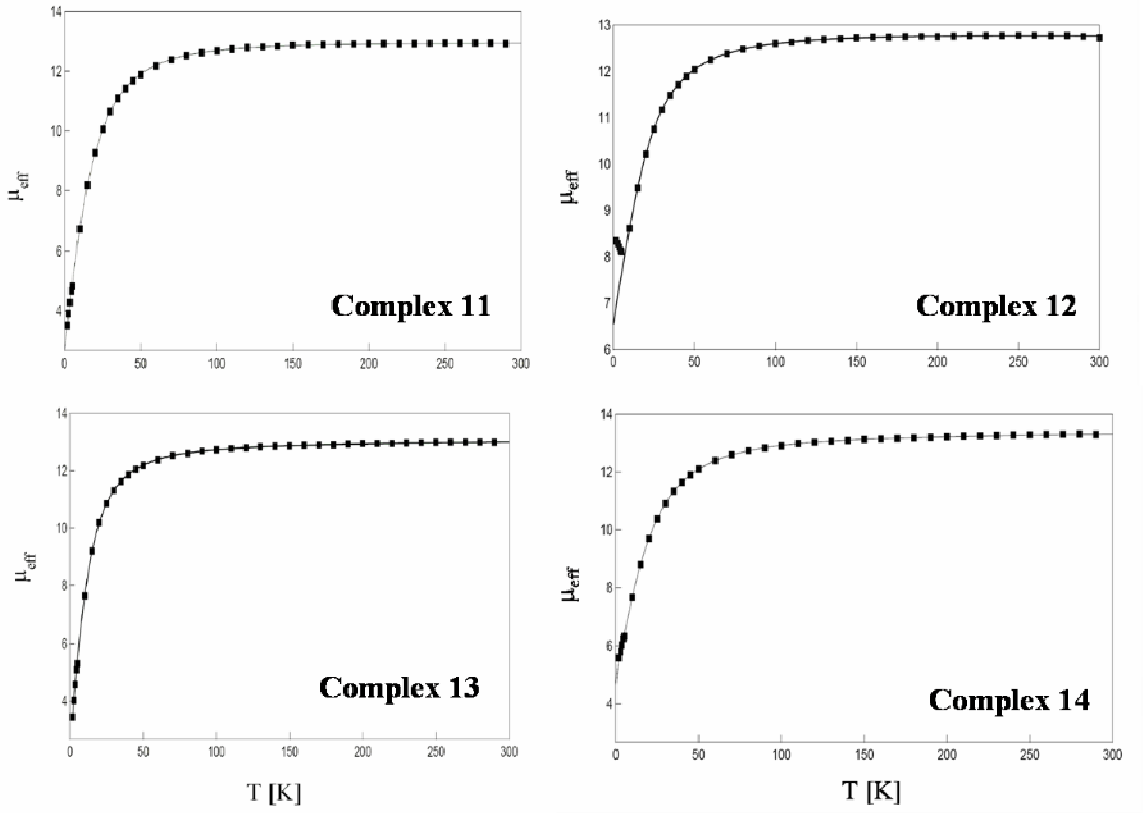

Figure 5.14. Plot of μ_{eff} *vs. T* for **11-14** in an applied dc field of 0.1 T with theoretical fits shown as solid black curves.

Table 5.9. Comparison of J-values for **11- 14** (block diagonalization) with selected mixed-valent [Mn_6] complexes reported in the literature (DFT calculations).

Complex	**J-values (cm^{-1})**				
	J_d (J_1)	**J_c (J_2)**	**J_b (J_3)**	**J_e (J_4)**	**J_a (J_5)**
$[Mn_6(O_2CMe)_6(tmp)_2(edea)_2]$ (**11**)	+0.87	-2.11	+2.36	+1.71	-4.17
$[Mn_6(O_2CMe)_6(tmp)_2(mdea)]$ (**12**)	+1.84	-1.25	+2.06	-1.32	-3.45
$[Mn_6(O_2CCF_3)_6(teaH)_2(tmp)_2]\cdot 2CH_3CN$ (**13**)	-0.08	-1.67	+1.44	+0.94	-1.64
$[Mn_6(O_2CPh)_6(tmp)_2(Edea)_2]\cdot 2Et_2O$ (**14**)	+4.65	-1.92	+3.27	-0.88	-7.26
$[Mn_6(O_2CCMe_3)_8(tmp)_2(py)_2]$ [6]	-5.99	-0.72	+3.02	+0.31	+1.46
$[Mn_6(O_2CCH_3)_8(tmp)_2(py)_4]\cdot 2py$ [7]	-7.6	-5.0	+6.8	+0.2	+0.7
$[Mn_6(O_2CCH_3)_8(thme)_2(py)_4]\cdot 2py$ [7]	-5.2	-2.2	+0.5	+2.1	+4.9

In order to determine the spin ground state of the complexes reported herein, variable-field dc magnetic susceptibility data were also collected at applied fields of 0.1-5 T and plotted as reduced magnetization $M/N_{\mu B}$ *vs.* H/T, where N is Avogadro's number and μ_B is the Bohr magneton. The reduced magnetization plots for complexes **11-14** are all very similar in saturation magnetization value (6.5-7.5 μ_B at 5 T) as well as the presence of axial zero-field splitting evidenced by the non-superimposable nature of the isofields. The data were least-squares fit using the same spin Hamiltonian used in the previous chapters which includes an axial zero-field splitting ($D\hat{S}_z^2$) and isotropic Zeeman interactions ($g\mu_0\mu_B\hat{S}H_z$) terms. Once again, this model assumes that only the ground state is being populated and thus may not be an accurate description in the case of a poorly isolated ground state (low-lying excited states).

The reduced magnetization for **12** is plotted in Figure 5.15 with theoretical fits shown as solid black curves. The high-field data (5, 4, 3, and 2 T) for **12** were fit reasonably well to a $S = 5$ ground state with g fixed at 1.9 and a D-value of -0.91 cm^{-1}. The low-field data (0.1, 0.5, 1, 2, and 3 T) fit very well to a $S = 4$ ground state with g = 1.8 and D/k_B = -0.52 cm^{-1}. These results are very close to the fitting parameters found for Rajaraman's $[Mn_6(O_2CCMe_3)_8(tmp)_2(py)_2]$ rod which was found to have the same D-value of -0.52 cm^{-1} ($g = 1.73$, $S = 3$) when fit up to 3 T.[2] Milios's $[Mn_6]$ SMMs were also similar with best fits of the reduced magnetization data (H = 0.1 - 4 T) with parameters of $S = 4$, $g = 1.82$, D/k_B = -0.44 cm^{-1} for $[Mn_6(O_2CMe)_8(thme)_2(py)_4] \cdot 2py$ and $S = 4$, $g = 1.97$, D/k_B = -0.58 cm^{-1} for $[Mn_6(O_2CMe)_8(tmp)_2(py)_4] \cdot 2py$.[3]

The reduced magnetization for complexes **11**, **13**, and **14** (Figures 5.16, 5.17 and 5.18, respectively) proved more difficult to obtain reasonable fits which indicates that

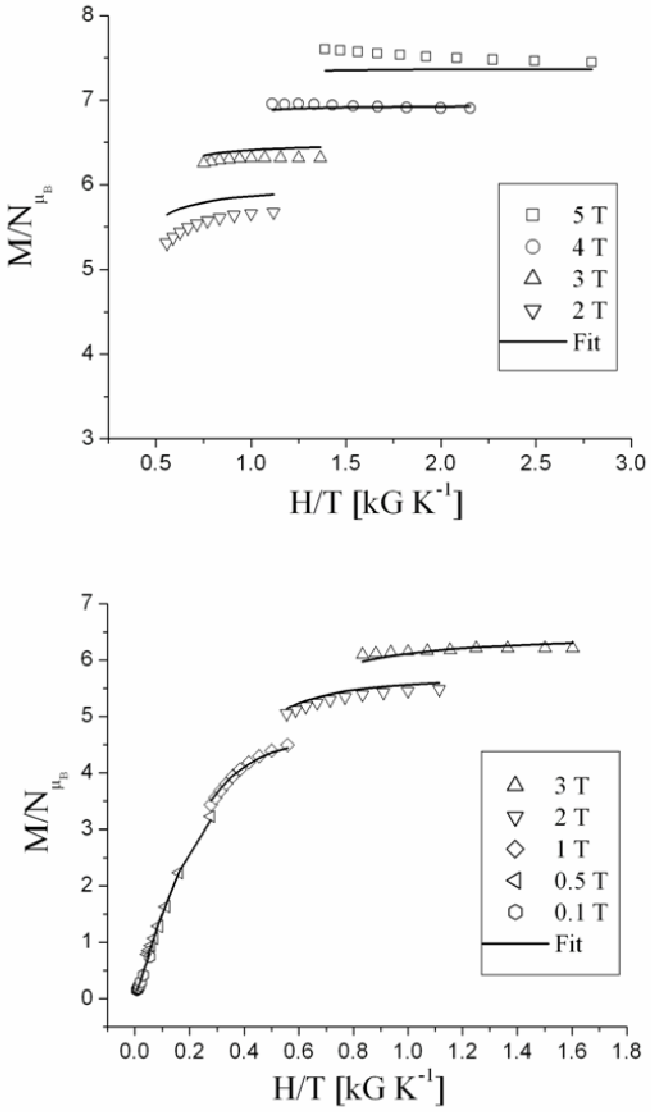

Figure 5.15. Reduced magnetization for $[Mn_6(O_2CCH_3)_6mdeaH)_2(tmp)_2]$ **(12)** with fitting parameters of $S = 5$, $g =$ 1.9 (fixed), and D/k_B = -0.91 cm^{-1} at high fields (top) and $S = 4$, $g = 1.8$, and D/k_B = -0.52 cm^{-1} at low fields (bottom).

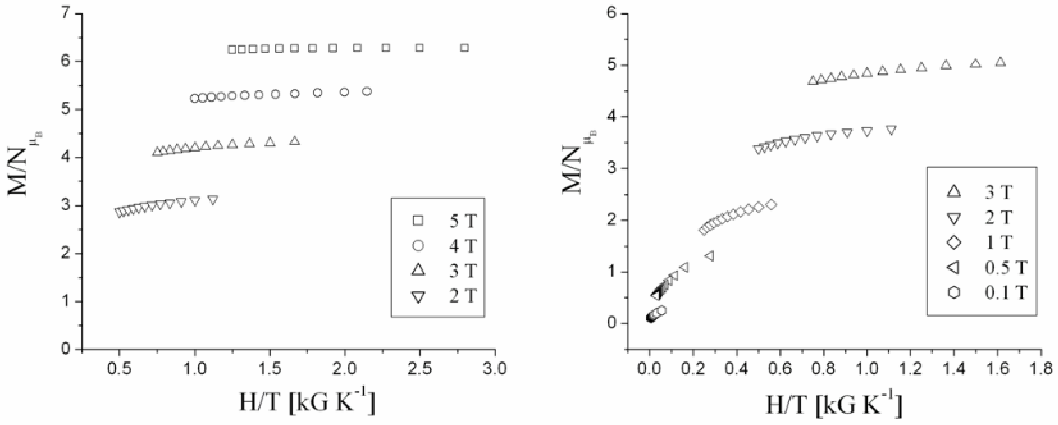

Figure 5.16. Reduced magnetization for $[Mn_6(O_2CCH_3)_6(EdeaH)_2(tmp)_2]$ **(11)** at high fields (left) and low fields (right).

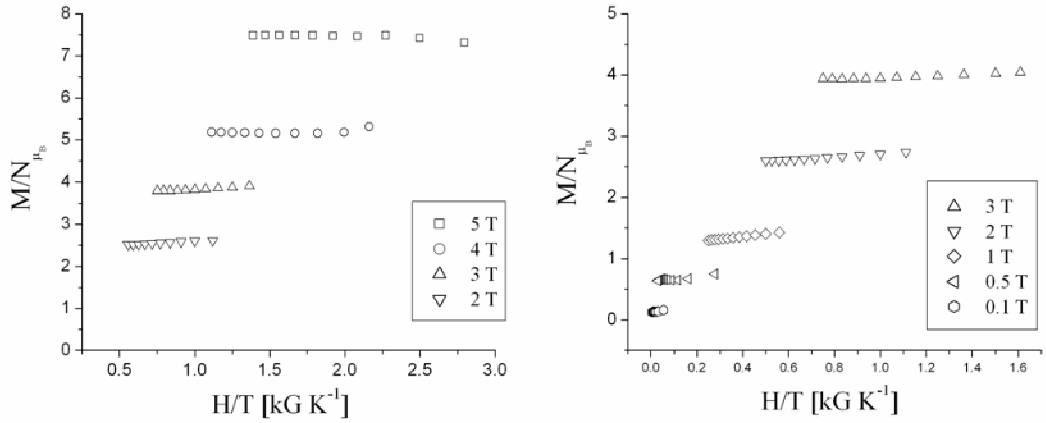

Figure 5.17. Reduced magnetization for $[Mn_6(O_2CCF_3)_6(teaH_2)_2(tmp)_2] \cdot 2MeCN$ **(13)** at high fields (left) and low fields (right).

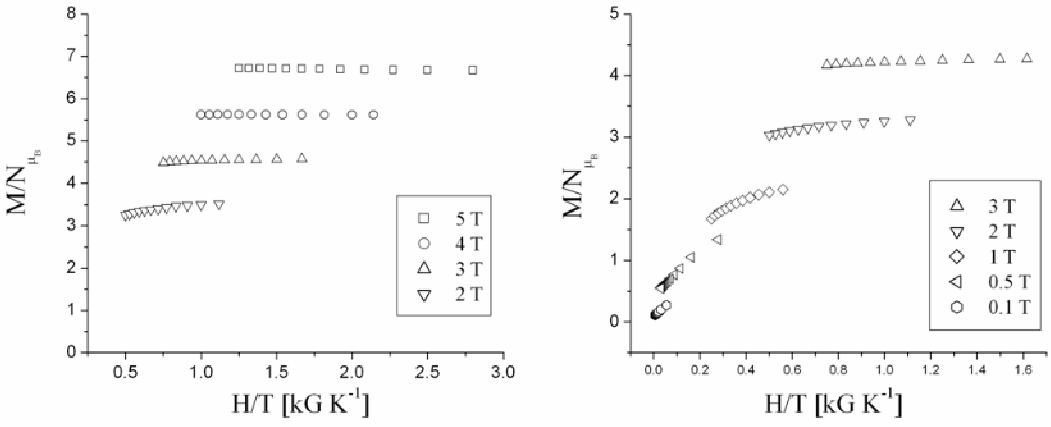

Figure 5.18. Reduced magnetization for $[Mn_6(O_2CPh)_6(EdeaH)_2(tmp)_2] \cdot 2Et_2O$ **(14)** at high fields (left) and low fields (right).

these complexes likely possess many low-lying excited states. With a poorly-defined ground sate, population of multiple excited states could very well be occurring at higher fields which is not accounted for in this model. However, the magnetization saturation value at 5 T for all four complexes suggests a spin ground state around $S = 3$ or $S = 4$ which is consistent with the fitting parameters found for complex **12**.

5.3.3. AC Magnetic Susceptibility

Ac magnetic susceptibility data (plotted in Figures 5.19-5.22) were collected on all four complexes in the temperature range of 1.8-5 K in a 0.99 Oe ac field oscillating at frequencies from 50-10,000 Hz. The top portions of Figures 5.19-5.22 show the product of molar in-phase susceptibility and the absolute temperature, $\chi_M'T$, plotted vs. the absolute temperature, T. The bottom portion of the plots shows the molar out-of-phase ac susceptibility, χ_M'', plotted vs. T. A frequency-dependent out-of-phase signal in the ac susceptibility is indicative of slow magnetization relaxation relative to the frequency of the external oscillating ac field.

Complexes **11** and **14** show significant frequency-dependent out-of-phase signals in the ac susceptibility with maximum values at 10,000 Hz occurring around 2.5 K. Complex **12** also exhibits this behavior but the maxima in the high-frequency out-of-phase data occur below 2 K which is beyond the capabilities of our instrumentation. Finally, complex **13** shows a very weak out-of-phase signal in this temperature range even at the highest frequencies measured. All of the previously reported mixed-valent [Mn_6] rod-shaped complexes show little to no frequency-dependent out-of-phase signals in the ac susceptibility up to frequencies of 1300 Hz.[2,3]

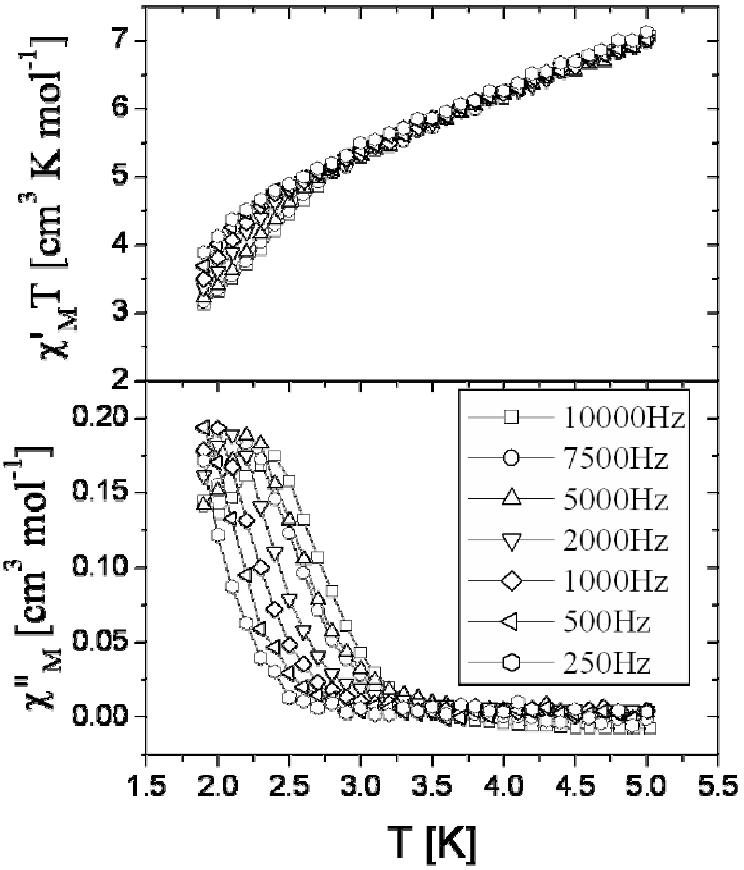

Figure 5.19. (Top) In-phase, $\chi_M'T$, and (bottom) out-of-phase, χ_M'', ac magnetic susceptibility for $[Mn_6(O_2CCH_3)_6(EdeaH)_2(tmp)_2]$ **(11)**.

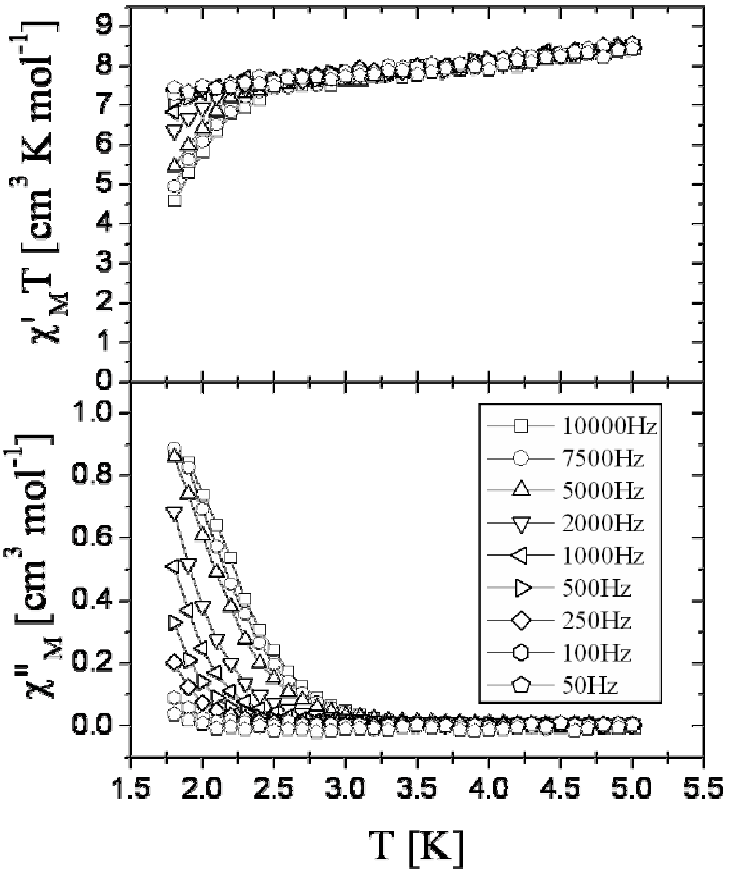

Figure 5.20. (Top) In-phase, $\chi_M'T$, and (bottom) out-of-phase, χ_M'', ac magnetic susceptibility for $[Mn_6(O_2CCH_3)_6mdeaH)_2(tmp)_2]$ **(12).**

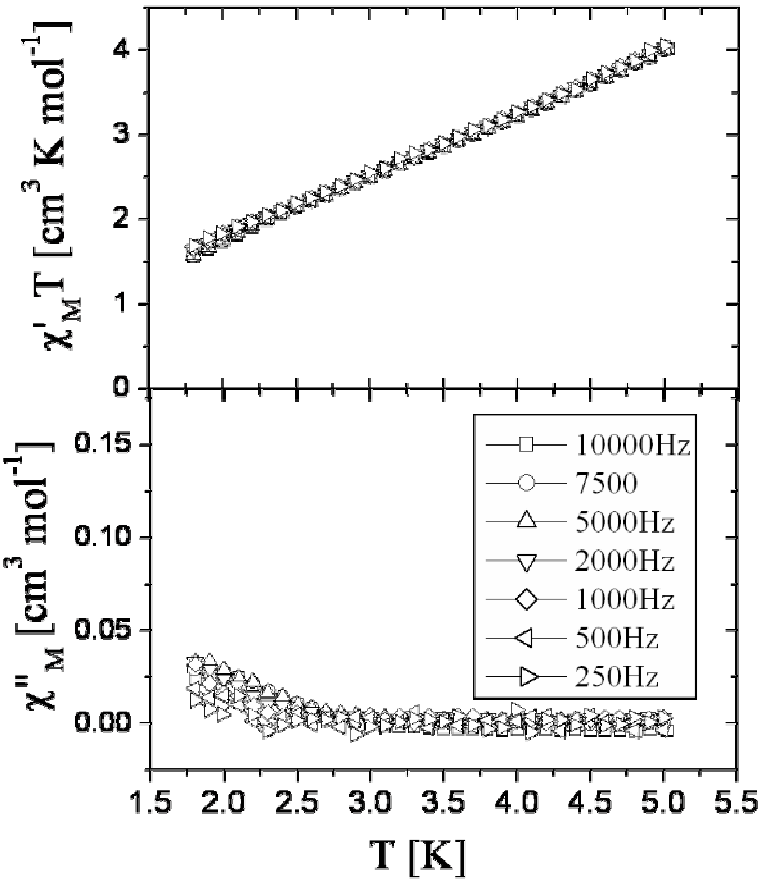

Figure 5.21. (Top) In-phase, $\chi_M'T$, and (bottom) out-of-phase, χ_M'', ac magnetic susceptibility for $[Mn_6(O_2CCF_3)_6(teaH_2)_2(tmp)_2] \cdot 2MeCN$ **(13).**

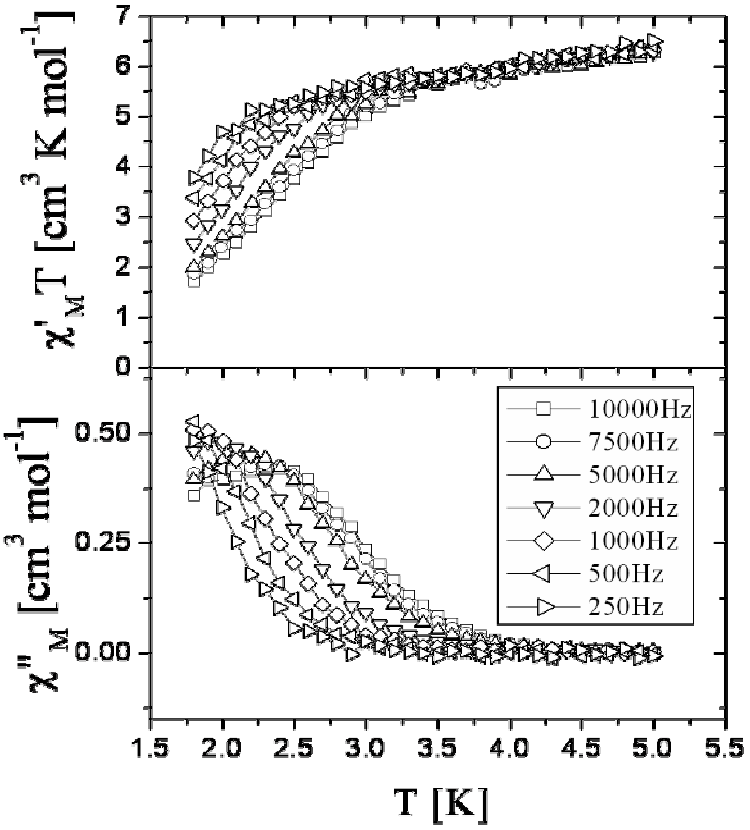

Figure 5.22. (Top) In-phase, $\chi_M'T$, and (bottom) out-of-phase, χ_M'', ac magnetic susceptibility for $[Mn_6(O_2CPh)_6(EdeaH)_2(tmp)_2] \cdot 2Et_2O$ **(14).**

To further corroborate the ground state spin values predicted by the ac magnetic data, the low frequency in-phase ac susceptibility data were further analyzed. Extrapolation of the 250 Hz $\chi_M'T$ data to zero K gives a value which can be compared to that predicted by the spin-only formula. The extrapolated $\chi_M'T$ values for complexes **11**, **12**, and **13** most closely corresponded to ground state spins of S = 2, 3, and 1, respectively, whereas that for **14** fell between ground states of S = 2 and S = 3. These results are fairly consistent with the S = 3 or S = 4 ground states suggested by reduced magnetization data.

Also, the spin-states extrapolated from ac susceptibility data are typically considered a more accurate description of the ground state since these data are collected in the absence of an applied dc magnetic field which can often lead to population of excited states as discussed above in the dc magnetic studies section. The lower spin of complex **13** might also explain the lack of a significant out-of-phase signal in the ac susceptibility above 1.8 K and may indicate that this complex is not a SMM. This result is also consistent with the *J*-values obtained for **13** from the dc magnetic studies which showed very weak exchange and an antiferromagnetic Mn(III)-Mn(III) interaction, leading to a small overall spin.

5.3.4. Structural Considerations

Although complexes **11-14** have the same core structures, there are some significant differences in their overall spin and magnetic behavior. For instance, in the [Mn_6] complexes reported my Manoli *et al.*[3] in 2006, it was found that a larger Mn-O-Mn angle leads to an antiferromagnetic exchange interaction and a smaller Mn-O-Mn

bridging angle leads to a ferromagnetic exchange interaction between the two Mn(III) ions. This subtle difference in bond angles was enough to cause a "switch" from S = 0 to S = 4 in complexes of similar geometry.

Similarly, there are some subtle differences in Mn-O-Mn bridge angles in **11-14** which could lead to the variation we see in the ground state spins of these four complexes. Also, intermolecular interactions can have a detrimental effect on magnetic exchange in SMMs. This may explain the low spin and weak out-of-phase signal in complex **13** which has a significant amount of intermolecular interactions between the co-crystallized MeCN solvate molecules and the CF_3 substituents on the [Mn_6] units, as described in the crystallographic section (see Figure 5.9). These interactions can decrease the overall spin and subsequently the effective barrier to reversal of the magnetization.

5.4. Conclusions

Four new mixed-valent rod-shaped [Mn_6] complexes have been synthesized and characterized using the tripodal ligand, *tris*-hydroxymethyl propane ($tmpH_3$). Single-crystal x-ray diffraction revealed well-ordered structures with a $[Mn^{II}_4Mn^{III}_2(\mu_2\text{-}OR)_4(\mu_3\text{-}OR)_4]^{6+}$ core. Both dc and ac magnetic susceptibility studies were used to determine the ground state spin, axial anisotropy, and the overall nature of the magnetic exchange in these complexes. Magnetic exchange interactions between neighboring Mn ions in the complex were determined by block-diagonalization of the dc data and compared to those found for previously reported analogs determined by DFT calculations. Significant differences in these values lead to further analysis of the spin

ground states through variable-field dc measurements and ac magnetic susceptibility studies.

All four of the complexes reported and discussed herein possess non-zero spin ground states ($S \leq 4$), appreciable zero-field splitting, and frequency-dependent out-of-phase signals in the ac susceptibility; all of these are characteristics of SMM behavior. However, only complexes **11**, **12**, and **14** are likely to be SMMs since **13** has a low spin ground state ($S \approx 1$) and a very weak out-of-phase ac signal even in an ac field oscillating at 10,000 Hz. These molecules are an important addition to the family of [Mn_6] rod-shaped complexes since they exhibit yet another variation of the Mn-oxo core found in these structures and show promise as SMMs. Although complexes **11-14** have analogous core structures, it is interesting to note how subtle structural differences and intermolecular interactions can have dramatic effects on the overall magnetic properties of the complexes.

This chapter, in part, is a reprint of the material as it appears in: Heroux, K. J.; Shah, S. J.; O'Brien, J. R.; DiPasquale, A. G.; Nakano, M.; Hendrickson, D. N. "Rod-shaped [Mn_6] complexes as single-molecule magnets", *Inorganica Chimica Acta,* **2010**, doi:10.1016/j.ica.2010.04.013, *in press.* The dissertation author was the primary author of this paper.

5.5. References

(1) (a) Sessoli, R.; Tsai, H.-L.; Schake, A. R.; Wang, S.; Vincent, J. B.; Folting, K.; Gatteschi, D.; Christou, G.; Hendrickson, D. N. *J. Am. Chem. Soc.* **1993**, *115*, 1804. (b) Sessoli, R.;Gatteschi, D.; Caneschi, A.; Novak, M. A. *Nature* **1993**, *365*, 141.

(2) Rajaraman, G.; Murugesu, M.; Sanudo, E. C.; Soler, M.; Wernsdorfer, W.; Helliwell, M.; Muryn, C.; Raftery, J.; Teat, S. J.; Christou, G.; Brechin E. K. *J. Am. Chem. Soc*. **2004,** *126*, 15445.

(3) Milios, C. J.; Manoli, M.; Rajaraman, G.; Mishra, A.; Budd, L. E.; White, F.; Parsons, S.; Wernsdorfer, W.; Christou, G.; Brechin E. K. *Inorg. Chem.* **2006**, *45*, 6782.

(4) Milios, C. J.; Inglis, R.; Vinslava, A.; Bagai, R.; Wernsdorfer, W.; Parsons, S.; Perlepes, S. P.; Christou, G.; Brechin, E. K. *J. Am. Chem. Soc.* **2007**, *129,* 12505.

(5) Baillie, M. J.; Brown, D. H.; Moss, K. C.; Sharp, D. W. A. *J. Chem. Soc. A* **1968**, 3110.

(6) Vincent, J. B.; Chang, H.-R.; Folting, F.; Huffman, J. C.; Christou, G.; Hendrickson, D. N. *J. Am. Chem. Soc.* **1987**, *109*, 5703.

Chapter 6:

Superexchange through Dicyanamide Bridges in Dinuclear Complexes and Single-Molecule Magnets

6.1 Introduction

The presence of superexchange[1,2] between paramagnetic metal centers has been an important topic for chemists and physicists for many years. Superexchange is a general term used to describe the coupling interaction between two next-to-nearest neighbor cations propagated through a non-magnetic anion or bridge. The orientation and geometry of the non-magnetic bridge often dictate the nature and magnitude of magnetic exchange that occurs. Typically, superexchange interactions are strongly antiferromagnetic; however, if the two next-to-nearest neighbor cations are connected at nearly 90° to the bridging non-magnetic anion, then the interaction can be ferromagnetic.[1,2]

Much of the work in this area of research has focused on Cu(II) complexes which exhibit antiferromagnetic exchange between the paramagnetic metal ions.[3-15] However, the nature of these interactions and the factors that influence them have yet to be fully realized. The degree of magnetic exchange between two paramagnetic metal centers is governed not only by the length of the bridging ligand but also by such factors as orbital overlap, bond angles, and delocalization of electrons.[3,16]

Due to the tremendous versatility of the dicyanamide ($N(CN)_2^-$ or dca^-) ligand, dca-bridged polynuclear complexes have been extensively studied in recent years. The eight different binding modes of the dca^- monoanion (shown in Figure 6.1) lead to a wide array of complexes of various topologies and magnetic characteristics. Depending on the coordination mode encountered, the dca^- ligand can form 1D chains, 2D arrays, and even 3D networks with the help of bridging ancillary ligands, H-bonding interactions, and intermolecular π–π stacking. Some of the magnetic properties

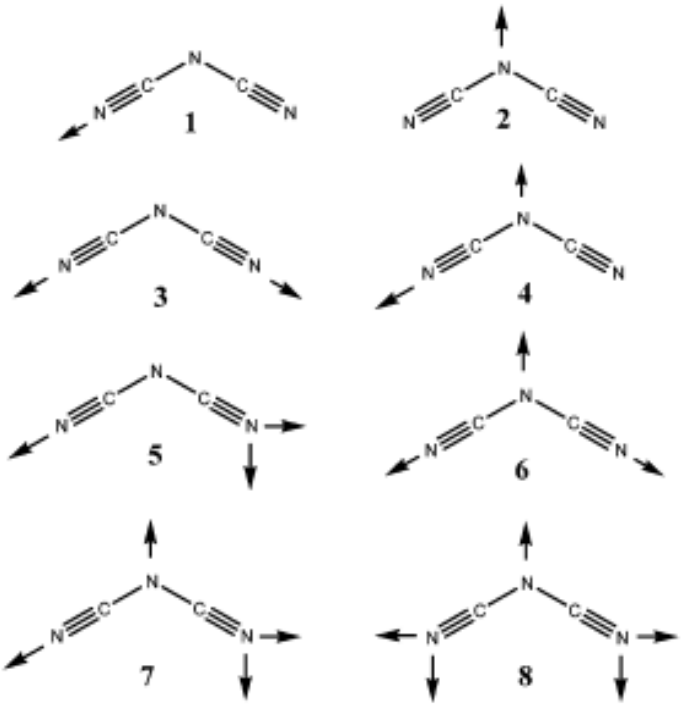

Figure 6.1. Coordination modes of the dicyanamide anion.

previously observed in these complexes include ferromagnetism, spin-canted antiferromagnetism, and paramagnetism.[16] Intermolecular superexchange pathways have also become increasingly important in the area of single-molecule magnets (SMM). As described in the Introduction Chapter, even small interactions between neighboring molecules can greatly affect the magnetic and quantum properties of the individual SMMs (exchange-biased quantum tunneling,[17-19] quantum phase interference,[20,21] decoherence,[22] etc.).

In 2005, Miyasaka *et al.*[23] reported the first 2D networks of covalently-linked [Mn_4] SMMs exhibiting weak magnetic exchange through dca^- bridges. Figure 6.2 shows the core structure and crystal packing diagrams of one such complex, $[Mn_4(hmp)_4(Hpdm)_2(dca)_2](ClO_4)_2 \cdot 2H_2O \cdot 2MeCN$, where Hhmp and H_2pdm are 2-hydroxymethylpyridine and pyridine-2,6-dimethanol, respectively. However, the weak antiferromagnetic exchange observed in such a complex system cannot be definitively attributed to the dca^- bridge since other intermolecular interactions such as appreciable $\pi-\pi$ stacking between adjacent [Mn_4] units may also induce this type of exchange as seen is most dca-bridged networks.

There are numerous other examples of dicyanamide-linked complexes of various metals including Mn, Ni, Co, Fe, and Cu ions. However, most of these materials form 1D chains or 2D arrays involving, not only dca^- bridges, but many other intermolecular pathways that could support magnetic exchange. Thus, it is nearly impossible to determine the magnitude of magnetic exchange propagated solely through the dca^- bridge in this type of network.

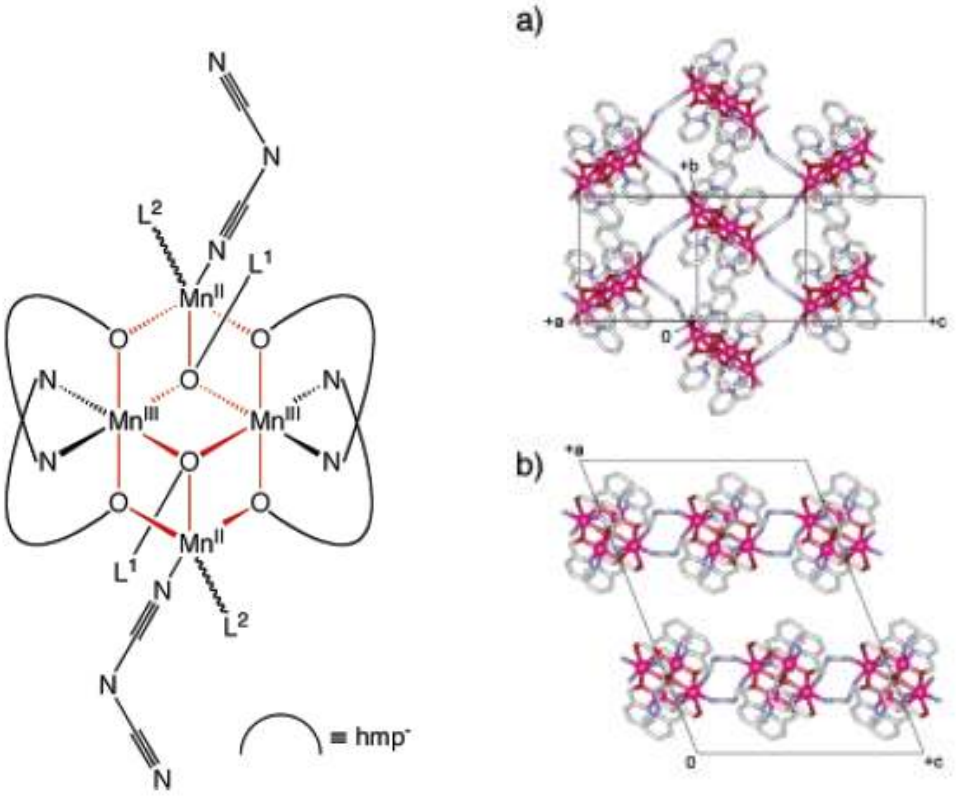

Figure 6.2. (left) core structure and (right) crystal packing diagrams of $[Mn_4(hmp)_4(Hpdm)_2(dca)_2](ClO_4)_2 \cdot 2H_2O \cdot 2MeCN$.

For example, the $[Cu(dca)(pcl)(H_2O)]_2$ complex,[24] where pcl is picolinic acid ($C_6H_4NO_2$), consists of two square pyramidal Cu(II) ions doubly bridged by two $\mu_{1,5}$-dca^- ligands. Weak Cu-Cu and Cu-N intermolecular contacts between adjacent dinuclear units as well as H-bonding interactions between water and carboxylate ligands form a chain-like 2D network. From the magnetic susceptibility data, a strong antiferromagnetic exchange parameter of J = -34.8 cm^{-1} was found between the two Cu(II) centers. However, because this value is more than an order of magnitude higher than any other Cu(II)-$(dca)_2$-Cu(II) interactions, this magnetic exchange is better explained by the Cu-Cu and picolinate-H_2O pathways as opposed to the dca^- bridge alone. Another example is the $[Cu_2(dmphen)_2(dca)_4]$ 1D chain,[4] where dmphen is 2,9-dimethyl-1,10-phenanthroline. This complex was found to have a J-value of -3.4 cm^{-1} which was reported as being the largest coupling constant for a double end-to-end dca^- bridge at the time. However, considerable π–π stacking occurs between adjacent phenanthroline rings in this network which could account for some of the magnetic exchange observed between the Cu(II) ions.

The most common coordination environment adopted by the dca^- ligand is the end-to-end ($\mu_{1,5}$) bridging mode (*3* in Figure 6.1) which has been shown to induce weak magnetic exchange between paramagnetic metal ions in various cluster complexes.[16] However, there are only three examples of discrete dinuclear Cu(II) complexes in the literature exhibiting this single end-to-end dicyanamide bridge. One, reported by Potočňák *et al.* in 2002, is the $[Cu(bpy)_2(dca)(bpy)_2Cu](ClO_4)_3$ dinuclear complex,[25] where bpy is 2, 2′-bipyridine. Another is $[Cu(tacn)(Cl)(dca)(Cl)(tacn)Cu](ClO_4)$, where tacn is 1,4,7-triazacyclononane, reported by Wang *et al.* in 2004.[5] The Cu(II) ions in

both of these complexes exhibit distorted trigonal bipyramidal geometry with the dca^- ligand bound in an axial position, most likely leading to a favorable overlap between the metal and ligand bonding orbitals. However, neither of these dinuclear complexes was magnetically characterized so the exchange across the dca^- bridge in these examples is unknown.

Lastly, Karmakar *et al.* reported the complex $[Cu(L^1)(dca)(L^1)Cu](ClO_4)$,[26] where L^1 is the Schiff base N,N-dimethylethylene-N′-(pyridine-2-carbaldiiminato), which is shown in Figure 6.3. The Cu(II) ions in this complex are both square planar in geometry and the dca^- bridge has a central C-N-C angle of 120°, typical of these dinuclear species. Magnetic susceptibility studies on this complex revealed a weak antiferromagnetic interaction with a J-value of -0.20 cm^{-1}. This exchange is attributed to a small overlap of the magnetic d_x^2-$_y^2$ orbitals of the two Cu(II) ions.

In the 1970s, a series of $[Cu_2(tren)_2(dca)]Y_3$ dinuclear complexes, where tren is 2, 2′, 2″-triaminotriethylamine and Y is ClO_4^-, BF_4^-, PF_6^-, or BPh_4^- , were previously prepared in this laboratory in order to study their magnetic exchange pathways.[12,27] Variation of the counterion was studied in order to determine its influence, if any, on the structural and magnetic properties of these complexes. Since the counterions play a major role in the molecular packing of the dinuclear $[Cu_2(tren)_2(dca)]^{3+}$ cations, changes in the intermolecular interactions throughout the crystal lattice are expected to occur.[1] Previously reported Cu(II) dinuclear complexes exhibiting the end-to-end dca^- bridge typically have a central C-N-C angle of 120-130°.[3-5,23,25,26] Based on IR, Raman, and EPR data, it was initially suggested that the BPh_4^- analog in this series of copper

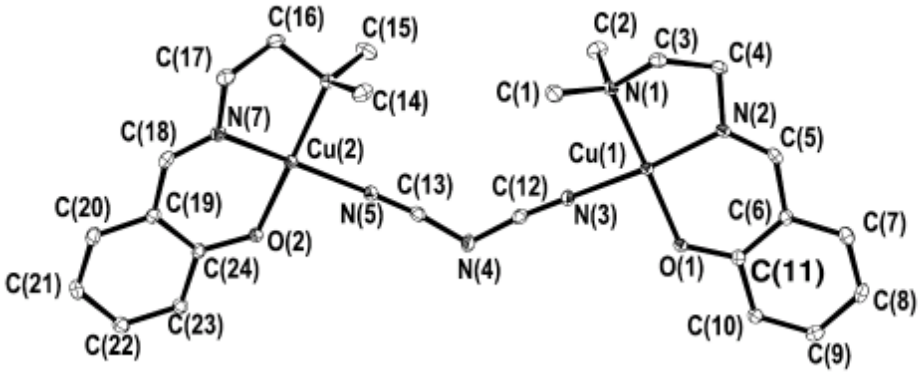

Figure 6.3. ORTEP of $[Cu(L^1)(dca)(L^1)Cu](ClO_4)$ with ClO_4^- anion omitted for clarity.

complexes may have an unprecedented linear dca^- bridge due to its unique magnetic properties, thus obtaining a crystal structure became an intriguing challenge. [12,27]

To further investigate this matter, crystals of the dinuclear complex $[Cu_2(tren)_2(dca)](BPh_4)_3$ as well its closely related mononuclear counterpart $[Cu(tren)(dca)](BPh_4)$ were prepared via a modified synthesis. This simple system (supported by x-ray crystal structures and dc magnetic susceptibility data) allows for a more accurate determination of the magnitude of magnetic exchange propagated through a single dicyanamide bridge.

6.2 Experimental Section

6.2.1. Preparation

All reactions were performed under aerobic conditions. All reagents and ligands were purchased from Sigma Aldrich and used without further purification.

$[Cu_2(tren)_2(dca)](BPh_4)_3$ (15). The $[Cu_2(tren)_2(dca)]^{3+}$ cation was prepared by dissolving 0.25 g (1 mmol) $CuSO_4 \cdot 5H_2O$, 0.15 mL (1 mmol) tren, and 0.045 g (0.5 mmol) dca^- in 40 mL of distilled water giving a transparent blue solution. For the anion, 0.34 g (1 mmol) $NaBPh_4$ was dissolved in 40 mL of a 3:1 EtOH:H_2O solution. Direct layering of the anion solution over the cation solution in layering tubes (or U-tube diffusion) resulted in light blue precipitate at the interface and large blue needle-shaped crystals of **15** in 70% yield. Elemental analysis for $C_{86}H_{96}B_3Cu_2N_{11}$: calc'd (found), C 71.57 (71.25), H 6.70 (6.94), N 10.68 (10.79). Selected FT-IR Data (KBr, cm^{-1}): 3432 (s, br), 3288 (m), 3053 (w), 2204 (s), 1578 (m), 1477 (m), 1426 (m), 1384 (m), 1059 (m), 734 (m), 710 (m), 612 (w).

[Cu(tren)(dca)](BPh$_4$) (16). The cation and anion portions of complex **16** are prepared in the same manner as complex **15** above. Direct addition of the anion solution to the cation solution results in the formation of an immediate light blue precipitate which can be filtered off and washed with EtOH. Recrystallization of the precipitate in MeCN with diisopropyl ether vapor diffusion affords large blue-green needle-shaped crystals of **16** in 20% yield. Elemental analysis for $C_{32}H_{38}BCuN_7$: calc'd (found), C 64.59 (64.48), H 6.44 (6.27), N 16.48 (16.79). Selected FT-IR Data (KBr, cm^{-1}): 3433 (m, br), 3327 (m), 3262 (m), 3053 (w), 2291 (m), 2241 (m), 2178 (s), 1578 (w), 1468 (w), 1346 (w), 1057 (w), 988 (w), 740 (m), 707 (m), 611 (w), 532 (w).

6.2.2. X-Ray Crystallography

Crystals were mounted on a CryoLoop© with Paratone-N© oil. Diffraction intensity data were collected at 100 K on a Bruker Smart Apex CCD diffractometer with Mo Kα radiation, integrated using Bruker SAINT software program, and corrected for absorption using the Bruker SADABS program. Complexes **15** and **16** were solved by direct methods (SHELXS-97), developed by successive difference Fourier syntheses, and refined by full matrix least squares on all F^2 data. All non-hydrogen atoms were refined anisotropically by full-matrix least-squares (SHELXL-97). Crystallographic data and refinement parameters for **15** and **16** are given in Table 6.1. Selected interatomic bond distances and angles for **15** and **16** can be found in Table 6.2.

Table 6.1. Crystallographic data and refinement parameters for $[Cu_2(tren)_2(dca)](BPh_4)_3$ **(15)** and $[Cu(tren)(dca)](BPh_4)$ **(16).**

	15	**16**
Formula	$Cu_2C_{86}H_{96}BN_{11}$	$CuC_{32}H_{38}BN_7$
FW	1443.25	595.04
T [K]	100(2)	100(2)
λ [Å]	0.71073	0.71073
Crystal system	monoclinic	monoclinic
Space group	C2/c	$P2_1$
a [Å]	36.093(7)	10.6007(13)
b [Å]	10.7780(18)	9.7138(12)
c [Å]	19.854(3)	14.3402(17)
α [deg]	90	90
β [deg]	109.325(2)	93.002(2)
γ [deg]	90	90
V [Å^3]	7288(2)	1474.6(3)
Z	4	2
D_{calc} [mg m^{-3}]	1.315	1.340
Abs. coefficient [mm^{-1}]	0.639	0.775
F(000)	3048	626
Theta range [deg]	1.98 to 28.26	1.92 to 28.27
Comp. to theta [25.00°]	99.9 %	99.8 %
Max. and min. transmission	0.9811 and 0.8828	0.9623 and 0.9265
Data / restraints / param.	8379 / 0 / 461	6170 / 1 / 370
Goodness-of-fit on F2	1.114	1.006
R(F)[a] [I > 2σ(I)]	0.0426	0.0335
R(wF^2)[b] [I > 2σ(I)]	0.096	0.0686
Largest diff. peak and hole [e.Å^{-3}]	0.513 and -0.344	0.484 and -0.371

[a] $R = \Sigma||F_o| - |F_c||/\Sigma|F_o|$. [b] $R(\omega F^2) = \{\Sigma[\omega(F_o^2 - F_c^2)^2]/\Sigma[\omega(F_o^2)^2]\}^{1/2}$;
$\omega = 1/[\sigma^2(F_o^2) + (aP)^2 + bP]$, $P = [2F_c^2 + \max(F_o, 0)]/3$.

Table 6.2. Selected interatomic distances [Å] and angles [°] for complexes **15** and **16**.

$[Cu_2(tren)_2(dca)](BPh_4)_3$, 15			
Cu(1)-N(1)	2.0469(16)	**C(7)-N(6)-C(7′)**	**121.8(2)**
Cu(1)-N(2)	2.0374(16)	N(6)-C(7)-N(5)	173.7(2)
Cu(1)-N(3)	2.0333(17)	C(7)-N(5)-Cu(1)	153.65(16)
Cu(1)-N(4)	2.1548(17)	N(1)-Cu(1)-N(5)	171.47(7)
Cu(1)-N(5)	1.9589(16)		
N(5)-C(7)	1.156(3)		
C(7)-N(6)	1.297(2)		
$[Cu(tren)(dca)](BPh_4)$, 16			
Cu(1)-N(1)	2.0691(19)	**C(7)-N(6)-C(8)**	**119.9(2)**
Cu(1)-N(2)	2.138(2)	N(5)-C(7)-N(6)	173.2(3)
Cu(1)-N(3)	2.052(2)	N(7)-C(8)-N(6)	173.4(3)
Cu(1)-N(4)	2.0434(18)	C(7)-N(5)-Cu(1)	177.7(2)
Cu(1)-N(5)	1.9587(18)	N(4)-Cu(1)-N(5)	176.55(9)
N(5)-C(7)	1.146(3)		
C(7)-N(6)	1.308(3)		

6.2.3. Physical Measurements

FT-IR spectra were collected using a Thermo-Nicolet Avatar series spectrometer. Elemental analyses were performed by NuMega Resonance Labs (San Diego, CA) for **15** and **16**. Dc magnetic susceptibility measurements were collected on microcrystalline samples using a Quantum Design MPMS-5 magnetometer with a 5.5 Tesla magnet. Diamagnetic corrections of magnetic susceptibility data were made employing Pascal's constants.

6.3. Results and Discussion

6.3.1. Infrared Spectroscopy

The nitrile stretching region of the IR spectrum of **15** shows three distinct bands at 2350, 2275, and 2204 cm^{-1} corresponding to the $\nu_{as}+\nu_s$ (CN), ν_{as} (CN), and ν_s (CN) bands, respectively. These three frequencies also correspond very closely to those reported previously for the same compound with same nitriles streches occurring at 2350, 2275, and 2210 cm^{-1}.[12,27] Coordination of the ligand to the metal is evidenced by the shift of these bands to higher frequency as compared to those for free dca^- in its sodium salt which occur at 2286, 2232, and 2129 cm^{-1}.[16]

The IR spectrum of **16** also contains three nitrile stretches which are all shifted to lower frequencies; 2291, 2241, and 2178 cm^{-1} for $\nu_{as}+\nu_s$ (CN), ν_{as} (CN), and ν_s (CN), respectively, which are consistent with a monodentate dca^- ligand. Thus, complex **15** contains a bridging dca^- ligand while a terminal dca^- ligand is found in complex **16**. Interestingly, the IR spectra of the previously studied BF_4^-, ClO_4^-, and PF_6^- analogs of **15** show C≡N stretching bands that correspond more closely to those of the

mononuclear complex, **16**. For example, the PF_6^- salt has three C≡N stretches at 2290, 2220, and 2180 cm^{-1}, nearly identical to those found for **16**.[12,27] This new evidence indicates that only the BPh_4^- derivative of the previously studied series is in fact a dinuclear species while the others are likely to contain a monodentate dca^- ligand. This explains why only the BPh_4^- salt exhibits magnetic exchange across the dicyanamide bridge which will be further discussed in the Magnetic Susceptibility section.

6.3.2. Description of Crystal Structures

$[Cu_2(tren)_2(dca)](BPh_4)_3$ (15). Figure 6.4 shows an ORTEP of **15** which crystallizes in the monoclinic C2/c space group. The asymmetric unit contains one-half of the target molecule with the other half generated by the -x, y, -z + ½ symmetry transformation. The structure contains two *pseudo* trigonal-bipyramidal Cu(II) ions directly linked by a planar dicyanamide bridge. The dca^- ligand is coordinated axially to both Cu(II) ions in an end-to-end ($\mu_{1,5}$) bridging mode through the nitrile nitrogen atoms. The four remaining binding sites on each Cu(II) center are occupied by the four chelating nitrogen atoms of the tren ligands.

The dca^- bridge in **15** has a central C-N-C bridge angle of 121.8(2)° which clearly indicates a nonlinear bridge as expected from previous dca-linked dimers. In fact, this bridge angle falls within the expected range of most $\mu_{1,5}$-dca bridged complexes of first-row transition metals.[3-5,23,25,26] The $[Cu_2(tren)_2(dca)]^{3+}$ cation is balanced out by three BPh_4^- monoanions. A packing diagram can be found in Figure 6.5 which emphasizes how the BPh_4^- anions provide significant insulation between neighboring dinuclear units with the closest intermolecular Cu···Cu distance being > 10

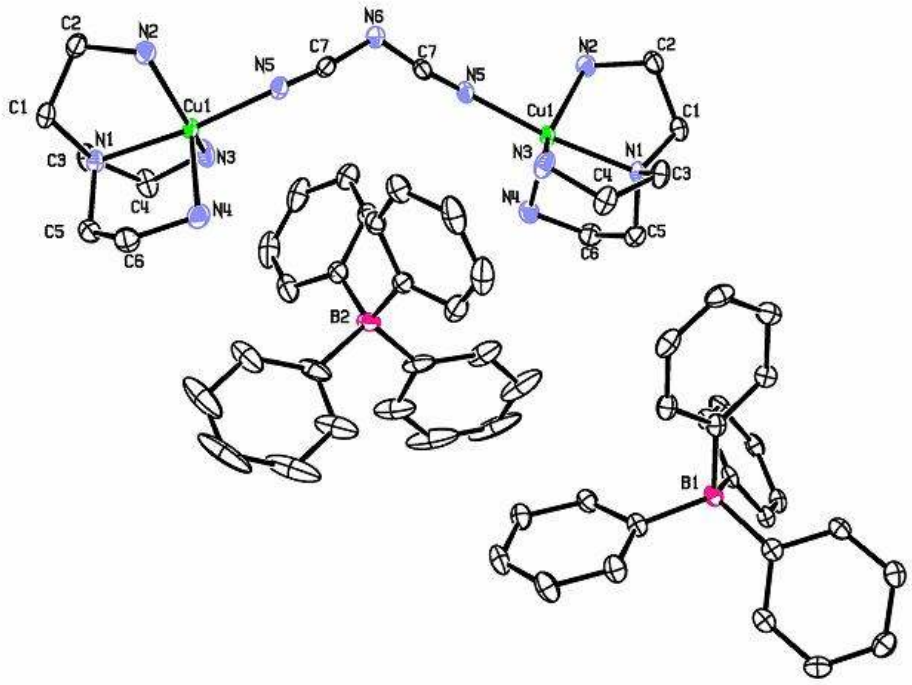

Figure 6.4. ORTEP of $[Cu_2(tren)_2(dca)]$ $(BPh_4)_3$ **(15)** with thermal ellipsoids drawn at 50% probability level and hydrogen atoms omitted for clarity.

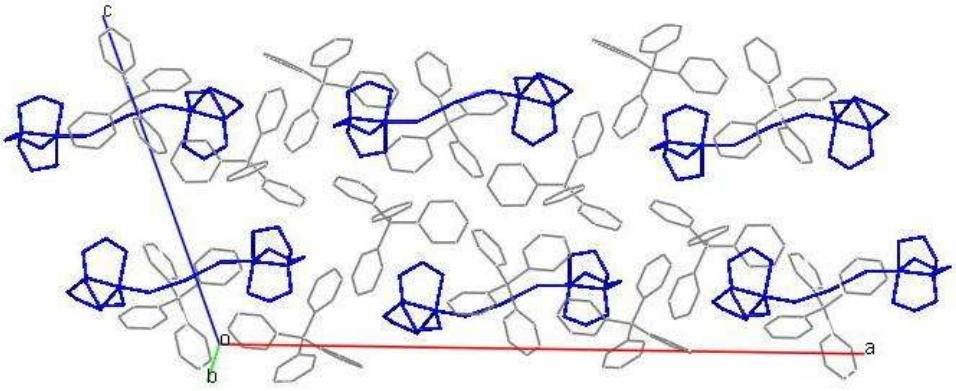

Figure 6.5. Crystal packing of $[Cu_2(tren)_2(dca)]$ $(BPh_4)_3$ **(15)** with the $[Cu_2(tren)_2(dca)]^{3+}$ units in blue and the BPh_4^- anions in grey.

Å. Therefore, no intermolecular H-bonding or van der Waals contacts are observed. Also, there are no solvent molecules co-crystallized with complex **15**.

[Cu(tren)(dca)](BPh$_4$) (16). Complex **16** crystallizes in the monoclinic P2$_1$ space group and an ORTEP of the structure can be found in Figure 6.6. The asymmetric unit contains one entire molecule with two mononuclear units per unit cell related by inversion. One BPh_4^- anion is found as the counterion in this crystal structure and no solvent molecules are present. Complex **16** contains one $[Cu(tren)]^{2+}$ moiety which is bound to a terminal dicyanamide ligand. The Cu(II) ion adopts a 5-coordinate trigonal-bipyramidal geometry with the four tren nitrogen atoms and one nitrile nitrogen atom of the dca^- ligand in an axial coordination site. Because the dca^- is not bridging in this molecule, the central C-N-C bridge angle is slightly smaller at 119.9(2)°. In **15**, the bridge angle increases slightly most likely to minimize cation-cation repulsion. The crystal packing of the $[Cu(tren)(dca)]^{1+}$ cation (Figure 6.7) shows intermolecular H-bonding interactions between the uncoordinated nitrile nitrogen atom of the terminal dca^- ligand and an amine proton from the tren ligand of an adjacent mononuclear unit.

The crystal structures of a similar Cu(II) dinuclear/mononuclear system have previously been reported. The $[Cu_2(bpy)_4(dca)](ClO_4)_3 \cdot 0.5$ EtOH dinuclear complex,[5] mentioned in the introduction to this chapter, contains two distorted trigonal-bipyramidal Cu(II) centers, a planar dca^- bridge, and a similar bridge angle. The central dca^- angle is 125.3(3)°, only slightly larger than the tren analog. Upon recrystallization of $[Cu_2(bpy)_4(dca)](ClO_4)_3$ from a mixture of ethanol and water, the mononuclear species, $[Cu(bpy)_2(dca)]ClO_4$,[5] is obtained. (Both structures are depicted in Figure 6.8.) The crystal structure is again very similar to that of the tren analog, **16**, in that the

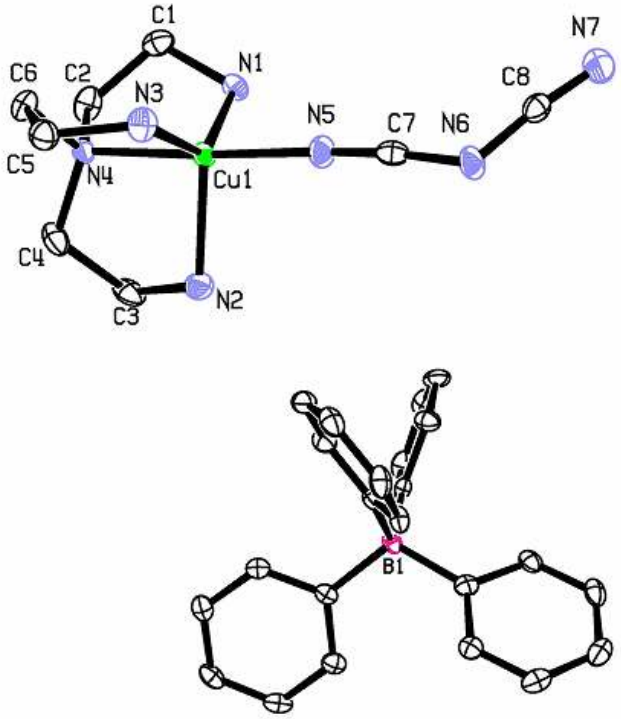

Figure 6.6. ORTEP of [Cu(tren)(dca)](BPh_4) **(16)** with thermal ellipsoids drawn at 50% probability level and hydrogen atoms omitted for clarity.

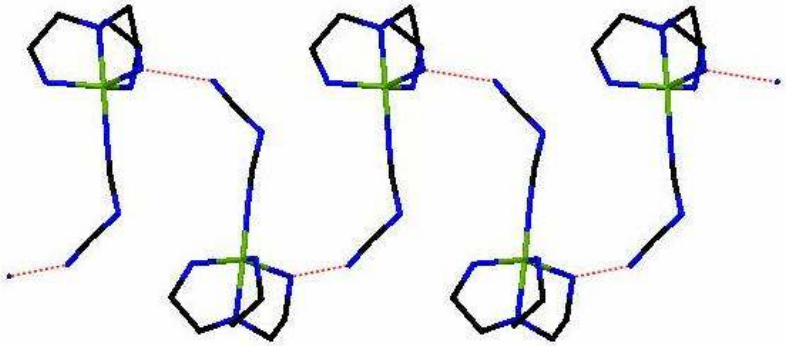

Figure 6.7 Intermolecular H-bonding pathway in [Cu(tren)(dca)](BPh_4) **(16)**.

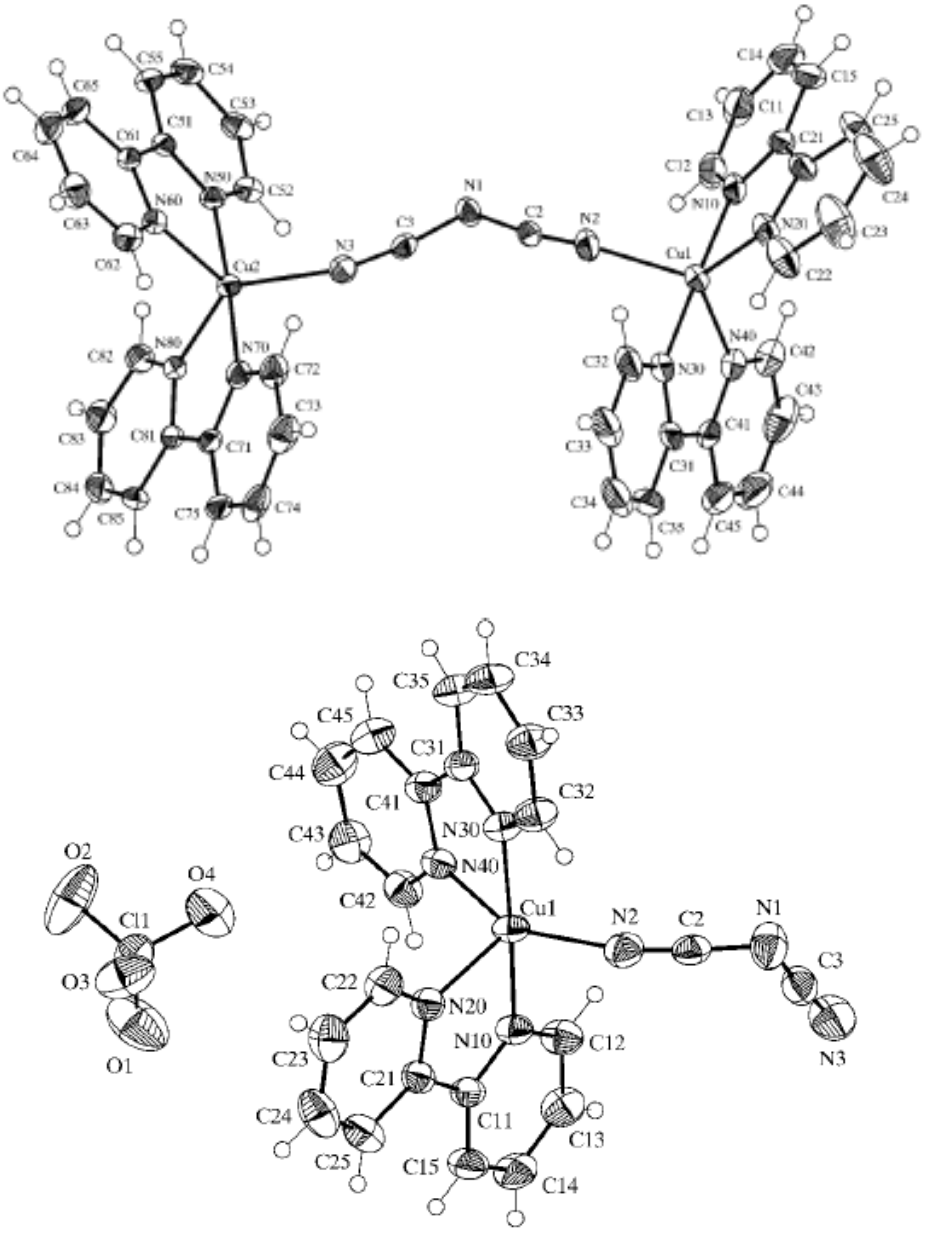

Figure 6.8. (top) The structure of $[Cu_2(bpy)_4(dca)](ClO_4)_3 \cdot 0.5$ EtOH and (bottom) $[Cu(bpy)_2(dca)]ClO_4$ with displacement ellipsoids drawn at 40% and 50% probability levels, respectively, and hydrogen atoms shown as small spheres of arbitrary radii.

Cu(II) ion exhibits distorted trigonal-bipyramidal geometry and the terminal dca^- ligand has a central C-N-C bridge angle of 119.4(2)°. However, the $[Cu(bpy)_2(dca)]^{1+}$ cation does not exhibit intermolecular hydrogen bonding interactions as seen in **16**.

6.3.3. Magnetic Susceptibility Studies

The effective magnetic moment, μ_{eff}, per Cu(II) ion is a convenient way of plotting and analyzing magnetic susceptibility data, particularly for symmetric dinuclear complexes. The values for μ_{eff} (measured in Bohr magneton or μ_B) can readily indicate the number of unpaired electrons per metal ion, effects of spin-orbit coupling, and the presence of exchange interactions as evident in the following magnetic susceptibility studies of **15** and **16**.

Figure 6.9 shows the μ_{eff}/Cu *vs. T* data for **15** collected in an applied magnetic field of 0.1 T and a temperature range of 300-1.8 K. The μ_{eff} at 300 K is ~1.8 μ_B (close to the value expected for one non-interacting unpaired electron per metal at 1.73 μ_B) and steadily decreases with temperature until about 25 K at which point the magnetization drops off dramatically to a final μ_{eff} of ~0.5 μ_B at 1.8 K. This decrease in μ_{eff} indicates that the two unpaired electrons in the complex are interacting with one another through antiferromagnetic exchange. The simple isotropic Heisenberg spin Hamiltonian for two interacting $S = 1/2$ spins, $\hat{H} = -2J\hat{S}_1\hat{S}_2$, was used to model this system and the data were fit to the Heisenberg-Dirac-Van Vleck formula,[28]

$$\chi_M = \left(\frac{Ng^2\mu_B^2}{3kT}\right)\frac{\sum[S_T(S_T+1)(2S_T+1)e^{\frac{-E(S_T)}{k_BT}}}{\sum(2S_T+1)e^{\frac{-E(S_T)}{k_BT}}} \qquad (6.1)$$

where χ is the molar magnetic susceptibility, J is the exchange parameter, g is the Landé g-tensor, S is the spin operator, $E(S_T)$ is the microstate eigenenergy, k_B is the Boltzman constant, and N is Avogadro's number.

The data in Figure 6.9 were fit over the entire temperature range with g = 2.1 and J = -5.6 K (-3.86 cm^{-1}) with a temperature-independent paramagnetism (TIP) term fixed at 120 x 10^{-6} cgsu, standard for two Cu(II) centers.[29] Complex **15** was also found to have a S = 0 ground state. Since there are no solvate molecules, H-bonding, or intermolecular contacts in the crystal packing of **15**, the primary pathway of the magnetic exchange is believed to be through the dca^- bridge as opposed to any intermolecular or through-space interactions.

To confirm the dca^- exchange pathway in **15**, the magnetic data for complex **16** were also determined. Because **16** is a mononuclear species with a terminal dca^- ligand, any observed magnetic exchange must be attributed to an H-bonding pathway between adjacent units or a direct dipole-dipole interaction between neighboring Cu(II) ions. Interestingly, the closest intermolecular Cu···Cu distance in the crystal lattice of **16** and the intramolecular Cu···Cu distance in **15** are both 7.6 Å (Figure 6.10). In 1974, Smith and Pilbrow[30] used the dipolar contribution to the zero-field splitting parameter, D_{dd}, as an estimate of the dipole-dipole interaction between two metals separated by a specific distance using the equation,

$$D_{dd} = 0.325\, g^2/R^3 \cdot (1-3\cos^2\theta), \qquad (6.2)$$

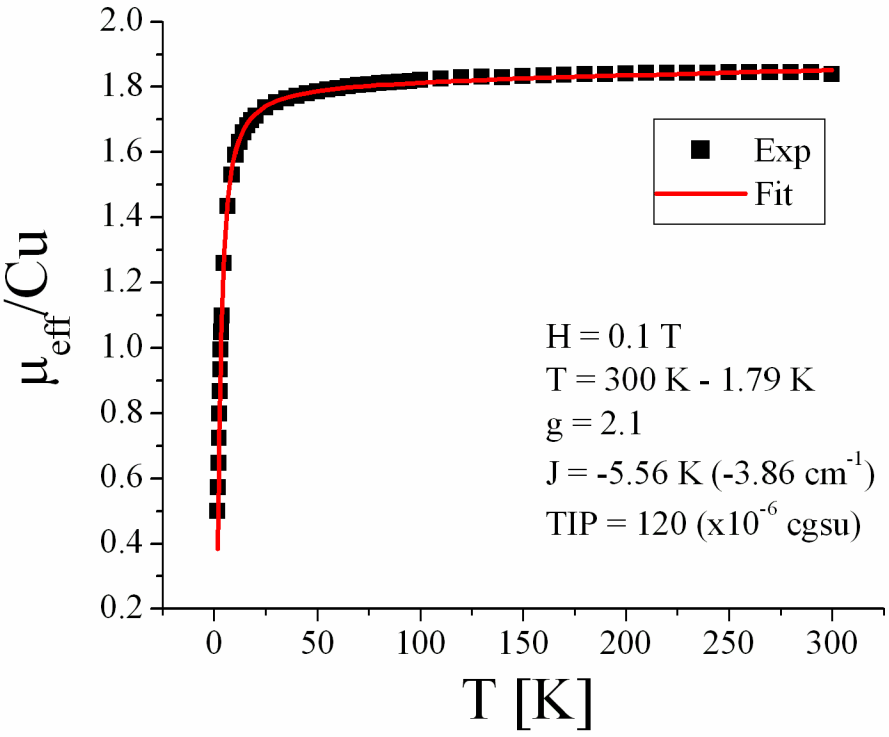

Figure 6.9. μ_{eff}/Cu vs. T for $[Cu_2(tren)_2(dca)]$ $(BPh_4)_3$ **(15)** with theoretical fit shown as solid red curve.

where g is the g_z value from EPR data (or from magnetic susceptibility data), R is the metal-metal distance in Å, and θ is the angle between the magnetic field and R.[30] Since D_{dd} is maximized when θ is zero, the equation can be simplified to

$$D_{dd} = 0.65\, g^2/R^3. \qquad (6.3)$$

With a Cu···Cu distance of 7.7 Å and a g-value of 2.1 from the $\chi_M T$ data, the maximum D_{dd} value for **15** or **16** is estimated to be 0.007 cm^{-1}. Thus, if a dipole-dipole exchange interaction does exist, it would only account for a very small portion of the total exchange calculated from the $\chi_M T$ data. However, as shown in Figure 6.11, the effective magnetic moment of **16** remains essentially constant over the entire temperature range of 300-1.8 K. Therefore, no magnetic exchange is observed in **16**, thus confirming that the antiferromagnetic coupling seen in **15** can be decisively assigned to through-bond exchange propagated solely by the dicyanamide bridge.

6.3.4. Structural Considerations

The geometry of the Cu(II) ion seems to play an important role in the magnetic interaction with the dicyanamide ligand. Using tren and structurally similar ligands such as 4-diethylenetriamineacetic acid, or dtma, is essential to the isolation of these dimers and their magnetic exchange pathways. These ligands force each Cu(II) ion into a 5-coordinate trigonal-bipyramidal geometry which helps prevent polymerization. The $Cu(tren)^{2+}$ species has also been found to be relatively resistant to reduction which is important when incorporating bridging ligands such as CN^- into the system.[3]

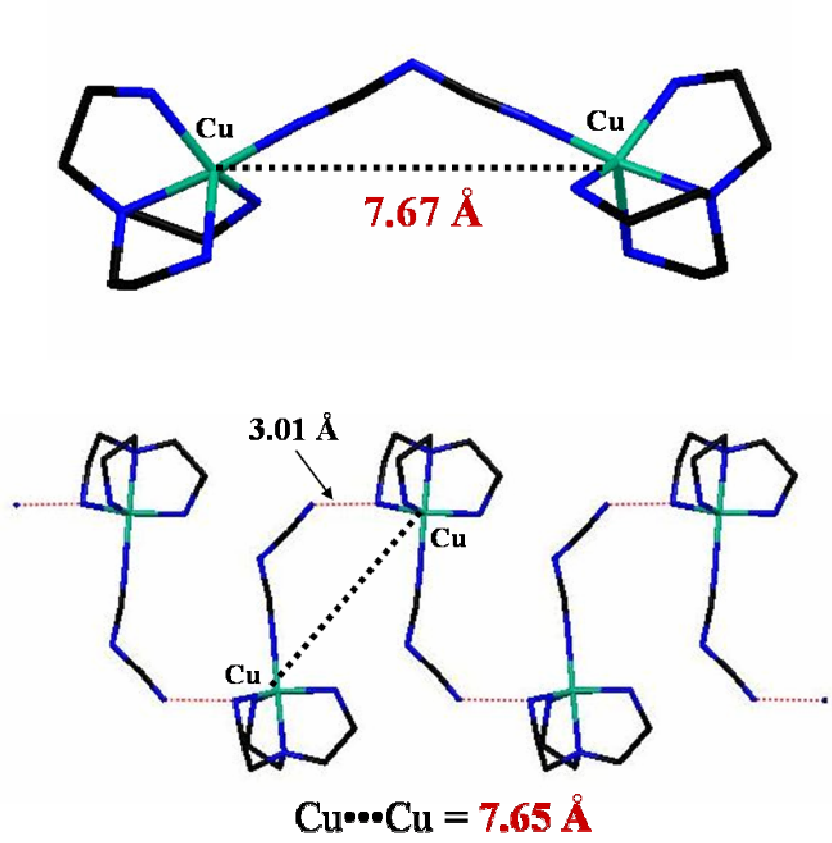

Figure 6.10. Through-space Cu(II)···Cu(II) distances in $[Cu_2(tren)_2(dca)](BPh_4)_3$ (**15**, top) and $[Cu(tren)(dca)](BPh_4)$ (**16**, bottom).

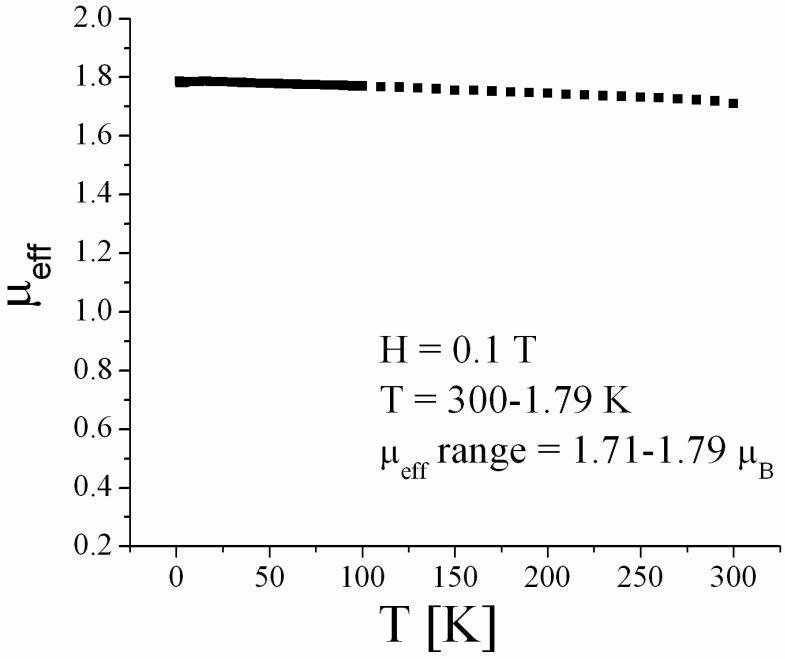

Figure 6.11. μ_{eff} *vs. T* for [Cu(tren)(dca)](BPh_4) **(16)** in applied field of 0.1 T.

Furthermore, the d-orbital splitting around a trigonal-bipyramidal d^9 Cu(II) ion places an unpaired electron in the d_{z^2} orbital. This situation is ideal for inducing magnetic exchange through a σ-bond pathway since the d_{z^2} orbital is pointed directly at the dca^- bridge which is bound in an axial fashion to the Cu(II) ion.

Table 6.3 lists some previously reported dinuclear complexes of Cu(II) with other bridging ligands along with their respective coupling constants. All of the *J*-values for these dinuclear complexes are negative (indicating antiferromagnetic exchange) but differ significantly in magnitude as the ligands and counterions are altered. As expected, the shorter bridging ligands such as imidazolate (im) and p-phenylenediamine (PPD) exhibit significantly larger coupling constants than the dca-bridged complexes.[13,14] Benzidine (BZD), as shown in the dinuclear Cu(II) species in Figure 6.12, has considerable π-character but only facilitates weak antiferromagnetic coupling of roughly the same magnitude found in **15**. Also, though the phenyl rings of the benzidine bridge are planar, they form dihedral angles of 13.8° and 22.5° with respect to the connecting C-C bond.[14] With appropriate overlap of orbitals, increased π-interactions between the metal d-orbitals and the bridging ligand could enhance the intramolecular magnetic exchange. However, these studies have shown that the major contributor to superexchange in these examples is through the σ-pathway. [13-15]

Though the antiferromagnetic exchange in **15** is small compared to some other commonly used bridging ligands, it is the largest [Cu(II)-dca-Cu(II)] interaction reported to date. Other than the three dinuclear Cu(II) complexes discussed in the introduction, the remaining dca-bridged Cu(II) complexes in the literature form 1D chains as well as 2D and even 3D arrays containing both single and double dca^- bridges.

Table 6.3. Coupling constants (J) for **15** and selected dinuclear Cu(II) complexes.

Complex	**J** [cm^{-1}]	**Reference**
$[Cu_2(tren)_2(dca)](BPh_4)_3$, **(15)**	**-3.9**	*this work*
$[Cu_2(tren)_2(BZD)]Y_4$	**-4.5, -3.7, -3.3** (for Y = NO_3^-, ClO_4^-, and PF_6^-)	*14*
$[Cu_2(tren)_2(PPD)]Y_4$	**-35.1, -26.2, -19.8** (for Y = NO_3^-, ClO_4^-, and PF_6^-)	*14*
$[Cu_2(tren)_2(DDA)](PF_6)$	**-17.6**	*14*
$[Cu_2(tren)_2(im)](ClO_4)$	**-38**	*13*
$[Cu_2(dtma)_2(im)](ClO_4)$	**-47**	*13*
$[Cu_2(dien)_2(\mu\text{-}Me_2dicyd)](CF_3SO_3)_2$	**-10.63**	*15*
$[Cu_2(dien)_2(\mu\text{-}Cl_2dicyd)](CF_3SO_3)_2$	**-4.5**	*15*

BZD is benzidine, *PPD* is p-phenylenediamine, *DDA* is durenediamine, *im* is imidazole, *dtma* is 4-diethylenetriamineacetic acid, and *Me_2dicyd* and *Cl_2dicyd* are 2,5-dimethyl- and 2,5-dichloro-1,4-dicyanamidobenzene, respectively.

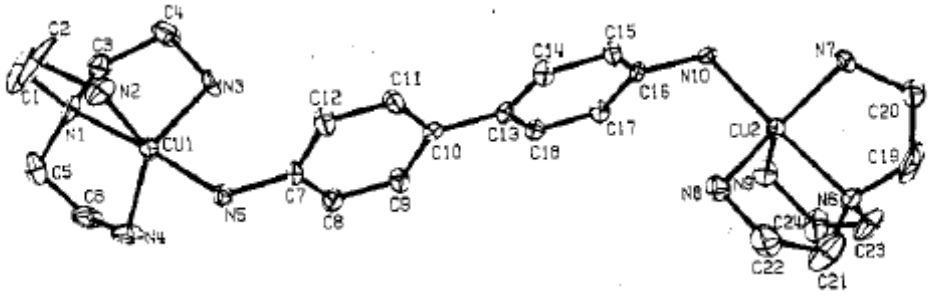

Figure 6.12. ORTEP of $[Cu_2(tren)_2(BZD)](NO_3)_4$ with nitrate anions and hydrogen atoms omitted for clarity.

Table 6.4. Coupling constants (*J*) for selected single dca-bridged Cu(II) networks.

Complex	**J** [cm^{-1}]	**Reference**
$[Cu(Hambi)(dca)_2]$	**-0.33**	*6*
$[Cu(pn)(dca)_2]_n$	**-0.76**	*7*
$[Cu_2(L^1)_2(dca)_2]_2$	**-0.44**	*8*
$[Cu(dmphen)(dca)(NO_3)]_n$	**-0.57**	*5*
$[Cu(et_2\text{-}en)(dca)_2]_n$	**-0.58**	*9*
$[Cu(L^2)]_2(dca)(ClO_4)$	**-0.20**	*4*
$[Cu(L^3)(dca)]_n$	**-1.41**	*10*
$[Cu(L^4)(dca)_2]_n$	**-0.35**	*11*

Hambi is 2-aminomethylbenzimidazole, *pn* is 1,2-diaminopropane, L^1 is 1,5,9-triazacyclododecane, *dmphen* is 2,9-dimehtyl-1,10-phenanthroline, et_2-*en* is N,N-diethyl-ethylendiamine, L^2 is N,N-dimethylehtylene-N′-salicylaldiiminato, L^3 is $C_6H_5C(O)(CHC(CH_3)=NCH_2CH_2N(CH_3)_2$, and L^4 is N,N-diethyl-1,2-ethanediamine.

As mentioned previously, these complexes often exhibit weak antiferromagnetic coupling which is mainly attributed to through-bond interactions across the dca^- bridges despite the presence of possible alternative magnetic exchange pathways. Table 6.4 gives a list of single dca-bridged Cu(II) networks and their coupling constants for comparison. In most of these selected complexes, the antiferromagnetic exchange is an order of magnitude smaller than the *J*-value found for **15** (J = -3.9 cm^{-1}).[4,6-11,26] Though this exchange parameter seems high in comparison to other [Cu(II)-dca-Cu(II)] interactions, the absence of any intermolecular contacts in the crystal structure as well as the magnetic data for the mononuclear species confirms that this interaction is propagated solely by the $\mu_{1,5}$-dca bridge.

6.3.5. Implications for Dicyanamide-Linked SMMs

Recently, the dicyanamide ligand has been used to covalently link [Mn_4] dicubane single-molecule magnets (SMMs): $[Mn_4(hmp)_4(Hpdm)_2(dca)_2](ClO_4)_2 \cdot 2H_2O \cdot 2MeCN$, $[Mn_4(hmp)_4Br_2(OMe)_2(dca)_2] \cdot 0.5H_2O \cdot 2THF$, and $[Mn_4(hmp)_6(dca)_2](ClO_4)_2$,[23] where Hhmp and H_2pdm are 2-hydroxymethylpyridine and pyridine-2,6-dimethanol, respectively (see Figure 6.2). Each $[Mn^{II}_2Mn^{III}_2]$ double cuboidal core has an S = 9 ground state as a result of both Mn(II)-Mn(III) and Mn(III)-Mn(III) ferromagnetic coupling. All three complexes form 2D-networks of dca-linked [Mn_4] units. In $[Mn_4(hmp)_6(dca)_2](ClO_4)_2$, a canted antiferromagnetic interaction between the anisotropic [Mn_4] SMMs was observed. The coupling constant (*J*) for this exchange pathway was found to be -0.06 K (-0.04 cm^{-1}) which is consistent with other [Mn(II)-dca-Mn(II)] interactions and is well-known to be weakly antiferromagnetic.

Though there are weak interlayer π–π interactions present in this network, the primary pathway of the magnetic coupling is presumed to be through the dicyanamide bridges.[23]

Based on this data, the [Cu(II)-dca-Cu(II)] interaction seems to be a much stronger exchange pathway than that of the [Mn(II)-dca-Mn(II)] interaction found in these dicyanamide-linked SMMs. Several factors are thought to explain this observation. First, the Cu(II)-N bond is more covalent in nature than the Mn(II)-N bond[31] and thus a stronger interaction with the dicyanamide ligand is expected to occur in the Cu(II) case. The Cu(II)-N (nitrile of dca ligand) distance in **15** is 1.96 Å whereas the average Mn(II)-N distance in the dca-linked [Mn_4] network is slightly longer at 2.17 Å. Second, the Mn(II) ions in $[Mn_4(hmp)_6(dca)_2](ClO_4)_2$ adopt a 6-coordinate *pseudo*-octahedral geometry which leads to less favorable overlap of the metal d-orbitals containing unpaired electrons and the orbitals of the bridging ligand. Lastly, the Mn(II) ions in adjacent [Mn_4] units are doubly-bridged by two dca^- ligands. This leads to multiple exchange pathways between the clusters which distribute the magnetic interaction over a larger area, thus diminishing the magnitude of any single pathway.

Using bridging ligands like dicyanamide provides a powerful synthetic tool for directing intermolecular exchange in SMMs. As described in the Introduction Chapter, many quantum phenomena have been observed as a result of such interactions. Understanding and gaining control over these intermolecular interactions can further tune and enhance the intrinsic properties of SMMs.[3]

6.4. Conclusions

The crystal structures of both **15** and **16** are consistent with the literature in terms of Cu(II) geometry, bridge angles, and the possible binding modes of dca^- in Cu(II) complexes. Complex **15** exhibits antiferromagnetic exchange with a coupling constant of -5.6 K (or -3.9 cm^{-1}) which is the largest Cu(II)-dca-Cu(II) magnetic interaction known to date. In fact, the coupling in **15** is even larger than two Cu(II) ions doubly-bridged by dicyanamide which is typically twice the magnitude of a single dca^- bridge.[32] The surprisingly large antiferromagnetic interaction in **15** was established by the fact that there are no other possible intermolecular pathways present in the crystal structure and there is no magnetic exchange observed in the mononuclear complex **16**.

The mononuclear complex, **16**, shows no magnetic coupling despite extensive intramolecular H-bonding and a Cu···Cu distance of 7.7 Å (equivalent to the intramolecular Cu···Cu distance in **15**) which rules out any direct dipole-dipole exchange in **15**. Thus, the major pathway for magnetic coupling in **15** can be definitively attributed to a through-bond interaction across the dca^- bridge.

Though the exchange is only weakly antiferromagnetic, the Cu(II)-dca bridge exhibits a stronger interaction than the Mn(II)-dca linkage, as expected. This study has successfully demonstrated that the dicyanamide ion is capable of propagating a much greater magnetic exchange interaction between Cu(II) ions than previously reported. An appreciable antiferromagnetic exchange interaction can indeed be supported by an end-to-end dicyanamide bridge by optimizing orbital overlap between the ligand and the metal centers. Finally, with a better understanding of the magnetic exchange across a discrete dicyanamide linkage, this work has shown the promise of dicyanamide as a

viable superexchange pathway for further tuning of the intermolecular interactions in SMMs.

This chapter includes material currently being prepared for submission for publication: Heroux, K. J.; DiPasquale, A. G.; Rheingold, A. L.; Hendrickson, D. N. "The viability of dicyanamide as a superexchange pathway between paramagnetic metal centers". The dissertation author was the primary investigator and author of this paper.

6.5. References

(1) Anderson, P. W. *Physical Review,* **1950**, *70(2)*, 350-356.

(2) Kramers, H. A. *Physica*, **1934**, *1*,182.

(3) Felthouse, T. R.; Hendrickson, D. N. *Inorg. Chem.* **1978**, *17(9),* 2636.

(4) Carranza, J.; Sletten, J.; Lloret, F.; Julve, M. *Inorg. Chim. Acta.* **2004**, *357*, 3304-3316.

(5) Wang, Z. D.; Han, W.; Yan, S. P.; Liao, D. Z.; Jiang, Z. H.; Cheng, P. *Acta Cryst.* **2004**, *E60*, m1137-m1138.

(6) Kou, H. Z.; He, Y. *Chem. Lett.* **2003**, *32(10),* 902-903.

(7) Chen, X. Y.; Cheng, P.; Zhao, B.; Yan, S. P.; Liao, D. Z.; Jiang, Z. H. *J. Mol. Struct.* **2003**, *655*, 179-184.

(8) Gu, W.; Bian, H. D.; Xu, J. Y.; Liu, Z. Q. ; Cheng, P. ; Yan, S. P.; Liao, D. Z. ; Jiang, Z. H. *Inorg. Chem. Comm.* **2003**, *6*, 966-970.

(9) Konar, S.; Dalai, S.; Ribas, J.; Drew, M. G. B.; Zangrando, E.; Chaudhuri, N. R. *Inorg. Chim. Acta.* **2004**, *357*, 4208-4214.

(10) Sen, S.; Mitra, S.; Hughes, D. L.; Rosair, G.; Desplaches, C. *Inorg. Chim. Acta*. **2007**, *360*, 4085-4092.

(11) Mal, D.; Tuchagues, J. P.; Chakraborty, S.; Mukherjee, A. K.; Sen, R.; Koner, S. *Inorg. Chim. Acta*. **2006**, *359*, 4431-4435.

(12) Bieksza, D. S.; Hendrickson, D. N. *Inorganic Chemistry* **1977**, *16*, 924-929.

(13) Zongwan, M.; Degang, F.; Qinwei, H.; Wenxia, T.; Kaibei, Y. *Polyhedron*. **1993**, *12(12),* 1465- 1469.

(14) Felthouse, T. R.; Hendrickson, D. N. *Inorg. Chem.* **1978**, *17(9),* 2636.

(15) Cheruiyot, L. L.; Thompson, J. E.; Greedan, J. E.; Liu, G.; Crutchley, R. J. *Can. J. Chem*. **1995**, *73*, 573-580.

(16) Armentano, D.; De Munno, G.; Guerra, F.; Julve, M.; Lloret, F. *Inorg. Chem.* **2006**, *45*,4626-4636.

(17) Wernsdorfer, W.; Allaga-Alcalde, N.; Hendrickson, D. N.; Christou, G. *Nature* **2002**, *416*, 406-409.

(18) Yang, E. C.; Harden, N.; Wernsdorfer, W.; Zakharov, L.; Brechin, E. K.; Rheingold, A. L.; Christou, G.; Hendrickson, D. N. *Polyhedron* **2003**, *22*, 1857-1863.

(19) Yang, E. C.; Wernsdorfer, W.; Zakharov, L. N.; Karaki, Y.; Yamaguchi, A.; Isidro, R. M.; Lu, G. D.; Wilson, S. A.; Rheingold, A. L.; Ishimoto, H.; Hendrickson, D. N. *Inorganic Chemistry* **2006**, *45*, 529-546.

(20) Ramsey, C. M.; del Barco, E.; Hill, S.; Shah, S. J.; Beedle, C. C.; Hendrickson, D. N. *Nat Phys* **2008**, *4*, 277-281.

(21) Henderson, J. J.; Koo, C.; Feng, P. L.; del Barco, E.; Hill, S.; Tupitsyn, I. S.; Stamp, P. C. E.; Hendrickson, D. N. *Physical Review Letters* **2009**, *103*, 017202.

(22) Hill, S.; Edwards, R. S.; Aliaga-Alcalde, N.; Christou, G. *Science* **2003**, *302*, 1015-1018.

(23) Miyasaka, H.; Nakata, K.; Lecren, L.; Coulon, C.; Nakazawa, Y.; Fujisaki, T.; Sugiura, K.; Yamashita, M.; Clerac, R. *J. Am. Chem. Soc*. **2006**, *128(11),* 3770- 3783.

(24) Shi, Q.; Hu, M. L.; Xiao, H. P.; Li, X. H. *Inorg. Chem. Comm*. **2005**, *8*, 1169-1172.

(25) Potočňák, I.; Burčák, M.; Massa, W.; Jäger, L. *Acta Cryst.* **2002**, *C58*, m523-m528.

(26) Karmakar, R.; Choudhury, C. R.; Hughes, D. L.; Yap, G. P. A.; El Fallah, M. S.; Desplanches, C.; Sutter, J. P.; Mitra, S. *Inorg. Chim. Acta.* **2006**, *359*, 1184-1192.

(27) David. S. Bieksza, *Ph.D. Thesis*, University of Illinois at Urbana-Champaign, 1978.

(28) Van Vleck, J. H. *The Theory of Electric and Magnetic Susceptibilities*; Oxford Univ. Press., 1965.

(29) Kahn, O. *Molecular magnetism*; VCH: New York, NY, **1993**.

(30) (a) Smith, T. D. and Pilbrow, J. R. *Coord. Chem. Rev.* **1974**, *13*, 173. (b) Francesconi, L. C.; *Ph.D. Thesis*, University of Illinois at Urbana-Champaign, **1980**.

(31) Wayland, B.B.; Drago, R. S. *J. Am. Chem. Soc.* **1965**, *87(11),* 2372.

(32) Manson, J. L.; Schlueter, J. A.; Nygren, C. L. *Dalton Trans*. **2007**, 646-652.